

# Proton Conduction and Gas Permeation through Polymer Electrolyte Membranes during Water Electrolysis

Maximilian Schalenbach

Energie & Umwelt / Energy & Environment Band / Volume 426 ISBN 978-3-95806-333-4



Forschungszentrum Jülich GmbH Institut für Energie- und Klimaforschung Elektrochemische Verfahrenstechnik (IEK-3)

# Proton Conduction and Gas Permeation through Polymer Electrolyte Membranes during Water Electrolysis

Maximilian Schalenbach

Schriften des Forschungszentrums Jülich Reihe Energie & Umwelt/Energy & Environment Bibliografische Information der Deutschen Nationalbibliothek. Die Deutsche Nationalbibliothek verzeichnet diese Publikation in der Deutschen Nationalbibliografie; detaillierte Bibliografische Daten sind im Internet über http://dnb.d-nb.de abrufbar.

Herausgeber Forschungszentrum Jülich GmbH

und Vertrieb: Zentralbibliothek, Verlag

52425 Jülich

Tel.: +49 2461 61-5368 Fax: +49 2461 61-6103 zb-publikation@fz-juelich.de

www.fz-juelich.de/zb

Umschlaggestaltung: Grafische Medien, Forschungszentrum Jülich GmbH

Druck: Grafische Medien, Forschungszentrum Jülich GmbH

Copyright: Forschungszentrum Jülich 2018

Schriften des Forschungszentrums Jülich Reihe Energie & Umwelt / Energy & Environment, Band / Volume 426

D 82 (Diss., RWTH Aachen University, 2018)

ISSN 1866-1793 ISBN 978-3-95806-333-4

Vollständig frei verfügbar über das Publikationsportal des Forschungszentrums Jülich (JuSER) unter www.fz-juelich.de/zb/openaccess.



This is an Open Access publication distributed under the terms of the <u>Creative Commons Attribution License 4.0</u>, which permits unrestricted use, distribution, and reproduction in any medium, provided the original work is properly cited.

#### **Abstract**

Water electrolysis is an effective, durable and emission free technique to convert electrical energy by the electrochemical decomposition of water into chemical energy. During water electrolysis in an acidic electrolyte, water is oxidized to oxygen and protons at the anode. The protons permeate through the electrolyte to the cathode where they are reduced to hydrogen. Acidic polymer electrolyte membranes (PEMs) are typically used to provide the proton conductivity between the electrodes and to separate the evolved gases. The proton conduction in PEMs takes place in an aqueous phase in the form of water channels that are separated from the solid polymeric phase. This thesis is dedicated to a multiscale description of the permeation of protons and gases through PEMs during water electrolysis, characterizing the physical processes within the microscopic structure of PEMs (in the order of  $10^{-9}$  m) and the resulting macroscopic efficiency loss.

In the literature, the best characterized PEM is Nafion<sup>®</sup>, which serves as an exemplary material for the physical transport processes in PEMs. Using impedance spectroscopy, the proton conductivity of Nafion<sup>®</sup> membranes was measured to be constant in a frequency range of three orders of magnitude and below amplitudes of 1 V. By relating the length scale of the proton movement in Nafion<sup>®</sup> to the applied frequencies and voltages, the conduction was found to be independent of scattering processes between protons and pore walls of the water channels. Moreover, the conductivity of an aqueous solution with similar proton concentration as the water channels in Nafion<sup>®</sup> was found to be  $6.0 \pm 0.7$  times higher than that of Nafion<sup>®</sup> membranes. The origins for this reduced macroscopic conductivity were ascribed to microscopic geometric restrictions for the proton permeation through the morphology of the aqueous phase.

By using the electrochemical monitoring technique, the gas permeability of Nafion<sup>®</sup> membranes was measured to be independent of pressure, which was explained by a solely diffusive permeation process. The alternating permeation through the aqueous phase, solid phase and their intermediate phase was modeled with a resistor network that represents the microscopic structure of Nafion<sup>®</sup>. By comparing measured and modeled hydrogen permeabilities of Nafion<sup>®</sup>, water was estimated to act as a plasticizer that increases the permeability of the solid polymeric phase. The conductivities and permeabilities of six different PEMs were examined and compared.

A model to describe the hydrogen and oxygen cross-permeation through PEMs during water electrolysis was developed, in which the influence of the proton flux on the gas diffusion was physically described. This model was evaluated with measured anodic hydrogen contents of an operating electrolysis cell. Based on this model and the measured proton conductivity and gas permeability of Nafion<sup>®</sup>, the efficiency loss caused by the proton conduction and gas cross-permeation during water electrolysis was modeled and used to computationally optimize the membrane thickness. To reduce the efficiency loss that is caused by the hydrogen cross-permeation through the PEM during water electrolysis, a novel technique with an additional electrode in the electrolyte was introduced, where hydrogen in the PEM is electrochemically oxidized and sent back to the cathode. In the focus of efficiency, pressurized operation and atmospheric pressure operation in combination with subsequent compression were compared.

# Kurzfassung

Wasserelektrolyse ist eine effektive, langlebige und emissionsfreie Technologie um elektrische Energie durch die elektrochemische Zersetzung von Wasser in chemische Energie umzuwandeln. Bei der Wasserelektrolyse in sauren Elektrolyten wird Wasser an der Anode zu Sauerstoff und Protonen oxidiert. Die Protonen permieren durch den Elektrolyten zur Kathode und werden dort zu Wasserstoff reduziert. Saure Polymerelektrolytmembranen (PEM) werden typischerweise benutzt um die Protonenleitfähigkeit zwischen den Elektroden zu gewährleisten und um die produzierten Gase zu separieren. Die Protonenleitung in PEMs findet in einer wässrigen Phase in der Form von Wasserkanälen statt, welche von der polymeren Phase getrennt sind. Diese Arbeit ist der Beschreibung der Protonen- und Gaspermeation durch die PEM während der Wasserelektrolyse gewidmet, wobei physikalische Prozesse auf mikroskopischer Ebene der PEM (GröSSenordnung von  $10^{-9}$  m) sowie der makroskopische Effizienzverlust charakterisiert werden.

Die in der Literatur am besten charakterisierte PEM ist Nafion<sup>®</sup>, an der exemplarisch die physikalischen Transportprozesse in PEMs untersucht werden. Mittels Impedanzspektroskopie wurde innerhalb von drei Frequenzdekaden und unterhalb von Amplituden von 1 V eine konstante Protonenleitfähigkeit gemessen. Durch Berechnung der Längenskala der Protonenpermeation als Funktion der Frequenz und Amplitude konnte gezeigt werden, dass die Leitfähigkeit nicht von Streuprozessen an Porwänden beeinflusst wird. Wässrige Lösungen mit der gleichen Protonenkonzentration wie in den Wasserkanälen von Nafion<sup>®</sup> zeigten eine  $6.0 \pm 0.7$  Mal höhere Leitfähigkeit als jene von Nafion<sup>®</sup> selbst. Die Ursachen für die reduzierte makroskopische Leitfähigkeit wurden mit geometrischen Einschränkungen der Protonenpermeation durch die Morphologie der wässrigen Phase begründet.

Durch Verwendung elektrochemischer Messmethoden wurde gezeigt, dass die Gaspermeabilität von Nafion<sup>®</sup> druckunabhängig ist, was auf einen diffusiven Permeationsprozess zurückzuführen ist. Die wechselnde Permeation durch die wässrige, polymere und dazwischenliegende Phase wurde mit einem Widerstandsnetzwerk welches die mikroskopische Struktur von Nafion<sup>®</sup> wiedergibt simuliert. Der Vergleich von gemessenen und simulierten Wasserstoffpermeabilitäten ergab, dass Wasser als Weichmacher agiert und damit die Permeabilität der polymeren Phase erhöht.

Die Wasserstoff- und Sauerstoffpermeation durch die PEM während der Wasserelektrolyse wurde durch ein physikalisches Modell beschrieben, das die Wechselwirkung zwischen Protonen- und Gaspermeation berücksichtigt. Dieses Modell wurde mit gemessenen anodischen Wasserstoffgehältern einer Elektrolysezelle evaluiert. Basierend auf diesem Modell und den gemessenen Leitfähigkeiten sowie Permeabilitäten wurden Effizienzverluste durch die Protonenleitung und den Gasdurchtritt in Elektrolysezellen in Abhängigkeit der Membrandicke simuliert. Um den Effizienzverlust durch den Wasserstoffdurchtritt zu reduzieren, wurde eine neue Technik mit einer zusätzlichen Elektrode im Elektrolyten entwickelt, an der Wasserstoff in der PEM oxidiert und zurück zur Kathode geschickt wird. Auf der Grundlage des aufgestellten Modells wurde die Effizienz von Druckbetrieb im Vergleich zu Niederdruckbetrieb in Kombination mit nachfolgender mechanischer Komprimierung diskutiert.

# **Contents**

| 1 | Intr | oduction  | 1  |  |  |  |  |
|---|------|---|----|--|--|--|--|
| 2 | Fun  | damentals   | 5  |  |  |  |  |
|   | 2.1  | Water electrolysis  | 5  |  |  |  |  |
|   |      | 2.1.1 Thermodynamics  | 5  |  |  |  |  |
|   |      | 2.1.2 Voltage-current characteristic                                    | 9  |  |  |  |  |
|   |      | 2.1.3 Setup   | 12 |  |  |  |  |
|   |      | 2.1.4 Cell efficiency   | 14 |  |  |  |  |
|   |      | 2.1.5 Gas crossover and safety issues                                   | 16 |  |  |  |  |
|   | 2.2  | Proton conduction in aqueous solutions and PEMs                         | 16 |  |  |  |  |
|   |      | 2.2.1 Physical description of the ionic conductivity                    | 18 |  |  |  |  |
|   |      | 2.2.2 Ionic conductivities at ACs and DCs                               | 19 |  |  |  |  |
|   | 2.3  | Gas diffusion   | 21 |  |  |  |  |
|   |      | 2.3.1 Permeability, diffusion and solubility                            | 21 |  |  |  |  |
|   |      | 2.3.2 Polymers  | 22 |  |  |  |  |
|   |      | 2.3.3 Water   | 23 |  |  |  |  |
|   | 2.4  | Characteristics of polymer electrolyte membranes                        | 25 |  |  |  |  |
|   | 2.5  | Thermodynamics of gas compression                                       | 27 |  |  |  |  |
| 3 | Ove  | erview of current literature  | 30 |  |  |  |  |
|   | 3.1  | Structure and water content of Nafion $^{\circledR}$                    |    |  |  |  |  |
|   | 3.2  | Conductivity of Nafion <sup>®</sup>                                     |    |  |  |  |  |
|   | 3.3  | Gas permeability of Nafion <sup>®</sup>                                 | 32 |  |  |  |  |
|   | 3.4  | Gas purities during water electrolysis                                  | 33 |  |  |  |  |
| 4 | Met  | hods  | 35 |  |  |  |  |
|   | 4.1  | Impedance spectroscopy  | 35 |  |  |  |  |
|   | 4.2  | Electrochemical monitoring technique                                    | 37 |  |  |  |  |
|   |      | 4.2.1 Measurement principle   | 37 |  |  |  |  |
|   |      | 4.2.2 Setups  | 38 |  |  |  |  |
|   | 4.3  | Resistor network modeling   | 42 |  |  |  |  |
|   | 4.4  | Measurement of the anodic hydrogen content                              | 42 |  |  |  |  |
| 5 | Pro  | ton conduction in Nafion®   | 46 |  |  |  |  |
|   | 5.1  | Scattering of protons at pore walls                                     | 46 |  |  |  |  |
|   |      | 5.1.1 Impedance spectra of Nafion®                                      | 46 |  |  |  |  |
|   |      | 5.1.2 Movement of the protons in the water channels                     | 48 |  |  |  |  |
|   | 5.2  | Conductivities of Nafion $^{\circledR}$ membranes and aqueous solutions | 50 |  |  |  |  |

IV Contents

|   | 5.3 | Physic   | cal effects that reduce the proton conductivity of Nafion $^{\circledR}$ $\dots$ | 54  |
|---|-----|----------|--|-----|
|   | 5.4 | Synop    | osis of the chapter  | 55  |
| 6 | Нус | lrogen   | and Oxygen Permeabilities of Nafion®   | 57  |
|   | 6.1 | Influe   | nce of ambient conditions  | 57  |
|   |     | 6.1.1    | Pressure   | 57  |
|   |     | 6.1.2    | Relative humidity  | 59  |
|   |     | 6.1.3    | Temperature  | 61  |
|   | 6.2 | Influe   | nce of the solubilities  | 65  |
|   | 6.3 | Pathw    | vays for the gas permeation  | 66  |
|   | 6.4 |          | osis of the chapter  | 67  |
| 7 | Res | istor ne | etwork modeling of the gas permeation through Nafion®                            | 69  |
|   | 7.1 |          | l development  | 69  |
|   |     | 7.1.1    | Resistor network model   | 70  |
|   |     | 7.1.2    | Permeabilities of the aqueous and solid phase                                    | 76  |
|   |     | 7.1.3    | Simulation of the gas permeability   | 79  |
|   | 7.2 | Appli    | cation of the model to the experimental data                                     | 82  |
|   |     | 7.2.1    | Variation of the intermediate phase  | 82  |
|   |     | 7.2.2    | Variation of the solid phase   | 84  |
|   |     | 7.2.3    | Deviations from the Boltzmann distribution                                       | 85  |
|   | 7.3 | Discu    | ssion  | 87  |
|   |     | 7.3.1    | Increased permeability of the intermediate phase                                 | 88  |
|   |     | 7.3.2    | Softening of the solid phase   | 89  |
|   |     | 7.3.3    | Influence of the water content on the modeled permeability                       | 90  |
|   |     | 7.3.4    | Impact of the different phases   | 90  |
|   |     | 7.3.5    | Improvement of PEMs  | 91  |
|   | 7.4 | Synop    | osis of the chapter  | 93  |
| 8 | Cha | racteriz | zation of different polymer electrolyte membranes                                | 95  |
|   |     |          | uctiviities  | 96  |
|   | 8.2 | Perme    | eabilities   | 97  |
|   | 8.3 |          | of conductivities to permeabilities  | 98  |
|   | 8.4 |          | osis of the chapter  | 99  |
| 9 | Gas | perme    | ation through the membrane during water electrolysis                             | 100 |
|   | 9.1 | -        | l pressure increase in the catalyst layer  | 101 |
|   |     | 9.1.1    | Influence of concentration and differential pressure differences                 | 102 |
|   |     | 9.1.2    | Quantitative description   | 103 |

Contents

|    | 9.2 Gas p |         | ermeatior  | n fluxes   | . 105 |
|----|-----------|---------|------------|--|-------|
|    |           | 9.2.1   | Separate   | e description of the permeation fluxes                   | . 105 |
|    |           |         | 9.2.1.1    | Diffusion  | . 106 |
|    |           |         | 9.2.1.2    | Proton permeation  | . 107 |
|    |           |         | 9.2.1.3    | Ratio of the permeation fluxes                           | . 110 |
|    |           | 9.2.2   | Interacti  | ing description of the permeation fluxes                 | . 114 |
|    |           |         | 9.2.2.1    | Mathematical description of the interaction              | . 114 |
|    |           |         | 9.2.2.2    | Concentration profiles of the gases in the aqueous pha   |       |
|    |           | 9.2.3   | -          | rison of the separated and interacting description       |       |
|    | 9.3       | Anodi   | , .        | en content   |       |
|    |           | 9.3.1   | Hydrog     | en oxidation at the anodic catalyst                      |       |
|    |           | 9.3.2   | Experim    | nental evaluation of the model                           |       |
|    |           |         | 9.3.2.1    | Influence of the cathodic partial pressure increase fact |       |
|    |           |         | 9.3.2.2    | Influence of the proton permeation                       |       |
|    |           | 9.3.3   | 0 1        | essure electrolysis                                      |       |
|    | 9.4       | Synop   | sis of the | chapter  | . 126 |
| 10 | Effic     | iency o | of pressu  | rized water electrolysis                                 | 128   |
|    |           | -       | -          | s and reaction kinetics                                  |       |
|    |           |         |            | and membrane thickness optimization                      |       |
|    |           |         |            |  |       |
|    |           |         |            | d and differential pressure operation                    |       |
|    |           |         |            | re of parameters   |       |
|    | 10.3      | Pressu  | rized ele  | ctrolysis <i>vs.</i> subsequent compression              | . 133 |
|    |           | 10.3.1  | Details o  | of the comparison  | . 134 |
|    |           | 10.3.2  | Energy     | consumption of a compressor                              | . 135 |
|    |           | 10.3.3  | Compar     | rison of the efficiencies                                | . 136 |
|    | 10.4      | Synop   | sis of the | chapter  | . 139 |
| 11 | Flec      | trochen | nical mit  | igation of hydrogen crossover                            | 141   |
|    |           |         |            |  |       |
|    |           |         |            | l characterization                                       |       |
|    |           |         |            | l and current density of the additional electrode        |       |
|    |           |         |            | e of the additional electrode on the cell voltage        |       |
|    | 11.3      |         |            | anodic gas purity  |       |
|    |           |         | -          | application  |       |
|    |           |         | _          | chapter  |       |
|    |           |         |            |  |       |
| 12 |           | ussion  |            | ometwo and magazonia must suffer a CDEM-                 | 152   |
|    |           |         | 1 0        | ometry and macroscopic properties of PEMs                |       |
|    | 12.2      | EIIICIE | ncy and o  | operation parameters                                     | . 155 |

VI Contents

| 13               | Sum             | mary    |  | 157 |  |
|------------------|-----------------|---------|--|-----|--|
| 14               | Atta            | chment  | t  | 160 |  |
|                  | 14.1            | Electro | ode preparation  | 160 |  |
|                  | 14.2            | Additi  | onal information to the conductivity measurements                          | 160 |  |
|                  |                 | 14.2.1  | Capacitances between the water channels                                    | 161 |  |
|                  |                 | 14.2.2  | Procedure to determine the proton conductivity of HCl $\ldots$ .           | 162 |  |
|                  |                 | 14.2.3  | Fitting procedure and error calculation                                    | 163 |  |
|                  |                 | 14.2.4  | Derivation of the geometric restrictions factor                            | 164 |  |
|                  |                 | 14.2.5  | Influence of the water content on the estimated values $\ \ldots \ \ldots$ | 168 |  |
|                  | 14.3            | Additi  | onal information to the permeability measurements                          | 168 |  |
|                  |                 | 14.3.1  | Electrochemical half-cell with sulfuric acid electrolyte                   | 169 |  |
|                  |                 | 14.3.2  | Electrochemical cell with Nafion $^{\circledR}$ electrolyte                | 170 |  |
|                  |                 | 14.3.3  | Cell for the measurement of the dry PEMs $\ \ldots \ \ldots \ \ldots$      | 171 |  |
|                  |                 | 14.3.4  | Saturation current density   | 172 |  |
|                  | 14.4            | Resisto | or network modeling  | 173 |  |
|                  |                 | 14.4.1  | Simulated oxygen permeability of fully hydrated Nafion ${}^{\mathbb{R}}$   | 173 |  |
|                  |                 | 14.4.2  | Codes  | 175 |  |
|                  | 14.5            | Relatio | on of adiabatic compression to isothermal compression                      | 179 |  |
|                  | 14.6            | Setup   | to mitigate hydrogen crossover   | 181 |  |
| Lis              | t of f          | igures  |  | 182 |  |
| List of tables 1 |                 |         |  |     |  |
| No               | Nomenclature 19 |         |  |     |  |
| Bil              | oliog           | raphy   |  | 195 |  |

# 1 Introduction

By applying a voltage to two electrodes immersed in an aqueous solution, the electrochemical decomposition of water was discovered in the early  $19^{th}$  century [1]. During this process called water electrolysis, hydrogen evolves at the electrode with the negative pole, the cathode, while oxygen evolves at the electrode with the positive pole, the anode. Today, about 200 years later, water electrolysis is considered to be a clean and emission-free technique to convert overcapacities of intermittent electrical energy supply from renewables into chemical energy in the form of hydrogen [2,3]. The hydrogen produced can be used to generate electricity by employing fuel cells [4], for the methanation of  $CO_2$  [5], for the combustion in heat engines [6] and for the combustion to generate heat, to name just a few. With the aim of storing the produced hydrogen under pressure, the pressurized evolution of hydrogen during water electrolysis may reduce the energy consumption in comparison to mechanical compression techniques [7].

Similar to the very first setups in the 19<sup>th</sup> century [1], the use of liquid electrolytes is the most simple approach for water electrolysis [8]. The aqueous electrolyte between the anode and the cathode must provide protons or hydroxide ions as charge carriers and has to be conductive to those in order to enable the reactions at both electrodes [9]. The conductivity of the electrolyte typically increases with the concentration of the charge carriers until (typically at several moles per liter) interactions between the permeating ions prevent a further increase of the conductivity [10, page 20]. Thus, typically either strong alkaline or strong acidic aqueous solutions are used as the electrolyte for low-temperature water electrolysis [11, page 41]. Besides liquid acids or liquid lyes, polymer electrolyte membranes (PEMs) can be used as the electrolyte for water electrolysis [12, 13]. These materials are either solid acids or solid lyes, where functional groups in a polymer matrix introduce protons or hydroxide ions [14]. The hydrophilic properties of the functional groups cause water uptake [15, 16], forming an aqueous phase that is separated in the form of water channels from the solid polymeric phase [17]. In this aqueous phase the protons or hydroxide ions are dissolved [14].

In PEMs, the charge of the mobile ions is balanced by ions with the opposite charge that are covalently bonded to the polymer matrix [18, 19]. The amount of mobile ions which can leave the PEM is negligible since the mobile ions are attracted by the electrostatic force to the covalently bonded ions with the counter charge [20, 21]. Consequently, the electroneutrality of the PEM is maintained. Thus, an advantage of using PEMs for water electrolysis is that only the components that are in direct

2 1 Introduction

contact with the PEM are exposed to the corrosive protons or hydroxide ions of its aqueous phase. In contrast, when liquid electrolytes are used, these can also corrode cell and system components of a water electrolyzer which are not directly involved in the electrochemical reaction of the water decomposition [22]. Moreover, another advantage of PEM water electrolysis is the usage of composite electrodes that consist of catalyst nanoparticles and polymer electrolyte binder [23]. With these nanoparticles, high surface-areas of the catalysts ( $85\,\mathrm{m}^2/\mathrm{g}$  [24]) can be achieved. Alkaline PEMs with mobile hydroxide anions suffer from low durabilities (<1,000 hours [25]), whereas the more stable acidic PEMs are expected to supply service lifes of 100,000 hours in industrial water electrolysis plants [26].

Driven by Brownian motion, the hydrogen and oxygen produced during water electrolysis diffuse through liquid or polymer electrolytes [27, 28], a phenomenon commonly referred to as gas crossover [29]. Gas crossover increases with higher operating pressures and leads to efficiency loss [29,30]. Explosive mixtures of hydrogen and oxygen can occur by the mixing of the cathodic and anodic gases and thereby cause serious safety issues [31,32]. Compared to liquid electrolytes, a further advantage of the usage of PEMs is that differential pressures between the anodic and cathodic compartment can be applied [33]. Therewith, hydrogen pressurization is enabled while the anode can be operated at atmospheric pressure, which reduces the oxygen cross-permeation.

In the literature, the best characterized PEM is Nafion<sup>®</sup> (DuPont<sup>TM</sup>), a perfluorinated sulfonic acid [34]. The microscopic structure of Nafion<sup>®</sup> has been characterized by methods such as small angle x-ray scattering [35], small angle neutron scattering [36,37] and atomic force microscopy [38,39]. The most precise depiction of the three dimensional morphology of the aqueous phase in Nafion<sup>®</sup> was reported by cryo electron tomography measurements [40]. Moreover, the proton conductivity of Nafion<sup>®</sup> was experimentally examined by electrochemical impedance spectroscopy [41,42], while the microscopic proton conduction mechanisms in aqueous solutions and PEMs have been studied by molecular dynamic simulations [21,43]. In addition, the electrochemical monitoring technique was used to study the hydrogen and oxygen cross-permeation through Nafion<sup>®</sup> [27,44]

### Aims of this work

The aim of this thesis is to provide a multiscale description of the transport processes of proton and gases through the PEM of water electrolyzers. Within this aim, the state-of-the-art understanding of the physical transport processes of protons and

gases through the microscopic structure of Nafion® as a representative for the material class of PEMs shall be improved. Impedance spectroscopy with amplitude and frequency variation shall be used to vary the permeation path lengths of protons and to examine their interaction with pore walls. By comparing precisely measured conductivities of Nafion® membranes and aqueous solutions, the effect of the water channel morphology and proton mobility on the overall conductivity of Nafion<sup>®</sup> will be estimated. New methods to precisely measure the hydrogen permeability of PEMs as a function of pressure, relative humidity and temperature shall be developed. On the basis of these precise measurements, the contribution of the driving forces of differential pressure and diffusion on the overall permeability of Nafion® will be quantified. In order to understand the pathways of the gas permeation through Nafion® membranes, the activation energies for the permeation through water, dry Nafion<sup>®</sup> and fully hydrated Nafion® membranes shall be analyzed. These information will be used in order to develop a resistor network model that describes the hydrogen permeation through the microscopic structure of Nafion® membranes. A physical model to describe the interaction between the proton, hydrogen and oxygen transport through the membrane shall be developed.

On the macroscopic scale, the proton conductivities and hydrogen permeabilities of different PEMs shall be examined. A modeled to describe the gas crossover in PEM water electrolysis cells shall be developed and evaluated with precisely measured anodic hydrogen contents. The influence of gas-crossover and proton resistance on the efficiency during water electrolysis shall be physically modeled in order to computationally optimize the membrane thickness as a function of the operation parameters. Finally, the efficiency of pressurized operation and atmospheric pressure operation with subsequent mechanical compression will be compared.

To pursue the discussed objectives, this thesis is structured as follows:

- The physical fundamentals that the subsequent chapters refer to will be briefly reviewed.
- The developed experimental methods to precisely measure the proton conductivity and the hydrogen and oxygen permeabilities will be presented.
- The influence of the water channel geometry on the proton conductivity of Nafion<sup>®</sup> will be experimentally examined.
- Precise measurements of the gas permeation through Nafion<sup>®</sup> will be presented.
- A resistor network model for the gas permeation through Nafion<sup>®</sup> will be presented, which refers to the measured hydrogen and oxygen permeabilities.

4 1 Introduction

 The conductivities and hydrogen permeabilities of six different PEMs will be compared.

- The hydrogen and oxygen cross-permeation during PEM water electrolysis will be characterized by an analytical model and compared with measurements of the anodic hydrogen content.
- The impact the gas cross-permeation and the proton conduction through the PEM on the efficiency of water electrolysis is described by a physical model.
- A novel technique to electrochemically mitigate the hydrogen cross-permeation during PEM water electrolysis will be presented and characterized.
- In a discussion, the results of the different chapters will be related to one another.
- Finally, the most important findings of this work will be highlighted.

In this chapter, the fundamental physics that are used in this thesis will be briefly reviewed. With regard to the research topic of the permeation of protons and gases through PEMs and their influence on the efficiency, following aspects of water electrolysis will be discussed:

- A general overview of PEM water electrolysis.
- The physics of proton transport in aqueous solutions and PEMs.
- The physics of gas diffusion through liquids and polymers.
- Characteristics and types of PEMs.
- The thermodynamics of gas compression.

# 2.1 Water electrolysis

In this section, the general physical properties of water electrolysis including thermodynamics and kinetics of the reactions, the voltage-current characteristic, the setup, efficiency and gas crossover will be elucidated. Parts of this work were previously published [45,46].

## 2.1.1 Thermodynamics

Water electrolysis in an acidic electrolyte means the oxidation of water at the anode

$$2H_2O \rightarrow O_2 + 4H^+ + 4e^-$$
, (2.1.1)

while protons are reduced at the cathode

$$2H^+ + 2e^- \rightarrow H_2$$
. (2.1.2)

The driving force for this reaction is an applied voltage to both electrodes. With a current I between the electrodes, the produced amount of hydrogen n in the time t can be determined by Faraday's law of electrolysis

$$n = \frac{I t}{z F}, \qquad (2.1.3)$$

where F = 96485 C/mol denotes the Faraday constant and z = 2 the amount of electrons which are involved in the electrochemical conversion of water to one hydrogen

molecule (eq. 2.1.2). With reference to the stoichiometric composition of water, half the amount of oxygen in comparison to hydrogen is produced by the electrochemical decomposition of water.

The potential energy, which can be adsorbed by the i-th type of substance involved in a chemical reaction is generally defined as the chemical potential  $\mu^i$ . During the reaction, the amount of substance  $n^i$  of the i-th reactants and products are altered. The set of all the different  $n^i$  involved in the reactions during water electrolysis is in the following represented by  $\{n^i\}$ . Besides the chemical potentials of the different involved species, the thermodynamic process of water electrolysis is further characterized by the thermodynamic properties of the system in the form of pressure p, volume V, temperature T and entropy  $\tilde{S}$ . Bulk properties of the system (p and T), which do not depend on the size of the system, are commonly referred to as intensive properties [47, page 14]. In contrast, extensive properties ( $\mu$ ,  $\tilde{S}$ , and T) are additive for independent subsystems [47, page 14].

Thermodynamic processes are typically described by thermodynamic potentials, which are a function of the overall chemical potentials ( $\sum_i \mu^i n^i$ ), one other extensive property and one intensive property. For instance, Gibbs free energy  $\tilde{G}(T, p, \{n^i\})$  is the thermodynamic potential which depends on temperature and pressure. In the differential form this thermodynamic potential is defined as [47, page 158]:

$$d\tilde{G}(T, p, \{n^i\}) = -\tilde{S} dT + V dp + \sum_i \mu^i dn^i$$
(2.1.4)

The amount of substance of the *i*-th species is related by

$$dn^i = \nu^i d\xi \tag{2.1.5}$$

to its stoichiometric number  $v^i$  and the extent of the reaction  $\xi$  [47, page 340]. The stoichiometric numbers of the products are positive, while those of the reactants are negative. Using Legendre transformation, the dependence on the extensive property and the intensive property of Gibbs free energy can be altered. Accordingly, the thermodynamic potentials of the enthalpy  $\tilde{H}(\tilde{S}, p, \{n^i\})$ , internal energy  $\tilde{U}(\tilde{S}, V, \{n^i\})$  and Helmholtz free energy  $\tilde{F}(T, V, \{n^i\})$  can be derived [48, 136]. Water electrolysis is typically conducted at isothermal and isobaric conditions (T, p = const.) [9, 30]. In this case, the partial derivative of the differential form of Gibbs free energy in the extent of the reaction equals the change of Gibbs free energy  $(\Delta \tilde{G})$  during the process [47, page 341]:

$$\Delta \tilde{G} = \left(\frac{\partial \tilde{G}(\{n^i\})}{\partial \xi}\right)_{p,T} = \sum_{i} \nu^i \mu^i$$
 (2.1.6)

Gibbs free energy thus describes the reversible usable work of the chemical reaction at isothermal and isobaric conditions [47, page 252]. To electrochemically decompose liquid water, the transformation of the state of matter to the gaseous products is accompanied by an increase of the entropy [9]. The thermodynamic energy related to this transformation of the state of matter is described by the enthalpy of vaporization, that equals  $T\Delta \tilde{S}$  at isothermal conditions [9]. Thus, the total thermodynamic energy required to electrochemically decompose water includes the reversible work plus the irreversible work in the form the enthalpy of vaporization. With reference to isothermal and isobaric operation conditions of water electrolysis the enthalpy can be determined by the Gibbs-Helmholtz relation [47, page 360]:

$$\Delta \tilde{H} = \Delta \tilde{G} + T \Delta \tilde{S} \tag{2.1.7}$$

In fuel cells, water is formed by the electrochemical conversion of hydrogen and oxygen, enabling the reversed reaction pathway compared to water electrolysis. The thermodynamic reversible energy of the electrochemical reaction is described by Gibbs free energy [49], while the related reversible voltage  $U_{rev}$  equals [47, page 407]:

$$U_{\text{rev}} = \frac{\Delta \tilde{G}}{z \, F} \,, \tag{2.1.8}$$

To drive the reaction of water electrolysis the applied woltage must be higher than the reversible voltage [9], which equals  $1.23 \,\mathrm{V}$  at ambient pressure and temperature. Similar to the latter equation, the enthalpy can also be related to a voltage, which is defined as the enthalpic voltage  $U_{\mathrm{en}}$  [50].

When water electrolysis is conducted at voltages U between the reversible voltage and the enthalpic voltage ( $U_{\rm rev} \leq U \leq U_{\rm en}$ ), the heat of the cell is consumed in order to balance the heat of vaporization spent for the reaction. In this case, the reaction is an endothermic process and additional heat input is necessary to maintain a constant temperature of the electrolysis cell [51]. Applying the enthalpic voltage to an electrolysis cell would maintain its temperature when the system does not exchange heat with the environment, which is the case for a perfectly thermally insulated system [50,51]. At these conditions, water electrolysis is simultaneously an isothermal and adiabatic process. When higher voltages as the enthalpic voltage are applied ( $U \geq U_{\rm en}$ ), the excess energy is converted in the form of kinetic losses and ohmic losses to heat, which means that the reaction is an exothermic process [51]. In this case, the heat produced must be removed from the electrolysis cell to prevent overheating.

To characterize the chemical potential of a species as a function of the environment, its chemical activity  $a^i$  is typically employed, which is a measure for the effective concentration of the considered species. The chemical activity of a substance is defined

by

$$\mu^{i} = \mu_{0}^{i} + R T \ln(a^{i}), \qquad (2.1.9)$$

where  $R=8.314\,\mathrm{J\,mol^{-1}\,K^{-1}}$  denotes the gas constant,  $\mu^i$  the chemical potential and  $\mu^i_0$  the chemical potential at standard ambient temperature and pressure [47, page 265]. Using this definition and equation 2.1.6, the change of Gibbs free energy with different constant temperatures and constant pressures can be expressed as a function of the activities

$$\Delta \tilde{G} = \Delta \tilde{G}_0 + RT \sum_i v^i \ln(a^i) , \qquad (2.1.10)$$

where  $\Delta \tilde{G}_0 = \sum_i v^i \mu_0^i$  refers to standard ambient temperature and pressure [47, page 342]. Using the relation between the reversible voltage and Gibbs free energy (eq. 2.1.8), the potential  $\varphi_N$  of the electrochemical reaction (defined as Nernst potential) can be determined

$$\varphi_{\mathrm{N}} = \varphi_0 + \frac{\mathrm{k_B} \, T}{\mathrm{F}} \ln \left( \prod_i (a^i)^{\nu^i} \right) ,$$
(2.1.11)

where  $\varphi_0 = \frac{\Delta \tilde{G}_0}{2\Gamma}$  denotes standard potential of this reaction. This standard potential is typically defined in relation to the potential of the hydrogen-proton redox couple (eq. 2.1.2) at standard ambient temperature and pressure [10, page 90].

Calculating the Nernst potentials of the half reactions (eq. 2.1.1 and 2.1.2) of acidic water electrolysis yields a potential of

$$\varphi^{a} = \varphi_{0} + \frac{RT}{2F} \ln \left( \frac{a_{H^{+}}^{2} \sqrt{a_{O_{2}}}}{a_{H_{2}O}} \right)$$
 (2.1.12)

for the anode and a potential of

$$\varphi^{c} = \varphi_{0}^{c} + \frac{RT}{2F} \ln \left( \frac{a_{H^{+}}^{2}}{a_{H_{2}}} \right)$$
(2.1.13)

for the cathode. Hydrogen and oxygen have small solubilities in water ( $<3 \times 10^{-6}$  mol cm<sup>-3</sup> bar<sup>-3</sup>) [52], which allows to approximate their activities by their concentrations  $c_{\rm gas}$  normalized to the reference standard concentration  $c_0$  at standard ambient pressure  $p_0$ :

$$a_{\rm gas} = \frac{c_{\rm gas}}{c_0} \tag{2.1.14}$$

The concentrations of a gas dissolved in a medium is typically proportional to its partial pressure  $p_{\rm gas}$  in the gaseous phase as described by Henry's law

$$c_{\rm gas} = p_{\rm gas} S_{\rm gas} , \qquad (2.1.15)$$

where  $S_{\rm gas}$  denoted the solubility of this gas in this medium. The solubilities  $S_{\rm gas}$  of hydrogen and oxygen in water are independent of pressure below 100 bar [52]. When liquid water is present at the electrodes, the water activity can be approximated as unity [53]. The thermodynamic reversible voltage required for the electrochemical decomposition of water equals the difference of the potentials of both half reactions (eq. 2.1.12 and 2.1.12), as described by the Nernst voltage  $U_{\rm N}$  of water electrolysis

$$U_{\rm N} = \varphi^{\rm a} - \varphi^{\rm c} = U_{\rm rev} + \frac{RT}{2F} \ln \left( \frac{p_{\rm H_2} \sqrt{p_{\rm O_2}}}{p_0^{3/2}} \right) ,$$
 (2.1.16)

where  $U_{\text{rev}} = \varphi_0^{\text{a}} - \varphi_0^{\text{c}}$ . The temperature dependence of the reversible voltage for the electrochemical decomposition of liquid water is given by [54]:

$$U_{\text{rev}} = \frac{1}{2F} \left( -159.6 \frac{J}{\text{K mol}} T + 2.847 \times 10^5 \frac{J}{\text{mol}} \right)$$
 (2.1.17)

#### 2.1.2 Voltage-current characteristic

When water is electrochemically decomposed, the bonds of the reactants must be cleaved to form those of the products. These processes are accompanied by potential barriers that arise from binding energies of the electrons in the bonds of the reactants and products [55]. To overcome these potential barriers and to enable the reaction, an activation energy  $E_A$  must be spent [47, page 168]. This activation energy can be supplied by the kinetic energy of the particles involved in the reaction in the form of random thermal movement. In the thermal equilibrium, the mean kinetic energy of the molecules with randomly distributed thermal movement is proportional to the temperature of the system [56, page 209]. The fraction of particles Y which have a higher kinetic energy than an arbitrary energy E is described by the Boltzmann distribution [47, page 771]

$$Y = e^{-E/(k_B T)}$$
, (2.1.18)

where  $k_{\rm B} = 1.38 \times 10^{-23}$  J/K denotes the Boltzmann constant. The reaction rate f of a reaction is proportional to the fraction of the particles that have a higher energy than the activation energy  $E_{\rm A}$  necessary for this reaction, which leads based on the latter equation to

$$f \propto e^{-E_{\rm A}/(k_{\rm B}T)}$$
, (2.1.19)

as first experimentally observed by Arrhenius in 1889 [47, page 168]. Higher temperatures proportionally increase the mean kinetic energy of the thermal movement and consequently reduce the energy difference to the activation energy. Accordingly, the reaction rate described by the Arrhenius relation increases exponentially with higher temperatures. In order to reduce the activation energies and to thereby increase the reaction rate of water electrolysis, catalysts are employed at the electrodes [57]. At the

catalyst the reactants and products are adsorped so that the energy barriers for the cleavage and formation of their bonds are reduced [55,57].

Higher differences of the electrode potentials to the thermodynamic Nernst potentials reduce the activation energies for the electrochemical reactions [10, page 160], which consequently increase the reaction rate that is described by the Arrhenius relation (eq. 2.1.19). In the case of water electrolysis, the reaction rate corresponds to the electrochemical current, which can be measured by the charge transfer between the electrodes according to Faraday's law (eq. 2.1.3). The potential differences of the electrode potentials and the thermodynamic Nernst potentials are commonly denoted as kinetic overvoltages  $\tilde{\eta}$ . The decrease of the activation energy for an electrochemical reaction is typically assumed to correlate linearly with its kinetic overvoltage [10, page 160ff]. Using this approach, the current at a catalyst can be related to the kinetic overpotential of the reaction, which is commonly referred to as Butler-Volmer relation [10, page 166]. The procedure to derive the Butler-Volmer relation is discussed in textbooks [10, page 166] and will not be considered here in detail.

During water electrolysis, the proton production at the anode (eq. 2.1.1) and proton consumption at the cathode (eq. 2.1.2) lead to the permeation of protons through the membrane. Simultaneously electrons are forced by a power supply to permeate from the anodic to the cathodic catalyst. According to Ohms law

$$U_{\Omega} = RI \,, \tag{2.1.20}$$

the current I of protons or electrons in a conductor is proportional to a voltage drop  $U_{\Omega}$ , while the proportionality constant R is defined as ohmic resistance. The physical origin of the voltage drop in an electric conductor is scattering of the electrons with ions and other electrons of the conductor. In case of the ion conduction through an electrolyte, the permeating ions scatter with other ions and molecules in the electrolyte. In both media, the electric conductor and the electrolyte, targeted kinetic energy of the charge carrier movement is transferred to the scattering partners. Random thermal movement in the form of heat results.

The ohmic resistance of a conductor depends on its geometry. Using the specific conductivity  $\kappa$ , the conductivity of a material can be described independent of the geometry of the conductor. In the case of a planar conductor with thickness d and cross-sectional area A between the contacts, the specific conductivity is related by

$$\kappa = \frac{d}{A R} \tag{2.1.21}$$

to the ohmic resistance. In a PEM water electrolyzer, the electrodes are typically of

a planar geometry and are arranged face to face in a parallel alignment [58]. Hence, with reference to this geometry, the current is typically normalized to the cell area by using the current density j. The resistance is also typically normalized to the cell area, defined as area resistance  $R_{\text{area}}$ :

$$R_{\text{area}} = \frac{d}{\kappa} \tag{2.1.22}$$

Hence, by combining the latter equations, the ohmic drop  $U_{\Omega}$  at the PEM water electrolysis cell can be described by the product of the area resistance and the current density:

$$U_{\Omega} = R_{\text{area}} j \tag{2.1.23}$$

The cell voltage as a function of the current density is typically used in order to describe the performance of the electrochemical processes in a water electrolysis cell. The cell voltage equals the sum of the Nernst voltage, kinetic overvoltages  $\tilde{\eta}$  and the ohmic voltage drop  $U_{\Omega}$  [33]:

$$U(j) = U_{N} + R_{\text{area}} j + \tilde{\eta}(j)$$
 (2.1.24)

In addition, mass transport losses can occur, which however are not considered here in detail as these contributions do not significantly contribute to the cell voltage at moderate current densities (see Figure 2.1.1).

Figure 2.1.1 shows a typical voltage-current characteristic of a PEM water electroly-zer. When the concentrations of the reactants at the catalysts are reduced by the electrochemical reactions [49], mass transport losses can occur. At the anode, these losses occur when more water is oxidized than transported to the catalyst. In this case, the activity of water is reduced by a lower amount of water at the anodic catalyst. This reduction of the water activity consequently increases the anodic Nernst potential (eq. 2.1.12). Typically, this increase of the Nernst voltage at the anodic catalyst is described by an additional term  $U_{\text{mass}}$  in the form of

$$U_{\text{mass}} \propto -\ln\left(1 - \frac{j}{j_{\text{lim}}}\right)$$
 (2.1.25)

that is added to equation 2.1.24, where  $j_{\rm lim}$  denotes the limiting current density [10, page 192]. At the limiting current density, the reaction rate is limited by the occurrence of water at the anodic catalyst. In this case, higher cell voltages do not increase the current [10, page 192]. In case of  $j << j_{\rm lim}$ , this contribution to the voltage-current characteristic is negligible, which is typically the case for PEM water electrolysis cells that are operated at moderate current densities [33, 60]. Thus, models presented in the literature [33, 60] that describe the voltage-current characteristic of PEM water electrolysis cells neglected the contributions of mass transport losses.

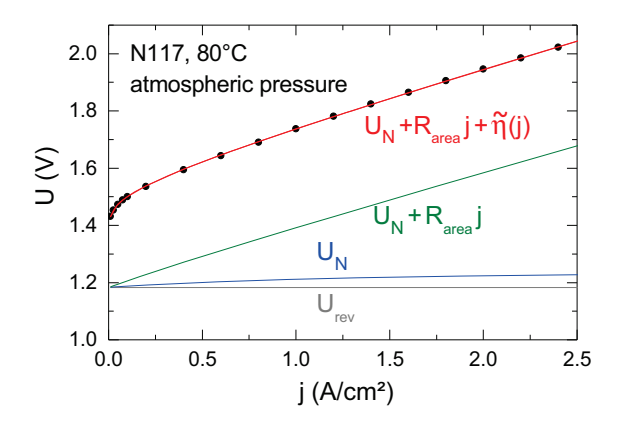


Figure 2.1.1: Voltage-current characteristic of a PEM water electrolyzer cell. Black points: Measured values of a PEM water electrolyzer cell with the setup described in Section 4.4. Gray line: Reversible voltage. Blue: Nernst voltage. The increase of the Nernst voltage toward higher current densities is ascribed to a partial pressure increase of hydrogen and oxygen in the electrodes (see Section 9.1 for detailed discussion). Green: Contributions of the Nernst voltage and the ohmic drop. Red line: Fit of equation equation 2.1.24 to the data. The kinetic overvoltages  $\tilde{\eta}(j)$  were approximated by logarithmic shaped contributions of the Butler Volmer relation for the limit of large kinetic overvoltages [59].

#### 2.1.3 **Setup**

In a PEM water electrolyzer, the electrodes are typically laminated onto the PEM [61], building a construction that is commonly referred to as catalyst coated membrane (CCM). In this alignment, the electrodes are composed of the catalyst and a polymer electrolyte binder. An electrode of this form is typically referred to as catalyst layer [62, 63]. During the electrochemical water decomposition, the reactants (water at the anode and protons at the cathode) must gain access to the catalyst in the catalyst layers. In addition, the produced hydrogen and oxygen must be transported away from the catalyst layers to the gas outlets of the cell [64], so that the reactants again gain access to the catalysts. Hence, the catalyst layer must be porous in order to enable the transport of the involved species in the reaction.

Besides the transport of hydrogen, oxygen, and water to the catalyst, also electrons and protons are involved in the electrochemical reactions. Accordingly, the catalyst layer must be conductive to electrons and protons in order to enable the electrochemical reactions at the catalyst particles [65, 66]. In summary, an electron conducting phase [67], a proton conducting phase [65] and a porous phase for the transport of water and the produced gases [68] must occur in catalyst layers. The interfacial region at the catalyst where all these phases meet is commonly referred to as the triple

phase boundary [69]. In catalyst layers, the metal catalyst and its support typically provide electron conduction [67], while the polymer binder is proton conducting and provides mechanical stability [66,70]. The transport of the reactants and the products proceeds through pores in the catalyst layer [69].

The transitions metals from the 8<sup>th</sup> to the 10<sup>th</sup> raw of the periodic table display the best active components for metal catalysts in water electrolyzers [71–73]. The electrochemical activity of these metals has been attributed to their *d*-band character [55,74]. The iron group (iron, cobalt, and nickel) is stable in the alkaline regime [75], while only those of the platinum metal group show sufficient activity for reactions and stability to corrosion in the acidic electrolytes [58]. To reduce the amount of the rare and costly platinum group metals in the electrodes the size of the catalyst particles can be decreased. The smaller the particles the higher the surface-to-weight ratio of the precious metal catalyst [76]. By attaching the catalyst particles to electron conducting supports [77], a sufficient electrical conductivity of the catalyst layer can be supplied even at low catalyst loadings such as 0.05 mg platinum per square centimeter of electrode area [78]. These supports must be resistant to corrosion, which is for instance fulfilled by carbon for the cathode [77] and passivated titanium [79] or tin oxide [80] for the anode.

The most active pure metal catalyst for the hydrogen evolution reaction at the cathode is platinum [72]. Thus, typically platinum nanoparticles supported on carbon are employed as the state-of-the-art catalysts for the cathode in acidic water electrolyzers [58,81]. The standard potentials of the platinum metals are below 1.2 V and thus below the anodic potential for the oxygen evolution reaction [82]. However, the metals can be protected to corrosion by oxide or hydroxide layers in the anodic environment [83]. Peuckert et al. [84] examined the surface of platinum in an acidic electrolyte as a function of the potential using x-ray photoelectron spectrocopy. This study revealed that several layers of the surface of platinum metal are oxidized to oxides or hydroxides at the anodic potentials that are typically applied in a water electrolyzer. Danilovic et al. [85] reported that higher stabilities of the oxide layers of platinum metals decrease their activity for the oxygen evolution reaction. This behavior was ascribed to oxide transitions of the platinum metals during the oxygen evolution reaction [86]. Iridium oxide is considered to show the best compromise between the both properties, activity for the oxygen evolution reaction and stability to corrosion at anodic potentials [58].

In order to electrically contact the electrodes, the CCM is typically mechanically pressed between two current collectors [58]. These current collectors must be conductive to electrons and permeable to gases and water. Typically sintered titanium

bodies are used as current collectors for the anode [87], while porous carbon fleeces or papers are used as cathodic current collectors [58]. In the case of differential pressure electrolysis, where the cathodic pressure is higher than the anodic pressure, the CCM is pressed onto the anodic current collector [33]. The CCM can mechanically withstand high differential pressures in the order of  $100 \, \text{bar}$  [33] when the pores of the sintered titanium bodies are in the order of  $5 - 20 \, \mu \text{m}$  [87].

In a PEM water electrolysis cell, the current is applied to two flow fields which contact the anodic and cathodic current collectors [58]. The flow fields are typically structured with channels through which water is pumped during operation. These channels are in direct contact to the current collectors [88]. The convective water flow carries the produced gases to the gas outlets of the cell and balances the heat dissipation in the case of an exothermic reaction. To achieve high power densities, the cells are typically arranged in a series connection. In this case bipolar metal plates separate neighboring cells [89]. This alignment is commonly referred to as stack of electrolysis cells [88]. The entire system of the water electrolyzer consists of water pumps, power electronics, separators to separate the water from the produced gases, and further system components [89]. These system components are beyond the scope of the research in this thesis and thus are not discussed.

#### 2.1.4 Cell efficiency

The most general definition of water electrolysis efficiency  $\eta$  is given by the chemical energy that contains a produced amount of hydrogen to the energy that is spend to produce this amount. In steady states, this ratio equals the power  $P_{\text{ideal}}$  that is thermodynamically required for a certain hydrogen production rate divided by the electrical power  $P_{\text{real}}$  for it expended:

$$\eta = \frac{P_{\text{ideal}}}{P_{\text{real}}} \tag{2.1.26}$$

The efficiency aspects discussed in this thesis are focused on the electrochemical efficiency of water electrolysis, which describes the efficiency on the level of the electrochemical cell. On this level, the energy consumption of heaters, water pumps, power electronics and other system components are not included.

On the cell level, the spent power equals the product of the applied voltage U and the corresponding current I. The ideal power required for the same hydrogen output rate equals the thermodynamic reference voltage  $U_{\rm ref}$  (reversible or enthalpic voltage) times the current that leads to hydrogen output of the water electrolyzer. The current loss  $I_{\rm loss}$  is here defined as the amount of the current applied which does not result

in hydrogen that leaves the cathodic gas outlet. The current, which leads to the hydrogen output thus equals the difference of the total current I applied and the current loss  $I_{loss}$ . By using these definitions, the latter equation can be written as:

$$\eta = \frac{U_{\text{ref}}(I - I_{\text{loss}})}{III} \tag{2.1.27}$$

This equation can be transposed to

$$\eta = \underbrace{\left(\frac{U_{\text{ref}}}{U}\right)}_{\eta_{\text{LL}}} \times \underbrace{\left(1 - \frac{I_{\text{loss}}}{I}\right)}_{\eta_{C}}, \tag{2.1.28}$$

where  $\eta_{\rm U}$  is defined as the voltage efficiency and  $\eta_{\rm C}$  as the current efficiency (or Faradaic efficiency). By transposing the latter equation, the current efficiency can be expressed as

$$\eta_{\rm C} = \frac{I - I_{\rm loss}}{I} = \frac{Q_{\rm ideal}}{Q_{\rm real}}, \qquad (2.1.29)$$

where  $Q_{\text{ideal}}$  denotes the ideal charge to electrochemically produce a certain amount of hydrogen and  $Q_{\text{real}}$  the charge spent for this amount [9].

The efficiency loss normalized to the reversible voltage ( $U_{\rm ref} = U_{\rm rev}$ ) is attributable to the current loss, kinetic overvoltages and the ohmic drop. In addition, the pressurized gas evolution during water electrolysis decreases this efficiency as further discussed in Chapter 10. When the enthalpic voltage is used as reference voltage, the heat balance of the cell and the current loss can be included in the efficiency calculations. In this case, only the contributions of the ohmic loss and the kinetic overvoltages that exceed of the enthalpic voltage reduce the efficiency. This thesis will focus on the ohmic drop at the membrane and the current efficiency. Both contributions are included by the efficiency normalized to the reversible voltage, which thus will be taken as the reference voltage. The heat balance of the electrolysis cell is beyond the scope of this research and thus is not considered in this thesis.

At cathodic potentials hydrogen is adsorped at the typically employed platinum catalyst [84,90]. When oxygen permeates from the anode through the PEM to the cathode, it is adsorped at the cathodic catalyst. This adsorped oxygen can be catalytically or electrochemically reacted with adsorped hydrogen [91,92] forming water, hydrogen peroxide, or radicals [91,92]. Hydrogen that permeated through the PEM mixes with the anodic oxygen, since it does not react at the anodic iridium oxide catalyst (Section 9.3). This cross-permeated hydrogen is assumed to be not useable for further technical applications. In summary, the cross-permeation of both gases lead to a loss of the produced hydrogen and therewith to a decrease of the current effi-

ciency and mixed potentials at the electrodes. Other sources than the hydrogen and oxygen cross-permeation (such as leackages [93], parasitic currents<sup>1</sup> or side reactions) that could lead to a reduction of the current efficiency are (at least at the beginning of life) typically negligible.

#### 2.1.5 Gas crossover and safety issues

As discussed in the last paragraph, hydrogen that permeates through the PEM mixes with the oxygen produced at the anode. When the hydrogen is evolved under pressure during water electrolysis, the lower explosion limit of 4 mol% H<sub>2</sub> in O<sub>2</sub> at the anode may be exceeded [32]. To circumvent explosive anodic gas mixtures, current collectors plated with platinum can be employed, where hydrogen and oxygen at least partly catalytically react forming water [31,94]. Another method to avoid mixing of both gases at the anode is using platinum nanoparticles inside the PEM. Both gases can catalytically react at the catalyst nanoparticles. As a consequence, the concentration of both gases inside the PEM is reduces. Consequently, the permeation of hydrogen from the cathode through the PEM to the anode is avoided. Furthermore, external catalytic recombination reactors were explored to reduce the anodic hydrogen content [31,94]. All the solutions involving a catalytic recombination of hydrogen and oxygen can solve safety issues related that are to the exceedance of the threshold of the anodic gas composition. However, these approaches reduce the current efficiency as described by equation 2.1.28.

# 2.2 Proton conduction in aqueous solutions and PEMs

When two electrodes with a potential difference are immersed into an electrolyte, the electrolyte is polarized by the orientation of dipoles and the displacement of its mobile ions from their equilibrium position. At electrostatic conditions (constant voltage and no current), potential differences between an electrode and the electrolyte are shielded by the dipoles and mobile ions of the electrolyte in the form of electrochemical double layers (at the length scale of a nanometers or less) directly at the electrode [10, page 124ff]. As a result, the electric field inside the electrolyte is negligible under electrostatic conditions (in analogy to that in electrical conductors). However, when a current between the electrodes occurs, an ohmic potential drop inside the electrodes can only a discussed in Section 2.1.2. A direct current (DC) between the electrodes can only

 $<sup>^1\</sup>text{The polymer}$  electrolyte membrane is an insulator for the electron conduction and hence parasitic electrical currents through the membrane do typically not occur. The electric resistance of a Nafion  $^{(\!R\!)}$  membrane can be measured at direct currents below the decomposition voltage of water. With graphite electrodes pressed onto a Nafion  $^{(\!R\!)}$  membrane, the conductivity of Nafion  $^{(\!R\!)}$  is below  $1\,\mu\text{S}/\text{cm}$  at  $0.6\,\text{V}$  (limited by noise of the measurement), which means an at least five order of magnitude smaller resistance to protons than that to electrons.

be caused by electrochemical reactions at the electrodes. When alternating voltages are applied to the electrodes, alternating currents (ACs) can be caused by the displacement of ions from their equilibrium position. Morevoer, similar to DCs, ACs also can lead to electrochemical reactions at the electrodes.

The proton conduction in PEMs occurs within an aqueous phase in the form of water channels [21,95]. Thus, models that describe the proton conduction in PEMs are based on the same mechanisms as those of aqueous electrolytes [96,97]. In the solid or the liquid state of water, the water molecules form a hydrogen bond network [98–100] which is responsible for most of its unusual properties such as its high surface tension or its high boiling and high melting temperature with regard to its molecular mass. When ions permeate through water, at least some hydrogen bonds are cleaved and new formed [101]. The underlying dynamics for the formation and cleavage of these bonds was examined experimentally by methods such as *X*-ray adsorption [99] and infrared vibrational spectroscopy [100]. In addition, computational predictions on the dynamics of the hydrogen bond network were presented in the literature [102].

In water, the solution of ions is accompanied by the formation of hydration shells, where the polar water molecules at least partly shield the charge of the ions [103,104]. The structures of solvation shells are typically of dynamic order [105]. Ions also can form bonds coordination complexes, which are also surrounded by a solvation shell. For example, excess protons in water, which are introduced by an acid or which are a result the autoionization of water, form coordination complexes with water molecules. The coordination complex of one water molecule with a proton is defined as a hydronium ion  $H_3O^+$  [106–108]. In the literature, the environment of hydronium ions in water was examined by path integral simulations [109], infrared spectrosopy [100,107,110], and x-ray adsorption [99]. As an outcome of these studies, the hydronium ions were found to form shared proton complexes  $H_5O_2^+$  (Zundel cation), where two water molecules share the excess proton by hydrogen bonds, or solvated hydronium complexes  $H_9O_4^+$  (Eigen cation), where four water molecules share the excess proton by hydrogen bonds [111].

Grothuss first postulated in 1806, that protons can be passed between neighboring water molecules [112]. Later, the higher mobilities of protons and hydroxide ions in aqueous solution than those of other ions were ascribed to this mechanism that was named after its explorer [112, 113]. The Grothuss mechanism exclusively works for the conduction of protons and hydroxide ions through aqueous solutions, since these are the only species that can be transported by the exchange of protons along the hydrogen bond network. Based on the molecular dynamic simulations, the passing of the excess protons along the hydrogen bond network is believed to occur *via* an

interaction between Zundel cations ( $H_5O_2^+$ ) and Eigen cations ( $H_9O_4^+$ ) [112]. Moreover, the coordination complexes of the protons or hydroxide ions can permeate with their solvation shell through the electrolyte, commonly referred to as classical ion permeation. In the case of proton or hydroxide ion conduction through an aqueous electrolyte, the classical permeation and the conduction by the Grothuss mechanism occur simultaneously, while the detailed physical processes and interactions of these mechanisms are still debated in the literature [112]. In the following, the physical laws that characterize the ionic conductivity of an electrolyte are discussed. Moreover, the ionic conductivities of electrolytes at alternating and direct currents are elucidated.

#### 2.2.1 Physical description of the ionic conductivity

The mean velocity of a moving cation in the direction of an electric field (or an anion in the opposite direction) is described by the drift velocity  $\vec{v}_D$ . This movement of the ions leads to their scattering with molecules or ions in the electrolyte. During the scattering process, the targeted kinetic energy in the direction of the electric field is converted into randomly distributed thermal movement in the form of heat. The drift velocity  $\vec{v}_D$  of the *i*-th ionic species in the electrolyte is characterized by

$$\vec{v}_{\mathrm{D}}^{i} = a^{i} \, \tilde{t}^{i}, \tag{2.2.1}$$

where  $\tilde{t}$  denotes the mean scattering time and a the mean acceleration of these ions in the electric field  $\vec{E}$  inside the conductor. The drift velocity typically has a linear response to the electric field inside the conductor

$$\vec{v}_{\mathrm{D}}^{i} = Q^{i} \,\mu^{i} \,\vec{E} \,, \tag{2.2.2}$$

where the proportionality constant  $\mu^i$  is defined as the mechanical mobility of the *i*-th species with the charge  $Q^i$  in units of Coulomb. This mechanical mobility is be related by

$$Q^i \mu^i = \tilde{\mu}^i \tag{2.2.3}$$

to the ionic mobility  $\tilde{\mu}^i$ . The linear response of the ion movement in the electric field is characterized by Ohm's law in the microscopic formulation:

$$\vec{j}^i = \kappa^i \; \vec{E} \tag{2.2.4}$$

In general, the conductivity and mobility are tensors of second degree. However, owed to the isotropy of aqueous solutions, these tensors of second degree can be reduced to factors, while the vectors of the drift velocity and the external electric field can be reduced to their values. Setting equal the latter equation and equation 2.2.2 leads to the relation between the current density, drift velocity, mobility and

conductivity:

$$\frac{j^i}{\kappa^i} = \frac{v_{\rm D}^i}{\tilde{\mu}^i} \tag{2.2.5}$$

The current density of the *i*-th ionic species as a molar flux in terms of Faraday's law can be related to the drift velocity

$$j^i = v_D^i q^i c^i F$$
, (2.2.6)

where  $c^i$  denotes the concentration of these ions and  $q^i$  their charge normalized to the elementary charge. By combining the last two equations, the mobility can be related to the conductivity:

$$\tilde{\mu}^i = \frac{\kappa^i}{q^i c^i F} \tag{2.2.7}$$

The hydrogen bond network affects the proton conduction by the Grothuss mechanisms, the classical ion permeation and the structure of the solvation shells of the ions [114,115]. Theories that described the influence of temperature on the ionic mobility are rather complex and will not be considered here as these are beyond the scope of the research in this thesis.

#### 2.2.2 Ionic conductivities at ACs and DCs

As discussed in the beginning of this Section, the potential difference of two electrodes in an electrolyte displaces its mobile ions from their equilibrium position. In the case of a electrostatic conditions (no current), the electric field inside the electrolyte is negligible as it is shielded by electrochemical double layers. When the potentials of electrodes in an electrolyte are altered, the displacement of the mobile ions in the electrochemical double layer is changed. Capacitive currents result [10, page 124ff]. At constant voltages between the electrodes capacitive currents are negligible. In this case, currents between the electrodes can only be caused by electrochemical reactions. These electrochemical reactions are accompanied by kinetic losses (Section 2.1.2), which are at a stationary currents typically described by charge transfer resistances  $R_{\rm ct}$  [10, page 173].

To determine the conductivity of an electrolyte typically alternating currents used [116], in order to avoid the contributions of charge transfer resistances to measured resistance. In the case of sinusoidal ACs, the complex impedance

$$Z = Z' + iZ'' \tag{2.2.8}$$

is typically used to characterize the relation between voltage, current and the their phase angle. Figure 2.2.1 shows the equivalent circuit diagram that is typically used

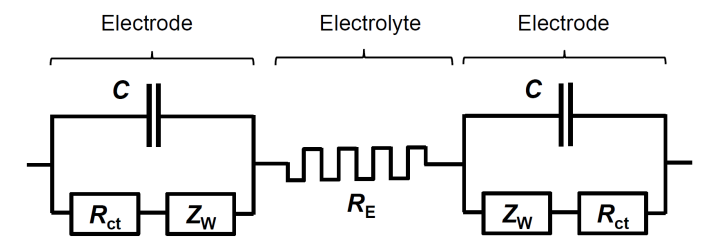


Figure 2.2.1: Illustration of the standard equivalent circuit diagram that is typically used to describe the impedance measurements of electrochemical cells (based on [10, page 14]).

for electrochemical cells with two electrodes immersed in an electrolyte. Electrochemical reactions are described by the charge transfer resistances  $R_{\rm ct}$  while Warburg impedance elements  $Z_{\rm W}$  [116] describe the influence of diffusion limitations on the reactions. Parallel to these contributions, electrochemical double layers contribute to capacitive currents [116]. With reference to sinosoidal alternating currents, the capacitances C contribute to the imaginary part of the impedance in the form of

$$Z'' = -\frac{1}{\omega C}, \qquad (2.2.9)$$

where  $\omega$  denotes the angular frequency of the alternating current. The ionic conduction through the electrolyte is characterized by an ohmic resistance  $R_{\rm E}$ . Contact resistances at the electrodes can occur, for example between the current collectors and the catalysts layers of an electrolysis cell, which can be added to the equivalent circuit presented in series. Moreover, inductances arise from the cables that are used for the connections, which also can be added to the equivalent circuit presented in series. When the electrodes in the equivalent circuit diagram depicted in Figure 2.2.1 have equal potential and are of equal geometry and material, their Warburg impedances, charge transfer resistances, and double layer capacitances are equal. Referring to this equality of the electrodes, the impedance of the equivalent circuit diagram illustrated in Figure 2.2.1 is characterized by:

$$Z = R_{\rm E} + \frac{2}{(R_{\rm ct} + Z_{\rm W})^{-1} - i\omega C}$$
 (2.2.10)

Towards high frequencies, the capacitive contributions to the impedance decrease (eq. 2.2.9). Accordingly, at high frequencies ( $\omega \to \infty$ ), the second term in equation 2.2.10 is negligible. Hence, the ionic resistance of the electrolyte between the electrodes equals the high frequency impedance of the cell minus contact resistances.

In an electrochemical cell under alternating currents, the movement of all mobile ions in the electrolyte contribute to the resistance measured. The ion transport num-

2.3 Gas diffusion 21

ber of the *i*-th ionic species characterizes its relative contribution to the conductivity of the electrolyte [10, page 26ff]. During PEM water electrolysis, protons are ideally the only species of mobile ions, as the anions are covalently bonded to the polymer matrix and thus immobile. Other mobile ions than protons (which can for example be caused by impurities) can only contribute to the conductivity of the PEM at direct currents when these are involved in the electrochemical reactions at the electrodes. For instance, when a proton is replaced by an alkali-metal cation, this cation cannot be reduced at the cathodic potentials and thus cannot contribute to the conductivity at direct currents. However, these ions contribute to capacitive currents. Further relations between the conductivities at direct and alternating currents with regard to aqueous solutions and PEMs will be discussed in Chapter 5.

At direct currents, the permeation of ions through an aqueous electrolyte is accompanied by the transport of water molecules in the coordination complexes and solvation shells. The convective water flux caused by the proton permeation through PEMs is commonly referred to as electro-osmotic water drag [117,118]. The dimensionless drag coefficient  $n_{\rm d}$  describes the number of water molecules dragged along with each proton. In the case of fully hydrated Nafion<sup>®</sup> at 80 °C, the mean of the found values in the literature [117,119] equals  $n_{\rm d} \approx 4$ .

#### 2.3 Gas diffusion

In the following, the diffusion of gases through liquids and polymers is physically described. This section was previously published [120].

## 2.3.1 Permeability, diffusion and solubility

Diffusion is the result of the Brownian motion of particles or molecules along a concentration gradient. A concentration difference  $\Delta c$  of molecules over a distance d yields a molar permeation flux density  $\Phi$ , as described by Fick's law

$$\Phi = -D \frac{\Delta c}{d} \,, \tag{2.3.1}$$

where D denotes the diffusion coefficient of the molecule in the considered medium. The gas permeability  $\varepsilon$  caused by the driving force of diffusion is the product of the diffusion coefficient and the solubility of this gas in this medium [52]:

$$\varepsilon_{\rm gas} = D_{\rm gas} \, S_{\rm gas} \tag{2.3.2}$$

When a membrane divides two compartments with different but time-independent partial pressures, the permeation flux through the membrane described by Fick's law

can be expressed a function of the partial pressure difference  $\Delta p_{\rm gas}$  in these compartments using equation 2.1.15 and 2.3.2:

$$\Phi_{\rm gas} = -\varepsilon_{\rm gas} \, \frac{\Delta p_{\rm gas}}{d} \tag{2.3.3}$$

For the purpose of simplification, the index 'gas' for the individual diffusion coefficients, permeabilities and solubilities of different gases is dropped in the following.

#### 2.3.2 Polymers

Theories that describe gas diffusion through polymers include random thermal movement of gas molecules in the polymer structure as reviewed by Rogers [121]. By a thermally activated process gas molecules can diffuse across the potential barriers that are comprised by the van der Waals forces between polymer chains [121]. The temperature dependence of the diffusion coefficient D is

$$D(T) \approx D_0(T) e^{-E_{\rm D}/(k_{\rm B}T)},$$
 (2.3.4)

where  $E_D$  denotes the activation energy for the diffusion [121]. The proportionality factor  $D_0(T)$  accounts for the distance between the equilibrium positions and the vibration frequency of the molecule in the diffusion coordinate [121]. This exponential temperature dependence represents the Boltzmann distribution (eq. 2.1.18), which describes the probability of a thermally activated diffusion process across the potential barriers [121].

The temperature dependencies of the gas solubilities in polymers are typically also approximated using the Boltzmann distribution

$$S(T) \approx S_0(T) e^{-\Delta H_S/(k_B T)}$$
, (2.3.5)

where  $H_S$  denotes the heat of solution and  $S_0(T)$  a proportional factor [121]. In small temperature ranges, both prefactors  $D_0(T)$  and  $S_0(T)$  can have a negligible temperature dependence, which allows them to be approximated as constant [121]. By combining the assumption of constant prefactors and the equations 2.3.2, 2.3.4, and 2.3.5, the permeabilities of gases through polymers are approximated by

$$\varepsilon(T) \approx D_0 \, S_0 \, e^{-(E_D + \Delta H_S)/(k_B T)} = \varepsilon_0 \, e^{-E_\varepsilon/(k_B T)} \,,$$
 (2.3.6)

where  $\varepsilon_0$  denotes the proportionality factor of the permeability and  $E_{\varepsilon}$  its activation energy.

2.3 Gas diffusion 23

#### 2.3.3 Water

Brownian motion due to the random thermal movement of molecules in a solution leads to a linear influence of the temperature on the diffusion coefficient

$$D = \mu k_B T$$
, (2.3.7)

where  $\mu$  denotes the mobility of the diffusing molecule in the medium and  $k_B$  the Boltzmann constant. This relation was first described by Einstein [122]. By Stokes' drag, the friction of the movement of gas molecules is approximated by

$$\frac{1}{\mu} = \beta C \iota , \qquad (2.3.8)$$

where  $\iota$  denotes the viscosity of the considered medium. The geometry of the diffusing molecule is taken into account by the parameter  $\beta$ . The Cunningham correction factor C describes non-continuum effects, which are not considered here in detail.

The temperature dependence of the viscosity of water is described by

$$\iota(T) = \iota_0 \ T \ e^{E_t/(k_B T)} \ , \tag{2.3.9}$$

where  $E_{\iota}$  denotes the corresponding activation energy and  $\iota_0$  an empirical constant [123]. By combining equation 2.3.7 and 2.3.8, the Stokes-Einstein relation is derived:

$$D(T) = \frac{k_{\rm B}}{\beta \, C \, \iota(T)} T \tag{2.3.10}$$

By inserting equation 2.3.9 into the Stokes-Einstein relation, the total temperature dependence of the diffusion coefficient can be calculated to

$$D(T) = \frac{k_{\rm B}}{\beta \, C \, \iota_0} \, e^{-E_{\rm I}/(k_{\rm B}T)} = D_0 \, e^{-E_{\rm D}/(k_{\rm B}T)} \,, \tag{2.3.11}$$

leading analogously to the diffusion in polymers to the character of a Boltzmann distribution. On the basis of the latter equation, the activation energy for the diffusion  $E_D$  can be identified by the activation energy of the viscosity  $E_\iota$ . However, these relations do not describe individual mobilities of different dissolved gases in water. These differences lead to individual proportionality factors  $D_0$  and individual activation energies for the diffusion of the different gases in water [124]. Accordingly, although hydrogen and oxygen are both non-polar diatomic gases, the approximation of  $E_D \approx E_\iota$  does not describe all of the effects in the gas-water system such as the influence of the size of the molecules. A more detailed discussion of the diffusion of dissolved gases in water is provided in the literature [125].

Table 2.3.1: Parameters from the literature [52] that characterize the mole fraction solubility (eq. 2.3.14) of hydrogen and oxygen in water.

| Gas   | $S_1$     | S <sub>2</sub> (K) | S <sub>3</sub> (K) |
|-------|-----------|--------------------|--------------------|
| $H_2$ | -48.1611  | 5528.45            | 16.8893            |
| $O_2$ | -66.73538 | 8747.547           | 24.45264           |

To determine the hydrogen and oxygen permeabilities of water, their diffusion coefficients and solubilities are required (eq. 2.3.2). The mole fraction of hydrogen or oxygen dissolved in water equals

$$\chi = \frac{n_{\rm gas}}{n_{\rm H_{2O}} + n_{\rm gas}} = \frac{c_{\rm gas}}{c_{\rm H_{2O}} + c_{\rm gas}},$$
 (2.3.12)

where n denotes the amount of substance and c the concentration. When  $c_{\rm H_2O}$  is far higher than  $c_{\rm gas}$ , the latter equation simplifies to:

$$\chi \approx \frac{c_{\rm gas}}{c_{\rm H_2O}} \tag{2.3.13}$$

The temperature dependence of the mole fraction for hydrogen and oxygen in water at atmospheric partial pressures ( $p_0 \approx 1$  bar) was reported in the literature [52] as:

$$\chi(T) = \exp[-S_1 + \frac{S_2}{T} + S_3 \ln(T/(100 \,\mathrm{K}))] \tag{2.3.14}$$

The values for the parameters  $S_1$ ,  $S_2$  and  $S_3$  are given in Table 2.3.1. By combining Henry's law (eq. 2.1.15) and the approximation for the mole fraction (eq. 2.3.13), the temperature dependence of the solubility is expressed as:

$$S(T) \approx \frac{\chi(T) c_{\text{H}_2\text{O}}(T)}{p_0} = \frac{\chi(T) \hat{\rho}_{\text{H}_2\text{O}}(T)}{p_0 M_{\text{H}_2\text{O}}}$$
(2.3.15)

The temperature dependence of the mole density of water  $\hat{\rho}_{\text{H}_2\text{O}}(T)$  was determined by a polynomial fit to the thermodynamic data of the NIST database [126]. The influence of pressures up to 100 bar on the solubilities were shown to be smaller 5 % [52]. By combing equations 2.3.2, 2.3.11 and 2.3.15, the temperature dependency of the gas permeability of water is given by:

$$\varepsilon(T) = S(T) D(T) \tag{2.3.16}$$

In order to estimate the activation energy of the hydrogen and oxygen permeabilities

in water, the latter equation was approximated by:

$$\varepsilon(T) \approx \varepsilon_0(T) e^{-(E_{\varepsilon})/(k_B T)}$$
, (2.3.17)

In summary, the Boltzmann distribution in the form of the equations 2.3.6 and 2.3.17 describes the gas permeabilities of polymers and water. These equations will be used for the interpretation of the measured influence of temperature on the hydrogen and oxygen permeabilities of the examined PEMs in this thesis.

# 2.4 Characteristics of polymer electrolyte membranes

Polymer electrolyte membranes (PEMs) consist of ionomer molecules, which are macromolecules that have a significant proportion of ionizable or ionic groups [127]. In the case of cation exchange PEMs, the negatively charged parts of the functional ionic groups are covalently bonded to polymeric repeat units while cations are ionically bonded to their negative counterpart [19, 128]. When a solvent such as water penetrates into the PEM, the cations can be dissolved in this solvent. By ion exchange, the sort of these dissolved and mobile cations can be changed [129–131]. In the case of proton exchange PEMs, which are required for acidic water electrolysis, the functional groups are acidic and provide mobile protons as charge carriers. When such a proton exchange PEM is in contact with humidified gases or liquid water, its hydrophilic acidic functional groups lead to water uptake [15,132]. As a consequence, the PEM swells. A phase separation between the aqueous phase and the solid polymeric phase takes place, comprising aqueous channels of water with the dissolved protons of the functional groups [17, 34], which are commonly referred to as water channels. The proton conduction of the PEM takes place in the aqueous phase in the form of water channels as discussed in Section 2.2.

In general, a proton exchange PEM for acidic water electrolysis should meet the following requirements:

- The proton conductivity should be as high as possible to minimize ohmic losses.
- To avoid parasitic electron currents between the electrodes through the PEM, it should be negligibly conductive to electrons.
- The hydrogen and oxygen permeabilities should be as low as possible in order to minimize the gas cross-permeation and the correlated efficiency loss.
- To avoid differential pressure driven water or gas permeation through the PEM, its pore diameters should be small as further discussed in Section 6.

26 2 Fundamentals

$$\begin{array}{c} [(\mathsf{CF}\,\mathsf{CF}_2)(\mathsf{CF}_2\,\mathsf{CF}_2)_{\mathsf{m}}]_{\mathsf{n}} \\ \mathsf{I} \\ \mathsf{O}\,\mathsf{CF}_2\,\mathsf{CF}\,\mathsf{O}\,\mathsf{CF}_2\,\mathsf{CF}_2\,\mathsf{SO}_3\,\mathsf{H} \\ \mathsf{I} \\ \mathsf{CF}_3 \end{array}$$

Figure 2.4.1: Structural formula of Nafion® adapted from [134].

- Chemical resistance to the decomposition by hydrogen peroxide and radicals that are produced at the cathodic platinum catalyst [133].
- High mechanical stability and high glass transition temperatures to avoid deformation and creep.

With regard to the efficiency, the decisive material property of a PEM is the ratio of its specific proton conductivity to its gas permeability, as further discussed in Chapter 10.2. Moreover, the thickness of the membrane will be shown to be the control parameter that is decisive to adjust the relation between current and voltage efficiency.

The most examined proton exchange PEM in the literature is Nafion<sup>®</sup> (DuPont), which is a perfluorinated sulfonic acid (PFSA) [34]. Figure 2.4.1 illustrates its chemical structural formula, while further information on the microscopic structure are described in Section 3.1. Besides perfluorinated sulfonic acid materials, a broad class of functionalized polymers are usable as PEMs for fuel cells or water electrolyzers [128, 135]. For example, fuel cells and water electrolyzers can be operated with non-fluorinated proton exchange PEMs that have an organic chemistry with sulfonated functional groups [135–137]. The poor chemical stability of these membranes and associated durability issues limits their application in fuel cells and water electrolyzers [128]. However, the proton conductivity of these materials was shown to reach similar values as that of Nafion<sup>®</sup> [138,139]. Moreover, the permeability of cross-linked membranes to hydrogen can be smaller than that of Nafion<sup>®</sup> [139]. This reduced gas permeability of membranes with an organic chemistry compared to perfluorinated sulfonic acids [139–141] makes these membranes promising to increase the efficiency of PEM water electrolysis.

To attain high proton conductivities, PEMs should moreover provide high proton concentrations in their aqueous phase [142]. In addition, the acidic strength of the functional groups is important, because the protons must be dissolved in the aqueous phase to contribute to the conductivity [142]. The acidic strength of Nafion<sup>®</sup> was reported to an acid dissociation constant that ranges between that of methanesulfonic acid with pKa = -1.0 and that of trifluoromethanesulfonic acid with pKa = -5.1 [143]. Non-fluorinated materials with aromatic bonded sulfonic acid groups were es-

timated to show significant smaller acidic strengths than that of Nafion<sup>®</sup> [143].

In Chapter 6 and 7, the mechanisms of gas permeation through PEMs and ways to reduce their gas permeabilities will be discussed. Moreover, in Chapter 6, the influence of the capillary pressure on the gas permeation forced by differential pressures will be discussed. Eikerling *et al.* [144] estimated the capillary pressure in Nafion<sup>®</sup> to the order of 100 bar. In general, the capillary pressure  $p_{\text{cap}}$  is reciprocally proportional to the radius  $r_{\text{cap}}$  of the capillary

$$p_{\rm cap} = \frac{2\,\sigma\cos(\theta)}{r_{\rm cap}}\,,\tag{2.4.1}$$

where  $\sigma$  denotes the surface tension of the liquid in the capillary and  $\theta$  its contact angle with the capillary pore. In a PEM, this liquid corresponds to the acidic aqueous solution in the capillaries that are formed by the water channels. Whereas an estimation of the capillary pressure in Nafion® by Eikerling  $et\ al.$  [144] was more complex, the last equation shows the general relation of increasing capillary pressures at smaller radii of the water channels and smaller contact angles.

Besides the proton conductivity and gas permeability of PEMs, also their mechanical and chemical stability are decisive properties for the application in water electrolyzers. Stucki et al. [133] showed that the lifetime of water electrolyzer is limited by the degradation of the PEM. This degradation is caused by hydrogen peroxide and radicals that are produced at the cathodic platinum catalyst by the catalytic reaction of hydrogen with cross-permeated oxygen [133]. Moreover, besides the chemical radical production, hydrogen peroxide can also be produced at the potentials of the cathodic platinum catalyst by the electrochemical two-electron reduction of oxygen [145].

### 2.5 Thermodynamics of gas compression

The thermodynamics of gas compression is relevant for the pressurized hydrogen evolution during water electrolysis and mechanical compression techniques. In the following, a brief review of fundamental equations that describe the gas compression are reviewed. The equation of state of an non-interacting gas is given by the ideal gas law:

$$pV = nRT (2.5.1)$$

To describe the non-ideal behavior of gases, the compressibility factor  $\tilde{Z}$  takes deviations from the ideal gas law into account [146]:

$$pV = \tilde{Z}nRT \tag{2.5.2}$$

28 2 Fundamentals

Accordingly, an ideal gas is characterized by a compressibility factor of  $\tilde{Z}=1$ . In this thesis hydrogen pressures of up to 50 bar at temperatures above 30 °C will be considered. Under these conditions, the compressibility factor ranges in between 1 and 1.03, as calculated based on the molar density of hydrogen stated in the NIST database [126] and the latter equation. For the purpose of simplification, this deviation of 3 % from the behavior of an ideal gas will be neglected for the calculations presented in this thesis.

During water electrolysis, hydrogen is typically produced at a constant temperature of the electrolysis cell. Thus, the required energy for electrolysis at a cathodic pressure  $p''_{\rm H_2}$  compared to a lower hydrogen pressure  $p'_{\rm H_2}$  at equal temperatures can be related to an isothermal electrochemical compression. The work required for the compression increases the Nernst voltage (eq 2.1.16). This increase of the Nernst voltage is with respect to equal oxygen pressures at the anode described by:

$$\Delta U_{\rm N} = U_{\rm N}(p_{\rm H_2}'') - U_{\rm N}(p_{\rm H_2}') = \frac{\rm RT}{2F} \ln \left( \frac{p_{\rm H_2}''}{p_{\rm H_2}'} \right), \tag{2.5.3}$$

In relation to an isothermal mechanical compression process, this voltage increase can be understood as work

$$W_{\rm iso} = -\int_{p_{\rm ini}}^{p_{\rm fin}} V \, \mathrm{d}p = nRT \ln \left(\frac{p_{\rm ini}}{p_{\rm fin}}\right) \,, \tag{2.5.4}$$

where the subscript 'ini' denotes the initial pressure of the gas and 'fin' its final pressure. Towards higher pressures than those considered in this thesis, the compressibility factor increasingly deviate from unity. In this case, the isothermal work in terms of the non-ideal behavior can be calculated to

$$W_{\rm iso} = nRT\tilde{Z} \ln \left( \frac{p_{\rm ini}}{p_{\rm fin}} \right) , \qquad (2.5.5)$$

where the compressibility factor can be approximated by the mean of its initial and final values [146]:

$$\tilde{Z} = \frac{\tilde{Z}_{\text{ini}} + \tilde{Z}_{\text{fin}}}{2} \tag{2.5.6}$$

The thermodynamic work required for the isothermal compression increases with higher temperatures (eq 2.5.4).

The work during compression has to be applied against the internal pressure of the gas and is thus counted as negative. Because the internal energy of the gas during isothermal process is constant ( $\Delta \tilde{U} = 0$ ), the negative of the heat exchange to the

environment balances the spent work by an increase of the gases' entropy:

$$-T\Delta \tilde{S} = W_{\rm iso} \tag{2.5.7}$$

When a gas is compressed by a mechanical compressor, the heat exchange with the environment can be small. In the case of a negligible heat exchange with the environment, the compression process is adiabatic, which means that the temperature of the gas increases during the compression process. During a isentropic compression process the temperature of the compressed gas increases, while heat exchange with the environment is allowed. The temperature increase during isentropic compression means, that a higher final pressure is required to achieve the same molar density as with an isothermal compression process. Thus, assuming the same initial temperatures and molar densities, compression by an isentropic or adiabatic process to a certain final mole density of the gas thermodynamically consumes more work than the compression to the same final mole density by an isothermal process.

At the end of an adiabatic or isentropic process, the compressed gas has a temperature of [47, page 50]

$$T_{\text{fin,ad}} = T_{\text{ini,ad}} \left( \frac{p_{\text{fin,ad}}}{p_{\text{ini,ad}}} \right)^{\frac{\gamma - 1}{\gamma}},$$
 (2.5.8)

where  $T_{\rm ini,ad}$  and  $p_{\rm ini,ad}$  denote the initial temperature and pressure at the beginning of the process and  $T_{\rm fin,ad}$  and  $p_{\rm fin,ad}$  the final temperature and pressure. The index  $\gamma$  is in the case of an adiabatic compression defined by the ratio of the heat capacities at constant pressure and constant volume ( $\gamma = 7/5$  for an idealized diatomic gas). Polytropic processes are characterized by values of the index between that of the isothermal and adiabatic idealization ( $1 < \gamma < 7/5$ ). The final pressure of an adiabatic or polytropic compression is related by

$$p_{\text{fin,ad}} = p_{\text{ini,ad}} \left(\frac{V_{\text{fin,ad}}}{V_{\text{ini,ad}}}\right)^{\gamma}$$
 (2.5.9)

to the change of the volume [47, page 50]. Using the relation between temperature, pressure, and volume described by the latter two equations, the thermodynamic work of an adiabatic or polytropic compression is given by:

$$W_{\rm ad} = \int_{p_{\rm ini,ad}}^{p_{\rm fin,ad}} V \, \mathrm{d}p = -\frac{1}{1-\gamma} \, nRT_{\rm ini,ad} \left( \left( \frac{p_{\rm fin,ad}}{p_{\rm ini,ad}} \right)^{\frac{\gamma-1}{\gamma}} - 1 \right) \tag{2.5.10}$$

## 3 Overview of current literature

The aim of this chapter is to give an overview of the literature that is related to the topics treated in this thesis. With reference to these works, the novelty of the experimental data and models in this thesis is motivated.

# 3.1 Structure and water content of Nafion®

Despite the water content of PEMs itself is not examined in this thesis, its is an important property for their proton conductivities and gas permeabilities [21,147]. In the literature, the structure of Nafion<sup>®</sup> is rigorously examined by several methods such as atomic force microscopy [38, 39, 148], small angle scattering techniques [36, 149, 150] and computational methods [34]. Moreover, the morphology of the aqueous phase in Nafion<sup>®</sup> was directly observed by means of cryo electron tomography [40]. This technique yielded the best description of the microscopic structure of Nafion<sup>®</sup> and the results of this study will be used to parameterize the developed resistor network model in Chapter 7. In the following, the literature that treats the water content of Nafion<sup>®</sup> is discussed in detail. Unfortunately, detailed information on the water content of the other PEMs that examined in Chapter 8 could not be found.

The water uptake of a PEM is typically characterized by  $\lambda$ , which refers to the amount of water molecules per sulfonic acid group. Kreuer [151] reported  $\lambda \approx 20$  for fully hydrated Nafion® (used as a synonym for Nafion® immersed in water) from room temperature to 95 °C. Within this temperature range, the deviations of  $\lambda$  in the data of Kreuer was below 3%, which means that no apparent dependence on temperature was observed. Based on these data, the influence of the temperature on the water content of fully hydrated Nafion<sup>®</sup> is assumed to be negligible. A change of the water content influences the morphology of the aqueous phase [21, 152]. The water uptake of  $\lambda \approx 20$  of fully hydrated Nafion<sup>®</sup> was confirmed by Evans *et al.* [153] with gravimetric measurements at room temperature. Zawodzinski [154] reported in 1993 a water content of  $\lambda \approx 22$  of fully hydrated Nafion<sup>®</sup>, which was also determined by gravimetric measurements. It is unclear, if these deviations come from a change the manufacturing procedure by DuPont<sup>TM</sup> (more than two decades between both measurements) such as the chemical stabilization [155] or a measurement error. Referring to the more recent results, a water content of  $\lambda = 20$  will be used for the calculations in this work.

Based on small angle scattering data, a controversial [134, 156] model of parallel

cylindrical water channels in fully hydrated Nafion® [35] led to an estimation of the volumetric water content  $\phi$  of 28 %. However, this estimation is not considered here as it deviates from all other data that are reviewed in the following. Another approach to interpret such small angle scattering data was given by Kreuer [156], who estimated the volume fraction of water (in the following denoted as volumetric water content) in fully hydrated Nafion<sup>®</sup> ( $\lambda=20$ ) to  $\phi\approx41\,\%$ . The most reliable measurements of the volumetric water content are probably those by volumetric methods, since these directly measure the influence of the water uptake on the volume expansion without a complex fitting procedure as in the case of small angle scattering data. The ratio of the swollen volume divided by the dry volume was measured by Evans et al. [153] to  $1.63 \pm 0.04$ , which corresponds to a volumetric water content of  $\phi \approx 39$  %. Weber et al. [152, 157] reported an approximately equal volumetric water content for  $\lambda = 20$ of  $\phi \approx 40\%$ . The cryo electron tomography by Allen *et al.* [40] revealed a volumetric water content of  $\phi \approx 42.5\%$  in Nafion<sup>®</sup>. However, this measurement is probably less precise than the volumetric measurements at room temperature, since the aqueous phase was frozen in the cryogenic environment during the tomography, so that the lower density ( $\approx 90\%$ ) of ice than that of water increased the measured volumetric water content. In this work, the volumetric water content of Nafion® used for the calculations was estimated to  $\phi \approx 40\%$ , based on the mean of the volumetric measurements (39% [153] and 40% [158]) and approximation derived from small angle scattering data (41 % [156]). The overall hydrophilic phase of Nafion® (including side chains and functional groups) was estimated by the cryo electron tomography reported by Allen et al. to have a higher volume fraction of approximately 56 % [40].

Zhao et~al.~[159] estimated the geometric tortuosity  $\tau_{\rm geo}$  of the water channels of Nafion using pulse-field gradient spin echo nuclear magnetic resonance to decrease towards larger water contents. At a water content of  $\lambda=6.5$  he reported a tortuosity below a value of two, while he did not report the tortuosity for larger water contents. Towards smaller volumetric water contents the network of the water channels are less connected so that consequently the tortuosity increases and the conductivity decreases. Hence, the tortuosity can be expected to further decrease towards the fully hydrated state of Nafion  $^{\circledR}$ .

# 3.2 Conductivity of Nafion®

Ion transport in PEMs occurs in an aqueous phase via water channels [21, 34, 39] that are separated from the solid polymeric phase [17, 34, 144]. The ionic conductivity of Nafion<sup>®</sup> increases towards higher water uptake [41, 42]. On the basis of computational simulations, the electrostatic force between the anions and the protons of the functional groups was reported to cause inhomogeneous distributions of the dissol-

ved protons in the water channels of Nafion<sup>®</sup> [20,21,160,161]. This inhomogeneous distribution is expected to reduce the proton mobility [20,21]. In addition, the influence of the sulfonated groups on the hydration, solvation, diffusion and mobility of the protons was computationally modeled [43,162–168]. Most of these studies came to the conclusion that the proton mobility inside the aqueous phase of Nafion<sup>®</sup> is reduced compared to that of aqueous solutions. Moreover, these studies predicted that this effect increases toward lower water contents. The influence of the morphology of the aqueous phase in Nafion<sup>®</sup> was estimated by various authors using resistor network modeling [21,152,169].

Studies, in which the conductivity of Nafion<sup>®</sup> was compared to those of liquid acids with a similar proton concentration as that its aqueous phase could not be found. Moreover, it is an open question whether scattering processes between protons and the pore walls influence the conductivity. Against this lack of knowledge, the influence of the interaction of protons with the pore walls of the water channels was experimentally examined in this thesis using impedance spectroscopy. Within this aim, the response of the proton conduction of fully hydrated Nafion<sup>®</sup> as a function of the length scale of the proton movement was examined using impedance spectroscopy with different excitation amplitudes and frequencies. Moreover, the differences between the proton conductivity of Nafion<sup>®</sup> membranes and those aqueous solutions with similar acidity were examined in this work, in order to relate the influence of the geometry of the water channels and the proton movement in fully hydrated Nafion<sup>®</sup> on its overall conductivity.

# 3.3 Gas permeability of Nafion®

The water channels required for ionic conductivity increase the gas permeabilities of the membranes [27,147]. Ito *et al.* [52] reviewed the hydrogen and oxygen permeabilities of fully hydrated Nafion<sup>®</sup> and revealed that the results from different authors varied by a factor of approximately five. The scattering of the data for dry Nafion<sup>®</sup> is even larger [52]. In addition, it is not experimentally clarified if differential pressure acts as a driving force for gas permeation through Nafion<sup>®</sup>. Accordingly, the origin of gas permeation through Nafion<sup>®</sup> was attributed to diffusion (Fick's law) and differential pressure forced contributions (Darcy's law) [7,170]. The hydrogen and oxygen permeabilities of Nafion<sup>®</sup> were reported to increase with its water uptake [27,147], which was attributed to permeation through the water channels. However, the detailed interplay of the permeabilities and hydration level was thus far not quantitatively described. Accordingly, pathways and mechanisms of gas permeation through PEMs are not well understood. Moreover, it is an unresolved question whether differential pressure driven permeation of gases or dissolved gases though the Nafion<sup>®</sup>

membrane significantly influence the gas permeation.

In order to overcome the described lack of knowledge, the hydrogen and oxygen permeabilities of Nafion® are characterized in detail in this thesis. Precise measurement techniques for the gas permeabilities of Nafion® as a function of relative humidity, pressure and temperature were developed. Within this aim, the electrochemical monitoring technique to measure a gas flux through Nafion® membranes [44,52] was modified, as explained in Section 4.2 in detail. Using the developed setups, the influence of differential pressures up to 4bar on the hydrogen permeability of Nafion<sup>®</sup> were found to be negligible, which led to the conclusion that diffusion is the dominating driving force for the permeation process. Furthermore, the interplay between the hydration level and the gas permeation path through the aqueous and solid phase of Nafion® was correlated with its microscopic structure. The temperature dependencies of the hydrogen and oxygen permeabilities of Nafion® are examined for the case of the fully hydrated state, where the water content is independent of the temperature [151]. Using a resistor network model approach, the experimental data is evaluated in order to understand the pathways for the gas permeation through Nafion® membranes.

### 3.4 Gas purities during water electrolysis

In the literature, several models to describe the gas crossover during water electrolysis were presented. However, these model and measured data that were supposed to evaluate these models were imprecise, as discussed in the following in more detail. Grigoriev et al. [30] presented in 2009 a model for water electrolysis, which was however never evaluated with experimental data. Later in same year, these authors [94] measured the anodic hydrogen of an operating PEM water electrolyzer. In this study, the authors did not describe how they measured the anodic hydrogen content. On the basis of the published data and measurements that are discussed in Section 4.4, it is here assumed, that the authors used a gas analyzer that is based on the combustion of hydrogen and oxygen on catalysts. The disadvantage of these gas analyzers is that they falsify the gas mixture that is measured. As the consequence, especially at low molar fluxes through the gas analyzer, the measured hydrogen contents are not trustworthy. A detailed discussion of the measurement techniques of the anodic hydrogen content is given in Section 4.4. In 2011, Grigoriev et al. [31] tried to fit a model for the anodic hydrogen content to experimental data. However, the model and the experimental data did not agree. Bensmann et al. [7] developed a model for the energetic evaluation of water electrolysis, however the authors never compared these modeled data to measured data. In this calculation, the authors did not consider the membrane thickness as a variable, which is however one of the most decisive parameters that determines the efficiency of water electrolysis.

The models presented by Grigoriev *et al.* and Bensmann *et al.* did not consider the transport processes inside the catalyst layers of the hydrogen and oxygen produced. However, as analyzed in Section 4.4, these transport processes significantly influence the gas cross-permeation. Moreover, a further drawback of the models presented in the literature is that the interaction between proton movement and gas diffusion was not described. Whether the gas crossover is driven by differential pressures or concentration differences was not considered by these models. As a result, the detailed hydrogen and oxygen cross-permeation during PEM water electrolysis was poorly understood.

To summarize, the models thus far presented in the literature were imprecise by a lack of fundamental physical understanding. Moreover, reliable data for the anodic hydrogen to evaluate these models was not presented. Against this lack of knowledge, more precise measurement data and an advanced physical model are presented in this thesis. This model includes the partial pressure increase that is caused by the gas evolution in the electrodes and the interaction between gas diffusion and proton migration. Moreover, the hydrogen and oxygen permeabilities of Nafion<sup>®</sup> membranes are measured by an *ex-situ* technique, so that reliable values for these parameters can be used for the experimental validation of the model. Using this approach, the modeled anodic hydrogen content shows excellent agreement with that measured.

## 4 Methods

In this chapter, the experimental methods used in this thesis will be presented. Each of the different setups used is characterized by a different letter from A to F.

### 4.1 Impedance spectroscopy

In the following, the setups used for the electrochemical impedance spectroscopy (EIS) of Nafion<sup>®</sup> membranes and aqueous solutions are described. The impedance of the aqueous solutions and the Nafion® membrane samples were measured using an impedance analyzer (Zahner, IM6) and two different setups. To measure the Nafion® membrane samples, a four-wire sensing configuration based on that proposed by Sone et al. [41] was used. This setup is in the following denoted as setup A and is illustrated in Figure 4.1.1A. In this setup, membrane strips of 15 mm width were woven around four platinum wires in a parallel alignment, that acted as the electrodes for the electrochemical impedance spectroscopy. These platinum wires were arranged with a distance of respectively 10 mm in an in-house made polytetrafluoroethylene (PTFE) cell. With reference to a standard four-wire sensing impedance measurement, an alternating current (AC) with a defined frequency was applied to the outer electrodes, while the voltage at the inner electrodes was measured. During the measurements, the cell with the membrane was immersed into a bath with deionized water (Millipore, Advantage A10, resistivity  $18 \,\mathrm{M}\Omega\,\mathrm{cm}$ ). A weight of 100 g was used to keep the membrane sample taut and to press it onto the electrodes. To measure the influence of temperature on the conductivity, the water bath with the PTFE cell was heated in a self made oven with rates of 0.1 K/min. During this temperature variation, the high frequency resistance<sup>1</sup> of the cell and the temperature of the water bath were simultaneously monitored over time. A Pt100 resistance thermometer (Electrotherm, K3-E-3LS-200) was immersed in the water bath and used to measure the temperature. Before measuring, the as-received Nafion® membranes were boiled for 20 min in deionized water. Additional boiling of the samples in acid (1M H<sub>2</sub>SO<sub>4</sub>) and subsequent rinsing by boiling in deionized water did not markedly change the conductivity.

In order to measure the ionic conductivity of aqueous solutions, these were filled into an in-house made 10 cm long PTFE block with a cylindrical hole of 2.2 cm diameter. Figure 4.1.1B illustrates this setup. The PTFE block was sandwiched between two electrodes made of carbon fleece (Freudenberg). These carbon fleeces

 $<sup>^{1}</sup>$ The high frequency resistance of an electrochemical cell (typically in between 1 kHz and 100 kHz) is dominated by the ohmic resistance of the electrolyte [116].

36 4 Methods

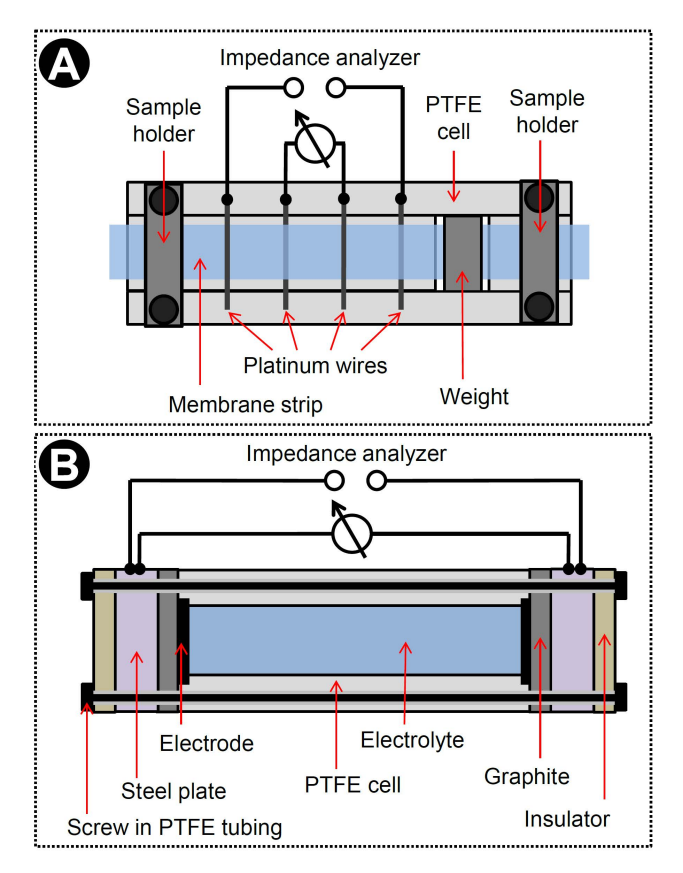


Figure 4.1.1: Schematic illustrations of the setups used to measure the impedance of membrane samples (A) and aqueous solutions (B).

were coated with Hispec9100 (Johnson Matthey) carbon supported platinum catalyst ( $1\,\mathrm{mg_{Pt}/cm^2}$ ) as described in the attachment (Section 14.1), in order to enlarge the surface areas of the electrodes and the related electrochemical capacitances. Based on the data of the HiSpec 9100 catalyst reported by the manufacturer [24] and the amount of the catalyst used, the surface area of the platinum catalyst was estimated to be approximately 850 times larger than that of the geometric electrode area. Graphite plates sealed and electrically contacted the porous carbon fleeces electrodes. Both carbon based materials were chemically resistant to corrosion by the hot acid solutions measured. Steel end plates were pressed onto the two graphite plates. These steel end plates were contacted by banana plugs with the impedance analyzer. Pseudo four-wire sensing was used, where two of the four wires were connected to one of the steel end plates, respectively. By using this configuration the impedance of the wires and contacts were eliminated. Besides the electrolyte resistance, also the resistances of the steel plates, graphite plates, and carbon fleece contributed to the measured impedance. These resistances of the apparatus were determined by reference

measurements, where the impedance of the cell was measured without the PTFE cylinder, so that the carbon fleece electrodes were directly pressed onto one another. The resistance of this alignment was measured to be negligible, meaning that the influence of the resistances of the apparatus had a negligible contribution to the total impedance of the aqueous solutions measured. In order to control the temperature, the cell was immersed in an in-house made oven, which could be heated with defined rates of 0.1 K min<sup>-1</sup>. The impedance of the samples was measured during up and down sweeps of the temperature and then averaged. To measure the temperature, a Pt100 thermometer (Unitherm) embedded in a heat shrink plastic tubing was in direct contact to the examined aqueous solution.

The impedance measurements of the samples/solutions (measured with setup A or B) were carried out during variation of the temperature with upward and downward ramps. Thanks to the low rates of the temperature ramps of  $\pm 0.1\,\mathrm{K\,min^{-1}}$ , significant differences between the measured impedance of a sample/solution as a function of the temperature for the upward and downward ramps could not be observed. The temperature dependency of the impedance of a sample/solution as a function of temperature was obtained by averaging the data from up and down sweeps. Data that was obtained by this method is presented in Chapter 5. As an alternative to this approach, the conductivity measurements that are presented in Chapter 8 were conducted at discrete temperatures, by waiting 15 min after a constant temperature was reached. Within the measurement precision both approaches led to equal measured conductivities.

### 4.2 Electrochemical monitoring technique

To measure hydrogen and oxygen permeabilities of Nafion<sup>®</sup> membranes, three different setups based on the electrochemical monitoring technique were employed. With this experimental technique, a molar flux is electrochemically converted at two electrodes under the diffusion-limiting condition [44,52,171]. Thereby, the current of this electrochemical reaction is monitored over time and correlated with the amount of substance by Faraday's law [52]. In the following, the measurement principle and the modifications of this technique that were employed to measure hydrogen and oxygen permeation through Nafion<sup>®</sup> membranes will be presented.

### 4.2.1 Measurement principle

The permeation flux of hydrogen through a PEM was measured by supplying hydrogen on one side of the membrane and nitrogen on the other side. When hydrogen

38 4 Methods

molecules permeated through the membrane, they reacted electrochemically at an electrode, which is denoted as the working electrode. Driven by a applied voltage that was applied to both electrodes, the hydrogen molecules permeating through the membrane were electrochemically oxidized at the working electrode. The protons gained by this reaction permeated through the electrolyte to the counter electrode where they were reduced to hydrogen. Nitrogen was purged along the electrolyte at the working electrode. Hence, the measured current between the working electrode and counter electrode was attributable to the electrochemical conversion of hydrogen permeating through the membrane. This molar hydrogen flux was correlated with the electrochemical current measured using Faraday's law, assuming that all hydrogen molecules permeating through the membrane were oxidized at the working electrode. This diffusion-limiting condition of the electrochemical reaction is discussed in the attachment in detail (Section 14.3.4). The procedure to measure oxygen permeation through the membrane was analogous.

To electrochemically oxidize the hydrogen that permeated through the membrane, the working electrode acted as the anode (+):

$$H_2 \to 2H^+ + 2e^-$$
 (4.2.1)

The counter electrode served as the cathode (-), at which the reverse electrochemical reaction took place. For the purpose of measuring oxygen permeation through the membrane, the voltage applied at the electrodes was switched. Hence, the oxygen that permeates through the membrane was electrochemically reduced at the working electrode, which acted as the cathode (-):

$$O_2 + 4H^+ + 4e^- \rightarrow 2H_2O$$
 (4.2.2)

In this case, water was oxidized by the reverse reaction pathway at the counter electrode (+).

### 4.2.2 Setups

In the following, the three different setups used to measure hydrogen and oxygen permeability of membranes will be presented. One setup was based on an electrochemical Devanathan and Stachurski half-cell [171]. This setup was originally employed to measure the permeation of hydrogen through metals [171]. Sethuraman *et al.* also applied a similar setup to determine the diffusion coefficients, the solubilities and the permeabilities of oxygen, carbon monoxide and hydrogen sulfide in Nafion<sup>®</sup> [44]. For this purpose, the time-dependent permeation fluxes of these gases

through Nafion<sup>®</sup> membranes were measured by the alternate purging of the reactive gases and inert nitrogen along the membranes. To enhance the precision of the measurement, in this thesis the permeation flux is measured at stationary conditions without consideration of its time-dependence. In turn, this restriction results in a loss of information about the diffusion coefficient and solubility. However, this compromise allowed to precisely measure the temperature dependence of the hydrogen and oxygen permeabilities of Nafion<sup>®</sup> and PTFE. The cell used is illustrated in Figure 4.2.1C. An aqueous 1 M sulfuric acid solution served as the electrolyte between the working electrode and counter electrode for the electrochemical conversion of the hydrogen and oxygen that permeated through the membrane. The Nafion<sup>®</sup> membranes were in contact with the aqueous sulfuric acid electrolyte and fully humidified gases that additionally carried water. Hence, the membranes were fully hydrated during the measurement with this setup.

The typical design of the Devanathan and Stachurski half-cell comprises a reference electrode that is immersed in the electrolyte between the working electrode and counter electrode [44]. The reference electrode is used to measure the potential of the working electrode in the electrolyte [44], while the voltage between the working electrode and reference electrode is kept constant using a potentiostat. However, the measured potential by reference electrodes is temperature-dependent and affected by noise. Capacitive currents caused by voltage variations between the working electrode and counter electrode result, which are inevitable in keeping the voltage between the working electrode and the reference electrode constant. To enhance the measurement precision by reduced noise and capacitive currents, constant voltages between the working electrode and the counter electrode were applied without using a reference electrode.

The second setup used is illustrated in Figure 4.2.1D and was similar to that first described by Sakai *et al.* [147], which was also used by other researchers [141,172]. By using a similar configuration, the influence of relative humidity and pressure on the hydrogen permeability of Nafion<sup>®</sup> was examined for this study. In this setup, the Nafion<sup>®</sup> membranes examined served as the electrolyte between the working electrode and counter electrode. Therefore, the Nafion<sup>®</sup> membranes were coated with two electrodes, as discussed in the attachment (Section 14.3). Hydrogen was then purged along the counter electrode, while nitrogen was purged along the working electrode on the other side of the Nafion<sup>®</sup> membrane. When hydrogen permeated through the membrane, it was electrochemically oxidized and sent back in the form of protons to the other side of the membrane. Thereby, the proton flux with the opposing direction of the hydrogen permeation carries approximately four water molecules per proton (Section 2.2.2). The influence of this water and proton flux on the gas

40 4 Methods

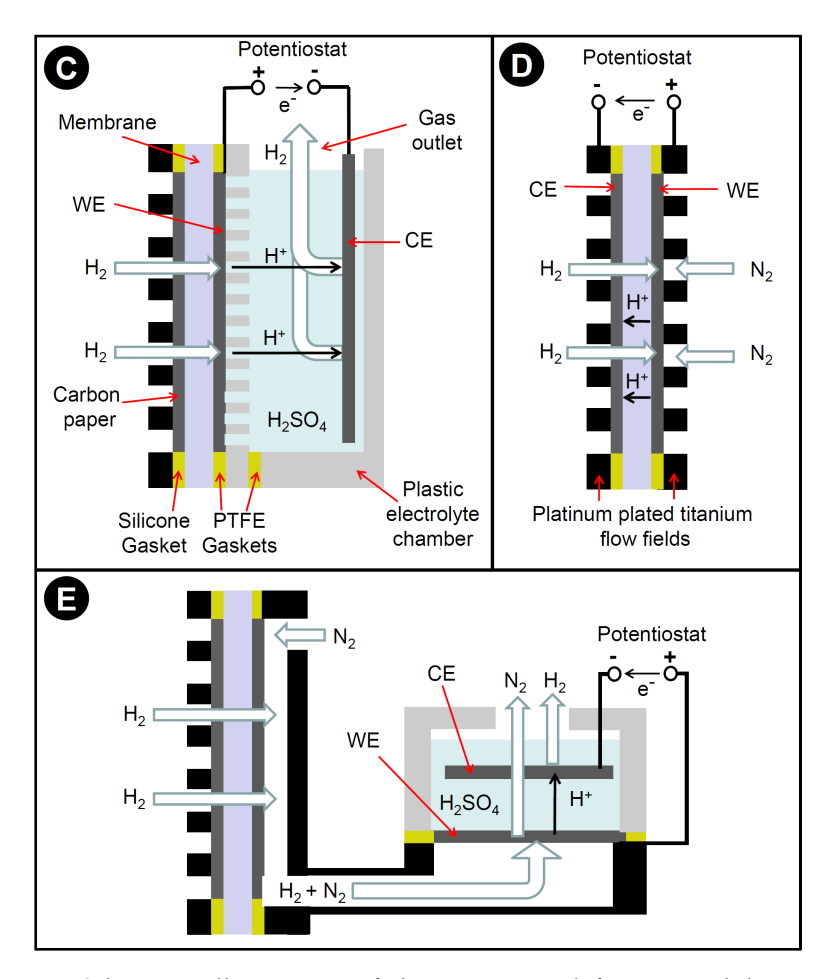


Figure 4.2.1: Schematic illustrations of the setups used for permeability measurements. WE: Working electrode. CE: Counter electrodes. (C): Electrochemical half-cell with aqueous sulfuric acid electrolyte. (D): Electrochemical cell, where the examined Nafion<sup>®</sup> membranes served as the electrolyte. (E): Setup used for dry Nafion<sup>®</sup> membranes.

permeation through the membrane measured is discussed in the attachment (Section 14.3).

The third setup illustrated in Figure 4.2.1E was used to measure the permeabilities of dry Nafion<sup>®</sup> membranes. In this setup, hydrogen was purged along one side of the dry Nafion<sup>®</sup> membranes, while nitrogen was purged along the other. The hydrogen permeating through the dry membrane was carried by the nitrogen flux into an electrochemical cell, where hydrogen in the gas flux was electrochemically converted. The resulting current was monitored over time. For this purpose, the hydrogen and nitrogen mixture was purged through a porous working electrode in an aqueous sul-

furic acid electrolyte, where the hydrogen in the gas mixture was electrochemically oxidized. At a counter electrode in this electrolyte, the reverse reaction took place. To measure the oxygen permeability of the dry Nafion<sup>®</sup> membranes, an analogous measurement procedure with respect to the different reactions at the electrodes and different applied voltages was used. Further details on the setups and measurements are stated in the attachment (Section 14.3).

During the permeability measurements the absolute pressure p at the membrane was kept constant. Using small gas fluxes (as discussed in Section 14.3), the pressure drop in the flow field that faced the membranes was negligible. This absolute pressure is the sum of the partial pressures of the supplied gas and water vapor. The water vapor in the cell was equal to that of saturated vapor pressure  $p_{\rm H_2O}$  (Section 6.1.2), which was calculated by Antoine's equation [173]

$$p_{\rm H_{2O}}(T) = 10^{5.11564 - \frac{1687.537K}{-42.98K+T}} \, {\rm bar} \, ,$$
 (4.2.3)

with the temperature in units of Kelvin and  $p_{\rm H_2O}$  in units of bar. This approximation deviates from the thermodynamic data of the NIST database [126] by less than 0.5%. In order to determine permeability by Fick's law (eq. 2.3.3), the partial pressure of the supplied gas is determined as a function of the absolute pressure p and  $p_{\rm H_2O}(T)$ :

$$p_{\text{gas}}(T) = p - p_{\text{H}_{2}\text{O}}(T),$$
 (4.2.4)

The influence of the absolute pressure p on the saturated vapor pressure  $p_{\rm H_2O}(T)$  is in the considered pressure range below 1 % [174] and thus will not be taken into account in this thesis.

During the measurements with the setups discussed, hydrogen or oxygen at the working electrode were instantaneously electrochemically converted to protons or water, respectively. Thus, their partial pressures at the working electrodes were negligible. As a result, in setup C and in setup D (Fig. 4.2.1C and 4.2.1D) the partial pressure difference of the gas  $\Delta p_{gas}$  between both sides of the membrane is:

$$\Delta p_{gas} = 0 \, \text{bar} - p_{gas} = -p_{gas} \tag{4.2.5}$$

In setup E (Fig. 4.2.1E), the gas permeating through the membrane was instantaneously carried by the nitrogen flux away from the membrane. Accordingly, equation 4.2.5 is also valid for this setup.

The molar permeation flux density  $\Phi$  of hydrogen or oxygen through the mem-

42 4 Methods

brane was determined by the measured current densities *j* using Faraday's law:

$$\Phi_{gas} = \frac{j}{z \, F} \tag{4.2.6}$$

By combining Fick's law (eq. 2.3.3), Faraday's law (eq. 4.2.6), and eq. 4.2.5, the permeability of the membrane for the considered gas was determined as a function of the electrochemical current measured:

$$\varepsilon_{\rm gas}(T) = j(T) \frac{d}{z \, \mathrm{F} \, p_{\rm gas}(T)}$$
 (4.2.7)

This equation is valid for stationary molar permeation flux densities  $\Phi_{gas}$  through the membranes. In the case of fully hydrated Nafion<sup>®</sup>, the noise caused by deviations from the stationary currents measured was smaller 3 % of the measured absolute values.

### 4.3 Resistor network modeling

In Section 7, the hydrogen and oxygen permeabilities of Nafion<sup>®</sup> will be simulated using a resistor network model, which was formulated using the open source package OpenPNM [175] in the program environment 'Phython'. A three-dimensional network with cubic connectivity composed of 200 resistor segments in all three direction was used to describe the resistor network, which thus consisted of 8 million resistor elements in total. In the simulations, the mole flux  $\dot{n}$  through the resistor network was computed using the algorithm for fickian diffusion in OpenPNM. The detailed development of the algorithm and the modeling of the microscopic structure of Nafion<sup>®</sup> will be discussed in Section 7.1.

### 4.4 Measurement of the anodic hydrogen content

The aim of this section is to describe the measurements of the anodic gas purities which are presented in Section 9.3. The measurements of the anodic hydrogen content (Section 9.3) and the voltage-current characteristic (presented in Figure 2.1.1) were conducted with an in-house made electrolysis cell. The active geometric area of the electrodes in this cell was  $25\,\mathrm{cm}^2$ . This cell consisted of titanium flow fields, which were plated with platinum at the anode. The cathodic flow fields were additionally gold plated in order to avoid hydrogen embrittlement of the titanium substrate. A sintered titanium body (GKN) with a thickness of 1.3 mm and grain sizes of  $100\,\mu\mathrm{m}$  was used as anodic current collector. Three carbon papers (Toray, TPG-H-120) were employed as the cathodic current collector. The cell was equipped with a Nafion N117 membrane that was coated with a cathodic Pt/C and an anodic IrO<sub>2</sub> catalyst layer.

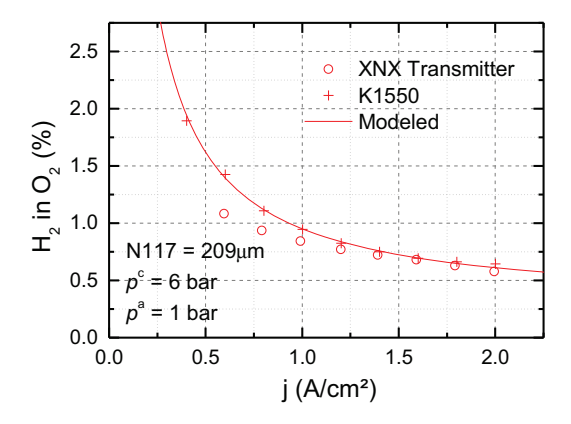


Figure 4.4.1: Measurements of the anodic hydrogen content as a function of the current density. The electrolysis cell was equipped with a Nafion<sup>®</sup> N117 membrane as discussed in the text in detail. Crosses: Measurements with the K1550 gas analyzer. Circles: Measurements with the XNX Transmitter gas analyzer.

The coating procedure of the electrodes and the electrode composition are discussed in the attachment in detail (see Section 14.1). All measurements with the electrolysis cell that are presented in this thesis were conducted at a cell temperature of 80 °C.

The electrolysis cell was placed in two different commercially available test stations which were manufactured by Greenlight Innovation and FuelCon. Individual water circulation loops were used for the anodic and cathodic compartments in both test stations. The hydrogen and oxygen produced in the electrolysis cell were carried by the water circulation through gas separators, in which the gases were dried. The Greenlight test station was equipped with a K1550 gas analyzer (HITECH Instruments) in order to measure the hydrogen content in the anodic exhaust gas of the cell. In the case of the FuelCon test station, a XNX Transmitter (Honeywell) was used to analyze the anodic exhaust gas. The K1550 gas analyzer measures the heat conductivity of the analyzed gas (hydrogen has a larger heat conductivity than oxygen), while the XNX Transmitter measures the heat resulting from the catalytic combustion of hydrogen and oxygen on a catalyst. The gas analyzers were calibrated using gas mixtures of 2% H<sub>2</sub> in O<sub>2</sub> (Linde) and pure oxygen. The analyzers scaled the measured heat conductivity or produced heat by the recombination of the gases linearly with the hydrogen content. To precisely measure the gas composition of the produced gases these must be dry. After drying in the gas separators, the water content of the measured gas composition was further reduced by purging the gas through humidity soaking silica gel (Merck-chemicals). The absolute error of the measured percental hydrogen content with the K1550 gas analyzer was approximately  $\pm 0.1$  %.

Figure 4.4.1 shows the measured anodic hydrogen contents with the gas analyzers introduced above. The measurements were conducted individually after one another

44 4 Methods

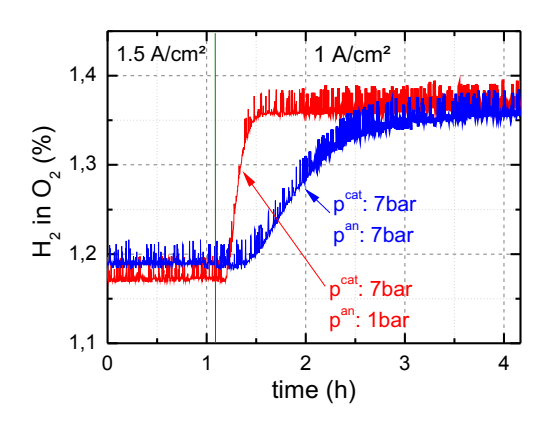


Figure 4.4.2: Time response of the measured anodic hydrogen content of a  $25\,\mathrm{cm}^2$  PEM water electrolysis cell at  $80\,^\circ\mathrm{C}$ . Left to the green vertical line: Operation current density of  $1.5\,\mathrm{A\,cm}^{-2}$ . Right to the green vertical line: Operation current density of  $1\,\mathrm{A\,cm}^{-2}$ . Blue line: Balanced pressure operation. Red: Differential pressure operation.

in order to avoid interferences of both gas analyzers. Above 1.2 A cm<sup>-2</sup>, the measured anodic hydrogen contents with both gas analyzers are approximately equal. However, towards lower current densities the hydrogen contents that were measured by the XNX Transmitter (catalytic reaction of hydrogen and oxygen) leads to significant lower values than that measured with the K1550 gas analyzer (heat conductivity of the gas mixture). As the catalytic reaction of both gases to water consumes twice as much hydrogen as oxygen, the molar composition of the gas mixture is influenced by the XNX Transmitter. The volumetric flux of the produced anodic gas is proportional to the current density. With approaching low volumetric fluxes, the influence of the catalytic recombination by the gas sensor on the composition of the probed gas increases. Accordingly, the measurements with the heat conducting sensor are considered to be more trustworthy and thus only these will be considered in the following parts of this thesis. Figure 4.4.1 also displays the modeled hydrogen content (calculated as described in Section 9.3). In the entire current density range considered, the modeled anodic hydrogen content is within the measurement error in agreement with the measured data of the K1550 gas analyzer.

Figure 4.4.2 shows the time response of the measured anodic hydrogen content with the K1550 gas analyzer. The data in this graph was measured by operating the water electrolysis cell at 7 bar cathodic pressure and anodic pressures of either 7 bar or 1 bar. Using atmospheric pressure at the anodic gas outlet, the measured anodic hydrogen content approaches a constant level after approximately less than 30 min, while in the case of the pressurized anodic operation a stationary signal was obtained after approximately 3 h. The molar density of the gas in the anodic compartment increases

approximately proportionally to its pressure (ideal gas law). Using the same current densities (leading to the same gas production rate), the time to exchange the molar composition of the anodic compartment is approximately proportional to the anodic pressure. Consequently, when the anodic pressure is enlarged by a factor of seven, the time to exchange the molar composition of the anodic compartment increases by approximately the same factor.

# 5 Proton conduction in Nafion®

In this chapter, the influence of the water channel geometries in Nafion<sup>®</sup> and the proton mobility in its aqueous phase on the overall proton conductivity is discussed. First, impedance spectra of a fully hydrated Nafion<sup>®</sup> (used as a synonym for Nafion<sup>®</sup> immersed in water) sample are presented and interpreted in detail. Second, the proton conductivities of Nafion<sup>®</sup> and aqueous solutions are compared and physical reasons for their deviations are elucidated. This chapter was published previously in the form of a research article [176].

### 5.1 Scattering of protons at pore walls

In the following, the response of the proton conduction in Nafion<sup>®</sup> to alternating currents (ACs) is analyzed using impedance spectroscopy. The measured response of the protons to the applied voltage is correlated to their the permeation length in the aqueous phase.

### 5.1.1 Impedance spectra of Nafion®

Figure 5.1.1 shows impedance spectra of a Nafion<sup>®</sup> N117 sample, measured with amplitudes of 0.001, 0.01, 0.1, and 1 V between the inner electrodes of setup A (Fig. 4.1.1). The distance d between the electrodes of the employed setup was 0.01 m. As discussed in Section 2.2.2, the proton conduction through an electrolyte is typically of an ohmic character, which implements a phase angle  $\theta$  of the impedance that equals  $0^{\circ}$ . Besides the ohmic resistance of the proton conduction, also capacitances and electrochemical processes at the electrodes contribute to the measured impedance (Section 2.2.2). Toward higher frequencies these contributions to the impedance decrease as they are short circuited by the decreasing impedance of the electrode capacitances. In the overall frequency range considered inductive contributions to the impedance are negligible as the measured impedance of the sample shows negligible or negative phase angles.

At a frequency of 1 kHz the measured phase angle was negligible for all the excitation amplitudes employed. Toward lower frequencies the phase angle decreases, as the influence of electrochemical electrode processes and double layer capacitances on the impedance increasingly contribute. The electrochemical processes at the electrodes depend on the excitation amplitude. At higher frequencies than 1 kHz the phase angle decreases independent of the excitation amplitude. This reduction of the phase

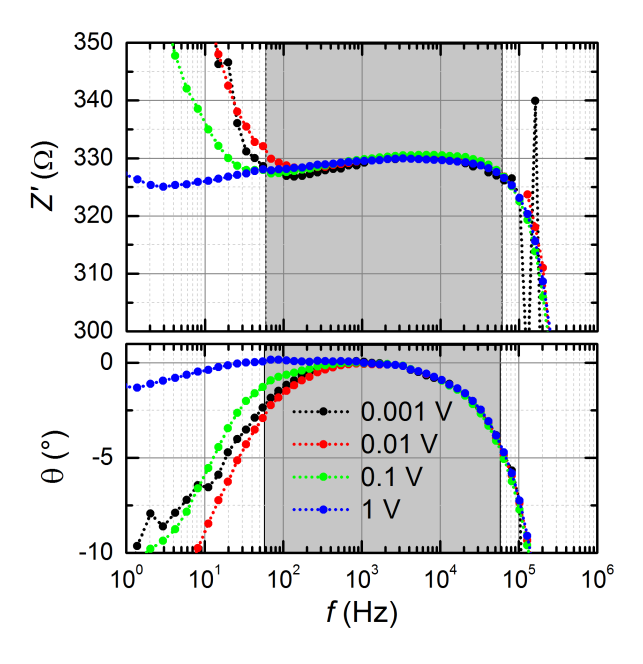


Figure 5.1.1: Impedance spectra of a Nafion<sup>®</sup> N117 sample at room temperature recorded with amplitudes from 0.001 V to 1 V between the inner electrodes of setup A (Fig. 4.1.1). Top: Real part of the impedance. Bottom: Phase angle. The gray shaded area between 70 Hz and 70 kHz indicates the frequencies at which the impedance is dominated by the ohmic proton conduction. Toward higher frequencies capacitive contributions to the impedance increasingly contribute, while toward lower frequencies the influence of electrochemical electrode processes on the impedance increase.

angle was attributed to the capacitance between the electrodes.

In the frequency range from 70 Hz to 70 kHz, the real part of the impedance was measured to be nearly constant (deviations below 2%), while the phase angle was between  $-5^{\circ}$  and  $0^{\circ}$ . With reference to these small phase angles and the constant resistance, ohmic resistances dominated the impedance in this frequency range. This ohmic resistance is attributable to the proton conduction through the measured sample. Higher or lower frequencies reduced the phase angle and varied the real part of the impedance. In the frequency range from 70 Hz to 70 kHz, the higher harmonics from the second to the tenth degree of the impedance were measured by the impedance analyzer to be below  $0.05\,\%$  of the total impedance. These negligible higher harmonics mean that the response of the proton conduction to the alternating electric field was linear within the measurement precision.

### 5.1.2 Movement of the protons in the water channels

Within three decades of frequencies and excitation amplitudes linear responses and a constant ohmic resistance of a fully hydrated Nafion<sup>®</sup> membrane were measured. Based of these observations, the aim of the following deliberations is to discuss if scattering processes between the protons and the pore walls affect the conductivity. For this purpose, the length scales of the microscopic structure of Nafion<sup>®</sup> and that of the permeation paths are compared. The average permeation length of protons (eq. 5.1.1) within one sign of the applied ACs is defined as l. To calculate l, only ohmic currents are considered, as these dominated the impedance.

The average permeation length covered by protons equals

$$l = v_{\rm D} t \,, \tag{5.1.1}$$

where t denotes the time that the current is applied and  $v_D$  the average drift velocity. In the case of an alternating current, the direction of the current changes every half of the inverse frequency f:

$$t = \frac{1}{2f} \tag{5.1.2}$$

Within one sign of the periodic sinusoidal excitation used for the impedance spectroscopy, the mean voltage  $\bar{U}$  equals

$$\bar{U} = \frac{1}{\sqrt{2}} U_0 \,, \tag{5.1.3}$$

where  $U_0$  denotes the peak voltage amplitude.

On the basis of Faraday's law, the drift velocity can be calculated by the ratio of the current I to the product of the proton density  $\rho_{H^+}$  and the cross-sectional area of the conductor:

$$v_{\rm D} = \frac{I}{\rho_{\rm H^+} A} \tag{5.1.4}$$

By also taking into account Ohm's law and equation 5.1.3, the latter equation can be written as:

$$v_{\rm D} = \frac{U_0}{\sqrt{2} R \rho_{\rm H^+} A} \tag{5.1.5}$$

The resistance in the latter equation can be expressed by the conductivity

$$v_{\rm D} = \frac{U_0 \,\kappa}{\sqrt{2} \,\rho_{\rm H^+} \,d} \,, \tag{5.1.6}$$

where d denotes the distance between the inner electrodes. With equation 5.1.1, 5.1.2 and 5.1.5 or 5.1.6, the average proton permeation length l can be calculated.

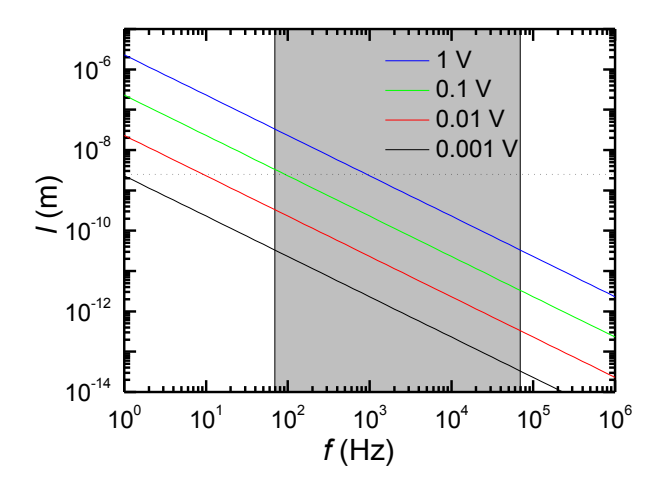


Figure 5.1.2: Calculated permeation lengths l of protons through the aqueous phase of Nafion® within one sign of the applied alternating voltage as a function of the frequency. Vertical dotted line: Mean diameter of the water channels of  $2.5 \times 10^{-9}$  m as measured by Allen  $et\ al.$  [40]. Gray shaded area: Frequencies, where the ohmic resistance of the membrane dominates the impedance measured (Fig. 5.1.1).

As derived in the next section, an aqueous solution with the same proton concentration as that in the aqueous phase of Nafion shows a proton conductivity of approximately 0.57 S/cm. With reference to a molar mass of water of 55 g/mol [126], a mole density of water 18.2 mol/l can be calculated. In Nafion the water uptake is  $\lambda \approx 20$  water molecules per acidic site (section 3.1). Thus, in an acid with same same proton concentration, the amount of proton equals approximately one-twentieth of that of water molecules. Accordingly, the proton density of such a solution equals  $\rho_{\rm H^+} = 8.7 \times 10^4 \, {\rm C/l}$ . With an excitation amplitude of 1 V, the drift velocity can be calculated to  $4.6 \times 10^{-5} \, {\rm m/s}$ .

In the case of the Nafion<sup>®</sup> membrane, a resistance of  $330\,\Omega$  was measured in the region of ohmic conductance. Including the sample geometry, equation 5.1.5 and an excitation amplitude of  $1\,\mathrm{V}$ , a drift velocity of  $7.8\times10^{-6}\,\mathrm{m/s}$  can be calculated. However, this value does not take into account the detours that result from the proton permeation in the water channels of the Nafion<sup>®</sup> membrane. Multiplying this value by a tortuosity of 6, as derived in the next section, the velocity includes the detours. With this approach the velocity equals the  $4.6\times10^{-5}\,\mathrm{m/s}$  that were calculated using the first approach. Using this value for the drift velocity, Figure 5.1.2 displays the permeation length l.

Allen et al. [40] measured the average diameter of the water channels in a fully hy-

drated Nafion<sup>®</sup> membrane to  $2.5 \times 10^{-9}\,\mathrm{m}$  (see Section 3.1). Figure 5.1.2 illustrates that within the frequency range from 70 Hz to 70 kHz) (where the ohmic proton conduction dominates the impedance spectra), the estimated permeation lengths of the protons in the water channels range from  $3.4 \times 10^{-8}\,\mathrm{m}$  to  $3.4 \times 10^{-14}\,\mathrm{m}$ . Although the protons were moved at the minimum by less than four orders of magnitude than the length scale of the water channels' diameter and at the maximum by distances that are approximately 14 times larger, the measured proton conductivity was equal. This equal conductivity indicates, that independent of the length scale of the proton permeation through fully hydrated Nafion<sup>®</sup>, the movement of the protons takes place on the same paths.

Scattering of protons at the pore walls of Nafion® would lead to non-linear responses, which could not be experimentally observed (negligible higher harmonics of the impedance measured). Moreover, if scattering processes occur at the pore walls, these would lead to an impedance that depends on the permeation length: at the length scale below the water channel diameter less scattering processes have to be expected than in the case of the permeation lengths that exceed the diameter of the water channels. In summary, if scattering processes of protons with pore pore walls had occurred, these did not lead to measurable contributions to the impedance.

In the attachment (Section 14.2), the capacitances between the water channels are estimated to be too small to contribute in a measurable amount to the impedance. Thus, the contributions of dead-end water channels (which do not show a connection between the electrodes) to the overall proton conduction at ACs are negligible. To summarize, the proton mobility in fully hydrated Nafion<sup>®</sup> was derived to be independent of the permeation length, as explained by the same paths of the proton movement. The response of the proton permeation to the excitation was linear, which led to the conclusion that scattering events of protons with the pore walls do not significantly contribute to the overall conductivity. Hence, the proton conductivities of fully hydrated Nafion<sup>®</sup> membranes at ACs and DCs are expected to be equal.

# 5.2 Conductivities of Nafion® membranes and aqueous solutions

In the following, the proton conductivity of Nafion<sup>®</sup> membranes is compared to those of aqueous solutions with equal proton concentrations as the aqueous phase in fully hydrated Nafion<sup>®</sup> membranes. Moreover, the influence of the water content on the proton conductivity of Nafion<sup>®</sup> membranes is discussed.

In contrast to Nafion<sup>®</sup> membranes, where the anions are covalently bonded to the polymer matrix and thus do not contribute to the measured AC conductivity, the anions of aqueous solutions move in the opposite direction to the cations. Thus, in aqueous solutions cations and anions contribute to the conductivity at ACs. The influence of different sizes of the anions, their movement, and their hydration shells on the conductivity is examined here for an aqueous hydrochlorid acid (HCl) solution and an aqueous trifluoromethanesulfonic acid (TMSA) solution. Like Nafion<sup>®</sup>, both aqueous acids are also superacids with acid strengths of pKa < -5 [143,177], which means that more than 99.999 % of their protons are dissociated. In order to determine the proton conductivity of the HCl solution, the contributions of the chloride ions to the overall conductivity were subtracted using the procedure described in the in the attachment (Section 14.2) in detail. In short, by this procedure the transport numbers of the potassium and chloride ions in the KCl solution were determined from its conductivity measured. With these values, the contributions of the chloride anions to the overall conductivity of the HCl solution were estimated. The measured conductivities of HCl and KCl are moreover compared to data reported in the literature (comparison graphed in Figure 5.2.1).

The proton mobility is due to the contributions of the Grothuss mechanism [112] (proton exchange along the hydrogen bond network) at least by a factor of 4.5 times larger than the mobility of other cations or anions (except the hydroxide anion, which is also conducted via the Grothuss mechanism) [178, page 761]. In addition, the anions (CF<sub>3</sub>SO $_3^-$ ) of TMSA are approximately eight times heavier and more spacious than the hydronium  $H_3O^+$  cations. Thus, the ion transport number of the anions of TMSA can be expected to be far smaller than that of the protons, which means that the effect of the anion movement on the overall conductivity of TMSA is expected to be negligible. However, these large anions may stand in the way for the proton conduction and thus reduce the proton mobility. Compared to the sulfonic acid functional groups of Nafion<sup>®</sup>, the sulfur in TMSA is also covalently bonded to fluorinated carbon, which means similar electronic environments.

At standard ambient temperature and pressure, the mole density of water equals  $\hat{\rho}_{\text{H}_2\text{O}} = 55.5\,\text{mol}\,\text{l}^{-1}$ , while the density variation of water from room temperature up to 85 °C is with less than 3 % negligible [126]. By dividing the mole density of water through the amount of water molecules per sulfonic acid group  $\lambda$ , the proton concentration  $c_{\text{H}^+}$  in the aqueous phase of Nafion® can be estimated. In the case of  $\lambda = 20$ ,  $c_{\text{H}^+}$  can be determined to:

$$c_{\mathrm{H}^{+}} = \frac{\hat{\rho}_{\mathrm{H}_2\mathrm{O}}}{\lambda} \approx 2.8 \,\mathrm{mol/l} \tag{5.2.1}$$

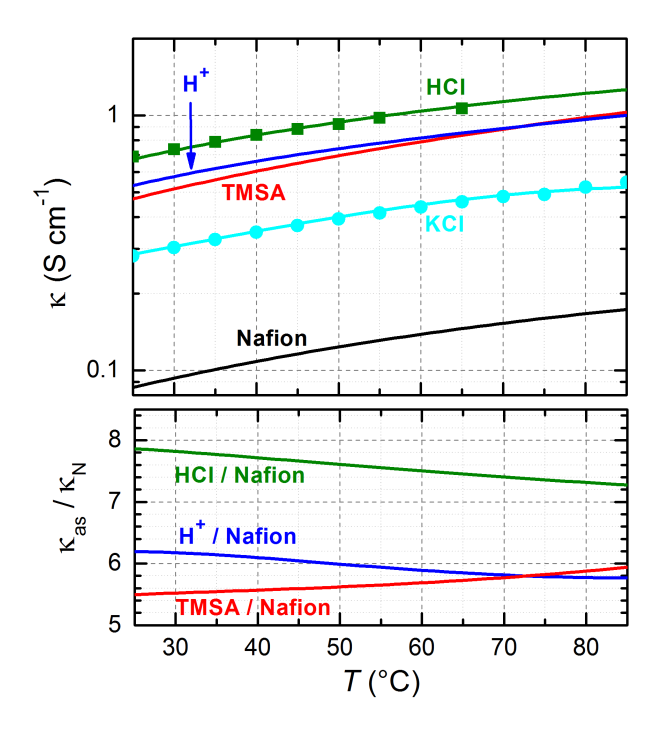


Figure 5.2.1: Top: Mean of the measured conductivities (solid lines) of HCl, KCl, TMSA and Nafion<sup>®</sup> as a function of temperature. The proton conductivity of the aqueous HCl solution denoted by H<sup>+</sup> was approximated as discussed in the attachment (Section 14.2). The aqueous solutions were of a molarity of  $2.8\,\mathrm{mol}\,1^{-1}$ , which corresponds to the molarity of the aqueous phase in fully hydrated Nafion<sup>®</sup> for  $\lambda=20$ . The fit parameters and a discussion of the measurement errors are also given in the attachment (Section 14.2). Squares: Literature data of the conductivity of HCl [179]. Dots: Literature data of the conductivity of KCl [180]. Bottom: Conductivities of the aqueous solutions (denoted as  $\kappa_{\rm as}$ ) in relation to that of Nafion<sup>®</sup> (denoted as  $\kappa_{\rm N}$ ). As discussed in the SI, the error of these ratios are approximately 12 % for the estimation of the proton conductivity of HCl and 10 % for HCl and TMSA.

Figure 5.2.1 shows the ionic conductivities of the aqueous HCl, KCl, and TMSA solutions with this molarity and the proton conductivity of Nafion  $^{\circledR}$  immersed in water. The influence of temperature on these conductivities was fitted by polynomials of third grade. The values of the fits and the discussion of measurement errors are given in the attachment (Section 14.2). Using the fits to the conductivities of the aqueous HCl and KCl solutions, the proton conductivity of the aqueous HCl solution was extracted as also discussed in the attachment (Section 14.2). In the total temperature range from 25  $^{\circ}$ C to 85  $^{\circ}$ C considered, the proton conductivity in HCl was estimated to be approximately 6.0  $\pm$  0.7 times higher (5.8  $\pm$  0.6 times for TMSA) than that of

Nafion<sup>®</sup> (Fig. 5.2.1). As discussed in Section 3.1, the water content of fully hydrated Nafion<sup>®</sup> is in the considered temperature range constant. Thus, the influence of temperature on the morphology of the aqueous phase and the solid phase is expected to be negligible. The similar temperature dependencies of the proton conductivities (constant ratios in Fig. 5.2.1) of Nafion<sup>®</sup> and the aqueous acids could mean, that the activation energies and the underlying mechanisms for the proton conduction in both media are similar.

In the following, the proton conductivity of Nafion<sup>®</sup> is analyzed as a function of the water content. Sone *et al.* [41] reported the proton conductivity of Nafion<sup>®</sup> in a humidified atmosphere as a function of the relative humidity (denoted as rh) using a similar setup as in this work. On the basis of experimental data reported in the literature, Eikerling *et al.* [144] described the water content of Nafion<sup>®</sup> as a function of the relative humidity at 20 °C by:

$$\lambda(rh) = 3 rh^{0.2} + 11 rh^4 \tag{5.2.2}$$

This water content was related to the volume fraction of water  $\phi$  by [152, 158]:

$$\phi = \frac{18\,\lambda}{550 + 18\,\lambda}\tag{5.2.3}$$

Using the conductivities reported by Sone *et al.* and the latter two relations, the proton conductivity of Nafion<sup>®</sup> as a function of the volumetric water content was calculated.

Figure 5.2.2 shows the influence of the volumetric water content on the conductivity of Nafion<sup>®</sup> (denoted as  $\kappa_N$ ) normalized to the proton conductivity of the aqueous HCl solution (denoted as  $\kappa_{as}$ ). This normalized conductivity was divided by the volume fraction of water leading to the relation:  $\frac{\kappa_N}{\kappa_{as}} \frac{1}{\phi}$ . With this expression, values smaller than unity are ascribable to geometric restrictions other than the volume fraction and reduced proton mobilities. The proton mobilities in the aqueous phase of Nafion<sup>®</sup> may decrease toward smaller water contents and originate from the inhomogeneous distribution of the protons in the water channels [20,21,160,161]. Toward lower water contents the tortuosity (as reported by Zhao *et al.* [159] using pulsed gradient spin echo NMR) increases and the connectivity between the water channels decreases. The morphology change resulting also decreases the conductivity.

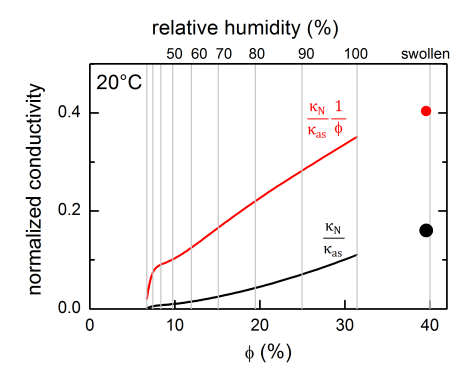


Figure 5.2.2: Normalized conductivities of Nafion<sup>®</sup> as a function of the volume fraction of water  $\phi$  exemplified for a temperature of 20 °C. Black: Normalization of the conductivity of Nafion<sup>®</sup> to the proton conductivity of an aqueous HCl solution. Red: Additional normalization to the water content. Vertical gray lines: Different relative humidities. Solid black and red lines: Based on the conductivities reported by Sone *et al.* [41]. Points: Based on the conductivities measured in this study.

# 5.3 Physical effects that reduce the proton conductivity of Nafion®

Following effects may cause the smaller proton conductivity of Nafion<sup>®</sup> in comparison to those of the aqueous solutions with equal molarity:

- The morphology of the aqueous phase in Nafion®.
- The functional groups and the side chains of Nafion<sup>®</sup> that penetrate into the aqueous phase [181]. These spacious anions may stand in the way of the proton conduction and thus may reduce the proton mobilities compared to aqueous solutions with smaller anions.
- The ions are homogeneously distributed in the aqueous solution, while the proton distribution in the water channels of Nafion<sup>®</sup> membranes is inhomogeneous [21]. This inhomogeneity is caused by the attractive electrostatic force of the protons to the anions, which are covalently bonded to the polymer matrix at the pore walls of the water channels [21]. As a result, the mobility of the protons in the water channels may be smaller than that of aqueous solutions [20,21].

The aim of the following discussion is to estimate the impact of these effects on the conductivity of fully hydrated Nafion<sup>®</sup> membranes. The geometric restrictions of the proton conduction caused by the morphology of the aqueous phase in Nafion<sup>®</sup> are related to the volume fraction of the aqueous phase in Nafion<sup>®</sup>, the connectivity of the water channels, the detours of the proton conduction in tortuous water channels,

and the varying diameter of the water channels. In the attachment, the sum of these geometric effects on the overall conductivity of Nafion  $^{\circledR}$  is physically described using the geometric restriction factor  $\zeta$ . This factor equals the ratio of the conductivity in the aqueous phase to the total conductivity of the membrane. With this factor, the proton conductivity of Nafion  $^{\circledR}$   $\kappa_N$  is related to that of an aqueous solution  $\kappa_{as}$  with the same proton concentration by

$$\frac{\kappa_{\rm N}}{\kappa_{\rm as}} = \frac{\mu_{\rm ap}}{\mu_{\rm as}} \, \zeta \,, \tag{5.3.1}$$

where  $\mu_{ap}$  represents the proton mobility in the aqueous phase of fully hydrated Nafion<sup>®</sup> and  $\mu_{as}$  that of an aqueous reference solution. Accordingly, the ratio of the mobilities and the geometric restriction factor are responsible for the different proton conductivity of Nafion<sup>®</sup> membranes in comparison to those of aqueous solutions. The geometric restrictions factor of fully hydrated Nafion<sup>®</sup> is estimated in Chapter 7 using a resistor network model approach. This model is based on a noise algorithm that was constructed to represent the structure of fully hydrated Nafion<sup>®</sup> in the form of the volume fractions, water channel diameters, and domain spacings that were reported by Allen et al. [40]. However, owed to the nature of the random algorithm used to model the structure of fully hydrated Nafion<sup>®</sup>, the modeled geometric restriction factor  $\zeta$  does not entirely represent the real structure of fully hydrated Nafion<sup>®</sup>. When the cryo electron tomography results reported by Allen *et al.* [40] could be described by a resistor network, the geometric restriction factor  $\zeta$  could be determined more precisely.

In the following, the proton mobility inside the aqueous phase of fully hydrated Nafion is estimated based on the discussed estimation of the geometric restriction factor  $\zeta$  and the measured conductivities. In the case of fully hydrated Nafion, the normalized conductivity was determined to  $\frac{\kappa_{\rm N}}{\kappa_{\rm as}} \approx 0.17 \pm 0.02$  (reciprocal of  $\frac{\kappa_{\rm as}}{\kappa_{\rm N}} \approx 6.0 \pm 0.7$ ). This value and the estimation of the geometric restriction factor are within the experimental error equal. Accordingly, using equation 5.3.1, equal proton mobilities inside the aqueous phase of fully hydrated Nafion and that of the aqueous solution of HCl can be estimated. Thus, the smaller conductivity of fully hydrated Nafion in comparison to aqueous solutions is expected to be mainly attributable to the morphology of the aqueous phase.

### 5.4 Synopsis of the chapter

In this chapter, the proton conductivities of Nafion<sup>®</sup> and aqueous solutions with an equal proton concentration as the aqueous phase in fully hydrated Nafion<sup>®</sup> were studied using electrochemical impedance spectroscopy. Based on the measured con-

ductivity of fully hydrated Nafion® and the calculated permeation length of the protons under alternating currents (ACs), the proton mobility was derived to be independent of scattering processes of protons at the pore walls of the water channels. The negligible influence of the permeation path length on the conductivity led to the conclusion, that protons move independently of the excitation amplitude and frequency on the same trajectories, which means equal AC and DC conductivities of fully hydrated Nafion<sup>®</sup>. The proton conductivity of an aqueous hydrochloric acid solution with an equal proton concentration as the water channels in fully hydrated Nafion® was found to be  $6.0 \pm 0.7$  times higher than that of Nafion<sup>®</sup>. The influence of the geometric restrictions by the proton permeation through the morphology of the aqueous phase in fully hydrated Nafion® was modeled in the literature. By comparison of the experimental data presented in this Chapter and the modeled influence of the morphology of the aqueous phase on the overall conductivity that will be presented in Chapter 7, the mean proton mobility in the aqueous phase of fully hydrated Nafion® was estimated to equal that of the aqueous acidic reference solutions. The decreasing conductivity of Nafion® toward smaller water contents was quantified and ascribed to increasing geometric restrictions of the proton conduction and a decreasing proton mobility in the aqueous phase.

# 6 Hydrogen and Oxygen Permeabilities of Nafion<sup>®</sup>

In this chapter, measurements of the gas permeation through Nafion<sup>®</sup> membranes as a function of pressure, relative humidity and temperature are presented. Based on these data, the pathways of the gas permeation through Nafion<sup>®</sup> will be qualitatively described. These results were published previously [120].

#### 6.1 Influence of ambient conditions

The main parameters that influence the hydrogen permeability of Nafion<sup>®</sup> membranes are pressure, relative humidity and temperature.

#### 6.1.1 Pressure

To examine the influence of differential pressure on the hydrogen permeation through a fully hydrated Nafion<sup>®</sup> N117 membrane at 80 °C setup D (Fig. 4.2.1D) was used. Different hydrogen pressures were applied at the cell inlet. Fully humidified hydrogen which additionally carried water was purged along the counter electrode. The partial pressure  $p_{\rm H_2}$  of the hydrogen in the cell was determined by deducting the calculated partial pressure of saturated water vapor  $p_{\rm sv}$  (eq. 4.2.3) from the absolute pressure p (eq. 4.2.4). On the other side of the membrane fully humidified nitrogen that additionally carried liquid water was supplied. The absolute pressure on this side of the membrane is defined as counter pressure. More details on the experimental realization of this setup are provided in the attachment (Section 14.3).

Figure 6.1.1 shows the hydrogen permeation flux density  $\Phi_{\rm H_2}$  through a Nafion<sup>®</sup> N117 membrane (determined by measured current density j using Faraday's law in the form of equation 4.2.6) as a function of  $p_{\rm H_2}$ . The data in this graph were described by a linear fit. The deviations of the measurements from this fit scatter randomly (with an absolute deviation below 3 %). The linear fit to this data passes the origin, so extrapolating  $p_{\rm H_2}$  to 0 bar implies  $\Phi_{\rm H_2} = 0\,{\rm mol\,s^{-1}cm^{-2}}$ . Accordingly, Fick's law (eq. 2.3.3) describes this relationship between  $p_{\rm H_2}$  and the resulting  $\Phi_{\rm H_2}$ . Thus, subtracting  $p_{\rm sv}$  from the absolute pressure p (eq. 4.2.4) exactly yielded the partial pressure of hydrogen  $p_{\rm H_2}$ . Deviations from the calculated partial pressure of hydrogen in comparison to its real partial pressure would lead to a constant offset, which would in turn lead to a deviation of the intercept with the ordinate. The slope of the linear relation is

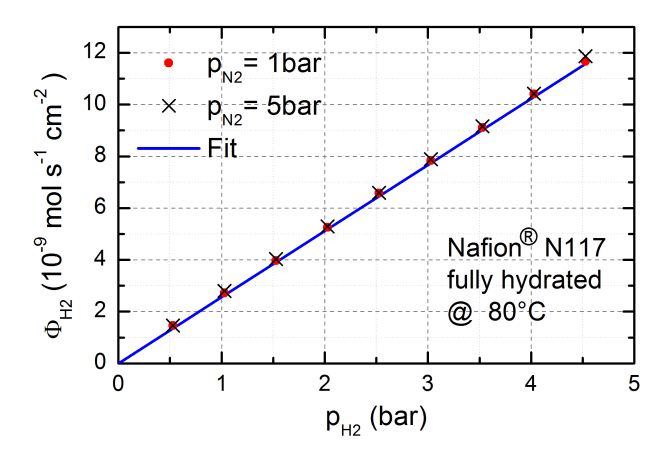


Figure 6.1.1: Measured hydrogen permeation flux density through a Nafion<sup>®</sup> N117 membrane as a function of the partial hydrogen pressure at the counter electrode. The absolute counter pressures of 1 bar (red dots) and 5 bar (black crosses) of humidified nitrogen at the working electrode led to equal current densities. Thus, differential pressure does not act as a driving force for gas permeation through Nafion<sup>®</sup>. The blue line represents the fit to the experimental data.

identified with the derivative of  $\Phi$  with respect to  $p_{\rm H_2}$ , which is proportional to the permeability (eq. 4.2.7). Thus, the constant slope of this relation implies that the permeability is independent of the pressure.

If differential pressure acted as a driving force for gas permeation through the membrane, the hydrogen permeability of the membrane at differential pressure would be larger than that at balanced pressure. However, considering the measurement precision, different counter pressures of either 1 bar or 5 bar of humidified nitrogen at the working electrode led to equal hydrogen permeation fluxes though the membrane (Figure 6.1.1). The permeability determined by fits to the measurements at the different counter pressures showed a difference of approximately 1 %, which can be attributed to the measurement error. Hence, the influence of differential pressure as a driving force for the permeation of gases through Nafion<sup>®</sup> was negligible in the pressure range considered.

At balanced and differential pressure the hydrogen permeation flux density  $\Phi$  through the Nafion<sup>®</sup> membrane depends on the applied hydrogen pressure and was independent of the counter pressure. Accordingly, differential pressure did not push hydrogen through the water channels. The applied differential pressures were smaller than the capillary pressures in the water channels, which were estimated by Eikerling *et al.* [144] to the order of 100 bar. When the applied differential pressures are below

the capillary pressure the water in the water channels cannot be blown out. The low differential pressure forced hydrogen permeability of Nafion and be attributable to a high friction of water permeation through Nafion. As a result, the hydrogen permeation through Nafion under the examined conditions is dominated by the driving force of diffusion. Accordingly, dissolved gases permeate by Brownian motion through the membrane. Following  $\varepsilon = D S$  (eq. 2.3.2), a pressure independent hydrogen permeability (as graphed in Fig. 6.1.1) means that the product of solubility and diffusion coefficient are also independent of pressure. The small hydrogen concentrations of hydrogen  $< 10^{-2} \, \text{mol/l} \, \text{in Nafion}$  [52] may cause a diffusion coefficient that is independent of pressure, which consequently means that the solubility of hydrogen is also independent of pressure.

When two or more species diffuse in a medium, these species can interact, as described by the Stefan-Maxwell relation [182–184]. When these influences are negligible, the Stefan-Maxwell relation can be reduced to Fick's law. During the measurements, the total hydrogen and nitrogen permeation fluxes through the membrane were in opposite directions. The measured independence of the hydrogen permeation from the nitrogen counter pressure indicates that the impact of the interaction of hydrogen and nitrogen molecules during the diffusion process was negligible. To summarize, the pressure independence of the measured hydrogen permeability of Nafion<sup>®</sup> revealed the following facts:

- The calculated partial pressure of saturated water vapor (eq. 4.2.3) influenced the absolute pressures applied during the measurements. Thus, by subtracting saturated vapor pressure  $p_{\rm sv}(T)$  from the absolute pressure p measured, the partial pressure of hydrogen  $p_{\rm H_2}$  at the counter electrode was precisely determined.
- In the examined pressure range, the counter pressure had within the measurement precision no impact on the hydrogen permeation through Nafion<sup>®</sup>. Thus, in the considered pressure range, the hydrogen permeation through Nafion<sup>®</sup> is dominated by the driving force of diffusion.

### 6.1.2 Relative humidity

Figure 6.1.2 shows the results of measuring the hydrogen permeability of a Nafion<sup>®</sup> NR212 membrane as a function of relative humidity using setup D (Fig. 4.2.1D). Humidified hydrogen was supplied at the counter electrode, while humidified nitrogen was supplied at the working electrode. Because Nafion<sup>®</sup> must adsorb water in order to conduct protons, the permeability of the dry membrane cannot be measured using this setup. Experimental details about this setup and the measurement procedure are described in the attachment (Section 14.3). To determine the hydrogen permeability of the membrane (eq. 4.2.7), the partial hydrogen pressure  $p_{\rm H_2}$  was again determined by

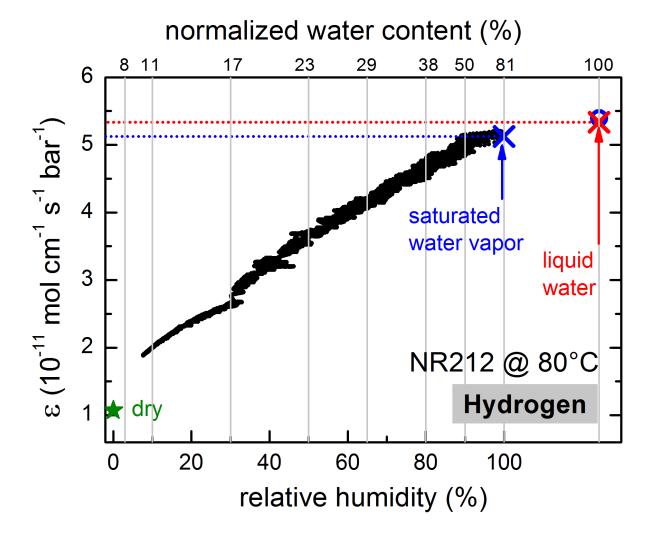


Figure 6.1.2: Hydrogen permeability of Nafion<sup>®</sup> at 80 °C as a function of relative humidity (bottom) and normalized water content (top and vertical gray lines). See the text for the calculation of the normalized water content. Black points: Measured hydrogen permeability using setup D (Fig. 4.2.1D) of a Nafion<sup>®</sup> NR212 membrane. Blue cross and dotted blue line: Mean of the measured permeability at rh = 100 %. Blue circle: Mean of the measured permeability at fully humidified gas fluxes which also carried liquid water. Red cross and dotted red line: Mean of the measured permeability using setup C. Green star: Mean of the permeability of dry Nafion<sup>®</sup> measured with setup E (Fig. 4.2.1E).

subtracting the partial pressure of water vapor from the absolute pressure (eq. 4.2.4). The relative humidity was determined by the ratio of the partial pressure of the water vapor to that of saturated water vapor.

The measurements were conducted at a sample temperature of 80 °C and atmospheric absolute pressure of the gases on both sides of the membrane. By purging the gases with varying relative humidity along the membrane, the hydration level of the Nafion membrane was altered. The water content of Nafion is typically characterized by  $\lambda$ , the amount of water per sulfonic acid group. Kreuer [151] reported that when Nafion is immersed in water, the amount of water per sulfonic acid group is  $\lambda \approx 20$  for the overall temperature range considered here. Moreover, he correlated the water content of Nafion at 80 °C in the form of  $\lambda$  as a function of relative humidity. In Figure 6.1.2, the water content in the form of  $\lambda$  as a function of the relative humidity was normalized to the value of  $\lambda$  in the fully hydrated state, where the Nafion membrane is in contact with liquid water.

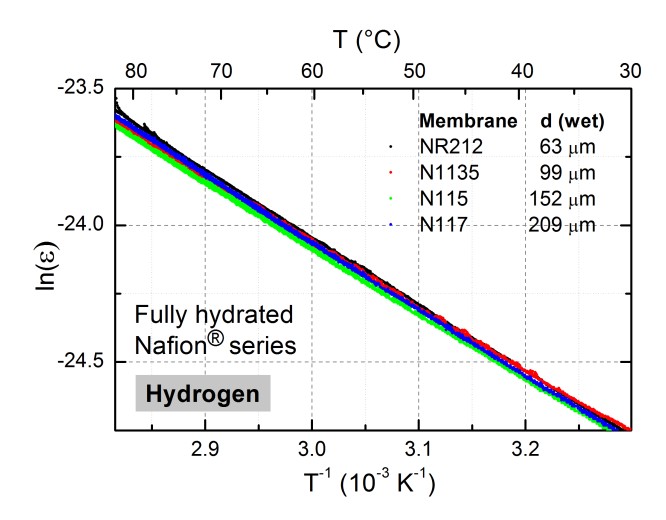


Figure 6.1.3: Measured hydrogen permeabilities ( $[\varepsilon] = \text{mol cm}^{-1} \, \text{s}^{-1} \, \text{bar}^{-1}$ ) of fully hydrated Nafion® membranes with various thicknesses as a function of temperature graphed in an Arrhenius plot. The permeabilities show an approximately linear relation in this depiction, which allows the estimation of their activation energies using the Boltzmann distribution (eq. 2.3.6).

The level of hydrogen permeability measured increased towards higher relative humidity. Saturated water vapor with dissolved hydrogen at full humidification led to approximately 3.5 % less permeability as in the case that the gas mixture additionally carried liquid water (Fig 6.1.2). This behavior may be attributed to different water contents of Nafion<sup>®</sup> at these conditions [151], as graphed in Figure 6.1.2. A qualitative explanation of the data will be given in Section 6.3, while a detailed quantitative analysis of this data will be given in the next chapter. When a proton flux through the membrane appears, convection may influence gas permeation through it. Within the experimental measurement error, equal hydrogen permeabilities of fully hydrated Nafion<sup>®</sup> were measured with setup C and setup E, as further discussed in the attachment (Section 14.3).

### 6.1.3 Temperature

In the following, the influence of temperature on the hydrogen and oxygen permeabilities of fully hydrated (wet) Nafion<sup>®</sup> and dry Nafion<sup>®</sup> are examined. In the fully hydrated state, when Nafion<sup>®</sup> is in contact with liquid water, its water uptake is independent of the temperature as characterized by  $\lambda \approx 20$  (see Section 3.1). Thus, in this case the temperature dependencies of the hydrogen and oxygen permeabilities of fully hydrated Nafion<sup>®</sup> are dominated by the physical permeation mechanisms.

The overall permeability of Nafion<sup>®</sup> is expected as a linear combination of those of the aqueous phase (eq. 2.3.17) and the solid phase (eq. 2.3.6). To measure the permeabilities of fully hydrated and dry Nafion<sup>®</sup> as a function of temperature, setup C (Fig. 4.2.1C) and setup E (Fig. 4.2.1E) were used. In the case of measuring the permeabilities of fully hydrated Nafion<sup>®</sup> membranes, the partial pressures of hydrogen or oxygen were determined by deducting the temperature dependent partial pressure of saturated water vapor (eq. 4.2.3) from the constant absolute pressures at the membranes using equation 4.2.4.

Figure 6.1.3 shows the measured hydrogen permeabilities of fully hydrated Nafion<sup>®</sup> membranes with various thicknesses in an Arrhenius plot. In this depiction, the measured temperature dependence of the permeability is approximately linear, as described by the Boltzmann distribution (eq. 2.3.6). The slopes of these lines in the plot correspond to the negative activation energies divided by the Boltzmann constant (eq. 2.3.6). Non-linear contributions to the permeability in this depiction will be discussed in the next chapter, when the measurements will be compared to the developed model.

The absolute pressures of fully humidified hydrogen of 2 bar, 3 bar, 4 bar and 5 bar were applied to fully hydrated Nafion<sup>®</sup> membranes with the different thicknesses stated in Figure 6.1.3. These different pressures and thicknesses as well as intrinsic variations of the membranes showed a negligible influence on the measured hydrogen permeability. At the mean temperature of 55 °C of the considered temperature range and at the different pressures, the permeabilities measured of the fully hydrated Nafion<sup>®</sup> membranes with the different thicknesses showed a standard deviation of 4.5 %. The standard deviation of the activation energies from these measured permeabilities was 2.2 % (Table 6.1.1). Variations in the membrane thicknesses contributed to the values of the absolute measured permeabilities which, however, did not influence the slope of the temperature dependence in Figure 6.1.3 and the activation energies thereby determined (eq. 2.3.6). Accordingly, the determined mean activation energy was affected by a smaller relative error than that of the mean absolute value of the permeability.

Figures 6.1.4 and 6.1.5 show the measured temperature dependencies of the hydrogen and oxygen permeabilities of fully hydrated Nafion<sup>®</sup>, dry Nafion<sup>®</sup> and polytetrafluoroethylene (PTFE). Moreover, these figures show the hydrogen and oxygen permeabilities of water, which were calculated on the basis of data from the literature [52,124] and the equations 2.3.17 and 2.3.15. The activation energies of the hydrogen and oxygen permeabilities of the different media were approximated by linear fits of  $\ln(\varepsilon)$  vs 1/T, as summarized in Table 6.1.1. The prefactors  $\varepsilon_0$  of these fits are

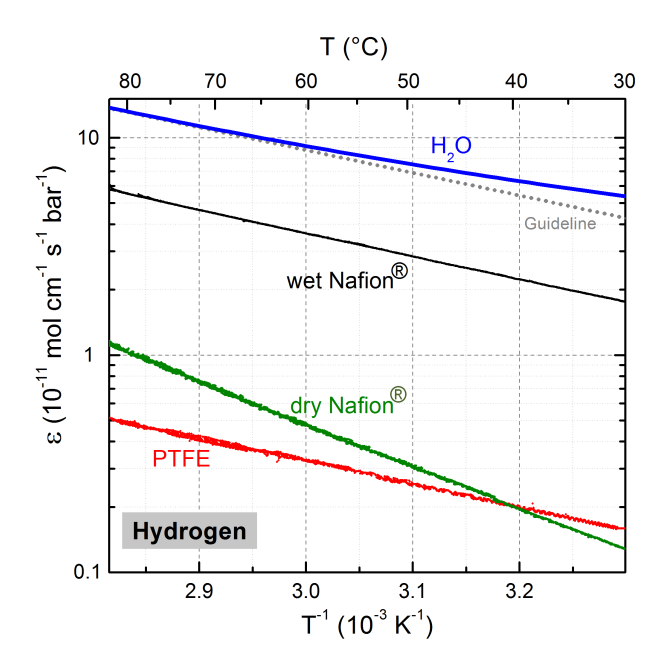


Figure 6.1.4: Modified Arrhenius plot (logarithmic scale of  $\varepsilon$  instead of  $\ln(\varepsilon)$ ) of the hydrogen permeabilities of water, Nafion<sup>®</sup>, and PTFE. Black points: Fully hydrated Nafion<sup>®</sup> (measured). Green Points: Dry Nafion<sup>®</sup> (measured). Red points: PTFE (measured). Blue line: Water [52,124] (calculated using eq. 2.3.17). Pointed gray line: guide to the eye with the slope of the permeability measurements of wet Nafion<sup>®</sup>.

outlined in the attachment (Section 14.3). In Table 6.1.2, the absolute values of the permeabilities are listed for temperatures of 30, 55 and 80 °C. Hydrogen and oxygen are both non-polar diatomic gases and thus the temperature dependencies and absolute values range in the same order of magnitude. The difference of the permeabilities of both gases in these media might be attributable to their different size and weight, as further discussed in Section 6.2.

The activation energies of the hydrogen and oxygen permeabilities of PTFE determined from the measurements are equal to those reported by Pasternak *et al.* [185] (Table 6.1.1). However, the absolute values of the permeabilities differ by a factor of approximately 2.5 for hydrogen and oxygen (Table 6.1.1). These differences were possibly caused by different densities of the PTFE samples that were used for the measurements. With the higher density of the PTFE sample, the mean free path of the gas molecules between the polymer chains decreases. Accordingly, in the case of gas diffusion over a defined distance, the amount of thermally activated diffusion prosses across the potential barriers comprised by the van der Waals forces between the polymer chains may increase with higher sample densities. Thereby, an increase of the

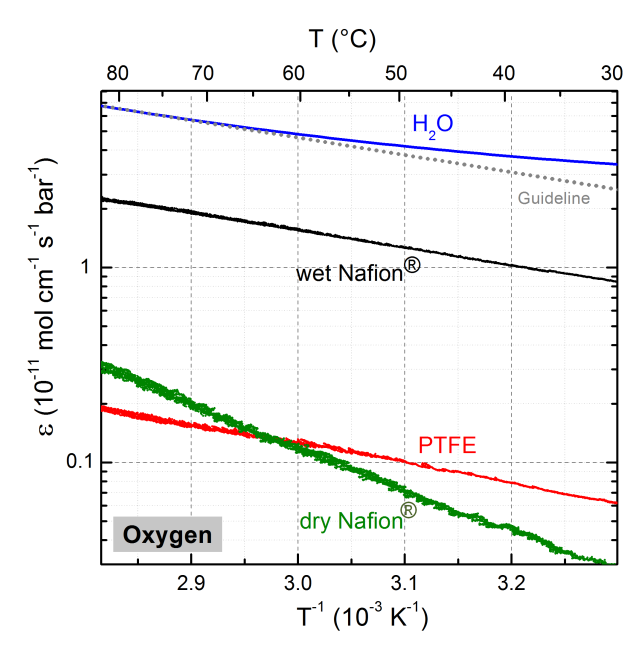


Figure 6.1.5: Modified Arrhenius plot of the oxygen permeabilities of water, Nafion<sup>®</sup>, and PTFE. In this graph the same color code as that in Figure 6.1.4 was used.

Table 6.1.1: Activation energies  $(E_A)$  in  $1 \times 10^{-20}\,\mathrm{J}$  for the diffusion, solubility and permeability of hydrogen and oxygen in water, fully hydrated (wet) Nafion<sup>®</sup>, dry Nafion<sup>®</sup> and PTFE. Approximations obtained from linear fits in the Arrhenius plot  $(\ln(\varepsilon) vs\ 1/T)$  to the measurements of this study are marked with '\*', where the errors were determined by the standard deviations between the measurements. Approximations obtained by linear fits in the Arrhenius plot to the data from the literature ( [52, 124], eq. 2.3.17 and 2.3.15) are marked with ' $\sharp$ '. Data from the literature of different authors that varied heavily [52] and that does not allow precise conclusions to be drawn is marked with ' $\sharp$ '. Information not available in the literature is marked with '-'. Cited data from the literature is marked with the reference. The prefactors related to these activation energies are given in the attachment (Section 14.3).

| Gas            | $E_{\rm A}  (10^{-20}  \rm J)$ | H <sub>2</sub> O        | Nafion® (wet)     | Nafion® (dry)   | PTFE*             | PTFE [185]     |
|----------------|--------------------------------|-------------------------|-------------------|-----------------|-------------------|----------------|
| H <sub>2</sub> | $E_{\varepsilon}$              | 2.68 #                  | $3.32 \pm 0.07$ * | $6.2 \pm 0.1$ * | $3.38 \pm 0.08$ * | 3.55 [185]     |
|                | $E_{ m D}$                     | $2.75 \pm 0.03^{[124]}$ | -                 | -               |                   | -              |
|                | $\Delta H_{ m S}$              | -0.07 <sup>‡</sup>      | -                 | -               |                   | -              |
| O <sub>2</sub> | $E_{\varepsilon}$              | 1.97 ‡                  | $2.81 \pm 0.02$ * | $7.1\pm0.2$ *   | $3.16 \pm 0.05$ * | 3.16 [185]     |
|                | $E_{\mathrm{D}}$               | $3.05 \pm 0.02$ [124]   | Ц                 | Ц               |                   | $4.37^{[185]}$ |
|                | $\Delta H_{ m S}$              | -1.08 <sup>‡</sup>      | Ц                 | Ц               |                   | -1.20 [185]    |

prefactor  $\varepsilon_0$  may result. The activation energy required for the jumps of the gas molecules across the potential barriers comprised by the van der Waals forces between the polymer chains may be retained for different sample densities, which possibly led to

| stated in Section 2.3. (*): Measured in this work. |       |                               |                 |                   |                   |             |
|--|-------|-------------------------------|-----------------|-------------------|-------------------|-------------|
| Gas  | T     | H <sub>2</sub> O <sup>♯</sup> | Nafion® (wet)*  | Nafion® (dry)*    | PTFE*             | PTFE [185]) |
|  | 30 °C | 5.36                          | $1.73 \pm 0.07$ | $0.14 \pm 0.02$   | $0.16 \pm 0.02$   | 0.39        |
| $H_2$  | 55 °C | 8.31                          | $3.16\pm0.14$   | $0.44 \pm 0.05$   | $0.29\pm0.03$     | 0.74        |
|  | 80 °C | 13.2                          | $5.32 \pm 0.25$ | $1.17\pm0.09$     | $0.49\pm0.05$     | 1.28        |
|  | 30 °C | 3.38                          | $0.97 \pm 0.09$ | $0.027 \pm 0.003$ | $0.062 \pm 0.008$ | 0.15        |
| $O_2$  | 55 °C | 4.55                          | $1.62\pm0.12$   | $0.099 \pm 0.007$ | $0.11 \pm 0.09$   | 0.27        |
|  | 80 °C | 6.55                          | $2.52\pm0.20$   | $0.30\pm0.03$     | $0.18\pm0.13$     | 0.45        |

Table 6.1.2: Values of the permeabilities in  $\varepsilon = 10^{-11}\,\mathrm{mol\,cm^{-1}\,s^{-1}\,bar^{-1}}$  at three different temperatures. (‡): Calculated by the data of Wise *et al.* [124] and the equations stated in Section 2.3. (\*): Measured in this work.

a reproduction of the activation energies reported by Pasternak [185].

#### 6.2 Influence of the solubilities

Wise  $et\ al.$  measured the influence of temperature on the diffusion coefficients D of hydrogen and oxygen in water and described this data with fits of the Boltzmann distribution [124] (eq. 2.3.11). The solubilities S of both gases in water are affected by polynomial terms (eq. 2.3.14), which cause deviations from the exponential temperature dependence described by the Boltzmann distribution [52]. Because  $\varepsilon=D\ S$  (eq. 2.3.2), the polynomial terms of the solubility also influence the hydrogen and oxygen permeabilities of water. This influence resulted in deviations from the Boltzmann distribution, which will be discussed in detail in the next chapter, when the measured permeabilities are compared with the modeled permeabilities. To approximate the activation energies of the hydrogen and oxygen permeabilities of water, linear fits to  $\ln(\varepsilon)\ vs\ 1/T$  were conducted (Table 6.1.1).

The activation energy of the hydrogen diffusion through water is approximately 10 % smaller than that of oxygen [124] (Table 6.1.1). This difference is attributable to the larger mobility of hydrogen, as its weight is less (1/16) and its size is smaller than that of oxygen (the Van-der-Waals radius of hydrogen is approximately 15 % smaller than that of oxygen [186], while the bonding length between the hydrogen atoms is approximately 39 % smaller than that of oxygen atoms [187]). However, the approximated activation energies of the permeabilities of water to both gases show opposite trends. The approximated activation energy of the permeability is the sum of the approximated heat of solution  $\Delta H_{\rm S}$  and the activation energy of the diffusion coefficient  $E_{\rm D}$  (eq. 2.3.6). With reference to the data in Table 6.1.1, the higher heat of solution of hydrogen in water causes a 42 % higher activation energy for the hydrogen permeability of water compared to that of oxygen.

The activation energy of the permeability of PTFE to hydrogen is also approximately 7% larger than that to oxygen. Pasternak et al. showed that the solubility of oxygen in PTFE is precisely describable with the Boltzmann distribution [185] (eq. 2.3.6). Due to a lack of data in the literature on the solubility and diffusion coefficient of hydrogen in PTFE, the cause of the 7 % higher activation energy for hydrogen permeability compared to that of oxygen could not be determined. Analogously to water, the activation energy for hydrogen diffusion through PTFE might be smaller than that for oxygen, while the influence of the solubility possibly leads to higher activation energy for the hydrogen permeability of PTFE compared to that of oxygen. The permeabilities of fully hydrated Nafion® show the same trend by a 18% higher activation energy of the hydrogen permeability than that of oxygen. This trend may also be attributable to a higher heat of solution of hydrogen in fully hydrated Nafion® compared to that of oxygen. As a result, the opposite trends for the activation energies of the diffusion coefficients may be overshadowed. In contrast, the approximated activation energy for the hydrogen permeability of dry Nafion<sup>®</sup> is smaller than that of oxygen (Table 6.1.1). Once again, the same trend for the activation energies for the diffusion of both gases is assumed, which is in this case possibly not overshadowed by a converse trend of the heat of solutions of both gases.

# 6.3 Pathways for the gas permeation

The measurements conducted and their correlation to the microscopic structure is qualitatively interpreted in the following, while a detailed quantitative analysis is presented in the next chapter. The hydration level of Nafion<sup>®</sup> increases with the relative humidity of the ambient atmosphere [144] and thereby enlarges hydrogen permeability (Fig. 6.1.2). When Nafion<sup>®</sup> is hydrated, the water is accumulated in the form of water channels [144]. The gas permeation through these water channels can bypass the pathways through the solid phase, as illustrated in Figure 6.2.1. Because the gas permeability of water is more than tenfold larger than that of dry Nafion<sup>®</sup> (Fig. 6.1.4 and 6.1.5), a higher water uptake of Nafion<sup>®</sup> increases its overall gas permeability. The alternating permeation through the aqueous and solid phase of the membrane are here defined as mixed pathways, where the large permeability of the aqueous phase is utilized while detours by the permeation through the morphology of the aqueous phase are avoided by shortcuts through the solid phase. As a result, the permeabilities of both phases account for the activation energy and absolute value of the permeability of the hydrated membrane.

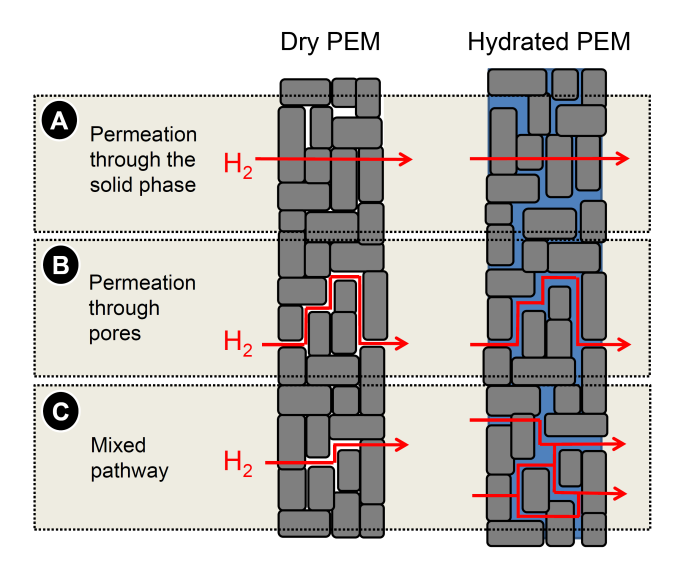


Figure 6.2.1: Descriptive sketch of the pathways (red arrows) for the gas permeation through a segment of a PEM exemplified for hydrogen molecules. The solid polymeric phase (agglomerate of ionomers) is depicted as the gray area, water as the blue area and pores filled with gas as the white area. Left: Dry PEM. Right: Hydrated PEM. The hydration of the PEM leads to the formation of water channels, where the permeability is approximately tenfold larger than that of the solid phase. (A): Permeation of gas molecules through the solid phase. (B): Permeation of gas molecules through pores or water channels. (C): Mixed pathways as a combination of alternating permeation through the aqueous and solid phase of the PEM.

# 6.4 Synopsis of the chapter

In this chapter, novel modifications of the electrochemical monitoring technique were employed to precisely measure the influence of pressure, relative humidity and temperature on the hydrogen permeability of Nafion<sup>®</sup>. Up to 5 bar, hydrogen permeability was independent of applied pressures on both sides of Nafion<sup>®</sup> membranes, which means that in this pressure range differential pressure has a negligible effect as a driving force for the gas permeation. Accordingly, gas permeation through Nafion<sup>®</sup> is of a solely diffusive nature. The hydrogen permeability of Nafion<sup>®</sup> increased towards higher water contents as a result of the formation of water channels and the approximately tenfold larger permeability of water than that of dry Nafion<sup>®</sup>. Alternating gas permeation through the aqueous and solid phase of Nafion<sup>®</sup> results, which leads to a total permeability that is influences by both phases. In the fully hydrated state, the water content of Nafion<sup>®</sup> is independent of the temperature (in the range of 20 °C to 95 °C), which means that the measured increase of the hydrogen and

oxygen permeabilities toward higher temperatures was ascribed to the temperature dependence of thermally activated mechanisms of the permeation. Using the determined permeabilities, the hydrogen and oxygen permeation fluxes through Nafion<sup>®</sup> membranes in fuel cells and water electrolyzers can be modeled with respect to applied pressures by using Fick's law of diffusion [45,188]. Based on the data presented, a resistor network model accounting for the alternating pathways of gas permeation through the aqueous and solid phase of fully hydrated Nafion<sup>®</sup> is presented in the next chapter.

# 7 Resistor network modeling of the gas permeation through Nafion<sup>®</sup>

In the previous chapter, the hydrogen and oxygen permeabilities of fully hydrated Nafion<sup>®</sup> were measured as a function of temperature. In the fully hydrated state, the water content of Nafion<sup>®</sup> is nearly independent of the temperature (see Section 3.1). As a consequence, the morphology of the aqueous phase in fully hydrated Nafion<sup>®</sup> is not altered by the influence of temperature. Accordingly, the temperature dependencies of the hydrogen and oxygen permeabilities of fully hydrated Nafion<sup>®</sup> were solely ascribed to the physical permeation mechanisms. The activation energies of the resulting permeabilities were approximated and interpreted as a mixture of those of the aqueous and solid phase, which was attributed to the alternating permeation through these phases.

In this chapter, a resistor network model is used to simulate the hydrogen and oxygen permeation through the microscopic structure of Nafion<sup>®</sup>, including the aqueous and solid phase, as well as a postulated intermediate phase at the boundary of these main phases. In the first section of this Chapter, the model will be presented. Second, the permeabilities of Nafion<sup>®</sup> will be simulated and compared to the experimental results of the first part. Within this aim, the influence of temperature and water content on the permeability of Nafion<sup>®</sup> will be considered and the permeabilities of the different phases will be estimated. Third, the physical effects that influence the permeabilities of the phases and the outcome of the simulations will be discussed. Based on this discussion, approaches for a rational design of polymer electrolyte membranes (PEMs) with reduced permeabilities will be elucidated. The model presented in the following was published previously [189].

# 7.1 Model development

In the following, the resistor network model to simulate the gas permeability of Nafion<sup>®</sup> is presented. In order to create a simulation domain that is physically representative for the microscopic structure of Nafion<sup>®</sup>, the data reviewed in Section 3.1 is employed. Next, the physical description of the permeabilities of the different phases is derived, followed by elucidating the simulation procedure.

#### 7.1.1 Resistor network model

Several approaches have been presented in literature to describe the influence of the morphology of the aqueous phase on the macroscopic conductivity of Nafion<sup>®</sup> using resistor networks [21,152,169]. In these works, Nafion<sup>®</sup> was modeled as consisting of two phases, the conducting aqueous phase and the non-conducting solid phase. In contrast to proton conduction where only the aqueous phase is conducting, gas permeation through the solid phase also contributes to the total permeability, although to a different extent than the aqueous phase. In addition, the intermediate phase between the solid phase and the aqueous phase influences the gas permeability, as described later. Accordingly, the model presented here consists of three distinct phases:

- The aqueous phase.
- The solid phase.
- The intermediate phase at the boundary of the water channels, where the aqueous phase meets the solid phase.

For the purpose of simplification, the permeabilities inside the phases are assumed to be homogeneously distributed, which means that the mean permeabilities of each of these phases are described by the model.

The resistor network for the calculation of the gas permeabilities of Nafion® was formulated using the open source package OpenPNM [175]. A three-dimensional network with cubic connectivity composed of 200 resistor segments in all three direction was used, which thus consisted of 8 million resistor elements in total. A flow chart of the algorithm is depicted in Figure 7.1.1. It essentially consists of two blocks of steps: first, the microscopic structure of Nafion® is modeled in a three-dimensional cubic domain based on experimental data reported in the literature (Figure 7.1.1, block I, steps 1-6). This structure then comprises the three distinct phases distributed across the calculation domain. The distribution of the phases is adjusted in order to match the literature values of the volume fractions of the solid/aqueous phase and the water channel dimensions in an iterative procedure. In Figure 7.1.2, a two dimensional section of the resulting model domain is shown. Second, the gas permeation through this calculation domain is then simulated and the total gas permeability of the modeled fully hydrated state of Nafion® is computed as a function of temperature (Figure 7.1.1, block II, steps 7-11). In order to fit the simulated permeability to the measured permeability, the permeabilities of the intermediate phase and the solid phase are varied using an iterative procedure. The detailed algorithm for the modeling of the microscopic structure is stated in the attachment (Section 14.4). The individual steps in block I are discussed in more detail in the following. The realization of block

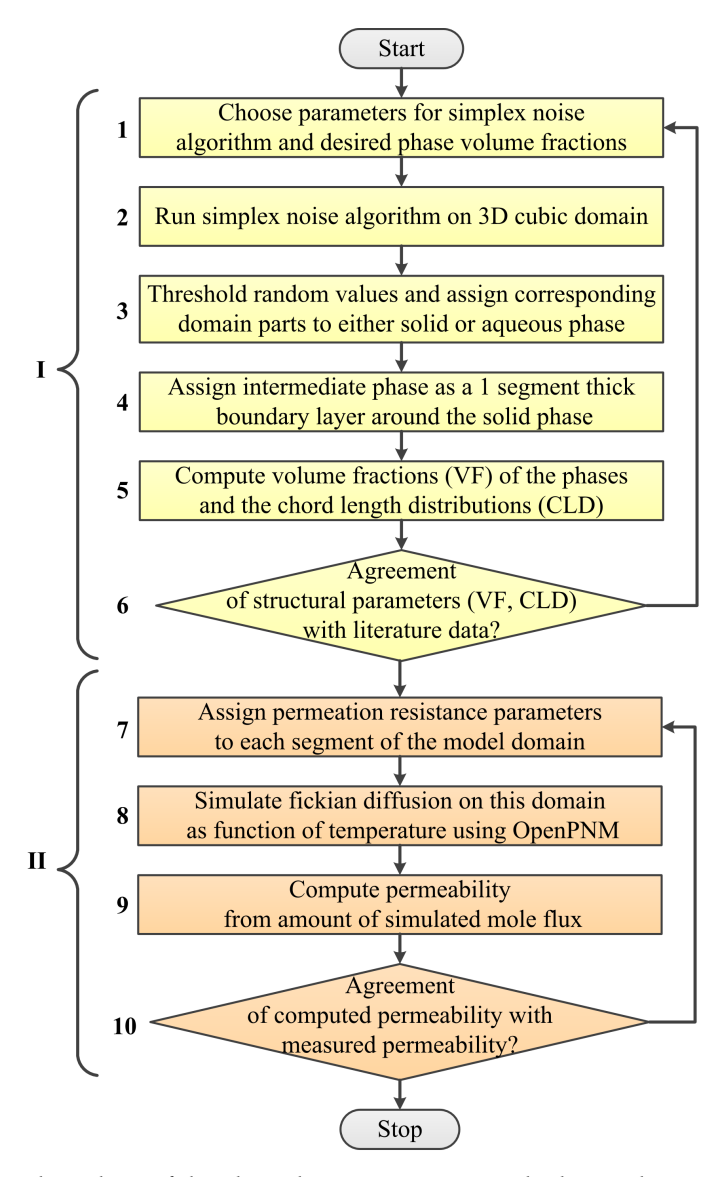


Figure 7.1.1: Flow chart of the algorithm to construct a calculation domain that represents the microscopic structure of Nafion<sup>®</sup> (block I, steps 1-6) and the subsequent algorithm to calculate the gas permeabilities of this calculation domain (block II, steps 7-10).

II is further discussed in section 7.1.3.

In step 1, random numbers between 0 and 1 were assigned to each element of the calculation domain using the simplex noise algorithm [190], which is a simpler version of the original perlin noise algorithm [191]. A thresholding was applied on this

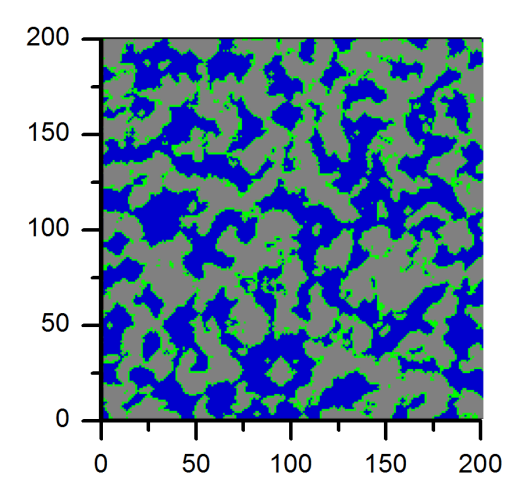


Figure 7.1.2: Two dimensional cross-section of the modeled three dimensional cubic structure of Nafion<sup>®</sup> with an edge length of 200 segments. One segment of the mesh corresponds to a cube with 2.1 Å edge length. Gray area: Solid phase. Blue area: Aqueous phase. Green area: Intermediate phase.

domain to assign all elements with values smaller than a certain threshold value to the aqueous phase, while the elements with higher values were assigned to the solid phase. All segments of the aqueous phase that are located at the interface to the solid phase are then relabeled to the intermediate phase, so that the intermediate phase is exactly one segment thick. The simplex noise algorithm as implemented in the python "noise" package was used [192], to which two parameters were passed, the frequency and the octave. These parameters define how correlated the clusters of random numbers are and therefore ultimately determine the distribution of the phases. The resulting phase distribution was fitted to the structure of fully hydrated Nafion® by adjusting the noise parameters so that the volume fractions and the so-called chord-length (defined later) distributions of the modeled structure matched reported literature values (step 5 of Figure 7.1.1). The volume fraction of a phase was calculated by counting the number of the segments of this phase and normalizing it to the total number of segments.

Table 7.1.1 shows the volume fractions of the phases in the modeled structure of fully hydrated Nafion<sup>®</sup> and that reported by Allen *et al.* [40]. Allen *et al.* determined the volume of the hydrophilic phase as 56 %, which includes the aqueous phase together with functional groups and the side chains of the ionomers. The remaining 44 % represent the hydrophobic phase, consisting of the polymeric backbone and the intermediate phase. The resulting microstructure is illustrated in Figure 7.1.2. A more quantitative analysis of the model structure is given below, showing that this approach describes a reasonable qualitative resemblance of the tomography results of Allen

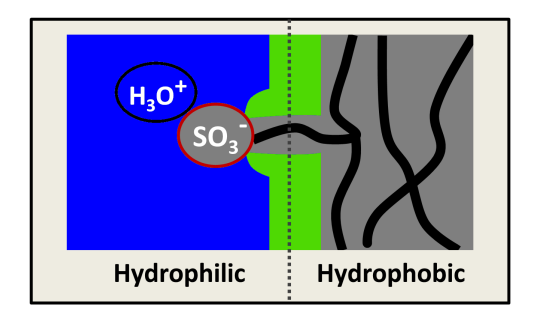


Figure 7.1.3: Schematic illustration of the microscopic phase distribution at a functional  $SO_3^-$  group in hydrated Nafion. Blue area: Aqueous phase. Green area: Intermediate phase. Gray area: Solid phase. Red-rimmed gray area:  $SO_3^-$  group. Black lines: Ionomer chains. Connection between the functional group and the solid phase by a side chain from an ionomer main chain. Dotted dark gray line: Separation between the phases as defined by Allen *et al.* [40].

Table 7.1.1: Volume fractions of the modeled phases in this study and those measured by Allen *et al.* [40]. As discussed in the text, the volumetric water content was modeled to approximately 40 %, which is smaller than that reported by Allen *et al.*, since the influence of the cryogenic environment in his setup expanded the volume of the aqueous phase.

| Phase        | Model | Allen et al. |
|--------------|-------|--------------|
| Aqueous      | 40 %  | 42.5 %       |
| Intermediate | 15%   | -            |
| Solid        | 44%   | -            |
| Hydrophilic  | -     | 56 %         |
| Hydrophobic  | -     | 44%          |

*et al.* [40]. In the model for the gas permeation presented here, the rigid side chains and the functional groups were assigned to the solid phase, since these are bonded to the polymer matrix. Choosing different definitions of the phases was necessary, as the contrasts Allen *et al.* obtained from electron tomography do not directly correlate with the gas permeabilities of the different phases. Figure 7.1.3 illustrates the different definitions of the phases.

Besides the volumes of the phases, also the arrangement of the water channels is a decisive property for the modeling of the structure of Nafion<sup>®</sup>. In fully hydrated Nafion<sup>®</sup>, Allen *et al.* [40] reported a water channel diameter of approximately  $25 \pm 2 \,\text{Å}$  with a domain spacing of approximately  $51 \pm 5 \,\text{Å}$  between the water channels. These values were striven to be reproduced in the model domain. The aqueous and intermediate phase were considered as one phase, referred to here as the high-phase, with a volume fraction equal to the hydrophilic phase defined by Allen *et al.* (Table 7.1.1). In order to evaluate the mean diameter of the water channels and the

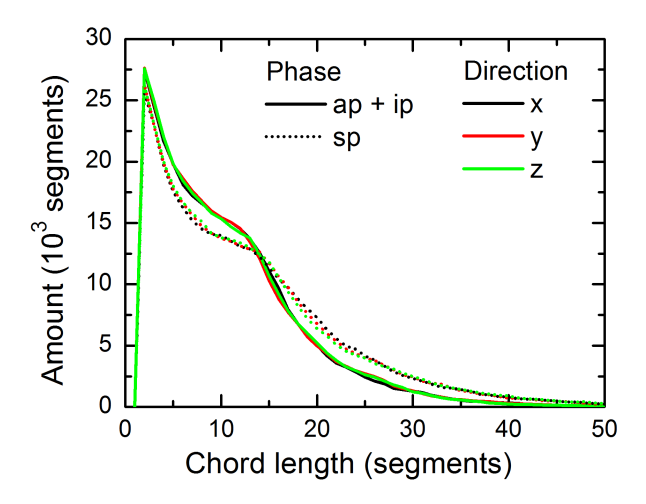


Figure 7.1.4: Chord length distribution of the modeled structure of Nafion<sup>®</sup> in the x, y, and z direction of the cubic network. Solid lines: High-phase (aqueous phase plus intermediate phase). Dotted lines: Solid phase.

domain spacing, in step 5 of Figure 7.1.1 the chord length in the *x*, *y*, and *z* direction of the modeled structure were calculated. The chord lengths are defined as the distances between the boundaries of the phases in one array of the x, y, or z direction. The chord-length distributions were obtained from an approach that was discussed by Torquato [193]. Figure 7.1.4 shows the counted chord lengths in the x, y, and zdirection for the high-phase and the solid phase of the model domain. The distributions in the different directions are approximately equal, meaning that the macroscopic character of the cubic network is isotropic. The mean chord lengths were determined to approximately 12 segments for the high-phase and 10 segments for the solid phase by the weighted average of the distributions graphed in Figure 7.1.4. Assuming a segment length of 2.1 Å, a mean diameter of the high-phase of 25.2 Å is described by the model domain, which agrees with the measured water channel diameter values by Allen et al. [40]. The mean domain spacing equals the sum of the mean chord lengths of the high-phase and the solid phase, which equals approximately 46 Å for the model domain, which also agrees to the data reported by Allen et al. [40] within the experimental measurement error of 5 Å. The model domain reflecting these values was ultimately constructed using parameters for the simplex noise algorithm of frequency equal to five and octave equal to four.

The thickness of the intermediate phase was assumed to be in the order of the length scale of the hydrogen bonds in the aqueous phase (as motivated later in Section 7.3), which was reported to equal 2 Å by Modig *et al.* [194]. The weaker character of the van der Waals bonds between the aqueous and solid phase were assumed to have a

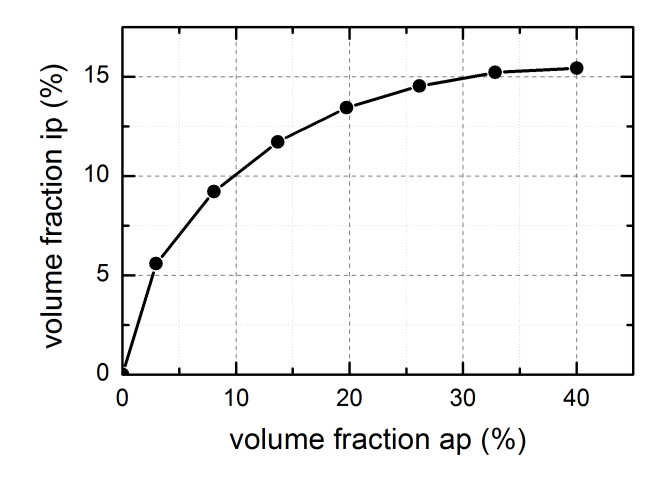


Figure 7.1.5: Modeled volume fraction of the intermediate phase (ip) as a function of the volume fraction of the aqueous phase (ap) as computed by varying their combined volume fraction.

slightly larger average bond length than the hydrogen bonds in the aqueous phase, as further discussed in Section 7.3. Accordingly, the distance between the aqueous and solid phase (described by one segment of the mesh) was modeled to be with 2 Å slightly larger than the hydrogen bond length.

In order to model the structure of Nafion<sup>®</sup> as a function of the volumetric water content, the volume fraction of the high-phase (aqueous phase plus intermediate phase) was varied. This variation was obtained by using the same parameters for the noise algorithm to distribute the random numbers, but choosing different thresholding values to change the volume fractions of the phases. Figure 7.1.5 shows the resulting volume fraction for the intermediate phase as a function of the volume fraction of the aqueous phase for varying the volume fraction of the high-phase. Reducing the volumetric water content from 40% to 10% leads to a reduction of the intermediate phase volume fraction from approximately 15.5% to just 10%. Thus, at volumetric water contents above 10%, the volume fraction of the intermediate phase is less sensitive to changes of water content as that of the aqueous phase.

Using equation 5.2.3, the water content  $\lambda$  in Nafion<sup>®</sup> was related to the volumetric water content  $\phi$  inside Nafion<sup>®</sup>. The relation between relative humidity and  $\lambda$  at 80 °C for Nafion<sup>®</sup> was measured by Kreuer [151]. Based on these data, the relative humidity was correlated with the normalized water content ( $\lambda$  as a function of the relative humidity normalized to  $\lambda \approx 20$  in the fully hydrated state) in Figure 6.1.2. Using the latter equation,  $\lambda$  was correlated to the volumetric water content  $\phi$ .

To summarize, in block I of Figure 7.1.1, the microscopic structure of Nafion<sup>®</sup> was recreated in the model domain based on the latest studies presented in the literature. The volume fractions of the phases, the mean water channel diameter, and the mean domain spacing were fitted to the experimentally determined values that were reported in literature. The model domain presented here was based on a random algorithm and incorporates the mean structural parameters of the microscopic structure of Nafion<sup>®</sup>. A more detailed model domain might be obtained by directly using the three dimensional data reported by cryo electron tomography by Allen *et al.* and directly simulating gas permeation on that domain. However, by using this approach, the intermediate phase would not be represented.

#### 7.1.2 Permeabilities of the aqueous and solid phase

In Section 2.3, the permeability of water  $\varepsilon_{\rm W}$  was described by a polynomial equation, while the permeability of dry Nafion  $\varepsilon_{\rm dN}$  and that of polymers in general was approximated by the Boltzmann distribution (Chapter 6). These relations will be used to assign permeation resistances to each segment of the resistor network model domain (step 7 in Fig. 7.1.1). In the following, the influence of the functional groups of Nafion and their acidity on the hydrogen and oxygen permeabilities of the aqueous phase in fully hydrated Nafion is approximated. This is relevant because the water uptake in the fully hydrated state of Nafion of  $\lambda \approx 20$  leads to a proton concentration of  $c_{\rm H^+} = \approx 2.8\,{\rm M}$  (see Chapter 5) inside the aqueous phase, where  $\tilde{\rho}_{\rm H_2O}$  denotes the mole density of water. The permeability equals  $\varepsilon = DS$  (Section 2.3). Accordingly, the solubilities S and the diffusion coefficients D of gases in the aqueous phase will be estimated in the following.

Generally, the solubility of gases in electrolytes decreases with higher concentrations of dissolved salts, acids, or lyes [195–197]. Typically, the solubility *S* as a function of the concentration in an aqueous solution is described by [195,196]

$$\log(S/S_{\rm w}) = -\sum K_{\rm i} c_{\rm i}$$
, (7.1.1)

where  $S_{\rm w}$  denotes the solubility of water,  $K_{\rm i}$  (or the K-value) a specific constant for the i-th type of ionic specie, and  $c_{\rm i}$  the concentration of this specie. These values are assumed to be equal for the diatomic and non-polar molecules of hydrogen and oxygen, as data reported in the literature for sulfuric acid solutions showed (in a 2.5 M solution of sulfuric acid  $S/S_{\rm w}$  equals 0.63 for hydrogen [196] and 0.65 for oxygen [195,197]). Narita  $et\ al.$  [195] reported that within the measurement precision, the temperature did not influence the ratio of S to  $S_{\rm w}$  for oxygen in sulfuric acid solutions. Moreover, they reported that the influence of the protons on the solubility is negligible ( $K_{\rm H^+}\approx 0$ ),

which means that in the case of the aqueous phase in Nafion possibly only the anion of the functional group influences the gas solubility. They moreover reported that the monovalent anions  $NO_3^-$ ,  $Cl^-$ ,  $HSO_4^-$ , and  $HCO_3^-$  have K-values of 0.013, 0.029, 0.069, and 0.083 l mol $^{-1}$ . A trend from these values regarding the size of the anions could not be identified. A K-value for the sulfonic acid functional group (the anion of the functional group in Nafion $^{(1)}$ ) has not been reported in literature thus far. Hence, based on the data available, the value for  $S/S_w$  can only be estimated to range in between the reported values for the monovalent anions reviewed.

In Section 2.3, the diffusion coefficient and the viscosity of solutions were physically described and related to each other. The product of both physical properties solely depends on the temperature and is thus approximately constant as a function of the concentration [198]. Due to a lack of literature data on the diffusion coefficients of gases in acidic solutions, data reported on the viscosity will be used in order to estimate the diffusion coefficient of the aqueous phase in Nafion<sup>®</sup>. Based on the constant product of diffusion coefficient and viscosity, the diffusion coefficient and the viscosity of the aqueous phase can be related to that of water:

$$D_{\rm ap} \iota_{\rm ap} = D_{\rm w} \iota_{\rm w} \tag{7.1.2}$$

Transposing this equation leads to an approximation of the diffusion coefficient in the acidic regime of the aqueous phase in fully hydrated Nafion<sup>®</sup>:

$$\frac{D_{\rm ap}}{D_{\rm w}} = \frac{\iota_{\rm w}}{\iota_{\rm ap}} \tag{7.1.3}$$

The ratio of the viscosity  $\iota$  of sulfuric acid with a proton concentration of 2.8 M to the viscosity of water ( $\iota_w$ ) was reported to equal constantly 0.75 in the temperature range from 25 °C to 75 °C [199]. This independence of  $\iota/\iota_w$  from the temperature is based on the theory (Section 2.3) also expected for other acids, while data on the temperature dependence of the viscosity of acids reported in the literature is rather scarce. The viscosities of the monovalent acids HCl, CH<sub>3</sub>COOH, and HCOOH found in the literature [200] are reported as a function of the concentration. In the case of these acids, the relation of the viscosities to the concentration is approximately linear

$$\iota_{\rm ap} \approx \iota_{\rm W} + a c \,, \tag{7.1.4}$$

where a denotes the proportionality constant and c the proton concentration, with an offset of  $\iota_w$ . This proportionality constant in the order of the acids mentioned before equals 0.056, 0.13, 0.027 kg m<sup>2</sup> s<sup>-1</sup> mol<sup>-1</sup> [200]. A trend between the size of the anions and the influence on the viscosity cannot be observed. The ratio of  $D/D_w$  is assumed to be equal for hydrogen and oxygen, since both are proportional to the fraction of

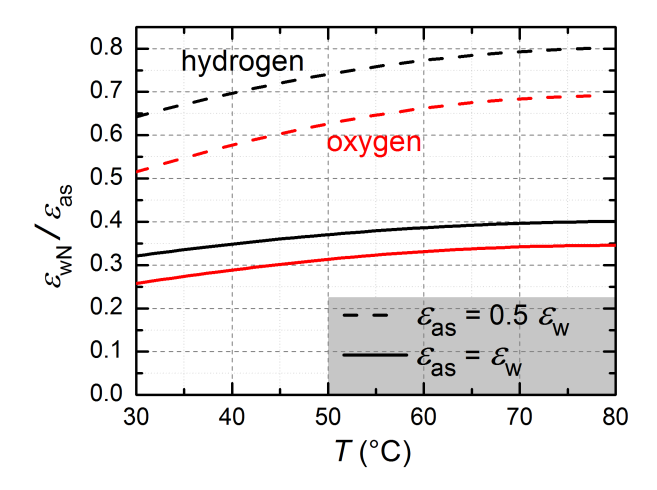


Figure 7.1.6: Ratio of the permeability of fully hydrated Nafion  $(\varepsilon_{wN})$  to that of aqueous solutions  $(\varepsilon_{as})$  based on the data presented in the previous chapter. Black: Ratio for the hydrogen permeabilities. Red: Ratio for the oxygen permeabilities. Solid lines: Permeability of the aqueous solution equals that of water. Dashed lines: Permeability of the aqueous phase is 50% smaller than that of water (eq. 7.1.5), which could be a result of the acidity of the aqueous phase in Nafion (see text for further explanations).

the viscosities (eq. 7.1.4).

Thus far, the functional groups of Nafion<sup>®</sup> were discussed to reduce the ratios  $S/S_w$  and  $D/D_w$  in the aqueous phase. Considering that  $\varepsilon = DS$  (Section 2.3), the acidity of the functional groups in Nafion<sup>®</sup> leads to a reduced permeability of the aqueous phase in Nafion<sup>®</sup> ( $\varepsilon_{ap}$ ) compared to that of pure water ( $\varepsilon_w$ ):

$$\varepsilon_{\rm ap}(T) = \frac{D}{D_{\rm w}} \frac{S}{S_{\rm w}} \, \varepsilon_{\rm w}(T) \tag{7.1.5}$$

However, precise values of the ratios for the aqueous phase in Nafion® could not be given. Based on the published data discussed above, the prefactor  $\frac{D}{D_{\rm w}} \times \frac{S}{S_{\rm w}}$  ranges from 0.8 at the maximum to 0.43 at the minimum. Therefore, this prefactor will be varied in a sensitivity analysis when running simulations on the resistor network model domain.

The temperature dependence of the ratios of the measured hydrogen and oxygen permeabilities of fully hydrated Nafion ( $\epsilon_{wN}$ ) to those of aqueous solutions ( $\epsilon_{as}$ ) are depicted in Figure 7.1.6. The permeability of the solid phase increases more strongly with temperature than that of the aqueous phase (as described by the activation energies (Chapter 6)). As a result, the ratios  $\epsilon_{wN}/\epsilon_{as}$  increase with temperature. The

hydrogen permeability of water is up to a factor of two larger than that of oxygen (Chapter 6). In the case of dry Nafion<sup>®</sup>, the permeability of hydrogen is at least four times larger. Consequently, the ratio  $\varepsilon_{wN}$  to  $\varepsilon_{as}$  is smaller for oxygen than for hydrogen.

#### 7.1.3 Simulation of the gas permeability

As shown in the previous chapter, the hydrogen and oxygen permeabilities of Nafion  $^{\circledR}$  are material constants, which are independent of the geometries of the membranes. Analogously to the relation of conductivity (here corresponding to the permeability) and resistance for electric conductors, the total gas permeation resistance  $\hat{R}_t$  of a membrane is related by

$$\hat{R}_{t} = \frac{d}{A \, \varepsilon_{t}} \tag{7.1.6}$$

to its total gas permeability  $\varepsilon_t$ , where its geometry is described by its thickness d and its cross sectional area A. As the total permeability  $\varepsilon_t$  of Nafion<sup>®</sup> is a material constant and thus independent of the sample geometry (Chapter 6), the overall membrane geometry in the form of d and A can analogously be chosen arbitrarily in the case of a resistor network model approach (if the model domain is large enough so that boundary effects are negligible) when determining the permeability. This total gas permeation resistance  $\hat{R}_t$  is composed of the contribution of the three phases, and therefore depends on the microscopic structure of Nafion<sup>®</sup>. Accordingly, each permeation resistance ultimately influences the overall gas permeability, as incorporated by assigning gas permeation resistances to each element of the resistor network model domain (Fig. 7.1.2, step 7 in Fig. 7.1.1). This assignment was achieved by adapting equation 7.1.6 to the individual segments of the resistor network, which leads to the resistance  $\hat{R}$  of one segment of the aqueous phase of

$$\hat{R}_{ap} = \frac{1}{l \, \varepsilon_{ap}} \,, \tag{7.1.7}$$

where l denotes the edge length of the cubic mesh segment of 2.1 Å. The resistances of the segments of the solid and intermediate phase are described analogously using the indexes 'ip' and 'sp'. In the resistor network, the resistance values between two neighbor segments equal the series resistor composed of half a segment of each phase.

In the previous section, the permeability was measured by applying a partial pressure gradient of hydrogen or oxygen to both sides of the Nafion<sup>®</sup> membranes. These experimental conditions were simulated in the present model by applying Dirichlet boundary conditions on the inlet and outlet faces of the calculation domain, corresponding to a partial pressure difference of  $\Delta p$ . In the simulations, the mole flux  $\dot{n}$ 

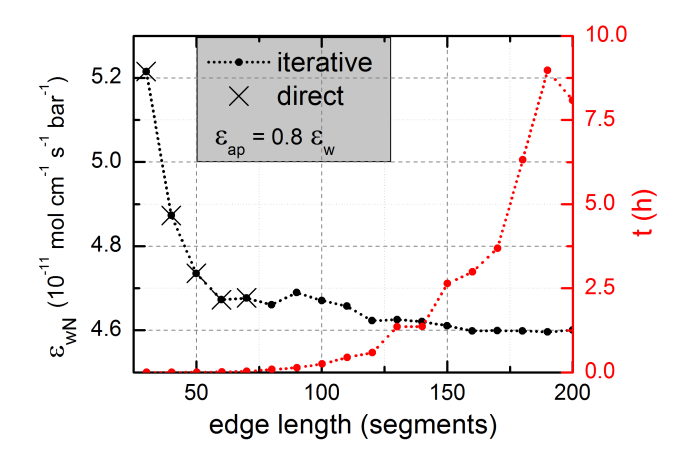


Figure 7.1.7: Modeled permeability of the resistor network as a function of the edge length of the cubic mesh. Black points connected with lines: Results of the iterative solver. Black crosses: Results of the direct solver. Red points and right scale: Computing time of the iterative solver.

through the resistor network was computed using the algorithm for Fickian diffusion in OpenPNM (step 8 in Figure 7.1.1). From the mole flux that was modeled to diffuse through the domain, the overall permeability was determined by

$$\varepsilon_{\rm t} = \dot{n} \frac{d}{A \, \Delta p} \,, \tag{7.1.8}$$

where d and A refer to the geometry of the total resistor network domain. The mole flux  $\dot{n}$  itself depends on A and d. Hence,  $\varepsilon_{\rm t}$  is independent of these geometric parameters. Analogously to the experimentally determined permeability, the modeled permeability is independent of the considered partial pressure difference, since the ratio of  $\dot{n}$  to  $\Delta p$  is constant.

Figure 7.1.7 shows the simulated permeability for  $\varepsilon_{ap} = \varepsilon_{ip} = 0.8 \, \varepsilon_w$  and the same permeability of the solid phase as that of dry Nafion ( $\varepsilon_{sp} = \varepsilon_{dN}$ ) as a function of the edge length of the cubic resistor network of the model domain. Boundary effects and different percolation paths led to a variation of the simulated permeability as a function of the cube size. With an edge length of 120 or larger, the influence on the cube size on the modeled permeability is smaller than 1% and therefore negligible (as the statistical mean reduces these impacts). The diffusion through the network was solved using OpenPNM, in which either the direct SuperLU solver or the iterative generalized minimal residual (GMRES) solver as implemented in the *scipy.sparse.linalg* package of SciPy [201] were used. Both solvers yielded almost equal simulated permeabilities with deviations below 0.1%. The direct solver required more random

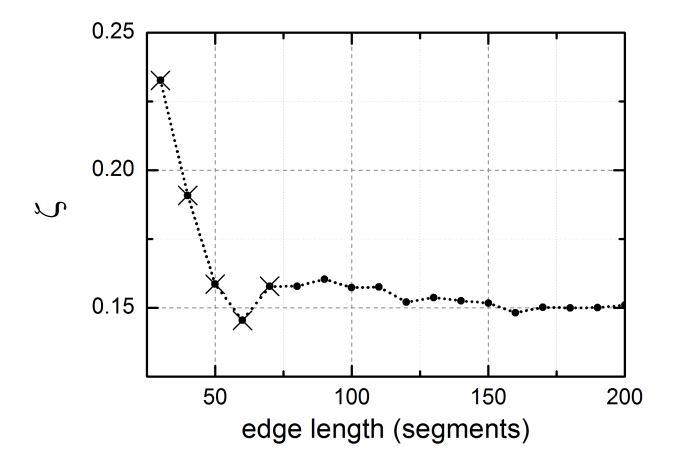


Figure 7.1.8: Geometric restriction factor  $\zeta$  for the permeation through the aqueous phase of the Nafion model domain (ratio of the simulated permeability when  $\varepsilon_{\rm sp}=\varepsilon_{\rm ip}=0$  to the simulated permeability with the aqueous phase spanning the whole domain) as a function of the edge length of the model domain. This geometric restriction factor directly influences the proton conduction. The gas permeation is less influenced by the percolation paths required for the proton conduction, since the gases can also permeate through the solid and intermediate phase. Points with lines: Iterative solver. Crosses: Direct solver.

access memory (RAM) of the computer, which limited the edge length to 70 segments using 16 giga byte of RAM. For larger domains, the iterative solver was used, as in this case 8 giga byte of RAM were sufficient independent of the mesh size. The calculations were conducted using a personal computer with four processor cores and a clock speed of 3.4 GHz.

Using the model domain of fully hydrated Nafion<sup>®</sup> described above, where however only the aqueous phase contributes to the gas permeation, the permeability was simulated. By this procedure, the phase distributions were retained, but the permeability of the intermediate and solid phase were set equal to zero ( $\varepsilon_{sp} = \varepsilon_{ip} = 0$ ). The permeability simulated with this configuration means that the whole model domain consisted only of the aqueous phase. The ratio of the permeability of the model domain for  $\varepsilon_{sp} = \varepsilon_{ip} = 0$  to the permeability of the aqueous phase covering the full domain are graphed in Figure 7.1.8. This ratio characterizes the geometric restriction for the gas permeation through the aqueous phase of the Nafion<sup>®</sup> model domain and will be described by the factor  $\zeta$ . As a result, the permeability of the aqueous phase is reduced by a simulated factor of  $\zeta \approx 0.15$  due to the morphology of the aqueous phase in the Nafion<sup>®</sup> model domain. The factor  $\zeta$  is a measure for the percolation path of the permeation through the aqueous phase. The maximum deviation between the mo-

deled permeabilities above an edge length of 120 segments is less than 4 %, which can be attributed to boundary effects discussed above. The geometric restrictions caused by the morphology of the aqueous phase also influence the proton conduction through Nafion<sup>®</sup>. Thus, the geometric restriction factor and can be interpreted as the factor by which the proton conduction of Nafion<sup>®</sup> is reduced in comparison to the mean conductivity inside the water channels (see Chapter 5).

# 7.2 Application of the model to the experimental data

In the following, the model presented in the previous chapter will be used to simulate the hydrogen permeability of fully hydrated Nafion <sup>®</sup>. These results are compared with the measured hydrogen permeability presented in the previous chapter. Thereafter, the influence of the water content on the permeability will be simulated. The model will be considered for two cases, a permeability of the aqueous phase of  $\varepsilon_{ap}=0.5~\varepsilon_{w}$  (defined as case A) and  $\varepsilon_{ap}=0.8~\varepsilon_{w}$  (defined as case B). These different values represent the estimated range of the influence of the functional groups on the permeability of the aqueous phase. The results of case A will be graphed in red, those of case B in ocher. The procedure to simulate the oxygen permeation through fully hydrated Nafion <sup>®</sup> was similar and is presented in the attachment (Section 14.4).

The temperature was discussed to negligibly influence the water content of fully hydrated Nafion<sup>®</sup> and the morphology of the aqueous phase (see Section 3.1). Thus, the influence of the temperature on the permeability of fully hydrated Nafion<sup>®</sup> is solely attributable to the variation of the permeabilities of the different phases. The permeability of the aqueous phase was estimated in the form of equation 7.1.5 and is considered for the two different cases described above. In order to fit the simulated permeability to the measured permeability, the permeabilities of the intermediate and solid phase will be varied separately. The simulated results and their deviations from the Boltzmann distribution will be compared to the measurements. The physical causes for the variation of the permeabilities will be discussed in Section 7.3, where also a parameter analysis will be given.

## 7.2.1 Variation of the intermediate phase

In the following, the gas permeation through the intermediate phase is assumed to be dominated by the rearrangement of the hydrogen bond network in the aqueous phase, as further discussed in Section 7.3.1. To describe the permeability of the intermediate phase ( $\varepsilon_{ip}$ ), the permeability of the aqueous phase ( $\varepsilon_{ap}$ ) times the interfacial

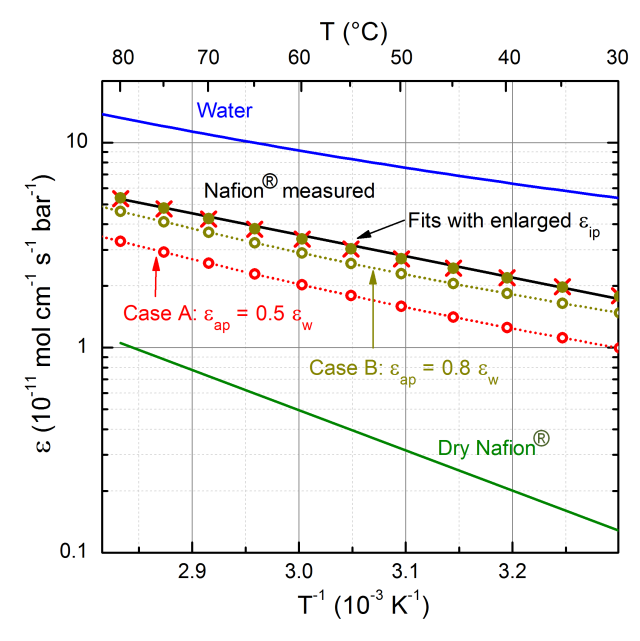


Figure 7.2.1: Hydrogen permeabilities in a modified Arrhenius plot (logarithmic scale of  $\varepsilon$  vs. 1/T) for the case of varying the permeability of the intermediate phase. Black: Mean of the measured permeability of fully hydrated Nafion<sup>®</sup>. Blue: Water (calculated). Dark green: Mean of the measured permeability of dry Nafion<sup>®</sup>. Red: Case A ( $\varepsilon_{ap}=0.5\ \varepsilon_{w}$ ). Ocher: Case B ( $\varepsilon_{ap}=0.8\ \varepsilon_{w}$ ). Open circles with dotted lines: Simulated permeabilities for  $\Lambda=1$ . Crosses: Simulated permeability for case A with  $\Lambda=10.3$ . Dots: Simulated permeability for case B with  $\Lambda=2.2$ .

permeation factor  $\Lambda$  will be used:

$$\varepsilon_{\rm ip} = \Lambda \, \varepsilon_{\rm ap}$$
(7.2.1)

The physical meaning of the interfacial permeation factor  $\Lambda$  will also be discussed in Section 7.3.1. The permeability of the solid phase of fully hydrated Nafion<sup>®</sup> will be assumed to equal that of dry Nafion<sup>®</sup> ( $\varepsilon_{sp}=\varepsilon_{dN}$ ). In order to fit the simulated permeability to the measured permeability, the value of  $\Lambda$  was altered by the principle of nested intervals. By interpolating between two simulated intervals that surrounded the measured permeability, the final value of  $\Lambda$  was approximated.

Figure 7.2.1 shows the measured hydrogen permeabilities of fully hydrated Nafion<sup>®</sup> and dry Nafion<sup>®</sup>, the hydrogen permeability of water calculated by the data reported in the literature (Section 2.3), and the simulated permeability of the resistor network. In the case of  $\Lambda = 1$ , the simulated permeability of fully hydrated Nafion<sup>®</sup> for case A

Table 7.2.1: Prefactors and activation energies for the softened solid phase of humidified Nafion<sup>®</sup> for case A and case B. These increased permeabilities are the solution for the fit in Figure 7.2.2.

|        | $\varepsilon_0  (10^{-7}  \text{mol cm}^{-1}  \text{s}^{-1}  \text{bar}^{-1})$ | $E_{\varepsilon} (10^{-20} \text{ J})$ |
|--------|--|--|
| case A | 2.53   | 4.28                                   |
| case B | 6.61   | 5.16                                   |

at 80 °C is approximately 37 % smaller than the measured permeability (13 % for case B). With  $\Lambda=10.3$  for case A and  $\Lambda=2.2$  for case B, the simulated permeabilities match the measured permeabilities.

### 7.2.2 Variation of the solid phase

So far, the simulated permeability was fitted to the measured permeability by enlarging the permeability of the intermediate phase. Alternatively, the permeability of the solid phase can be increased in order to increase the simulated permeability of the resistor network. In the following considerations, the permeability of the intermediate phase equals that of the aqueous phase ( $\Lambda = 1$ ). In order to fit the simulated permeability to the measured permeability for this boundary condition, the permeability of the solid phase was varied. The permeability of the solid phase was taken as that of dry Nafion® multiplied by different prefactors. With these parameters, the permeabilities were simulated for 30 °C and 80 °C. In an Arrhenius graph, these permeabilities for both temperatures were plotted and connected by a line, respectively. Two intersections of two of these simulated lines with the line that represents the measured permeability were calculated. At these two temperatures, the increased permeabilities of the solid phase had the right values to lead to an agreement of the simulated permeability and the measured permeability. A line to connect these increased permeabilities of the solid phase in the Arrhenius graph was calculated. The Boltzmann distribution describing this line was defined as the softened solid phase. This procedure was conducted for both, case A and case B. The parameters that describe the softened solid phases are stated in Table 7.2.1.

Figure 7.2.2 shows the simulated permeability with the parameters of the softened solid phase (Table 7.2.1). In the total temperature range, the simulated permeabilities match the measured permeabilities using this approach. Moreover, Figure 7.2.2 also shows the permeabilities of the softened solid phase for case A and case B. At 80 °C and for case A, the permeability of the softened solid phase was approximately 3.7 times larger than that of dry Nafion<sup>®</sup> (approximately 1.6 times for case B) while the ratio of the softened permeability to the measured permeability equals approximately 0.73 for case A and 0.31 for case B. In the case of dry Nafion<sup>®</sup>, the ratio of  $\varepsilon_{\rm dN}$  to  $\varepsilon_{\rm wN}$  equals approximately 0.2.

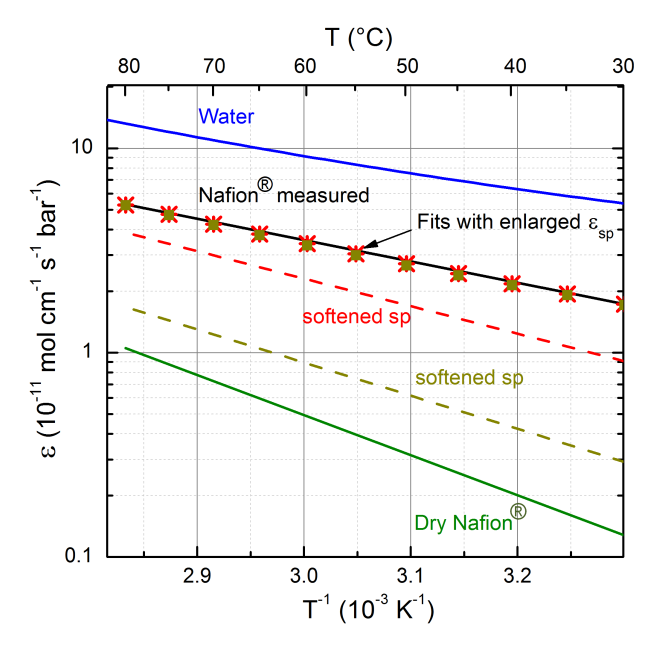


Figure 7.2.2: Hydrogen permeabilities in a modified Arrhenius plot for the case of an increases permeability of the solid phase. Dashed red line: Permeability of the softened solid phase for case A (parameters stated in Table 7.2.1). Dashed ocher line: Permeability of the softened solid phase for case B. Red stars: Simulated permeability for case A. Ocher squares: Simulated permeability for case B. Color code of the other lines equal that in Figure 7.2.1.

#### 7.2.3 Deviations from the Boltzmann distribution

In the following, the deviations of the measured and simulated permeabilities of fully hydrated Nafion<sup>®</sup> from the Boltzmann distribution will be discussed. The temperature dependence of the hydrogen and oxygen solubilities in water was described by polynomial and exponential terms, as discussed in the previous chapter. These polynomial terms also influenced the hydrogen and oxygen permeabilities of the aqueous phase ( $\varepsilon = DS$ ) and thereby caused deviations from the Boltzmann distribution and its linearity in the Arrhenius plot. Furthermore, the combination of the activation energies of the solid phase, the intermediate phase, and the aqueous phase also lead to non-linearity in the Arrhenius plot. These two sources for the deviation from the Boltzmann distribution contributed to the simulated permeability of fully hydrated Nafion<sup>®</sup>.

In order to compare the relative deviations of the hydrogen permeabilities of water and fully hydrated Nafion<sup>®</sup> from the linearized Boltzmann distribution  $\ln(\varepsilon) \propto 1/T$ ,

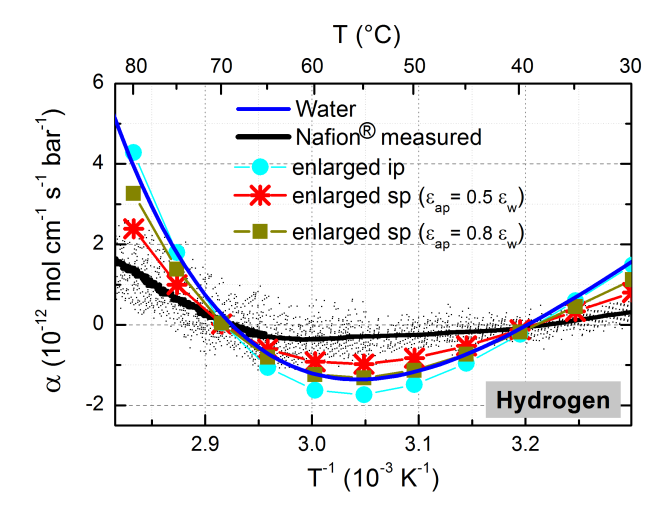


Figure 7.2.3: Deviation of the permeability from  $\ln(\varepsilon) \propto 1/T$  expressed by the deviation factor  $\alpha$  (eq. 7.2.2) as a function of the inverse temperature. Blue line: Water (calculated). Black points: Fully hydrated Nafion® (measured). Black line: Fully hydrated Nafion® (smoothed over a window of 500 measurement points). Cyan dots: Simulated permeability of Nafion® with an increased permeability of the intermediate phase. Red stars: Simulated permeability of Nafion® with the softened solid phase for case A. Ocher squares: Simulated permeability of Nafion® with the softened solid phase for case B.

the measured and simulated permeabilities of fully hydrated Nafion<sup>®</sup> were normalized to that of water. For this purpose, the normalization factor  $\alpha_n$  was defined, which was calculated by the ratio of the permeability of the aqueous phase at 55 °C to the permeability of the examined medium at the same temperature. In the case of fully hydrated Nafion<sup>®</sup> this factor equals  $\alpha_n = 2.33$ . The deviation factor  $\alpha$  is defined by the normalization factor times the difference of the permeability calculated from the linear fit in the Arrhenius plot  $(\varepsilon_{\rm fit}(T))$  and the calculated, simulated, or measured permeability  $\varepsilon(T)$  of the examined medium:

$$\alpha(T) = \alpha_{n} \left[ \varepsilon(T) - \varepsilon_{fit}(T) \right] \tag{7.2.2}$$

Lines were individually fitted to the permeabilities in the Arrhenius plot.

Figure 7.2.3 shows the deviation factors for the simulated and measured hydrogen permeabilities of water and fully hydrated Nafion<sup>®</sup> as a function of the inverse temperature. In order to reduce noise, the deviation factor of the measured permeability of fully hydrated Nafion<sup>®</sup> was smoothed over a window of 500 points. The temperature dependence of the smoothed deviation factor of the different measure-

7.3 Discussion 87

ments follows reproducibly the graphed trend in the form of a 'U' as a function of the temperature, while the relative deviations of the measured permeability from the Boltzmann distribution were below 2% of the absolute value. The deviation factor of the simulated permeability was determined using either the increased permeability of the intermediate phase or the increased permeability of the solid phase. In both cases the contributions of the polynomial terms that described the solubility in the aqueous phase also led to the 'U'-type form of the deviation factor as a function of the temperature. With the increased permeability of the intermediate phase (Section 7.2.1), the deviation factor is equal for case A and case B. With the increased permeability of the solid phase, the deviation factor was smaller for case A than for case B, since the contribution of the aqueous phase to the overall permeabilities was larger than that for the measured permeabilities, which could mean that the permeability of the aqueous phase is smaller than assumed.

#### 7.3 Discussion

With  $\Lambda = 1$  and  $\varepsilon_{sp} = \varepsilon_{dN}$ , the simulated permeability was shown to be smaller than the measured permeability of fully hydrated Nafion<sup>®</sup>. In order to fit the simulated permeability to the measured permeability, either the permeability of the intermediate phase or that of the solid phase were increased. After simulating the temperature dependence of the hydrogen permeability of fully hydrated Nafion<sup>®</sup>, which is mainly influenced by the physical permeation mechanisms as the water content is constant, the set of parameters for the different scenarios obtained was applied to simulate the hydrogen permeability of Nafion<sup>®</sup> as a function of the water content. As a result, the best representation of the measurements were obtained for the case of a small permeability of the aqueous phase (case A with  $\varepsilon_{ap} = 0.5 \, \varepsilon_{w}$ ) and the softened solid phase. Based on this analysis, the softening of the solid phase could be an essential effect that determines the permeability of hydrated Nafion<sup>®</sup>. Referring to the simulated impact of the water content on the permeability, a clear evidence for an increased permeability of the intermediate phase could not be identified. In the following, the physical causes for the increase of the permeabilities of the intermediate phase and the solid phase compared to that of the aqueous phase and that of dry Nafion<sup>®</sup> will be discussed. Thereafter, the influence of the permeation through the non-aqueous phases on the overall permeability of Nafion® will be estimated. Finally, approaches to reduce the permeability based on the presented relation between structure and permeability will be discussed.

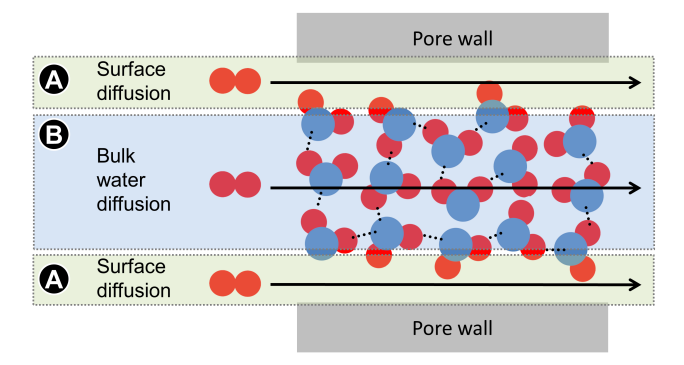


Figure 7.3.1: Schematic illustration of the hydrogen permeation through a water channel of Nafion<sup>®</sup>. In the case of the oxygen permeation the mechanisms may be similar. Red points: Hydrogen atoms. Blue points: Oxygen atoms. Dotted black lines: Hydrogen bonds. (A): Permeation in the intermediate phase between the aqueous phase and the pore walls. (B): Permeation through bulk of the aqueous phase. The less distinct hydrogen bond network in the intermediate phase possibly leads to a larger permeability than that through the bulk of the aqueous phase.

## 7.3.1 Increased permeability of the intermediate phase

At the boundaries of the water channels, water is in contact with the polymeric backbone of Nafion<sup>®</sup> [181,202,203]. This backbone has a similar structure to the monomers of PTFE, consisting of a carbon chain with two fluorine atoms at each carbon atom (see Section 2.4). The contact angle between water and PTFE is comparably large (approximately 100° [204]), which indicates weak molecular forces between PTFE and water. Thus, in this intermediate phase, the van der Waals forces between the aqueous phase and the solid phase may be weaker than those of the hydrogen bonds in the aqueous phase and the covalent bonds of the ionomers. As motivated in the following, these weak molecular forces might lead to larger diffusion coefficients and/or solubilities of the gases in the intermediate phase than in the aqueous phase.

Dissolved gases can only diffuse through water when the hydrogen bond network is thermally rearranged, for which hydrogen bonds are broken while others are build [98–100]. The rate of this rearrangement process limits the gas diffusion rate. As discussed above, in the intermediate phase the strength of the van der Waals bonds which have to thermally be broken to enable the diffusion process are weaker compared to the hydrogen bonds of the bulk of the aqueous phase. These weak forces of the non-hydrogen bonds in the intermediate phase are possibly too small to significantly influence the temperature dependence of the diffusion. However, to permeate through the intermediate phase, some hydrogen bonds of the overlap to the aqueous phase possibly have to be broken. To break these hydrogen bonds, the same activa-

7.3 Discussion 89

tion energy as that in bulk water was assumed (the factor  $\Lambda$  was multiplied to the permeability of the aqueous phase). In this sense, a larger value of  $\Lambda$  than unity means that less hydrogen bonds are broken by the diffusion through the intermediate phase than in the case of the diffusion through the aqueous phase. However, using this description, the activation energy of the diffusion that is dominated by the cleavage and the formation of the hydrogen bonds was assumed to be retained.

The intermediate phase was estimated to be slightly thicker than the hydrogen bond length of 2 Å. Based on the bonding lengths (in the order of 1-2 Å [187]) and the van der Waals radii (in the order of 1.5 Å [186]) of the hydrogen and oxygen atoms, their molecules can fit into and diffuse through the intermediate phase of the assumed dimensions. Hence, the gas molecules may at least partly permeate through the intermediate phase by weak interactions with the hydrogen bond network. Figure 7.3.1 illustrates the diffusion through a water channel and its two phases. Besides the diffusion coefficients, also the hydrogen and oxygen solubilities in the intermediate phase may be larger than those in the aqueous phase. Again, the weak van der Waals forces may enable larger concentrations of dissolved gas molecules in the intermediate phase than in the aqueous phase, since the dissolution of the gases may be weakly influenced by the strong hydrogen bond network. To summarize, by weak van der Waals forces in the intermediate phase and a possibly less distinct hydrogen bond network compared to that of the aqueous phase, large gas diffusion coefficients and solubilities were postulated.

## 7.3.2 Softening of the solid phase

As an alternative to the increased permeability of the intermediate phase, an increased permeability of the solid phase was assumed in order to fit the simulated permeability to the measured permeability of fully hydrated Nafion<sup>®</sup>. Nafion<sup>®</sup> swells by water uptake [153] which consequently leads to an increase of the mean distance r between the polymer chains. These increased distances may cause reduced van der Waals forces ( $\propto \frac{1}{r^6}$  according to the Lennard-Jones potential) between the polymer chains in the solid phase. In addition, possibly more significant, the inflation of water into the plasticized frame of the polymer network [203] may weaken the van der Waals forces between the polymer chains within the solid phase. Hence, liquid water and/or water vapor may act as a plasticizer that penetrates into the polymeric structure. Kreuer [151] reported a softening of the visco-elastic properties of Nafion<sup>®</sup> with larger water contents, which may be a result of these effects. To permeate through the polymer matrix, the potential barriers comprised by the van der Waals forces between the polymer chains have to be overcome (Section 2.3). Thus, gas molecules may

more easily diffuse between the polymer chains of the solid phase when the van der Waals forces between them are reduced. Accordingly, the assumed increase of the gas permeability of the solid phase and the reduced activation energy for the permeation in this phase towards larger water uptake may be caused by the described effect of water as a plasticizer. In addition, increased distances between the polymer chains may also cause increased hydrogen and oxygen solubilities in the solid phase.

#### 7.3.3 Influence of the water content on the modeled permeability

In the case of fully hydrated Nafion<sup>®</sup>, the influence of the softening of the solid phase on the permeability was estimated for the case A and B. When the water content of Nafion<sup>®</sup> is reduced, the concentration of the functional groups inside the water channels increases. Thereby, the diffusion coefficient and the solubility of the gases in the aqueous phase are affected (Section 7.1.2). These parameters are characterized by different power laws as a function of the acidity (exponential and linear, as described by eq. 7.1.1 and eq. 7.1.4), while the corresponding parameters  $K_i$  and a are not precisely known. Accordingly, the reduction of the water content decreases the permeability of the aqueous phase by an unknown extent. During the swelling of Nafion<sup>®</sup>, Haubold et al. [181] reported a shrinking of the regions where the bulk aqueous phase occurs and a swelling of the region where a mixture between the side chains of the ionomers and the aqueous phase prevails. This phase mixing and the detailed influence of the structure of the intermediate phase as a function of the relative humidity could not be parameterized. Moreover, the influence of the density of the functional groups on the permeability of the intermediate phase is also unknown, while the detailed extend of the softening of the solid phase on the permeability also remains questionable.

Thus far, the detailed influence of the decreasing water content on the permeabilities of the aqueous, intermediate, and solid phase was discussed to be unquantifiable. However, a reduction of the permeabilities of the aqueous and solid phase are expected for a decreasing water content (increasing molarity and hardening of the solid phase). To summarize, too many parameters are necessary to characterize the different phase permeabilities as a function of the water content in detail.

## 7.3.4 Impact of the different phases

When the permeabilities of the solid and intermediate phase are assumed to be negligible, the simulated permeability solely through the aqueous phase of fully hydrated Nafion<sup>®</sup> (defined as the geometric permeability of the aqueous phase  $\varepsilon_{ap}^{geo}$ ) was estimated to be reduced by the impact of the morphology of the aqueous phase by a

7.3 Discussion 91

factor of  $\zeta \approx 0.15$  (Fig 7.1.8). This relation is expressed by:

$$\varepsilon_{\rm ap}^{\rm geo} = \zeta \, \varepsilon_{\rm ap}$$
(7.3.1)

The same influence of the morphology has to be expected for the proton permeation through Nafion which solely takes place in the aqueous phase. However, the alternating gas permeation through all the phases reduces the impact of  $\zeta$  on the overall gas permeability, as detours through the aqueous phase or dead-end water channels can be bypassed by the permeation through the intermediate phase and the solid phase. The aim of the following consideration is to estimate the influence of the permeation through the intermediate phase and the solid phase on the overall gas permeability of Nafion This impact will be quantified by the ratio of the permeability of the geometric permeability of the aqueous phase  $\varepsilon_{\rm ap}^{\rm geo}$  to the permeability of fully hydrated Nafion  $\varepsilon_{\rm wN}$ .

The permeability of the aqueous phase can be expressed as  $\varepsilon_{aq} = \left(\frac{\varepsilon_{aq}}{\varepsilon_w}\right) \varepsilon_w$ , which leads with equation 7.3.1 to:

$$\frac{\varepsilon_{\rm ap}^{\rm geo}}{\varepsilon_{\rm wN}} = \zeta \, \frac{\varepsilon_{\rm w}}{\varepsilon_{\rm wN}} \, \frac{\varepsilon_{\rm ap}}{\varepsilon_{\rm w}} \tag{7.3.2}$$

Inserting the values of  $\varepsilon_{wN}$  and  $\varepsilon_{w}$  (stated in the previous chapter) for a temperature of 80 °C yields:

$$\frac{\varepsilon_{\rm ap}^{\rm geo}}{\varepsilon_{\rm wN}} \approx 0.37 \, \frac{\varepsilon_{\rm ap}}{\varepsilon_{\rm w}} \tag{7.3.3}$$

In the case A ( $\varepsilon_{ap}=0.5\,\varepsilon_{w}$ ), the ratio of  $\varepsilon_{ap}^{geo}$  to  $\varepsilon_{wN}$  can be estimated to a factor of 0.185 (for a temperature of 80 °C). Subtracting this value from unity means that approximately 81.5 % of the hydrogen permeability through fully hydrated Nafion is attributable to the permeation through the intermediate phase and the solid phase. In other words, the permeation through all the phases at 80 °C is larger by a factor of  $\varepsilon_{wN}/\varepsilon_{ap}^{geo}\approx 5.4$  than the permeation solely through the aqueous phase. Following the same procedure, in the case B ( $\varepsilon_{ap}=0.8\,\varepsilon_{w}$ ) approximately 70 % of the overall hydrogen permeability of Nafion can attributed to its solid phase. This means that  $\varepsilon_{wN}/\varepsilon_{ap}^{geo}\approx 3.3$  for case B. Towards lower water contents, the ratio of  $\varepsilon_{wN}$  to  $\varepsilon_{ap}^{geo}$  decreases and the influence of the intermediate phase and the solid phase on the overall permeability of Nafion increases.

## 7.3.5 Improvement of PEMs

In hydrated Nafion<sup>®</sup>, the gaps between the water channels comprised by the solid phase can be crossed by gas permeation, while protons cannot permeate through the solid phase. Accordingly, the detours for the permeation of protons through Nafion<sup>®</sup> are larger than that for the gas permeation, since the gas molecules can take short-

cuts through solid phase. The influence of this alternating permeation on the overall permeability of fully hydrated Nafion<sup>®</sup> was discussed in the latter paragraph, where the permeation through all the phases were estimated to increase the overall permeability by a factor of approximately 5.4 compared to the permeation solely through the aqueous phase. Based on the results thus far presented, five approaches to reduce the permeability of polymer electrolyte membranes (PEMs) and to simultaneously maintain the proton conductivity are suggested:

- A higher concentration of functional groups inside the water channels in order to decrease the solubilities and the diffusion coefficients of gases in the aqueous phase.
- Increased intermolecular forces between the aqueous phase and the solid phase in order to decrease the permeation through the intermediate phase.
- A reduced permeability of the solid phase.
- Cross-linking of the ionomers [139] to avoid a softening of the solid phase with water uptake.
- The avoidance of dead-end water channels.

In the following, these approaches will be discussed in more detail.

The gas solubility in electrolytic solutions was reported to decrease with a higher concentration of the ions [195–197]. Moreover, the viscosity of acids typically increases with a higher proton concentration [200], which consequently reduces the diffusion coefficient. Applied to PEMs, increasing the density of functional groups thus may lead to a decreased permeability of the aqueous phase. By the increase of the intermolecular forces between the water channels and the polymer backbone, the permeability of the intermediate region might be reduced. For this purpose, polymer backbones that show smaller contact angles with water (such as Polyethylene with approximately 89° [205]) than PTFE with approximately 100° [204] might decrease the permeability of the intermediate phase. Furthermore, by the choice of the polymer backbone, the permeability of the solid phase may be reduced. This decrease of the permeability of the solid phase can be achieved by larger van der Waals forces between the backbone of the PEM. For instance, the activation energy of the oxygen permeability of Polyethylene is by a factor of approximately 1.4 higher than that of PTFE [185] (which equals the polymer backbone of Nafion®). Thus, by variation of the polymer backbone of the ionomer, the permeation through the solid phase of a PEM may be reduced while other properties such as water uptake and proton conductivity may be retained. Moreover, the polymer chains can be connected by crosslinking, which also increases the activation energy for the gas permeability [206,207]. In addition, the cross-linking of the polymer chain increases the rigidity of the polymer matrix which may reduce the softening of the solid phase with water uptake.

Towards the design of the morphology of the aqueous phase in PEMs, dead end water channels should be avoided since these do not contribute to the overall proton conductivity of the PEM while they enable the high gas permeability of the mixed pathway. Furthermore, the gas permeability potentially depends on the diameter of the water channels, because their size is decisive for the volume of the intermediate phase. As shown in Figure 7.1.5, above volumetric water contents of 10%, the volumetric water content increases more strongly with the water content than that of the intermediate phase. Hence, by increasing the diameter of the water channels the relative contribution of the intermediate region to the permeation compared to permeation through bulk water might be reduced. However, by increasing the diameter of the water channels the capillary forces are reduced, which might reduce the ability to withstand differential pressure as a driving force for gas permeation. Moreover, increasing the diameter of the water channels could lead to a more inhomogeneous proton distribution which could reduce proton mobility [20,21,160,161]. To summarize, the aqueous phase necessary for the proton conduction leads to the formation of the intermediate phase, while the permeation through these both phases might be a physical restriction for the reduction of the gas permeability of PEMs while retaining the proton conductivity.

# 7.4 Synopsis of the chapter

In this chapter, the hydrogen and oxygen permeation through the aqueous, solid and intermediate phase of Nafion<sup>®</sup> was simulated using a resistor network. The structure of Nafion<sup>®</sup> was modeled morphologically representative based on recently reported tomography data. In order to fit the overall permeability determined with this model to the permeability measured in the previous chapter, the permeabilities of the intermediate phase and/or the solid phase had to be enlarged in comparison to those of the aqueous phase and dry Nafion<sup>®</sup>, respectively. The higher gas permeability of the intermediate phase was ascribed to a less distinct hydrogen bond network than that in the aqueous phase and weak van der Waals forces in this regime. An increase of the permeability of the solid phase in Nafion<sup>®</sup> may be attributable to a softening of the polymeric matrix by water uptake, as water may act as a plasticizer for the polymeric matrix. When the permeation through the intermediate phase and the solid phase are neglected, the morphology of the aqueous phase caused a simulated permeability of approximately 0.15 times that of the aqueous phase itself. The mixed pathways by the alternating gas permeation though all three phases was estimated to

increase the overall permeability of Nafion® by a factor of  $4.5\pm1.2$  compared to the simulated permeability of solely the aqueous phase. Hence, based on this estimation, approximately  $75\pm7$ % of the hydrogen permeability of fully hydrated Nafion® was ascribed to the influence of the permeation through the intermediate and solid phase. Based on the characterized gas permeation through Nafion®, approaches to reduce the permeability of novel PEMs were identified and discussed.

# 8 Characterization of different polymer electrolyte membranes

The aim of this chapter is to compare the conductivities and hydrogen permeabilities of different polymer electrolyte membranes (PEMs) which were commercially purchased or supplied by project partners. The thicknesses of the PEMs were measured using a micrometer directly after the membranes have been taken out of a beaker that was filled with deionized water. Thus, the stated thicknesses refer to the fully hydrated state of the PEMs. The thickness measurement was affected by an error of approximately  $\pm 6\,\%$ . The PEMs examined in this chapter are listed in the following enumeration:

- Nafion<sup>®</sup> (manufactured by DuPont) is the best studied PEM in the literature, as this material has been commercially available since several decades. It is a perfluorinated sulfonic acid (PFSA), while the detailed chemical structure was stated in Section 2.4. In the previous chapters, the conductivity and hydrogen permeability of this PEM were examined in detail. In the data sheet of the manufacturer [208] the equivalent weight of this membrane type is reported to  $EW = 1020 \pm 40\,\mathrm{mg/eq}$ . Nafion<sup>®</sup> membranes are available with thicknesses in the range from approximately  $60\,\mathrm{\mu m}$  to  $210\,\mathrm{\mu m}$ .
- F9120 (Fumatech) is like Nafion<sup>®</sup> a PFSA that consists of a similar fluorinated chemistry with sulfonic acid functional groups. The detailed chemical structure of this membrane type is however neither reported in the literature nor stated by the manufacturer. The equivalent weight is reported by the manufacturer to  $EW = 900 \,\text{mg/eq}$ . The thickness of the wet membrane was measured to 154 µm.
- F1820 (Fumatech) is also a PFSA but with a higher equivalent weight of  $EW=1800\,\mathrm{mg/eq}$ . Its detailed chemical structure is also unknown. The thickness of the wet membrane was measured to 145  $\mu$ m.
- Aquivion<sup>®</sup> E98-09S (manufactured by Solvay) is also a PFSA. In comparison to Nafion<sup>®</sup>, the manufacturer reported a shorter side chain. The equivalent weight of this membrane is reported by the manufacturer to  $EW = 980 \, \text{mg/eq}$ . The thickness of the wet membrane was measured to 113 µm.
- C201 (manufactured by Tokuyama company) consists of a non-fluorinated chemistry. Further information on this membrane type was neither reported by the manufacturer nor reported in the literature. The thickness of this membrane was measured to 32 µm.

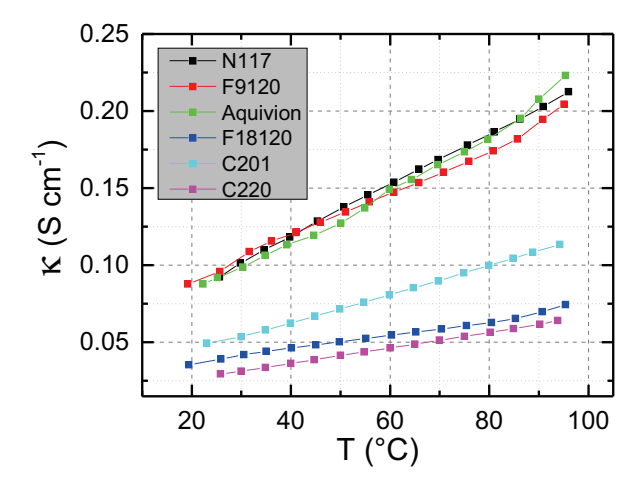


Figure 8.1.1: Measured conductivities with setup A (Section 4.1) of the different PEMs as a function of temperature. See explanation in the beginning of this chapter for further information on the different examined PEMs.

• C220 (manufactured by Tokuyama company) is also of a non-fluorinated chemistry. Again, further information about this membrane-type was not available. The thickness of the wet membrane was measured to 36 µm.

Literature that characterizes the volume fraction of water or the morphology of the aqueous phase is only reported for Nafion<sup>®</sup> (as discussed in Section 3.1). To characterize these properties costly methods such as small angle scattering techniques or cryo electron tomography are necessary, which are beyond the scope of this research. With reference to this lack of knowledge concerning the microscopic phase distributions in the other PEMs as Nafion<sup>®</sup>, the differences between the membranes are compared in terms of their macroscopic properties in the form of proton conductivity and hydrogen permeability. In Chapter 10, the conductivities and hydrogen permeabilities of PEMs and their ratio are derived to be decisive properties in terms of the overall efficiency of water electrolyzers. This chapter therefore aims at a benchmarking of these properties rather than a fundamental and deep understanding of the different material properties. To characterize conductivities and hydrogen permeabilities of the PEMs the methods discussed in Chapter 4 are used.

#### 8.1 Conductiviities

Figure 8.1.1 shows measured conductivities of the different PEMs as a function of temperature. All measurements were conducted with setup A under discrete temperature variation, as discussed in Section 4.1 in detail. The resistance of the membranes were red out from the recorded impedance spectra of the membranes at 1 kHz, where

8.2 Permeabilities 97

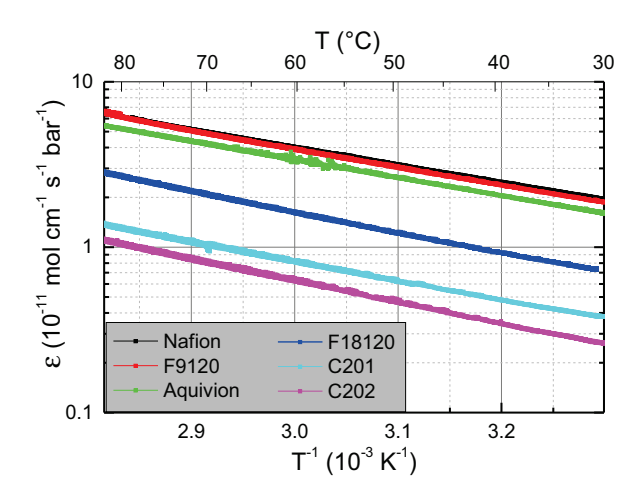


Figure 8.2.1: Measured hydrogen permeabilties of different PEMs as a function of the temperature.

the phase angle of the impedance was negligible and the Ohmic contribution to the impedance dominated. The measurement error of the conductivity is  $\pm 10\,\%$ , with reference to the propagation of errors of the measured sample geometries and the resistance determination. The highest conductivity of all membranes is supplied by the PFSA-type membranes Nafion<sup>®</sup>, F9120 and Aquivion<sup>®</sup>. The deviation of the measured conductivities of these membranes were below 10 % and thus within the measurement error. The PFSA material F18120 showed approximately one third of the conductivity of the other examined PFSA materials. This lower conductivity might be attributable to a smaller volumetric water content and a lower concentration of protons in the aqueous phase which is caused by the lower amount of functional groups. The membranes C201 and C220 showed approximately one half and one third of the conductivity of the Nafion<sup>®</sup> membrane, respectively.

### 8.2 Permeabilities

Figure 8.2.1 shows measured hydrogen permeabilities of the different PEMs as a function of the temperature. The measurements presented in this graph were conducted using setup C (Section 4.2). The measurement error is again mainly affected by the geometry of the sample and was estimated to  $\pm 10\,\%$  on the basis of the propagation of errors. Within this measurement precision, Nafion<sup>®</sup> and F9120 showed the same hydrogen permeabilities. The Aquivion<sup>®</sup> membrane showed an approximately 14 % lower hydrogen permeability as those of the Nafion<sup>®</sup> and F9120 membrane. The hydrogen permeability of the F18120 membrane is less than half of those of the F9120 and Nafion<sup>®</sup> membrane. Despite the polymeric phase was discussed in Chap-

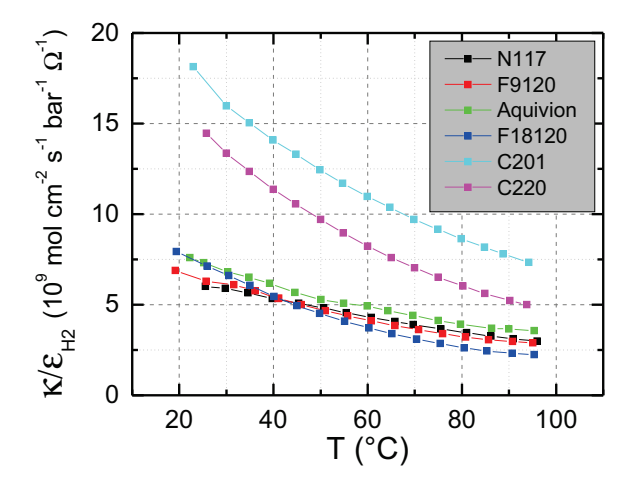


Figure 8.3.1: Ratio of the proton conductivities to the hydrogen permeabilities of the examined PEMs, calculated by the data graphed in Figure 8.1.1 and 8.2.1.

ter 7 to significantly influence the hydrogen permeability of Nafion<sup>®</sup>, it is still smaller than that of the aqueous phase. Accordingly, the lower hydrogen permeability of the F18120 membrane might be attributable to a lower volumetric water fraction of the aqueous phase. In Chapter 7, the permeability of the solid phase was discussed to depend on the water uptake. The smaller water uptake of the F18120 membrane thus might lead to a reduced softening of the polymeric phase compared to the other PFSA membranes. As a result, the polymeric phase in the fully hydrated F18120 membrane might be less permeable to hydrogen than that in the other fully hydrated PFSA membranes. The membranes with a hydrocarbon chemistry showed an at least six times smaller hydrogen permeability than that of the three PFSA membranes with a low equivalent weight (F9120, Nafion<sup>®</sup> and Aquivion<sup>®</sup>).

## 8.3 Ratios of conductivities to permeabilities

The ratio of the proton conductivity to the hydrogen permeability is an important parameter for overall efficiency of a water electrolysis cell, as later discussed in Section 12 in detail. The higher this ratio, the more efficient the cell can be. Figure 8.3.1 shows the ratio of the measured conductivities to the measured permeabilities of the different membranes, respectively. This ratio was calculated by dividing the measured values of the conductivity by linear fits to measured hydrogen permeabilities in Arrhenius plots, respectively. With reference to the propagation of errors, the ratios are affected by an error of approximately  $\pm 14$ %.

Within the error of the calculated ratio of the proton conductivity to the hydrogen

permeability, the PFSA membranes Nafion<sup>®</sup>, F9120 and Aquivion<sup>®</sup> show the same values. The F18120 membrane shows approximately the same ratio of  $\kappa$  to  $\varepsilon$  as that of the other PFSA membranes. In the case of the membranes with a non-fluorinated chemistry, the ratio of the proton conductivity to the hydrogen permeability is significantly higher than those of the PFSA membranes. The reason for this difference might be a less permeable polymeric phase, as further discussed in Section 12.

# 8.4 Synopsis of the chapter

In this Chapter, the proton conductivities and hydrogen permeabilities of six different PEMs were examined. Four of these PEMs were perfluorinated sulfonic acids (PF-SAs). Three of these four PFSA membranes had equivalent weights between 900 mg/eq and 1050 mg/eq, while the other showed an equivalent weight that is with 1800 mg/eq approximately twice as large as those of the others. The other two PEMs were purchased from the Tokuyama company and consisted of a non-fluorinated chemistry. The three PFSA membranes with the almost equal equivalent weights showed almost equal conductivities and hydrogen permeabilities. The PFSA membrane with the lower equivalent weight showed smaller proton conductivity and hydrogen permeability than those of the other PFSA membranes. The membranes with a hydrocarbon backbone chemistry showed less than half of the conductivities but less than one sixth of the hydrogen permeabilities of those of the PFSA membranes with low equivalent weight. As a result of these differences, the ratio of the proton conductivities to the hydrogen permeabilities of the hydrocarbon membranes were approximately two times higher than those of the PFSA membranes.

# 9 Gas permeation through the membrane during water electrolysis

In the previous chapters, the hydrogen and oxygen permeation through Nafion caused by diffusion were characterized and correlated with the microscopic geometries of the water channels. As discussed in the fundamentals chapter (Section 2.1), electrochemical water splitting at the electrodes leads to the permeation of protons from the anode through the PEM to the cathode. The proton flux through the membrane is accompanied by electro-osmotic water drag (Section 2.2.2). This proton and water transport through the PEM may result in a convective oxygen transport from the anode to the cathode, while the hydrogen permeation from the cathode to the anode may be simultaneously reduced. The aim of this chapter is to describe the hydrogen and oxygen cross-permeation through the PEM during water electrolysis. Moreover, the influence of the proton flux on the gas crossover shall be physically described. Figure 9.0.1 illustrates the physical transport processes of protons, water, hydrogen and oxygen through the PEM during water electrolysis. Differential pressure as a driving force for the gas permeation will be neglected since it did not lead to perceivable contributions to the measured gas permeability of Nafion (Chapter 6).

In the following, first the partial pressure increase in the catalyst layers during PEM water electrolysis that is caused by the oxygen and hydrogen evolution is physically described. Second, the hydrogen and oxygen cross-permeation through the PEM during water electrolysis is elucidated. Within this aim, the interaction of gas diffusion and proton permeation is physically described. Third, the anodic hydrogen content during water electrolysis will be calculated and compared to in-operando measurements of a water electrolysis cell. Based on these measurements, the pressure increase in the electrodes that is caused by the gas evolution is estimated. Moreover, on the basis of these measurements the extent of the interaction between the proton permeation and the gas diffusion is evaluated. The anodic hydrogen content is exemplarily modeled for a cathodic pressure of 30 bar, which is the minimum hydrogen pressure that is considered to be suitable for methanation processes and the direct integration of hydrogen into the natural gas grid [29]. The calculations in this chapter refer to the proton conductivity and gas permeability of Nafion at 80 °C, which is a temperature that typically constitutes a compromise between a reasonable lifetime and a good performance of PEM water electrolysis cells [209]. All considerations in this chapter refer to galvanostatic conditions (constant current densities). This chapter is based on several previously published studies [45,210,211].

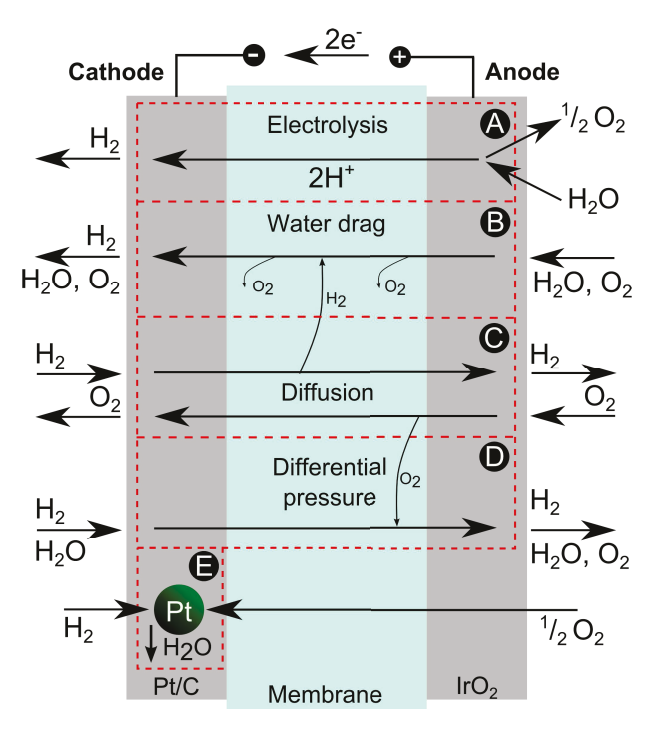


Figure 9.0.1: Schematic illustration showing the mechanisms that lead to the hydrogen and oxygen cross-permeation during PEM water electrolysis [45]. (A): Proton flux through the PEM. (B): Convective transport of dissolved oxygen and hydrogen in the aqueous phase caused by the proton flux through the PEM. The gases dissolved in the hydration shell of the protons may diffuse into the surrounding water as illustrated by tiny arrows. (C): Diffusion of oxygen and hydrogen through the PEM. (D): Permeation forced by differential pressure, which will be neglected based on the results in Chapter 6. (E): Catalytic reaction of hydrogen and oxygen on the cathodic platinum catalyst.

## 9.1 Partial pressure increase in the catalyst layer

As discussed in Section 2.1.3, a triple phase boundary must occur in the catalyst layers, where electrons, protons and water gain access to the catalyst. In addition, the produced hydrogen and oxygen must be transported from the catalysts in the electrodes to the gas outlets of the cell. The gas evolution enlarges the pressures in the electrodes, which is a consequence of mass transport and supersaturation [212, 213] by their electrolytic production.

# 9.1.1 Influence of concentration and differential pressure differences

The aim of the following deliberations is to estimate, whether diffusion or differential pressure driven permeation dominate the transport of produced gases from the catalyst at the inside of an electrode to its outside. Faraday's law relates the current density to the amount of produced hydrogen in the form of  $\Gamma_{\rm H_2}$  that denotes the molar production rate density of hydrogen at the cathode:

$$\Gamma_{\rm H_2} = \frac{j}{2F} \tag{9.1.1}$$

The produced hydrogen in the electrode must permeate to the cathodic gas outlet or to the anode. Moreover, it can be recombined with oxygen coming from the anode. When the gas crossover is small, the permeation flux density  $\Phi^{el}_{H_2}$  of hydrogen produced in the cathode to the cathodic gas outlet can be approximated as:

$$\Phi_{\rm H_2}^{\rm el} \approx \Gamma_{\rm H_2} \tag{9.1.2}$$

If differential pressure driven permeation does not contribute to the gas transport from the inside of the electrode to its outside, all the produced gases must be transported by diffusion. In the following, this case is assumed, in order to estimate how large the partial pressure difference  $\Delta p_{\rm H_2}^{\rm el}$  of hydrogen between the inside of the cathode and its outside would be when diffusion is the only driving force for the gas transport. The thickness of the electrodes for the acidic water electrolyzer were measured to approximately  $10\,\mu\text{m}$ , while hydrogen diffusivity in water was estimated to  $\varepsilon_{\rm H_2}^{\rm Fick} \approx 1\times 10^{-10}\,\mathrm{mol\,cm^{-1}\,s^{-1}\,bar^{-1}}$  at  $80\,^{\circ}\text{C}$  (see Chapter 6). By calculating  $\Phi_{\rm H_2}^{\rm el}$  for  $j=2\,\mathrm{A\,cm^{-2}}$  and by using Fick's law for an electrode thickness of  $d^{\rm el}=10\,\mu\text{m}$  and the  $\varepsilon_{\rm H_2}^{\rm Fick}$  of water,  $\Delta p_{\rm H_2}^{\rm el}$  can be calculated to 500 bar. This value can be considered as a lower approximation as the utilized value for the hydrogen permeability in water is higher than that of the polymer electrolyte in the electrodes. Moreover, the morphology of the impermeable electron conducting phase (catalyst and support) further reduces the permeability in comparison to that of pure water.

Based on the measurements of the anodic hydrogen content (that are presented in Section 9.3) and equation 9.1.3, the mean partial hydrogen pressure inside the cathode at  $2\,\mathrm{A\,cm^{-2}}$  can be approximated to be at maximum 16 bar higher than that at the gas outlet. Hence, if diffusion is the only driving force for the gas transport in the electrodes,  $\Delta p_{\mathrm{H}_2}^{\mathrm{el}}$  would be more than one order of magnitude higher than that derived from the measurements. Accordingly, diffusion cannot be the dominating driving force for the permeation of the produced gases from the electrode to the gas outlet. In the case of microporous structures such as the electrodes in the electrolyzers, the gas perme-

ation fluxes driven by differential pressures can be orders of magnitudes larger than those driven the diffusion [214]. Thus, the differential pressure driven permeation is considered to be the dominating driving force for the permeation of gases from the inside to the outside of the electrodes.

In the dense form of a membrane, Nafion<sup>®</sup> polymer electrolyte shows negligible permeability to differential pressures [120]. The mean diameter of water channels of Nafion<sup>®</sup> membranes was reported to approximately 2.5 nm (Section 3.1), while the mean pore diameters in the catalyst layers are typically at least one magnitude larger [215,216]. The pressure drop can be characterized by different power law dependencies of its radius depending on the form of the flow (laminar or turbulent) and parameters such as the pore roughness. However, all approaches which are typically used to describe the differential pressure driven permeation through pores got in common that the pressure drop decreases with the pipe diameter. In the case of the micro- or nanoporous structure of catalyst layers the exact influence of the pore diameter on the permeability is unknown as the fluid dynamics in the considered medium are unknown. However, it can be expected that the permeability significantly increases toward larger pore diameters in analogy to macroscopic systems. Thus, the different pore sizes in the electrodes and in the polymer electrolyte membrane are expected to lead to profoundly different permeabilities to differential pressures.

#### 9.1.2 Quantitative description

Mass transport phenomena in electrodes crucially depends on their structure in the form of porosity, thickness and composition. Accordingly, generalized values that characterize the partial pressure increase in the electrodes as a function of the current density cannot be given here. The permeation flux driven by diffusion is proportional to the partial pressure differences (Fick's law), while that originating from absolute pressures differences is also characterized by a linear response (Darcy's law). Besides hydrogen at the cathode and oxygen at the anode, saturated water vapor  $p_{\rm sv}$  occurs in the gaseous phase at the electrodes (Section 6.1.1). Hence, the differences between the partial pressures at the catalyst and the corresponding gas outlets are equal to the differences of the absolute pressures. Consequently, the pressure differences that drive both transport mechanisms (diffusion and differential pressure) are equal.

The hydrogen and oxygen produced during water electrolysis are typically saturated with water vapor [217]. The gas permeation flux from the inside of the electrode to its outside was shown to be proportional to the gas production rate and thus proportional to the current density (eq. 9.1.1). As described by Fick's law and Darcy's law, the partial or absolute pressure drop for the permeation through a medium is propor-

tional to the permeation flux. Hence, the pressure difference between the inside of the catalyst layer and the gas outlet scales linearly with the amount of produced gas. By combining these linear relations, the partial pressure  $p_{\rm H_2}^{\rm c}$  of hydrogen in the cathode scales linearly with the current density

$$p_{\rm H_2}^{\rm c} = p^{\rm c} + Y_{\rm H_2} j - p_{\rm sv} , \qquad (9.1.3)$$

where  $p^c$  denotes the absolute cathodic pressure. The proportionality factor  $Y_{H_2}$  is denoted as the cathodic partial pressure increase factor. This linear relation is only valid for laminar flows, where the pressure drop is proportional to the flux. In case of turbulent flows at high permeation rates, this linear relation does not hold valid. Thus, high current densities can possibly affect the partial pressure increase by a nonlinear trend.

At the anode, the oxygen evolution also leads to an increase of the partial oxygen pressure in the catalyst layer, which is described in analogy to that of hydrogen

$$p_{O_2}^{a} = p^{a} + Y_{O_2} j - p_{H_2O} , \qquad (9.1.4)$$

where  $p^a$  denotes the total pressure at the anodic gas outlet and  $Y_{O_2}$  the partial pressure increase factor for oxygen. In Section 9.3, the partial pressure increase factor for hydrogen will be estimated by fits to the measured anodic hydrogen contents of an operating electrolysis cell. In contrast, the anodic partial pressure increase cannot be determined by a measurement of the cathodic oxygen content, since both gases are catalytically recombined at the cathode (Section 2.1.5). Hence, a rough estimation will be used to calculate the partial pressure increase in the anodic catalyst layer. Assuming that the catalyst layers are of same thickness and similar structure, the partial pressure increase factor for oxygen is estimated by

$$Y_{O_2} \approx (\varepsilon_{H_2}/\varepsilon_{O_2}) \frac{1}{2} Y_{H_2} ,$$
 (9.1.5)

while the factor 1/2 takes into account that the oxygen production rate is half that of hydrogen. The ratio of the permeabilities describe the smaller permeability of the Nafion binder to oxygen than to hydrogen. In order to calculate the value for  $Y_{\rm O_2}$ , the permeabilities determined in Chapter 6 were used.

Thicker pore diameters of the current collectors than that of the electrodes result in lower capillary pressures. These thicker pores also reduce the friction for the gas permeation, which results in higher the permeabilities of the current collectors than that of the electrodes. Thus, the main contribution of the partial pressure increase at the catalyst is attributable to the permeation from the inside to the outside of the

electrodes. The physics in terms of Fick's law and Darcy's law that describes the permeation fluxes through electrodes and current collectors are equal. Thus, even if the permeation through the current collectors significantly impacts the pressure drop, its contributions are physically described by the equations presented above. In the flow fields, the evolved gases in the form of bubbles are convective carried along with the flux of liquid water. Thus, the contributions of the permeation inside the flow fields to the partial pressure increase factor are expected to be negligible.

When gases are evolved in water, more gas molecules can be dissolved than in equilibrium (gaseous phase over a saturated solution), which is commonly referred to as supersaturation [212,213,218,219]. This effect may also lead to a partial pressure increase of the produced gases in the catalyst layers. The contributions of supersaturation and the transport through all media (electrodes and current collectors) were all expressed by one partial pressure increase factor for each electrode, respectively.

# 9.2 Gas permeation fluxes

Based on mass conservation, the overall cross-permeation flux of a gas through a membrane is constant in the direction of the concentration gradient. Moreover, the permeation fluxes of a gas through a PEM by different mechanisms are additive. Thus, the total hydrogen permeation flux density  $\Phi_{\rm H_2}$  through the PEM equals the sum of the flux density caused by diffusion  $\Phi_{\rm H_2}^{\rm diff}$  and that caused by the proton permeation  $\Phi_{\rm H_2}^{\rm drag}$ :

$$\Phi_{\rm H_2} = \Phi_{\rm H_2}^{\rm diff} - \Phi_{\rm H_2}^{\rm drag} \tag{9.2.1}$$

The negative sign of  $\Phi_{H_2}^{drag}$  takes the opposing direction of the proton movement to that of the hydrogen diffusion into account (Fig. 9.0.1). The same relation is used for oxygen

$$\Phi_{_{\mathrm{O}_{2}}} = \Phi_{_{\mathrm{O}_{2}}}^{\mathrm{diff}} + \Phi_{_{\mathrm{O}_{2}}}^{\mathrm{drag}}$$
 , (9.2.2)

where both mechanisms lead to the oxygen transport in the direction from the anode to the cathode (Fig. 9.0.1). Thus, the signs of the oxygen permeation flux densities caused by both mechanisms are both positive.

#### 9.2.1 Separate description of the permeation fluxes

In the following, the hydrogen and oxygen cross-permeation flux densities caused by diffusion and the proton permeation are first considered separately. In the next section, a model to estimate the interactions of both mechanisms will be presented.

#### 9.2.1.1 Diffusion

In Chapter 6, the measured hydrogen permeation flux density through Nafion was described by Fick's law (eq. 2.3.3) and attributed to the driving force of diffusion. Applied on the PEM during water electrolysis, the partial hydrogen pressure difference between the anodic catalyst layer  $p_{\rm H_2}^{\rm a}$  and the cathodic catalyst layer  $p_{\rm H_2}^{\rm c}$  leads to a permeation flux density of:

$$\Phi_{\rm H_2}^{\rm diff} = \varepsilon_{\rm H_2} \frac{p_{\rm H_2}^{\rm c} - p_{\rm H_2}^{\rm a}}{d} \tag{9.2.3}$$

In Section 9.3, it will be shown, that hydrogen at the anodic iridium oxide catalyst is neither electrochemically oxidized nor catalytically reacted with anodic oxygen. Thus, the percental anodic hydrogen content can be calculated as the ratio of the hydrogen cross-permeation flux density  $\Phi_{\rm H_2}$  to the total anodic gas release rate density, which is the sum of the production rate density of oxygen  $\Gamma_{\rm O_2}$  and the hydrogen cross-permeation flux density  $\Phi_{\rm H_2}$ :

$$H_2 \text{ in } O_2 = \frac{\Phi_{H_2}}{\Gamma_{O_2} + \Phi_{H_2}} \times 100 \% \tag{9.2.4}$$

Based on this relation, the anodic partial pressure of hydrogen  $p_{H_2}^a$  equals the absolute anodic pressure  $p^a$  multiplied by the anodic hydrogen content:

$$p_{\rm H_2}^{\rm a} = p^{\rm a} \, \frac{\Phi_{\rm H_2}^{\rm diff}}{\Gamma_{\rm O_2} + \Phi_{\rm H_2}^{\rm diff}} \tag{9.2.5}$$

Inserting this expression for the anodic hydrogen pressure into Fick's law (eq. 9.2.3) yields:

$$\Phi_{\rm H_2}^{\rm diff} = \frac{\varepsilon_{\rm H_2}}{d} \left( p_{\rm H_2}^{\rm c} - p^{\rm a} \frac{\Phi_{\rm H_2}}{\Gamma_{\rm O_2} + \Phi_{\rm H_2}} \right) \tag{9.2.6}$$

When diffusion is the only driving force for the gas permeation through the membrane (assuming a negligible impact of the proton permeation on the gas crossover), the total hydrogen permeation flux in the latter equation can be replaced by that caused by diffusion. The quadratic equation resulting

$$\Phi_{\rm H_2}^{\rm diff} = -\frac{b}{2} \pm \sqrt{(\frac{b^2}{4}) + \Gamma_{\rm O_2} \ p_{\rm H_2}^{\rm c} \frac{\varepsilon_{\rm H_2}}{d}}$$
 (9.2.7)

with

$$b = \Gamma_{O_2} + \frac{\varepsilon_{H_2}}{d} (p^a - p_{H_2}^c)$$
 (9.2.8)

has two solutions of which only the positive solution is of a physical nature. This exact solution can be simplified when  $p_{\rm H_2}^{\rm c}>>p_{\rm H_2}^{\rm a}$ . In this case, the approximation

 $\Delta p_{\rm H_2} \approx -p_{\rm H_2}^{\rm c}$  can be inserted into equation 9.2.3:

$$\Phi_{\rm H_2}^{\rm diff} \approx \varepsilon_{\rm H_2} \frac{p_{\rm H_2}^{\rm c}}{d} \tag{9.2.9}$$

By using this simplified description, the back permeation from hydrogen at the anode to the cathode is neglected.

In contrast to the mixing of hydrogen and oxygen at the anode, the simultaneous appearance of both gases at the cathodic platinum catalyst results in their catalytic recombination (Section 2.1.5). Accordingly, the partial pressure of oxygen in the cathodic catalyst layer is assumed to be negligible, which means that  $p_{\rm O_2}^{\rm c}=0$  bar. Thus, using Fick's law, the permeation flux density of oxygen through the PEM that is caused by diffusion is described by:

$$\Phi_{\mathcal{O}_2}^{\text{diff}} = \varepsilon_{\mathcal{O}_2} \frac{p_{\mathcal{O}_2}^{\text{a}}}{d} \tag{9.2.10}$$

Accordingly, the oxygen cross-permeation through the membrane cannot be evaluated by measuring the cathodic oxygen content.

#### 9.2.1.2 Proton permeation

In the following, the hydrogen and oxygen cross-permeation flux densities that are caused by the proton permeation are estimated. A measurement technique to directly measure these contributions could not be developed. The experimental challenge in measuring the influence of the proton permeation on the gas transport is that for its occurrence protons must permeate through the PEM. The protons permeating through the PEM must be reduced at the cathode, which typically results in hydrogen evolution. Thus, the gas crossover that is caused by the proton permeation as described in Section 4.2 could not be directly measured as the evolved hydrogen would influence such a measurement. Alternatively, the gas permeation fluxes can be indirectly analyzed for instance by measuring the anodic hydrogen content during water electrolysis, as presented in Section 9.3. The hydrogen evolution at the cathode lead to the partial pressure increase in the electrodes, which itself influences the cross-permeation as later discussed in Section 9.1 in detail.

As the influence of proton permeation on the hydrogen and oxygen cross-permeation fluxes could not be examined by an direct experimental approach, an estimation for this mechanism is presented in the following. Therefore, the following assumptions are used:

• The factor *h* represents the ratio of the hydrogen concentration in the hydration

shell of the hydronium ions to the hydrogen concentration in the surrounding electrolyte. This factor is in the following defined as the 'hydration shell factor'.

• The entire aqueous phase inside the PEM is assumed to contribute to the proton conductivity. Accordingly, only the first and second water channel topologies that were introduced in Chapter 5 are assumed to occur.

As discussed in Section 7.1.2, the solubilities of hydrogen and oxygen in the acidic aqueous phase of Nafion are smaller than those in water, respectively. In Chapter 7, the hydrogen permeability of Nafion as a function of the temperature and water content was described using  $\varepsilon_{\rm ap} \approx 0.5 \, \varepsilon_{\rm w}$ . With reference to the equations stated in Section 7.1.2, the diffusion coefficient of hydrogen in the aqueous phase in Nafion was related to that of water by  $D_{\rm ap} \approx 0.85 D_{\rm w}$ . Moreover, in Section 7.1.2 the solubilities were estimated to  $S_{ap} \approx 0.59 S_w$ . The smaller solubility of the gases in the aqueous phase could mean, that in the vicinity of the functional groups and the excess protons less gas molecules are dissolved than between the water molecules itself. Such an inhomogeneous distribution of the dissolved gases can be described by an hydration shell factor that is smaller than unity. In Section 9.3.2, the value of the hydration shell factor is estimated by using in-operando measurements of the anodic hydrogen content during PEM water electrolysis. In order to characterize the contributions of the proton permeation to the hydrogen and oxygen cross-permeation, only the aqueous phase of the PEM is considered (intermediate and solid phase is neglected), as this is the only phase that is permeable to protons. Consequently, the interaction between both transport processes can only occur in the aqueous phase.

In Section 5, the water uptake of Nafion was characterized by the amount of water molecules per proton  $\lambda$ . The amount of water transported by the electro-osmotic drag mechanism was characterized by the drag-coefficient  $n_{\rm d}$  in Section 2.2. The ratio of both numbers represents the amount of water that is transported by the electro-osmotic drag mechanism normalized to the total amount of water in the aqueous phase of Nafion:

$$\frac{n_{\rm d}}{\lambda} \approx 0.3 \tag{9.2.11}$$

When the dissolved gases are homogeneously distributed in the aqueous phase (h = 1), the total amount of electrochemically dragged water contributes to  $\Phi_{\rm H_2}^{\rm drag}$  and  $\Phi_{\rm O_2}^{\rm drag}$ . The velocity distribution of the water molecules in the aqueous phase and the possibly smaller solubility of the gases in the vicinity of the hydronium ions are described by smaller value of h than unity.

In order to distinguish between the permeation through Nafion, pure water, and the aqueous phase of Nafion, the notations introduced in Table 9.2.1 are used in the following. As discussed in Chapter 5, the drift velocity of protons in an aqueous

Table 9.2.1: Remarks on the notation used in this section exemplified for an arbitrary physical property *P*.

P Property of Nafion

 $\hat{P}$  Property of the aqueous phase in Nafion

*P*<sup>as</sup> Property of an aqueous solution

 $P^{x}$  Property in the x-direction, which is orthogonal to the electrodes.

solution can be related by

$$v_{\rm H^+}^{as} = \frac{j}{c_{\rm H^+}^w \, \rm F} \tag{9.2.12}$$

to the current density. Applied to Nafion, the concentration of protons in the water channels was approximated as  $c_{\rm H^+}=2.8\,{\rm mol/l}$  (see Chapter 5). The current in a water electrolyzer is typically normalized to the cell area (Section 2.1.2), while only the cross-sectional area  $A_{\rm aq}$  of the aqueous phase of Nafion can contribute to the entire proton conductivity. Thus, the current density normalized to the cross-sectional area of the water channels is higher than that normalized to the cell area. Moreover, the tortuosity of the water channels leads to detours of the proton permeation. As a result, at a defined current density, the protons in the water channels move faster than they would in the case of a direct connection between the electrodes. The faster velocity of the protons thus compensates the detours that are caused by the tortuous water channels. Based on these deliberations, the mean drift velocity of protons in the water channels of a PEM is increased by the tortuosity and the normalization to the cross-sectional area of the aqueous phase:

$$\hat{v}_{H^{+}} = \frac{j}{\hat{c}_{H^{+}}} F \frac{A}{A_{ap}} \tau_{eff}$$
 (9.2.13)

With regard to the overall permeation flux of hydrogen through the PEM, the movement in the direction of the overall hydrogen concentration gradient (which corresponds to the shortest connection between the electrodes) is decisive. This direction equals the mean direction of the proton permeation through the PEM and is in the following defined as *x*-direction. Referring to a constant current density again, the velocity of the protons in this direction is not influenced by the tortuosity, since detours mean that velocities in other directions as the *x*-directions result. Thus, the drift velocity of protons in the *x*-direction is smaller than that in the direction of the respective water channels:

$$\hat{v}_{H^{+}}^{X} = \frac{j}{\hat{c}_{H^{+}} F} \frac{A}{A_{ap}}$$
 (9.2.14)

The amount of hydrogen atoms carried by the protons equals the concentration of hydrogen in the hydration shell  $(h \times \hat{c}_{H_2})$  times the relative amount of water molecules that carried through the PEM (calculated by the drag coefficient  $n_{\rm d}$  divided by the

amount of water molecules per sulfonic acid group  $\lambda$ ). Thus, the molar permeation flux density of hydrogen can be described by:

$$\hat{\Phi}_{\rm H_2}^{\rm drag} = \hat{v}_{\rm H^+}^{\rm x} \frac{n_{\rm d}}{\lambda} \, h \, \hat{c}_{\rm H_2} \tag{9.2.15}$$

In Section 9.3, the influence of different values for *h* on the simulated anodic hydrogen content in comparison with experimental data will be discussed. The molar permeation flux density of oxygen caused by the proton permeation can estimated using the same approach.

The concentrations of hydrogen and oxygen in the water channels of the PEM are a function of the position in the x-direction. The concentration profile in the membrane is influenced by diffusion and proton permeation as further discussed in Section 9.2.2.2. Thus, without knowing the precise concentration profile of the dissolved gases in the PEM, the gas transport by the proton permeation through the PEM cannot be exactly determined using the latter equation. However, based on the continuity equation and the correlated mass conservation, the hydrogen permeation flux through the membrane must be a constant over the distance and is thus independent of the position in the membrane. Hence, the mean concentration of hydrogen  $\bar{c}_{\rm H_2}$  in the aqueous phase can be taken as an approximation in order to calculate  $\hat{\Phi}_{\rm H_2}^{\rm drag}$ :

$$\hat{\Phi}_{H_2}^{drag} = \hat{v}_{H^+}^x \frac{n_d}{\lambda} h \, \bar{c}_{H_2} \tag{9.2.16}$$

In the case of oxygen, the equation can be derived in analogy.

#### 9.2.1.3 Ratio of the permeation fluxes

The aim of the following deliberations is to relate the contributions of the cross-permeation fluxes through the PEM caused by the proton movement to those caused by diffusion. Only the aqueous phase of the membrane is considered, which was discussed to contribute to both, proton conduction and gas cross-permeation. In this section the interaction of the hydrogen and oxygen permeation caused by diffusion and proton permeation is neglected. To compare the hydrogen and oxygen permeation fluxes caused by diffusion and proton permeation, the movement of the gas molecules in the x-direction is decisive. Analogously to the proton permeation, tortuous water channels means detours of the diffusing gas molecules in the aqueous phase. Thus, the diffusion coefficient of hydrogen in the x-direction decreases with higher values of the tortuosity  $\tau$ :

$$\hat{D}_{H_2}^{X} = \frac{1}{\tau} \, \hat{D}_{H_2} \,, \tag{9.2.17}$$

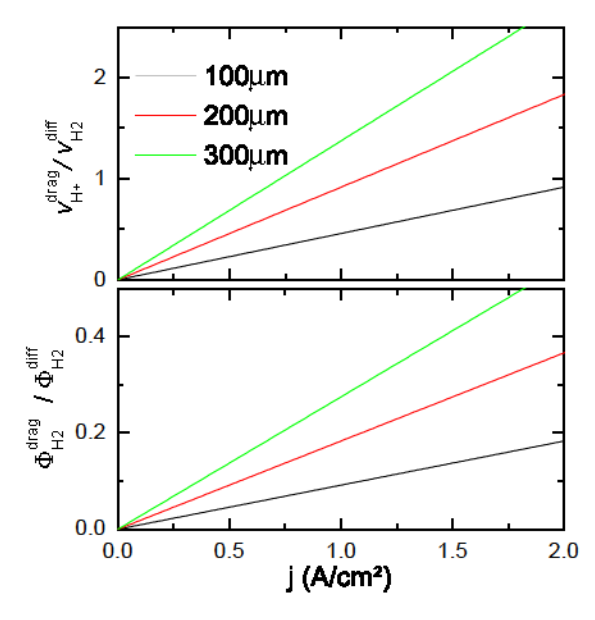


Figure 9.2.1: Modeled relations of the hydrogen permeation that is caused by the proton permeation and diffusion as a function of the current density. Membrane thicknesses of  $100\,\mu\text{m}$ ,  $200\,\mu\text{m}$  and  $300\,\mu\text{m}$  were used for the calculations as indicated by the color code in the figure. The calculations refer to a temperature of  $80\,^{\circ}\text{C}$  and the permeation through the aqueous phase of Nafion for an effective tortuosity of  $\tau_{\text{eff}}=1.5$ . By multiplying the graphed values by  $\hat{D}_{\text{H}_2}/\hat{D}_{\text{O}_2}=2.2$ , the displayed ratios can be approximated for the oxygen permeation. Top: Estimated ratio of the drift velocity of protons in the x-direction to the mean velocity of diffusion driven hydrogen molecules as calculated by equation 9.2.22. Bottom: Estimated ratio of the hydrogen permeation fluxes caused by the proton permeation to that caused by diffusion for a hydration shell factor of h=1 as calculated by equation 9.2.19.

The tortuosity  $\tau$  of fully hydrated Nafion is approximated based on the measurements reported by Zhao et~al.~ [159] to  $\tau_{\rm eff}\approx 1.5$  (Section 3.1). When a membrane separates a compartment with a defined partial hydrogen pressure from an another compartment with a negligible partial hydrogen pressure, Fick's law describes a linear concentration profile in the x-direction of the membrane. Thus, the mean hydrogen concentration  $\bar{c}_{\rm H_2}$  in the aqueous phase of the membrane is half of that of the total concentration difference  $\Delta \hat{c}_{\rm H_2}$  over the membrane thickness d. Therewith, the hydrogen permeation flux described by Fick's law equals:

$$\hat{\Phi}_{H_2}^{\text{diff}} = \hat{D}_{H_2}^{\times} \frac{2\bar{c}_{H_2}}{d}$$
 (9.2.18)

Using this relation, the ratio of the hydrogen permeation flux caused by the proton permeation (eq. 9.2.16) to that caused by diffusion (eq. 9.2.18) is calculated to:

$$\frac{\hat{\Phi}_{H_2}^{drag}}{\hat{\Phi}_{H_2}^{diff}} = \hat{v}_{H^+} \frac{n_d}{\lambda} h \frac{d}{2\hat{D}_{H_2}^{x}} \tau_{eff}$$
 (9.2.19)

This ratio is independent of the hydrogen concentration, which thus means independent of the position in the aqueous phase of the membrane (based on the constant permeation flux) and the applied pressures. Figure 9.2.1 graphically displays the latter equation. The diffusion coefficient was calculated based on the diffusion coefficients of hydrogen and oxygen in water that were reported by Wise *et al.* [124]. The velocity of the movement of hydrogen molecules through the aqueous phase of Nafion equals the permeation flux density of hydrogen through aqueous phase divided by the mean concentration of dissolved hydrogen:

$$\hat{v}_{H_2}^{\text{diff}} = \frac{\hat{\Phi}_{H_2}}{\hat{c}_{H_2}} \tag{9.2.20}$$

Inserting Fick's law of diffusion (eq. 2.3.1) into the latter equation yields:

$$\hat{v}_{H_2}^{\text{diff}} = \frac{\hat{D}_{H_2}^{\text{x}}}{d} \frac{\Delta \hat{c}_{H_2}}{\bar{c}_{H_2}}$$
(9.2.21)

Using the relation  $\bar{c}_{H_2}=0.5\Delta\hat{c}_{H_2}$  again and equation 9.2.14, the ratio of these velocities can be determined to:

$$\frac{\hat{v}_{\text{H}^{+}}}{\hat{v}_{\text{H}_{2}}^{\text{diff}}} = \frac{\lambda}{n_{\text{d}}} \frac{\hat{\Phi}_{\text{H}_{2}}^{\text{drag}}}{\hat{\Phi}_{\text{H}_{2}}^{\text{diff}}} \frac{1}{h}$$
(9.2.22)

Figure 9.2.1 also shows the estimated ratio of the proton drift velocity to the mean hydrogen molecule velocity that is driven by diffusion. In the case of the oxygen permeation, the same procedure for the estimations can be conducted. The only parameter that changes is the diffusion coefficient, which is different for both gases. Based on the data of Wise *et al.* [124] (which was reviewed in Table 6.1.1), the ratio of the diffusion coefficient of hydrogen to that of oxygen in water is  $\hat{D}_{\rm H_2}/\hat{D}_{\rm O_2}=2.2$ . By multiplying this factor to the estimated ratios of the permeation fluxes and the velocities determined for hydrogen those for oxygen can be calculated.

In Chapter 7, the hydrogen permeability solely through the aqueous phase of Nafion (impermeable intermediate and solid phase) was estimated to  $25\pm7\,\%$  of the permeability through all the phases at  $80\,^\circ\text{C}$ . This estimation of the percental contribution of the aqueous phase to the overall permeability is also used to weigh the contributions of the proton permeation (which only takes place in the aqueous phase)

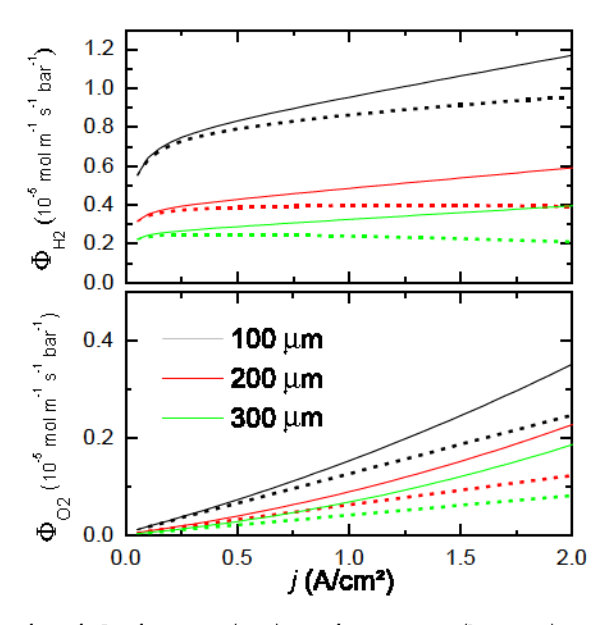


Figure 9.2.2: Simulated hydrogen (top) and oxygen (bottom) permeation fluxes through Nafion as a function of the current density for 80 °C and membrane thicknesses of 100 μm, 200 μm and 300 μm. A cathodic pressure of 30 bar, an anodic pressure of 1 bar and a hydration shell factor of unity were assumed for these calculations. Solid lines: Cross-permeation flux densities caused by diffusion and proton permeation. Dotted lines: Cross-permeation flux densities solely caused by diffusion.

to the overall gas permeation through Nafion:

$$\Phi_{H_2}^{drag} \approx 0.25 \ \hat{\Phi}_{H_2}^{drag} \tag{9.2.23}$$

By using the ratio of the permeation fluxes determined above, the total hydrogen and oxygen permeation fluxes through Nafion during water electrolysis can be determined. The permeation flux caused by diffusion (eq. 9.2.7) was determined, while the approximation of the ratio of the permeation fluxes (eq. ratio-permeation-fluxes) was used to describe for the contributions of the proton permeation (eq. 9.2.1):

$$\Phi_{\text{H}_2} = \Phi_{\text{H}_2}^{\text{diff}} - \left(\frac{\Phi_{\text{H}_2}^{\text{drag}}}{\Phi_{\text{H}_2}^{\text{diff}}}\right) \Phi_{\text{H}_2}^{\text{diff}}$$
(9.2.24)

In the case of oxygen, the procedure was conducted analogously (eq. 9.2.2):

$$\Phi_{\mathcal{O}_2} = \Phi_{\mathcal{O}_2}^{\text{diff}} + \left(\frac{\Phi_{\mathcal{O}_2}^{\text{drag}}}{\Phi_{\mathcal{O}_2}^{\text{diff}}}\right) \Phi_{\mathcal{O}_2}^{\text{diff}}$$
(9.2.25)

Table 9.2.2: Diffusion coefficients and solubilities of hydrogen and oxygen in water at 80 °C extracted from literature data [52, 124].

|       | $S \text{ (mol cm}^{-3} \text{ bar}^{-1})$ | $D (cm^2 s^- 1)$     |
|-------|--|----------------------|
| $H_2$ | $7.5 \times 10^{-7}$                       | $1.8 \times 10^{-4}$ |
| $O_2$ | $8.1 \times 10^{-7}$                       | $8.1 \times 10^{-5}$ |

Figure 9.2.2 shows the modeled total hydrogen and oxygen permeation flux densities in comparison to those solely caused by diffusion (eq. 9.2.29 and 9.2.38), exemplified for a PEM water electrolyzer that operates at a cathodic pressure of 30 bar and an anodic pressure of 1 bar. The increase of the permeation fluxes with the current density is caused by the partial pressure increase factor, while the proton permeation further influences the gas transport. The influence of the current on the cross-permeation fluxes of both mechanisms will be discussed in detail in Section 9.3.2. The absolute contribution of the proton permeation to the entire hydrogen permeation flux is independent of the membrane thickness. However, the thicker the membrane, the smaller is the permeation flux forced by diffusion. Thus, the relative contributions of the proton permeation to the hydrogen and oxygen cross-permeation increase with thicker membranes. This relation physically originates from the larger ratio of the proton velocity to the velocity of the gas diffusion with thicker membranes (as shown in Figure 9.2.1).

### 9.2.2 Interacting description of the permeation fluxes

Thus far, the cross-permeation fluxes caused by diffusion and that caused by proton permeation were related to one another without considering their interaction. In the following, this interaction is described by a differential equation using the assumptions introduced in Section 9.2.1.2 and 9.2.1.3. Only the gas transport through the aqueous phase is considered in this section again. Thus, under the assumption of an impermeable intermediate and solid phase, solely the interaction in the aqueous phase is considered here. The nomenclature introduced in Table 9.2.1 is not further employed, as all physical properties considered in the following refer to those of the aqueous phase in Nafion. Table 9.2.2 shows the diffusion coefficients and solubilities of hydrogen and oxygen in water that are used for the calculations presented in this section.

#### 9.2.2.1 Mathematical description of the interaction

As discussed in the last section, the diffusion leads to linear concentration profiles of hydrogen and oxygen in the aqueous phase of the PEM, while the influence of proton permeation leads to non-linear contributions. These alterations of the concentration profiles are modeled in the following. The variable *x* will be used to describe

the position in the *x*-direction of the membrane, which ranges from zero to the total membrane thickness *d*. The position at the cathode is defined as x=0, while that at the anode it is defined as x=d. As discussed in Section 9.2.1.3, mass conservation implements a constant permeation flux through the membrane that is independent of the position x in the aqueous phase of the membrane which means  $\Phi_{H_2}(x) = \Phi_{H_2}$ . A non-linear concentration profile in the membrane means that the relation

$$\frac{\Delta c}{\Delta x} = \frac{\mathrm{d}c(x)}{\mathrm{d}x} \tag{9.2.26}$$

thus far used to describe the permeation flux through the membrane in terms of Fick's law is no longer valid. Hence, the differential form of Fick's law must be used in the following

$$\Phi = -D c'(x) , (9.2.27)$$

where the deviation of c in x is abbreviated as c'(x). Using this description, the sum of the hydrogen cross-permeation flux densities (eq. 9.2.1) driven by the diffusion and the proton permeation equals

$$\Phi_{H_2} = \Phi_{H_2}^{\text{diff}} - \Phi_{H_2}^{\text{drag}} = -\hat{D}^{x} \,\hat{c}'(x) - a \,\hat{c}(x) \,, \tag{9.2.28}$$

where  $a = h \, \hat{v}_{\mathrm{H}^+}^{\mathrm{x}}(j) \, \frac{n_{\mathrm{d}}}{\lambda}$  with reference to equation 9.2.15.

In the following, the hydrogen movement in the x-direction is considered. The solution of this first-order linear ordinary differential equation equals

$$c(x) = k e^{\frac{-ax}{D}} - \frac{\Phi_{\text{H}_2}}{a} \,, \tag{9.2.29}$$

where k denotes a constant which has to be determined from the boundary conditions of the hydrogen concentration at the anode and the cathode. The concentration of hydrogen  $c^c$  at the cathode can determined by Henry's law with respect to the cathodic pressure, which was described in Section 9.1 by equation 9.1.3. The concentration of hydrogen  $c^a$  at the anode can be determined by calculating the anodic hydrogen content with equation 9.2.4. These boundary conditions are condensed in the following system of equation:

$$c^{c} = c(0) = k - \frac{\Phi_{H_2}}{\xi j} \tag{9.2.30}$$

$$c^{a} = c(d) = k e^{-\xi j d/\epsilon} - \frac{\Phi_{H_{2}}}{\xi j}$$
 (9.2.31)

$$c^{a} = \frac{p^{a}}{S_{H_{2}}} \frac{\Phi_{H_{2}}}{\Phi_{H_{2}} + \Gamma_{O_{2}}}$$
(9.2.32)

The latter equation is derived from equation 9.2.5, while the relation between the hydrogen concentration and pressure was calculated by Henry's law using the hydrogen solubility  $S_{\rm H_2}$ . Solving this system of equation yields

$$k = \frac{\Phi_{\text{H}_2}}{e^{-\xi j d/\epsilon}} \left( \frac{p^{\text{a}}}{\Phi_{\text{H}_2} + \Gamma_{\text{O}_2}} + \frac{1}{\xi j} \right)$$
(9.2.33)

$$\Phi_{\rm H_2} = -\frac{\vartheta}{2} \pm \sqrt{\frac{\vartheta^2}{4} + \frac{\Gamma_{\rm O_2} c^{\rm c} \xi j}{e^{-\xi jd/\epsilon} - 1}}$$
(9.2.34)

$$c^{a} = p^{a} \frac{\Phi_{H_{2}}}{\Phi_{H_{2}} + \Gamma_{O_{2}}}$$
 (9.2.35)

with

$$\vartheta = \Gamma_{O_2} + \frac{\xi j}{e^{-\xi jd/\epsilon} - 1} (p^a - c^c). \tag{9.2.36}$$

In the case of oxygen, the cross-permeation fluxes caused by diffusion and proton permeation both occur in the same direction from the anode to the cathode:

$$\Phi_{O_2} = \Phi_{O_2}^{\text{diff}} + \Phi_{O_2}^{\text{drag}} = -D c'(x) + a c(x)$$
(9.2.37)

The solution of this first-order linear ordinary differential equation equals

$$c(x) = \tilde{k} e^{\frac{ax}{D}} + \frac{\Phi_{O_2}}{a},$$
 (9.2.38)

where  $\tilde{k}$  denotes a constant that again has to be determined from the boundary conditions of the oxygen concentration at the anode and the cathode. The cathodic oxygen concentration is negligible, since oxygen at the cathode is catalytically reacted with hydrogen at the platinum catalyst (Section 2.1.5). Thus, the boundary conditions are described by:

$$c^{c} = 0 = c(0) = \tilde{k} + \frac{\Phi_{O_2}}{a}$$
 (9.2.39)

$$c^{a} = c(d) = \tilde{k} e^{\frac{ad}{D}} + \frac{\Phi_{O_{2}}}{a}$$
 (9.2.40)

The solution of this set of equations is:

$$\tilde{k} = -\frac{\Phi_{\text{O}_2}}{a} \tag{9.2.41}$$

$$\Phi_{O_2} = \frac{ac^{c}}{1 - e^{\frac{ad}{D}}} \tag{9.2.42}$$

#### 9.2.2.2 Concentration profiles of the gases in the aqueous phase

Thus far, the interaction of the gas permeation fluxes through the PEM during water electrolysis that is caused by diffusion and proton permeation was mathematically described. As a result, the solutions of the differential equations that describe the total permeation fluxes through the membrane were determined. Figure 9.2.3 shows the simulated concentration profile of hydrogen based on equation 9.2.29 in the aqueous phase of Nafion, exemplified for a membrane thickness of 150 µm with a cathodic pressure of 30 bar. In these calculations, the intermediate and solid phase were assumed to be impermeable, while the effective tortuosity  $\tau_{\text{eff}}$  was assumed to equal 1.5 and the hydration shell factor h was assumed to equal unity. The partial pressure increase factor was assumed to  $Y_{H_2} = 8 \text{ cm}^2 \text{ bar A}^{-1}$ , based on fits of the model to the measured anodic hydrogen content that will be presented in Section 9.3. The concentration of hydrogen at the cathode increases with higher current densities due to the partial pressure increase which is caused by the hydrogen evolution in the cathodic catalyst layer. In contrast, higher current densities decrease the concentration of hydrogen at the anode (eq. 9.2.4). The hydrogen permeation flux caused by the proton permeation leads to a slight deviation from the linear concentration profile that is caused by the hydrogen diffusion.

Figure 9.2.3 also shows the modeled concentration profile of oxygen in the aqueous phase based on equation 9.2.38, exemplified for a membrane thickness of 150  $\mu$ m at an anodic pressure of 1 bar. In Section 10.2, the operation at higher cathode than anodic pressures will be motivated based on an efficiency analysis. The partial pressure increase due to the oxygen evolution at the anode is relatively larger than that of hydrogen, since the pressure at the anode was chosen to be lower than that at the cathode. The influence of the proton permeation leads a slight deviation from the linear concentration profile that is caused by the oxygen diffusion.

#### 9.2.3 Comparison of the separated and interacting description

The aim of the following deliberations is to estimate the impact of the interaction of the gas permeation flux that are caused by diffusion and the proton permeation on the total permeation fluxes. The intermediate and solid phase are again assumed to be impermeable in order to compare the separated and interacting description of the total permeation fluxes. Figure 9.2.4 graphically illustrates the relative deviations in percent between both approaches as a function of the current density for different membrane thicknesses.

From a physical point of view, the velocity of the proton movement in relation to the velocity of diffusion driven gas movement is the decisive property for the interaction

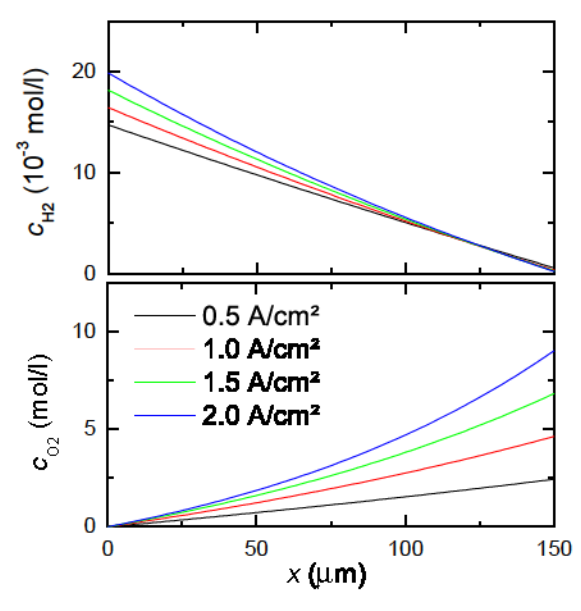


Figure 9.2.3: Modeled concentration profiles of hydrogen (top) and oxygen (bottom) in the aqueous phase of a Nafion membrane with 150  $\mu$ m thickness during water electrolysis at 80 °C for an effective tortuosity of 1.5 and hydration shell factor of unity. A cathodic pressure of 30 bar and an anodic pressure of 1 bar were assumed for these calculations.

of both gas transport mechanisms. In the case of a far slower proton movement than diffusion driven gas movement, the influence of the proton permeation on the concentration profile is negligible. However, when the velocity of the proton movement and that of the diffusion driven gas movement are of a similar scale, the proton movement can significantly contribute to the overall permeation fluxes. Hence, the interaction between gas diffusion and proton permeation increases with a higher ratio of the velocity of the proton movement to that of the diffusion driven gas movement (compare Figure 9.2.1). Thus, the deviations increase toward thicker membranes and higher current densities. The ratio of the velocities was estimated to be higher for oxygen compared to hydrogen, which means that the impact of the proton permeation on the entire oxygen permeation flux is higher than that in the case of hydrogen. Accordingly, the interaction between gas diffusion and proton permeation is estimated to be larger for the oxygen cross-permeation than that for hydrogen cross-permeation.

Thus far, the hydrogen and oxygen permeablities of the intermediate and solid phase were neglected. In Chapter 7, the hydrogen permeation through the aqueous phase was assumed to be responsible for  $25 \pm 7\%$  of the overall permeability of Nafion. Accordingly, the impact of the interaction thus far described on the overall permeability has to be multiplied by the same factor. As a result, the interaction of

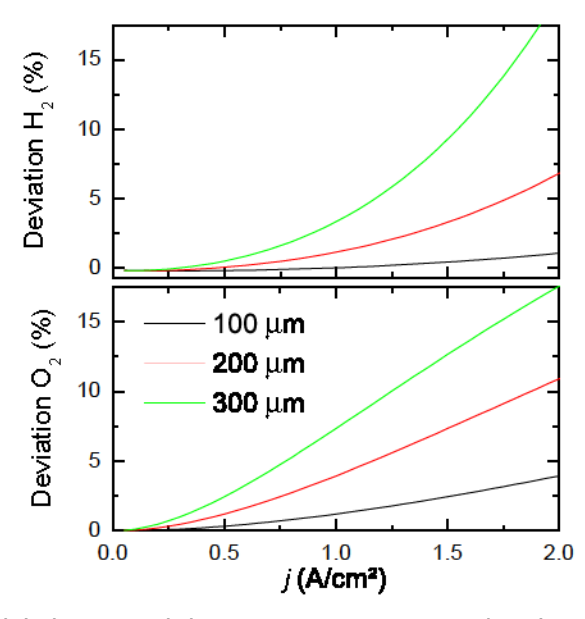


Figure 9.2.4: Modeled percental deviations of the separated and interacting description of the gas transport in the aqueous phase of Nafion during water electrolysis at 80 °C. A tortuosity of 1.5 and a hydration shell factor of unity were assumed for these calculations. Top: Deviations of the hydrogen cross-permeation fluxes. Bottom: Deviations of the oxygen permeation fluxes.

both transport mechanisms of at maximum 15% in the aqueous phase (displayed in Figure 9.2.4) reduces to approximately 4% when the diffusion through all the phases of Nafion is taken into account.

# 9.3 Anodic hydrogen content

Thus far, the hydrogen and oxygen permeation fluxes through the PEM and the partial pressure increase in the electrodes that is caused by the gas evolution were described by a physical model. The anodic hydrogen content was characterized by equation 9.2.4, assuming that hydrogen is neither electrochemically oxidized nor catalytically reacted at the anodic iridium oxide catalyst. This assumption is experimentally examined in the following. Thereafter, measurements of the anodic hydrogen content of a water electrolyzer are presented. By fits of equation 9.2.4 to this experimental data, the partial pressure increase factor of hydrogen and the hydration shell factor are estimated. In the case of the interacting description, the permeation flux through the solid phase of Nafion was neglected. Compared to the interacting description of the gas cross-permeation, the separated approach has the advantage that the measured macroscopic permeability (that was stated in Chapter 6) can be used for the calcula-

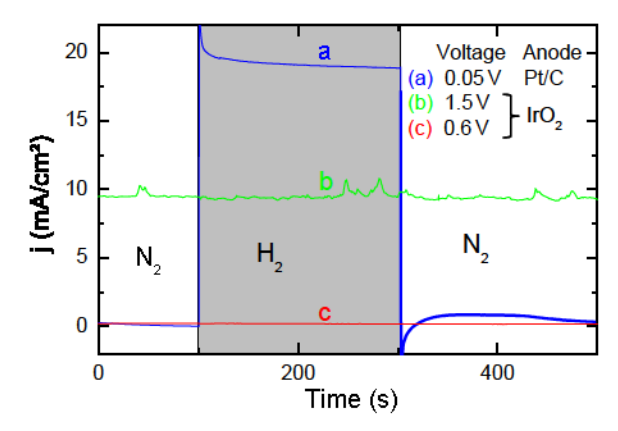


Figure 9.3.1: Current densities of an electrochemical hydrogen pump as a function of time [45]. Further explanations of the experimental setup are given in the text. Either a platinum catalyst (blue line) or an iridium oxide catalyst (red and green line) was employed at the anode. The anode was purged either with humidified nitrogen or humidified hydrogen. The time with hydrogen supply at the anode is shaded grayish. At a voltage of 1.5 V, the measured current of approximately  $10\,\mathrm{mA/cm^2}$  corresponded to the electrolysis of water.

tion of the diffusion driven cross-permeation. Hence, the solution of the separated approach to calculate the gas permeation fluxes (eq. 9.2.24 and 9.2.25) is used in this section. To calculate the contributions of the proton permeation to the gas crossover, the assumptions used in Section 9.2.1 were used.

#### 9.3.1 Hydrogen oxidation at the anodic catalyst

In order to examine if hydrogen is oxidized at the anodic iridium oxide (IrO<sub>2</sub>) catalyst, a PEM water electrolysis cell with an IrO<sub>2</sub> catalyst on one side and a carbon supported platinum catalyst (Pt/C) on the other side of the membrane was employed. This cell was operated as an electrochemical hydrogen pump [220], where hydrogen is oxidized at the anode. At the cathodes, hydrogen is evolved. Voltages of 0.05, 0.6 or 1.5 V were applied to the electrodes. The anode (the positive pole) was purged either with humidified hydrogen or with humidified nitrogen, while the cathode (the negative pole) was purged with humidified hydrogen. A current between the electrodes can result when hydrogen can be oxidized at the anodic catalyst. The current that resulted from the electrochemical reactions at the electrodes was measured. A detailed description of the setup is presented in the attachment (Section 4.4).

Figure 9.3.1 shows the measured current densities of three different variations of the setup, which are explained in the following. (a): The Pt/C catalyst layer acted as

anode with an applied DC voltage of  $0.05\,\mathrm{V}$ . By purging with nitrogen, a DC-current below  $0.5\,\mathrm{mA/cm^2}$  was measured, while purging with hydrogen yielded a current density of about  $18\,\mathrm{mA/cm^2}$ . This current can be attributed to the electrochemical oxidation of hydrogen at the anode and the reduction of protons at the cathode. (b): The voltage and gas supply was switched, so that the  $\mathrm{IrO_2}$  side acted as anode. A voltage of  $0.6\,\mathrm{V}$  was applied. Again, the anode was purged with either hydrogen or nitrogen, while the measured current stayed constant below  $0.5\,\mathrm{mA/cm^2}$ . (c): A voltage of  $1.5\,\mathrm{V}$  was applied to the same setup in order to simulate electrolysis potentials. Due to electrolysis, a current of approximately  $10\,\mathrm{mA/cm^2}$  was measured, independent whether the anode was purged with hydrogen or nitrogen. With reference to these measurements, significant hydrogen oxidation at the anodic  $\mathrm{IrO_2}$  catalyst could not be observed.

To explain why hydrogen is oxidized at the platinum catalyst but not at the iridium oxide catalyst, the mechanism of the hydrogen oxidation reaction is in the following considered in more detail. When hydrogen is oxidized at a catalyst, first hydrogen molecules must be adsorped at the catalyst [55]. Second, the hydrogen molecules are decomposed to hydrogen atoms, which are still adsorped on the surface of the catalyst [55]. Third, these hydrogen atoms leave their electrons at the catalyst and are dissolved as protons in the electrolyte [55]. Boodts et al. [221] reported that iridium oxide is a catalyst for the hydrogen evolution reaction, where the oxide can be at its surface electrochemically reduced to a metallic side. However, he also reported, that this reduction does not take place by hydrogen dissociation. Thus, hydrogen cannot be electrochemically oxidized at the iridium oxide catalyst. Using cyclic voltammetry, McIntyre et al. [222] observed that during potential alteration of an iridium oxide film from 0.25 V to 1.25 V (vs the reversible hydrogen electrode) the oxidation state of iridium oxide is changed between 3+ and 4+. Thus, in this potential region iridium oxide catalysts are always covered by oxide layers. At the higher anodic potentials during water electrolysis the catalyst is also oxidized, so that a metallic side for the adsorption of hydrogen on its surface is consequently also not available. As a result, hydrogen cannot be oxidized at the iridium oxide catalyst during water electrolysis. The catalytic reaction of hydrogen and oxygen also requires the simultaneous adsorption of both molecules or atoms on the surface of the catalyst. Consequently, the conclusions drawn based on the electrochemical measurements also mean that the chemical catalytic reactions of hydrogen and oxygen on the iridium oxide catalyst also does not occur.

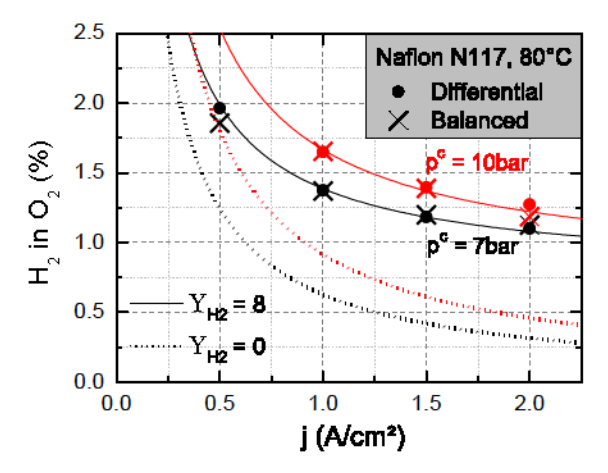


Figure 9.3.2: Anodic hydrogen content of an electrolysis cell operated at 80 °C and equipped with a Nafion N117 membrane. Cathodic pressures at the gas outlet of either 7 bar (black) of 10 bar (red) were applied. Points: Measurements at differential pressure operation with atmospheric anodic pressure. Crosses: Measurements at balanced pressure operation. Solid lines: Simulated anodic hydrogen content for  $Y_{\rm H_2} = 8\,{\rm cm}^2\,{\rm bar}\,{\rm A}^{-1}$ . Dotted lines: Simulated anodic hydrogen content for  $Y_{\rm H_2} = 0\,{\rm cm}^2\,{\rm bar}\,{\rm A}^{-1}$ . A hydration shell factor of h=0 was assumed for all the calculations graphed in this figure.

#### 9.3.2 Experimental evaluation of the model

In the following, measured anodic hydrogen contents of an operating PEM water electrolysis cell are presented and compared to the calculated anodic hydrogen contents using equation 9.2.4. The cell was operated with a Nafion N117 membrane. The measurements were conducted by applying absolute pressures of 7 bar or 10 bar at the cathodic gas outlet. At the anodic gas outlet, balanced or atmospheric pressure was used. To determine the anodic hydrogen content the K1550 gas analyzer which measured the heat conductivity in the anodic exhaust gas was used, while further information on the experimental setup are given in Section 4.4 and 4.4. The calculations were first conducted with a negligible hydration shell factor (h=0), while in Section 9.3.2.2 the influence of the hydration shell factor on the anodic hydrogen content is discussed in detail. (see Section 4.4 for further experimental information).

#### 9.3.2.1 Influence of the cathodic partial pressure increase factor

Figure 9.3.2 shows the measured and calculated anodic hydrogen content as a function of the current density for a hydration shell factor of h=0. Within the measurement precision, balanced pressure and differential pressure led to equal anodic hydrogen contents, confirming the results of Chapter 6, where differential pressure was shown

Table 9.3.1: Numeric values of the parameters that were used to calculate the anodic hydrogen content. (a): Obtained by the fits in Figure 9.3.2. (b): Estimated based on equation 9.1.5. (c): Data from Chapter 6.

| Gas   | $Y(\frac{bar cm^2}{A})$ | $\varepsilon (10^{-11} \frac{\text{mol}}{\text{cm s bar}})$ |
|-------|-------------------------|---|
| $H_2$ | 8 <sup>a</sup>          | 5.31 <sup>c</sup>   |
| $O_2$ | 9.6 <sup>b</sup>        | 2.26 <sup>c</sup>   |

to negligibly influence the gas permeation through Nafion. The only parameter of the model that was fitted to the measurements is the partial pressure increase factor  $Y_{H_2}$  (Section 9.1), while the thickness of the membrane d and the hydrogen permeability  $\varepsilon_{H_2}$  were determined experimentally (Chapter 6). Table 9.3.1 displays all the parameters used for the calculation of the anodic hydrogen content.

As discussed in Section 9.1, the partial pressure inside the cathodic catalyst layer increases proportionally to the current density. In Figure 9.3.2, the influence of the partial pressure increase factor on the anodic hydrogen content is illustrated. When the partial pressure increase in the electrodes is neglected, the measured and modeled data deviate by a factor of approximately two at  $2\,\mathrm{A\,cm^{-2}}$ . With a value of  $Y_{\mathrm{H}_2} = \mathrm{bar\,cm^2\,A^{-1}}$ , the modeled and measured values of the anodic hydrogen content agreed within the measurement precision. At  $2\,\mathrm{A/cm^2}$ , the estimated cathodic partial pressure increase by 16 bar leads to a significant higher cathodic pressure than at the cathodic gas outlet. Hence, the partial pressure increase factor strongly influences the hydrogen diffusion through the PEM during water electrolysis.

#### 9.3.2.2 Influence of the proton permeation

Thus far, the influence of the proton permeation and the accompanied electro-osmotic water drag on the modeled anodic hydrogen content was neglected by assuming a hydration shell factor of h=0. In the following, this effect and its contributions to the anodic hydrogen content are examined. In Section 9.2.1, the hydrogen and oxygen permeation fluxes caused by the proton permeation were physically described without considering their interaction. The deviations of the hydrogen cross-permeation fluxes by the separated and interacting description were estimated to approximately 2 % for a membrane thickness of 200  $\mu$ m and current densities up to 2 A/cm² (Section 9.2.3 and with reference to the additional influence of the intermediate and solid phase on the overall permeability). With respect to these low differences, the interaction between hydrogen diffusion and proton permeation is neglected in this section by using the separated approach to describe the permeation fluxes. Figure 9.3.3 shows fits of the anodic hydrogen content for various values of the hydration shell factor. The deviations of the fit from the experimental data increase toward higher values of the hydration shell factor h (Figure 9.3.3).

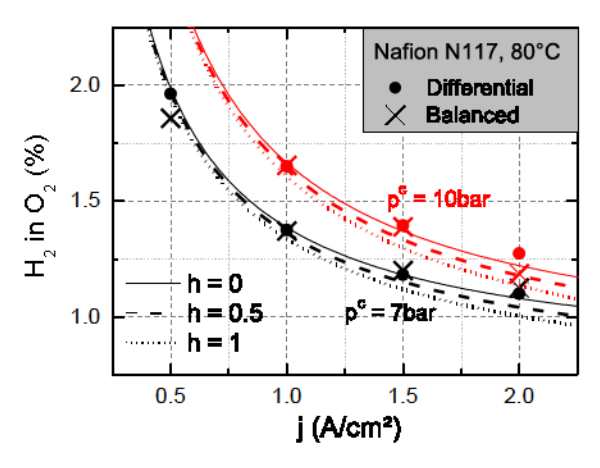


Figure 9.3.3: Points, crosses, and color code: Same notation as in Figure 9.3.2. The different design of the lines correspond to hydration shell factors h of 0, 0.5, or 1.

In the case of diffusion and small anodic hydrogen contents, the hydrogen cross-permeation flux density as a function of  $p_{\rm H_2}^{\rm c}$  can be described by the linear approximation in the form of equation 9.2.9. As discussed in Section 9.1, the partial pressure increase by the hydrogen evolution is proportional to the current density. To summarize, the pressure increase by the hydrogen evolution in the cathode affects the diffusion driven hydrogen cross-permeation proportionally to the current density:

$$\Phi_{\rm H_2}^{\rm diff} \propto Y_{\rm H_2} \, j \tag{9.3.1}$$

The hydrogen cross-permeation flux density caused by the proton permeation was calculated in Section 9.2.1.2 to

$$\Phi_{\rm H_2}^{\rm drag} \propto \bar{c}_{\rm H_2} j , \qquad (9.3.2)$$

while the mean concentration  $\bar{c}_{\rm H_2}$  inside the PEM was approximated by the concentration difference at both sides of the PEM. Assuming again a negligible anodic hydrogen content, the cathodic hydrogen concentration is based on Henry's law (eq. 2.1.15) proportional to the partial hydrogen pressure inside the cathodic catalyst layer (eq. 9.1.3). As a result, the hydrogen cross-permeation flux density caused by the proton permeation shows a linear and a quadratic term:

$$\Phi_{\rm H_2}^{\rm d\,rag} \propto p^{\rm c} \, j + Y_{\rm H_2} \, j^2 * k \,,$$
 (9.3.3)

where k denotes a proportionality constant. Figure 9.3.4 illustrates the hydrogen cross-permeation flux densities as a function of the current density for different values of the hydration shell factor, showing the influence of the linear and quadratic

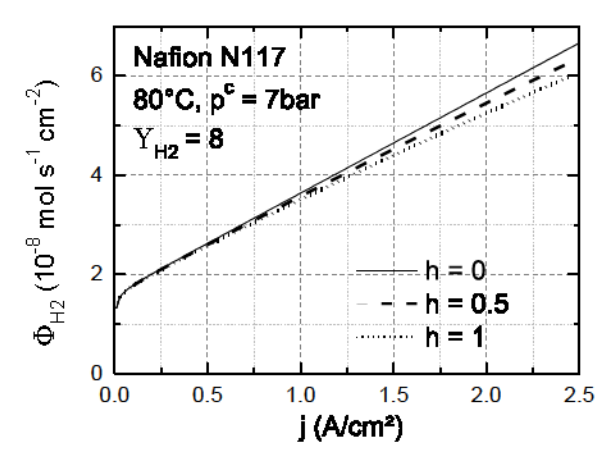


Figure 9.3.4: Modeled hydrogen cross-permeation fluxes for the fits to the cathodic pressure of 7 bar in Figure 9.3.3. The same notation as in Figure 9.3.3 is used.

term. Towards high current densities the influence of the quadratic term increases. As a result, the influence of the proton permeation on the hydrogen diffusion increases so that towards. To summarize, the contributions of the quadratic term that describes the influence of the proton permeation on the hydrogen cross-permeation fluxes are responsible for the decreasing precision of the fits towards higher values of h and higher current densities. The measured and calculated anodic hydrogen content agreed best at negligible values of the hydration shell factor h. However, within the measurement precision, the occurrence of contributions of the proton permeation to the hydrogen permeation through the PEM during water electrolysis cannot excluded. Small values of the hydration shell factor mean that the amount of hydrogen dissolved within the hydration shell of protons is negligible.

#### 9.3.3 High-pressure electrolysis

In the following, the model for the gas-crossover presented above is exemplified for a cathodic pressure of 30 bar during water electrolysis, as motivated in the beginning of this chapter. In these calculations, the permeability of Nafion and the partial pressure increase factors stated in Table 9.3.1 and a hydration shell factor of zero are used. Figure 9.3.5 shows the modeled anodic hydrogen contents at absolute cathodic pressures of 1 bar and 30 bar for different membrane thicknesses. When thicker membranes are employed, the hydrogen cross-permeation caused by the diffusion decreases (Fick's law), leading to smaller anodic hydrogen contents. At higher current densities, the increased oxygen production rate leads to a decreasing anodic hydrogen content (eq 9.2.4). As discussed in Section 9.3.2, the anodic hydrogen content is independent

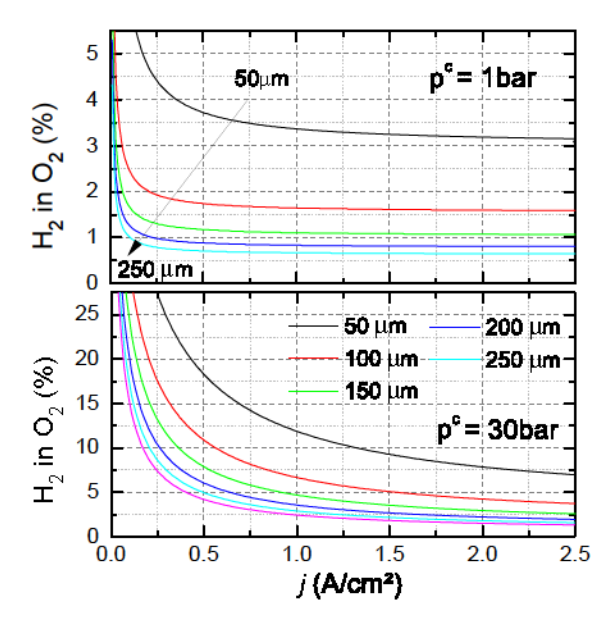


Figure 9.3.5: Modeled anodic hydrogen content (eq 9.2.4) for membrane thicknesses from 50  $\mu$ m to 250  $\mu$ m and a cathodic partial pressure increase factor of  $Y_{\rm H_2} = 8\,{\rm cm}^2\,{\rm bar}\,{\rm A}^{-1}$ . Top: Cathodic pressure of 1 bar. Bottom: Cathodic pressure of 30 bar.

of the anodic pressure. At partial load operation below  $0.5\,\mathrm{A/cm^2}$ , the safety limit of  $2\,\%$  hydrogen in oxygen was estimated to be significantly exceeded for PFSA membranes of up to  $250\,\mu\mathrm{m}$ . A further decrease of the anodic hydrogen content can be achieved by thicker membranes. However, in the next chapter thicker membranes will be shown to reduce the efficiency. By using catalytic recombination of hydrogen and oxygen in recombination reactors as discussed in Section 2.1.5, the safety threshold of hydrogen in the anodic compartment could be fulfilled even at high cathodic pressures.

# 9.4 Synopsis of the chapter

In this chapter, the hydrogen and oxygen cross-permeation fluxes during PEM water electrolysis were modeled, including the driving forces of diffusion and proton permeation. Both gas transport mechanisms were physically described by a simple separated approach and a more complex model that includes their interaction. Diffusion leads to a linear concentration profile of the gases in the membrane, while the influence of proton permeation was modeled to lead to non-linearity of these concentration profiles. The interactions between both gas transport mechanisms and their

influence on the concentration profile were described by differential equations. The deviations between the separated and interacting model description for the gas crossover were calculated to be smaller than 4%. The influence of the proton permeation on the anodic hydrogen content during water electrolysis was evaluated by fits to *inoperando* measurements. The calculated contributions of the proton permeation onto the anodic hydrogen content decreased the fit precision and were thus estimated to be negligible. This behavior was ascribed to a negligible amount of dissolved hydrogen in the hydration shell of the protons. The gas permeation through the intermediate and solid phase are independent of the interaction of gas diffusion and proton permeation in the aqueous phase. Their high impact on the overall permeability of Nafion was also identified as a reason for the small effect of the proton permeation in the aqueous phase on the overall gas crossover.

Besides the interaction of the transport mechanisms, the anodic hydrogen content was used to evaluate the cathodic partial pressure increase that is caused by the hydrogen evolution. The cathodic partial pressure increase was derived to affect the anodic hydrogen content as a function of the current density by a different power law dependency than the interaction between the proton permeation and the hydrogen diffusion. Accordingly, the cathodic partial pressure increase could be quantified by fits to the measured anodic hydrogen content and was shown to have a significant impact. Finally, the calculation of the anodic hydrogen content during PEM water electrolysis with Nafion membranes was exemplified for a cathodic pressure of 30 bar and for membrane thicknesses up to 250  $\mu$ m. In this case, the safety threshold of 2% hydrogen in the anodic exhaust gas was estimated to be exceeded at current densities below 1 A/cm<sup>2</sup>.

# 10 Efficiency of pressurized water electrolysis

The aim of this chapter is to physically describe the efficiency loss  $1-\eta$  that is caused by gas crossover, ohmic resistances and pressurized gas evolution during PEM water electrolysis. A physical model is presented which is used to optimize the membrane thickness with regard to the cell efficiency. In analogy to the previous chapter, the physical properties of Nafion® at 80 °C are considered in this chapter, while the modeled efficiency losses are exemplified for cathodic pressures of 1 bar and 30 bar. The calculations in this chapter are conducted using the separated description of gas diffusion and proton permeation which was introduced in the previous chapter. Safety issues related to high anodic hydrogen contents (Section 9.3.5) are assumed to be eliminated by external catalytic recombination reactors (see Section 2.1.5 for details). The efficiency of pressurized water electrolysis electrolysis and that of atmospheric pressure operation in combination with subsequent mechanical compression are compared. This chapter is based on previously published studies [45, 210, 211].

#### 10.1 General remarks and reaction kinetics

In Section 2.1.2, the influence of kinetic overvoltages on the cell voltage during water electrolysis was discussed. Thanks to the additive behavior of the different overvoltages that influence the cell voltage (eq. 2.1.24) their contributions to the voltage efficiency can be considered separately. Kinetic overvoltages depend on the catalysts, their surfaces and the structures of the catalyst layers. These properties are not within the scope of this research and thus kinetic overvoltages are neglected in the following. The reaction kinetics neither influence the gas crossover nor the ohmic drop in the membrane. Thus, by excluding kinetic overvoltages the parameters to describe the influence of the transport properties of the PEM on the cell efficiency are reduced to a minimum. As a result, the electrode design and the choice of catalyst do not affect the modeled efficiency loss that is presented in this chapter. If desired, kinetic overvoltages can be easily added to the model as discussed later. The Ohmic drop of the electron and proton conduction in the electrodes is also neglected for the model presented in the following, as these parameters only negligibly contribute to the overall cell efficiency. With reference to the dynamic load operation of water electrolysis that is required for the operation in combination with intermittent renewable energies, the current density is considered as the most important operation parameter. Hence, the current density is taken as the abscissa for all graphical illustrations of the modeled efficiency loss. Other properties as the current density are taken as constant parameters with exemplified variations.

Hence, the choice of the membrane thickness is a decisive parameter for the cell efficiency as it affects both, voltage and current efficiency.

# 10.2 Cell efficiency and membrane thickness optimization

In an acidic PEM water electrolyzer, the current efficiency is dominated by the cross-permeation of hydrogen and oxygen through the membrane (Section 2.1.4). Moreover, the proton conduction through the PEM also leads to an ohmic drop which reduces the voltage efficiency. The hydrogen and oxygen cross-permeation fluxes are proportional to the inverse membrane thickness (Fick's law), while the ohmic drop due to the proton conduction is proportional to the membrane thickness (Ohm's law). Hence, to optimize the cell efficiency a compromise between the current loss (dominated by the hydrogen and oxygen cross-permeation fluxes) and ohmic loss (dominated by the ohmic resistance of the membrane) must be found by a variation of the membrane thickness. This membrane thickness optimization is further a function of the parameters that will be discussed in Section 10.2.3.

#### 10.2.1 Model

In Section 2.1.4, the current efficiency was described as a function of the cell current I and the current loss  $I_{loss}$ . By normalizing these currents to the cell area, the current efficiency can be expressed as:

$$\eta_{\rm C} = 1 - \frac{j_{\rm loss}}{j_{\rm E}} \tag{10.2.1}$$

The current loss was mainly ascribed to the hydrogen and oxygen permeation through the PEM (Section 2.1.4). Oxygen that permeates through the membrane was assumed to be electrochemically reduced or catalytically reacted with hydrogen forming mainly water (Section 2.1.4). Thus, oxygen that permeated to the cathode consumes twice the amount of hydrogen. By using Faraday's law (eq. 4.2.6), the current densities of the latter equation can be expressed as function of the hydrogen and oxygen permeation flux densities ( $\Phi_{\rm H_2}$  and  $\Phi_{\rm O_2}$ ) and the hydrogen production rate density ( $\Gamma_{\rm H_2}$ ). Accordingly, the latter equation can be rewritten as:

$$\eta_{\rm C} = 1 - \frac{\Phi_{\rm H_2} + 2\Phi_{\rm O_2}}{\Gamma_{\rm H_2}} \tag{10.2.2}$$

The factor of two in the latter term takes the water formation at the cathodic catalyst into account, where two hydrogen molecules are consumed by each oxygen molecule that permeates through the membrane.

The voltage efficiency was discussed in Section 2.1.4. By neglecting kinetic overvoltages, the voltage efficiency is a function of the Nernst voltage  $U_N$  and the ohmic drop  $U_{\Omega}$ :

$$\eta_{\rm U} = \frac{U_{\rm ref}}{U_{\rm N} + U_{\rm O}} \tag{10.2.3}$$

The reversible voltage under standard ambient pressure and temperature serves as reference voltage  $U_{\rm ref}$ . Within this definition, the thermodynamic work of the pressurized hydrogen evolution under pressure (Section 2.5) describes an efficiency loss. This definition of the efficiency normalized to the standard temperature and pressure enables the comparison of different compression techniques that operate at different temperatures. The partial pressure increase in the electrodes (Section 9.1) consequently increase the local pressures at the catalysts and thus also the Nernst voltage. Moreover, the ohmic drop increases linearly toward higher current densities. As a result, the voltage efficiency decreases toward higher current densities. In contrast, the current efficiency increases toward higher current densities. The efficiency loss  $1-\eta$  of the cell (without kinetic overvoltages) is finally calculated by:

$$1 - \eta = 1 - \eta_{\rm U} \, \eta_{\rm C} \tag{10.2.4}$$

#### 10.2.2 Balanced and differential pressure operation

PEM water electrolysis can be conducted at balanced anodic and cathodic pressures or at differential pressures, where a higher cathodic than anodic pressure is applied. The aim of this section is to compare the efficiency of both operation conditions. Figure 10.2.1 shows the modeled cell efficiency loss at a cathodic pressure of  $p^c = 30$  bar with balanced pressure operation ( $p^a = 30 \, \text{bar}$ ) and with differential pressure operation ( $p^a = 1$  bar). At balanced pressure, the higher anodic partial pressure of oxygen than at differential pressure leads to a higher oxygen cross-permeation rate (eq. 9.2.10). As a result, the efficiency at balanced pressure operation was modeled to be smaller than that at differential pressure operation. Moreover, the pressurized oxygen evolution at balanced pressure operation leads to a higher Nernst voltage (eq. 2.1.16) compared to the oxygen evolution at differential pressures. Oxygen evolution at 30 bar thermodynamically requires approximately 30 mV more than at 1 bar (eq. 2.1.16), which is in relation to the other efficiency losses negligible. Hence, mainly the larger oxygen cross-permeation is responsible for the higher efficiency loss of balanced pressure operation compared to that at differential pressures. An advantage of higher anodic pressures is the lower percental water content of the anodic exhaust

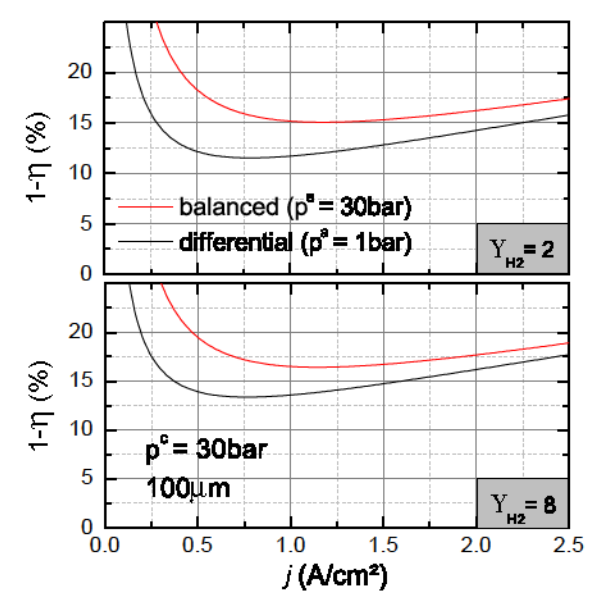


Figure 10.2.1: Modeled efficiency loss for 30 bar balanced (red) and differential (black) pressure operation and a membrane thickness of 100  $\mu m$ . Top:  $Y_{H_2}=2\,cm^2\,bar\,A^{-1}$ . Bottom:  $Y_{H_2}=8\,cm^2\,bar\,A^{-1}$ 

gas (as described by equation 9.1.4), which is especially relevant for the heat balance of the cell [217]. In the following, operation at differential pressures is considered, as this is typically more efficient than operation at balanced pressures.

### 10.2.3 Influence of parameters

The aim of this Section is to exemplarily consider the efficiency loss  $(1 - \eta)$  that is caused by the pressurized gas evolution, ohmic drop and gas cross-permeation of a PEM water electrolysis cell under variation of the operation parameters. Figure 10.2.2 shows the modeled efficiency loss for the following set of parameters:

- Current densities from 0 to 2A cm<sup>-1</sup>.
- Atmospheric anodic pressure.
- Either atmospheric or 30 bar cathodic pressure.
- Various membrane thicknesses from 50 μm to 250 μm.
- $\bullet$  Two different values of the partial pressure increase factor (Y  $_{H_2}=2\,cm^2\,bar\,A^{-1}$  and Y  $_{H_2}=8\,cm^2\,bar\,A^{-1}$ )

These parameters affect the efficiency loss as follows:

Effect of current density - The efficiency loss due to gas crossover dominates at small

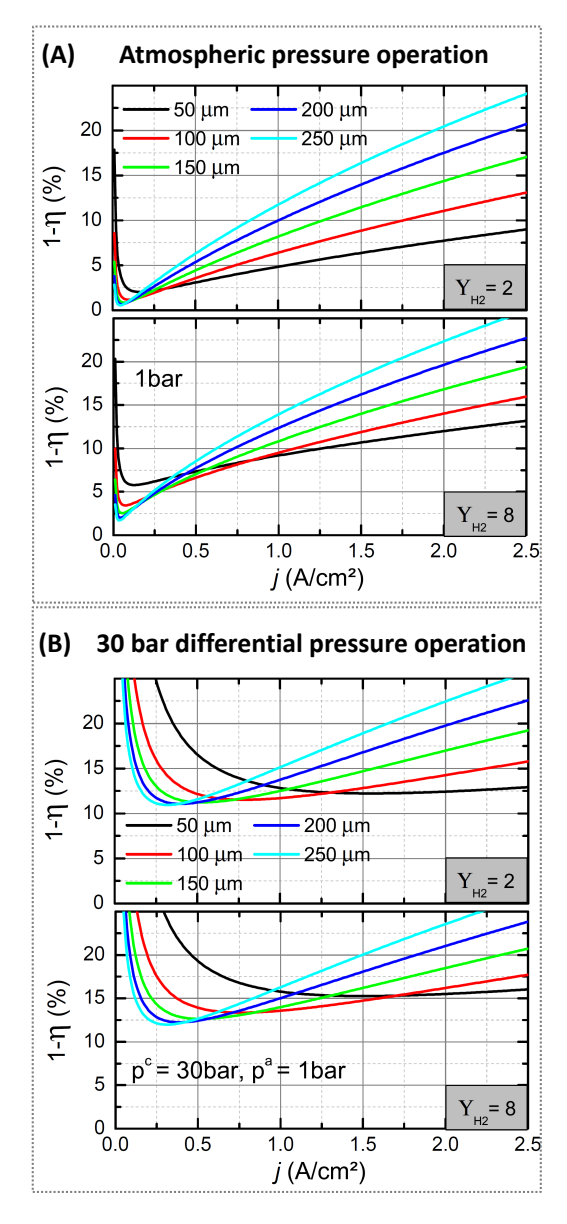


Figure 10.2.2: Modeled efficiency loss that is caused by gas crossover, pressurized gas evolution and the ohmic drop of the PEM. Top: Atmospheric pressure operation Bottom: 30 bar differential pressure operation. The efficiency loss was modeled for two different partial pressure increase factors ( $Y_{\rm H_2}=2\,{\rm cm^2\,bar\,A^{-1}}$  and  $Y_{\rm H_2}=8\,{\rm cm^2\,bar\,A^{-1}}$ ), as indicated in the plots, respectively. The efficiency loss was calculated for membrane thicknesses from  $50\,\mu m$  to  $250\,\mu m$  as indicated by the color code in the legend.

current densities. Negative slopes of tangentials to the efficiency loss as a function of the current density are a result of the gas crossover. The ohmic drop is dominant towards higher current densities where it leads to positive slopes of tangentials to the curves

**Effect of pressures -** Higher pressures increase the gas crossover and the Nernst voltage, as later discussed in Section 10.3.3 in detail. At a cathodic pressure of 30 bar, the efficiency loss that is caused by the hydrogen cross-permeation is especially at low current densities significantly higher than at atmospheric pressure operation.

Effect of membrane thickness - Thicker membranes reduce the hydrogen and oxygen cross-permeation but lead to increased cell resistances. In the case of the pressurized operation with a cathodic pressure of 30 bar a membrane thickness of approximately  $100\,\mu m$  was modeled to show on the average the highest efficiency with respect to the overall dynamic load range. In the case of atmospheric pressure operation, a membrane thickness of  $50\,\mu m$  or less was modeled to yield the highest efficiency.

**Effect of partial pressure increase factor -** Higher values of the partial pressure increase factors increase the Nernst voltage and the gas crossover. Consequently, this parameter influences both, current and voltage efficiency.

Besides the operation parameters and the partial pressure increase of the electrodes, the conductivity and permeability of the membrane are decisive for the considered efficiency loss. A higher proton conductivity of the membrane reduces the ohmic drop while lower hydrogen and oxygen permeabilities reduce the gas crossover. The membrane thickness is thus the control variable that adjust the ratio of ohmic losses to the losses that are caused by the gas crossover. The higher the ratios of the proton conductivity  $\kappa$  to the hydrogen and oxygen permeabilities, the more efficient the cell can be operated. Hydrocarbon membranes as those presented in Section 8 showed approximately two times higher ratios of proton conductivity to hydrogen permeability and thus could significantly increase the efficiency in comparison to the operation with Nafion<sup>®</sup> membranes.

# 10.3 Pressurized electrolysis *vs.* subsequent compression

In Figure 10.2.2, the gas-crossover at a cathodic pressure of 30 bar significantly increased the calculated efficiency loss. In general, higher cathodic pressures mean that thicker membranes are useful to reduce the hydrogen cross-permeation and its impact on the current efficiency. These thicker membranes are accompanied by higher area resistances (Section 2.1.2) that consequently reduce the voltage efficiency. Thus,

toward higher operating pressures the optimal membrane thickness increases. As a result, voltage efficiency and current efficiency decrease. The aim of the following deliberations is to compare the efficiency of pressurized water electrolysis to that of atmospheric pressure operation in combination with subsequent mechanical compression.

# 10.3.1 Details of the comparison

As discussed in Section 2.5, mechanical compression is typically of an isentropic character. The relation of the energy consumption of isentropic processes in comparison to that of isothermal processes is discussed in the attachment in detail (Section 14.5). Mechanical compressors with ionic liquid pistons are commercially available and achieve nearly isothermal compression [223]. Using such a commercially available devise, an energy consumption of 2.7 kWh to compress one kilogram of hydrogen from 5 bar to 900 bar was reported [223]. The temperature of the gas during the compression by the ionic liquid piston compressor was not reported and is assumed as 30 °C for the following deliberations. Based on equation 2.5.5, isothermal compression over the same pressure range as considered above but at 80 °C (conditions during PEM water electrolysis) requires thermodynamically approximately the same energy <sup>1</sup>. Accordingly, isothermal compression at 80 °C (that represents the temperature during water electrolysis) requires approximately the same amount of energy as the real energy consumption of the mechanical compression. Thermodynamically, the work required for isothermal compression is proportional to the temperature (eq. 2.5.4). With reference to the same pressure difference, isothermal compression at 30 °C requires 86 % of the thermodynamic work that is required to isothermally compress an ideal gas at 80 °C (eq. 2.5.4). Normalized to the isothermal process at 30 °C assumed for the subsequent isothermal compression, the energy consumption of the ionic liquid compressor discussed above means a compressor efficiency of 86 %.

When an ideal gas with a pressure of 30 bar at 80 °C is cooled to 30 °C, its pressure reduces to 25.75 bar (with reference to the ideal gas law in the form of equation 2.5.1). Hydrogen and oxygen produced by PEM water electrolysis are saturated with water vapor (Section 9.1). By cooling of the humidified hydrogen produced by water electrolysis, the decrease of the saturated vapor pressure (eq. 4.2.3) leads to the condensation of water which consequently also reduces the total pressure (eq. 4.2.4). In order to avoid the pressure decrease of the produced hydrogen by cooling, the vessel where the hydrogen gas is cooled can be connected to the cathodic gas outlet of the electrolysis cell. Thereby, the produced hydrogen can instantaneously balance

<sup>&</sup>lt;sup>1</sup>The energy consumption of the isothermal compression process was calculated by equation 2.5.5. The compressibility factor (eq. 2.5.6) was calculated based on the mole density of hydrogen reported in the NIST database [126] and equation 2.5.2.

the pressure decrease that is caused by the cooling process. By using this setup, the pressure of the produced hydrogen may be maintained during the cooling procedure. In order to compare the efficiency of pressurized water electrolysis with subsequent compression two different cases are considered in the following:

- 1. Water electrolysis at a cathodic pressure of 30 bar without any further compression.
- 2. A cathodic pressure of 1 bar and subsequent isothermal compression at  $30\,^{\circ}$ C to  $30\,\text{bar}$  with a compression efficiency of either  $100\,\%$ ,  $90\,\%$ ,  $80\,\%$ , or  $70\,\%$ .

In both cases the final temperature of the produced hydrogen gas is assumed as  $30\,^{\circ}\text{C}$ , while a pressure decrease of the cooling procedure is avoided as discussed above. The operating temperature of the water electrolysis cell is assumed as  $80\,^{\circ}\text{C}$ . Atmospheric anodic pressures and the conductivities and permeabilities of Nafion<sup>®</sup> membranes are used for the following calculations. Cathodic partial pressure increase factors of either two (assuming an the increase of the electrodes' porosities) or eight (as measured in Section 9.3) are considered.

The influence of the absolute pressure onto the saturated vapor pressure is negligible (below 1%) for the pressures considered here [174]. At a temperature of 80 °C, the saturated vapor pressure equals approximately 0.5 bar (eq. 4.2.3). Thus, at a pressure of 30 bar at the cathodic gas outlet of the electrolysis cell, the partial pressure of water vapor equals 1/60 of the total pressure. In the case of atmospheric pressure at the gas outlet this ratio equals one half. Accordingly, the relative amount of water which must be removed from the produced decreases towards higher cathodic pressures. The energy consumption related to this drying procedure is consequently lower for high pressure operation than for low pressure operation. Based on the model which is presented in the following, a detailed system analysis of water electrolysis including the energy consumption for the hydrogen drying can be conducted, which is however beyond the scope of the research in this thesis. Accordingly, the water content of the produced hydrogen by water electrolysis, its influence on the heat balance of the cell and the energy consumption for its drying are neglected for the following deliberations.

# 10.3.2 Energy consumption of a compressor

In order to include the energy consumption  $E_{\rm comp}$  of a subsequent isothermal compressor into the calculations of the efficiency presented in the Section 10.2, the consumed energy during subsequent compression is expressed by a voltage  $U_{\rm comp}$ :

$$U_{\rm comp} = \frac{1}{2F} E_{\rm comp} \tag{10.3.1}$$

This voltage is counted to the voltage efficiency

$$\eta_U = \frac{U_{\text{rev}}}{U_{\text{N}} + U_{\Omega} + U_{\text{comp}}}, \qquad (10.3.2)$$

while kinetic overvoltages are neglected again. The energy consumption of the compressor is related by

$$E_{\rm comp} = \eta_{\rm comp} W_{\rm comp} \tag{10.3.3}$$

to the compressor efficiency  $\eta_{\text{comp}}$  and the spend thermodynamic work  $W_{\text{comp}}$  during the compression process.

### 10.3.3 Comparison of the efficiencies

The aim of this section is to quantitatively compare the energy consumption water electrolysis at pressurized operation and atmospheric pressure operation in combination with subsequent mechanical compression. To start with, the thermodynamics of the compression processes is considered, while the contributions that are caused by ohmic drop and gas cross-permeation are neglected. Thus, this analysis is independent of the conductivity and permeability membrane and its thickness. With reference to equation 10.3.1, the thermodynamic energy consumption is expressed as a voltage, which is the sum of the Nernst voltage  $U_N$  and the voltage equivalent  $U_{comp}$  of the compressor (eq. 10.3.1). Figure 10.3.1 shows  $U_N + U_{comp}$  calculated for the cases discussed. At current density close to 0 A/cm<sup>2</sup>, the partial pressure increase in the electrodes is small and thus only slightly impacts the voltages. In this case, pressurized electrolysis is characterized by approximately the same voltages as that of atmospheric pressure operation in combination with subsequent mechanical compression. The agreement results from a similar energy consumption of the mechanical compression and that of isothermal compression during pressurized water electrolysis (see Section 10.3.1).

The partial pressure increase of the gases in the electrodes increases proportionally to the current density. As a consequence, the Nernst voltage increases logarithmically as a function of the current density. This increase of the voltage reduces toward smaller values of partial pressure increase factors (Fig. 10.3.1). Higher pressures at the gas outlets lead to a reduced percental impact of the current density on the overall pressure at the catalyst. The relative increase of the Nernst voltage that is caused by the gas evolution decreases toward higher operating pressures (Fig. 10.3.1), which can be attributed to the logarithmic dependence of the thermodynamic energy consumption of compression as a function of pressure (see Section 2.3). Thus, as further shown in Figure 10.3.1, the thermodynamical voltage of pressurized water electrolysis is at current densities above  $0.1\,\mathrm{A/cm^2}$  for  $Y_{\mathrm{H_2}} = 8\,\mathrm{cm^2\,bar\,A^{-1}}$  (0.5 A/cm² for

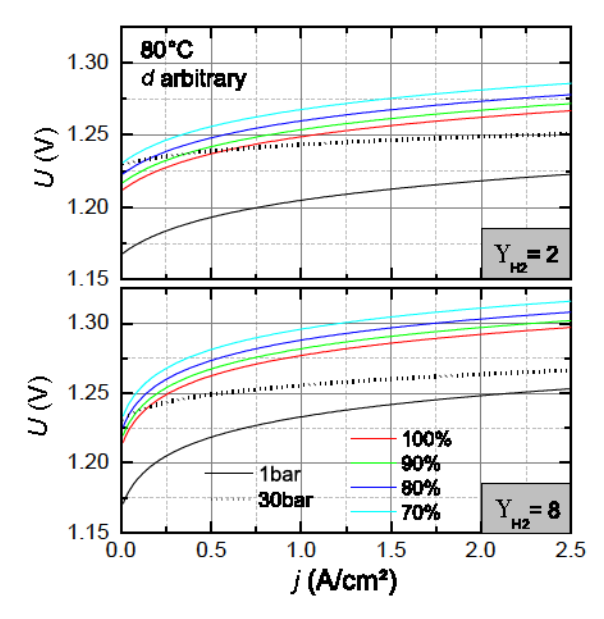


Figure 10.3.1: Sum of the modeled voltages that are caused by the pressurized gas evolution during water electrolysis and isothermal subsequent compression ( $U_{\rm N}+U_{\rm comp}$ ). Dotted black line: Modeled Nernst voltage of the direct hydrogen pressurization during water electrolysis at 30 bar cathodic pressure and atmospheric anodic pressure ( $U_{\rm comp}=0$ ). Solid black line: Modeled Nernst voltage at atmospheric pressure water electrolysis ( $U_{\rm comp}=0$ ). Colored lines: Modeled  $U_{\rm N}+U_{\rm comp}$  of atmospheric pressure water electrolysis with subsequent isothermal compression at 30 °C. The compressor efficiencies are given by color code in the legend. Top:  $Y_{\rm H_2}=2\,{\rm cm}^2\,{\rm bar}\,{\rm A}^{-1}$ . Bottom:  $Y_{\rm H_2}=8\,{\rm cm}^2\,{\rm bar}\,{\rm A}^{-1}$ .

 $Y_{\rm H_2}=2\,{\rm cm^2\,bar\,A^{-1}})$  higher than that of the atmospheric pressure water electrolysis with subsequent compression. Thus, the partial pressure increase that is caused by the gas evolution leads to lower values of  $U_N$  of pressurized water electrolysis compared to that for  $U_N+U_{\rm comp}$  of atmospheric pressure electrolysis with  $\eta_{\rm comp}=100\,\%$  over almost the entire dynamic load range. In summary, by neglecting the gas crosspermeation and the ohmic drop, the efficiency of pressurized PEM water electrolysis is higher than that of atmospheric pressure electrolysis with low-temperature isothermal subsequent compression.

The aim of the following calculations is to include the effect of gas crossover which was thus far neglected. In Section 10.2, the membrane thickness was optimized with regard to the efficiency. At 30 bar cathodic pressure and with respect to the overall dynamic load range considered, the optimum membrane thickness was estimated to  $100\,\mu\text{m}$ , whereas for atmospheric pressure water electrolysis a membrane thicknesses of  $50\,\mu\text{m}$  was modeled to optimize the efficiency. In the following, these mem-

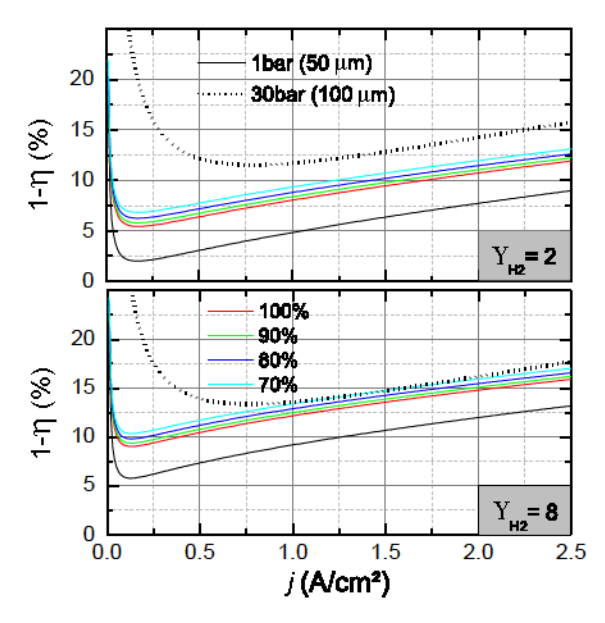


Figure 10.3.2: Comparison of the modeled efficiency loss of pressurized water electrolysis (dotted black line, membrane thickness of  $100\,\mu\text{m}$ ) to atmospheric pressure electrolysis (solid black line, membrane thickness of  $50\,\mu\text{m}$ ) in combination with subsequent mechanical compression (colored lines) of different compression efficiencies. A final pressure of  $30\,\text{bar}$  at  $30\,^\circ\text{C}$  is considered for both cases.

brane thicknesses are assumed for both operation conditions, in order to compare both operation conditions with their optimum efficiencies, respectively. Figure 10.3.2 shows the efficiency loss of pressurized water electrolysis to that of atmospheric pressure water electrolysis in combination with subsequent mechanical compression. The ohmic drop and gas cross-permeation is in the case of atmospheric pressure operation smaller than that in the case of the pressurized operation. As a result, with  $Y_{\rm H_2} = 8\,{\rm cm}^2\,{\rm bar}\,A^{-1}$  the efficiency of atmospheric pressure electrolysis with subsequent compression is at a compressor efficiency of at least 80 % (60 % for  $Y_{\rm H_2} = 2\,{\rm cm}^2\,{\rm bar}\,A^{-1}$ ) higher than that of pressurized water electrolysis over the total dynamic load range. Besides efficiency, the safety issues related to high anodic hydrogen contents can be avoided by the atmospheric electrolysis in combination with subsequent mechanical compression (Fig. 9.3.5).

In summary, the efficiency loss of pressurized electrolysis at 30 bar and 80 °C with Nafion® membranes can be undercut over the total dynamic load range by atmospheric pressure electrolysis in combination with state-of-the-art compression techniques. From a thermodynamical point of view, the isothermal compression by water electrolysis at 80 °C was discussed to lead to the same energy consumption than that by a

state-of-the-art compressor. However, the influence of the partial pressure increase in the electrodes on the Nernst voltage decreases towards higher operating pressures. As a result, without the contributions of the gas crossover, pressurized water electrolysis was shown to be more efficient than atmospheric pressure electrolysis with subsequent compression. However, the impact of the hydrogen and oxygen crossover on the efficiency is larger than the advantages of the pressurized operation. As a result, the efficiency of pressurized operation is smaller than that of atmospheric pressure operation in combination with subsequent compression (for  $Y_{H_2} = 2 \text{ cm}^2 \text{ bar A}^{-1}$ ). The modeled comparison of pressurized water electrolysis and atmospheric pressure water electrolysis with subsequent compression was sensitive to alterations of the partial pressure increase factor Y<sub>H2</sub>. Thus, this parameter significantly influences the comparative efficiency analysis of different operating pressures. The hydrogen crossover increases approximately proportional to the cathodic pressure (eq. 9.2.3). Consequently, the higher the desired hydrogen pressure, the more efficient is low-pressure electrolysis in combination with subsequent mechanical compression in comparison to the direct pressurized operation in the cell.

# 10.4 Synopsis of the chapter

In this chapter, the efficiency loss that is caused by pressurized gas evolution, proton conduction and gas crossover during PEM water electrolysis was discussed. Within this aim, an analytical model was developed, which describes the cell efficiency as a function of the current density, operating pressures, partial pressure increase factors, membrane thickness and the membrane properties in the form of the hydrogen permeability, oxygen permeability and proton conductivity. By using this model, a membrane thickness optimization as a function of the current density was exemplified for atmospheric pressure electrolysis and pressurized electrolysis with a cathodic pressure of 30 bar. The efficiency loss of balanced pressure operation was calculated to be higher than that of differential pressure operation. This difference was ascribed to the larger oxygen cross-permeation during balanced pressure operation than that during differential pressure operation. Moreover, the efficiencies of pressurized electrolysis and atmospheric pressure electrolysis with subsequent mechanical compression were compared. With respect to state-of-the art efficiencies of hydrogen compressors, atmospheric pressure PEM water electrolysis with subsequent compression was modeled to be more efficient than the direct pressurization of hydrogen during water electrolysis. However, the heat balance of the cell and the energy consumption of the drying procedure of the produced hydrogen was not considered in these calculations. These effects influence the comparison of the operation conditions for the benefit of the pressurized operation. The partial pressure increase factors of the electrodes were

found to have a decisive factor impact on the efficiency of PEM water electrolysis and the optimum operating pressures.

# 11 Electrochemical mitigation of hydrogen crossover

In the following, a method to electrochemically mitigate the hydrogen cross-permeation during PEM water electrolysis will be presented and experimentally examined. This chapter was published previously in the form of a research article [46]. To prevent any possibility of confusion concerning the notation, the current density of water electrolysis is in the following denoted as  $j = j_E$ , while the applied voltage to the anode and cathode of the PEM water electrolysis cell will be denoted as  $U = U_E$ . Moreover, the terms anode and cathode will always refer to those electrodes where the oxygen evolution reaction and the hydrogen evolution reaction take place, respectively. To experimentally characterize this technique, an absolute cathodic pressure of 50 bar and atmospheric pressure at the anode were applied to the examined water electrolysis cell. Further details on the setup are discussed in the attachment (Section 14.6). All experiments were conducted with a cell of an active area of 25 cm<sup>2</sup>.

### 11.1 Introduction

Based on the results of Chapter 9, a far higher cathodic than anodic pressure in a PEM water electrolysis cell leads to a far larger hydrogen than oxygen crossover. With reference to the 49 bar differential pressure operation of the examined cell in this chapter, the oxygen crossover is neglected. In order to reduce the current efficiency loss and to improve the safety aspects of pressurized water electrolysis, an electrochemical technique to mitigate the hydrogen cross-permeation during water electrolysis is presented in this chapter. This novel method involves an additional electrode in between the anode and cathode, where the hydrogen is electrochemically oxidized before it cross-permeates through the PEM. An applied voltage between the additional electrode and the cathode electrochemically sends hydrogen at the additional electrode in the form of protons back to the cathode, where it comes from. Hence, by using this technique, the current efficiency loss caused by the hydrogen cross-permeation can be reduced. Alternatively, the additional electrode can also be connected by a resistor to the anode. In this case, the hydrogen at the additional electrode electrochemically reacts with the anodic oxygen to form water. Using this setup, the anodic potential is reduced by opposite overvoltages of the oxygen evolution and reduction reactions. Figure 11.1.1 illustrates this technique and the electrochemical reactions at the electrodes.

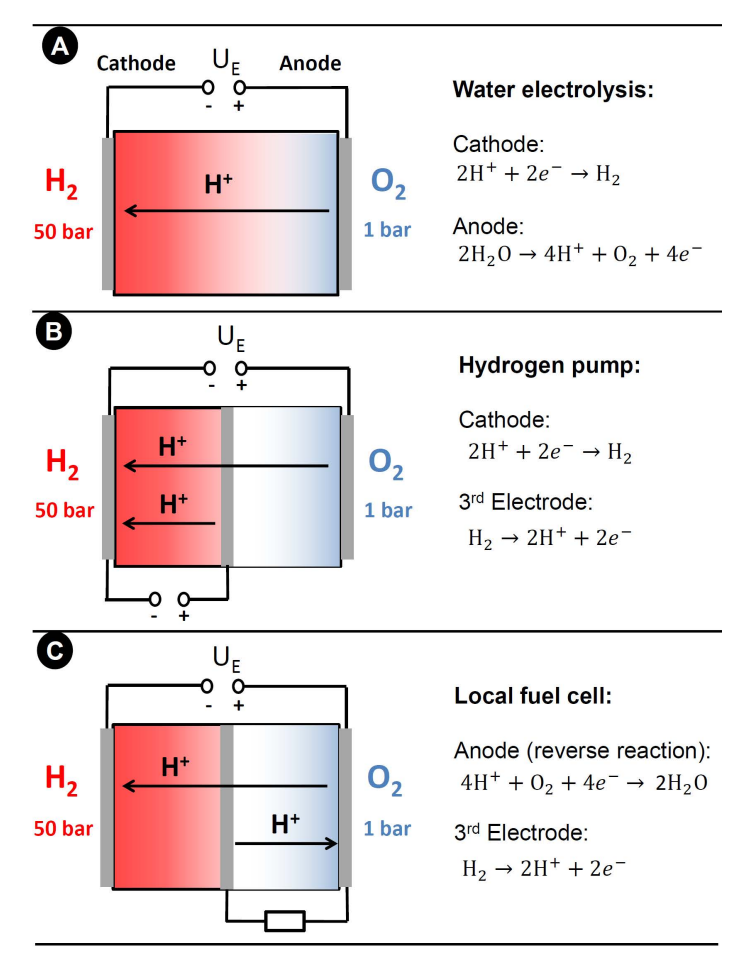


Figure 11.1.1: Schematic illustration of the electrochemical mitigation of the hydrogen cross-permeation during water electrolysis [46]. Left: Setups for the electrochemical mitigation of hydrogen cross-permeation through the membrane during differential pressure PEM water electrolysis. The red and blue shadings qualitatively represent the concentrations of hydrogen and oxygen in the PEM. Hydrogen is permeating from the cathode to the anode (from left to right), while oxygen is permeating in the opposite direction. Right: Electrochemical reactions at the electrodes of the different setups. (A): Acid water electrolysis. The reactions at the anode and the cathode also occur in the other setups. (B): Connection of the additional electrode to the cathode by a power supply. The hydrogen that permeates from the cathode to the additional electrode is electrochemically sent back to the cathode. (C) Connection of the additional electrode to the anode by a resistance. The hydrogen at the additional electrode electrochemically reacts with anodic oxygen, reducing the anodic overpotential.

#### 11.2 Electrochemical characterization

The additional electrode in the setup shown in Figure 11.1.1 was implemented in the form of a platinum based catalyst layer that was contacted by a titanium mesh. This electrode was embedded between two Nafion<sup>®</sup> NR1135 membranes, as further discussed in the attachment (Section 14.6). In the following, the characterization of the electrochemical processes at the electrodes is presented.

#### 11.2.1 Potential and current density of the additional electrode

The aim of this section is to characterize the potential-current relation at the additional electrode. To measure the influence of the potential  $\varphi_3$  of the additional (or third) electrode on the current j<sub>3</sub> of the electrochemical mitigation of the hydrogen crossover, the current density  $j_{\rm E}$  between the anode and cathode (defined as cell current density) was kept constant. To drive the electrochemical reaction for the mitigation of the hydrogen crossover at the additional electrode, its potential must be increased to supply the overvoltages for the electrochemical oxidation of hydrogen to protons. The additional electrode can be connected either by a power supply to the cathode (hydrogen pump, Fig. 11.1.1B) or by an electric load to the anode (local fuel cell, Fig. 11.1.1C). While hydrogen is electrochemically oxidized at the additional electrode, a corresponding electrochemical reduction reaction at either the cathode (hydrogen pump) or the anode (local fuel cell) must take place. These reactions are stated in Figure 11.1.1. The resulting voltage-current characteristics for the electrochemical mitigation of the hydrogen crossover are plotted in Figure 11.2.1. Positive currents of  $j_3$  mean connecting the additional electrode to the cathode, negative currents mean connecting it to the anode. To measure  $\varphi_3$ , the potential  $\varphi_C$  of the cathode served as reference. Accordingly, by measuring the voltage between the cathode and the additional electrode ( $\varphi_3 - \varphi_C$ ), the relative change of its potential was determined.

The current density at which all hydrogen at the additional electrode is electrochemically converted is in the following defined as saturation current density  $j_{\rm sat}$ . The shapes of the voltage-current characteristics in Figure 11.2.1 are dominated by the diffusion limitation of the current, which leads to a diverging potential difference between the additional electrode and the cathode ( $\varphi_3 - \varphi_C$ ) towards  $j_{\rm sat}$ . The saturation current density decreases with higher current densities, which is probably attributable to the influence of the electro-osmotic water drag onto the hydrogen cross-permeation as discussed in Chapter 9.

The ohmic drop due to the proton conduction from the anode to the cathode increases proportionally with the cell current density according to Ohm's law. This ohmic drop consequently increases the potential difference between the additional electrode

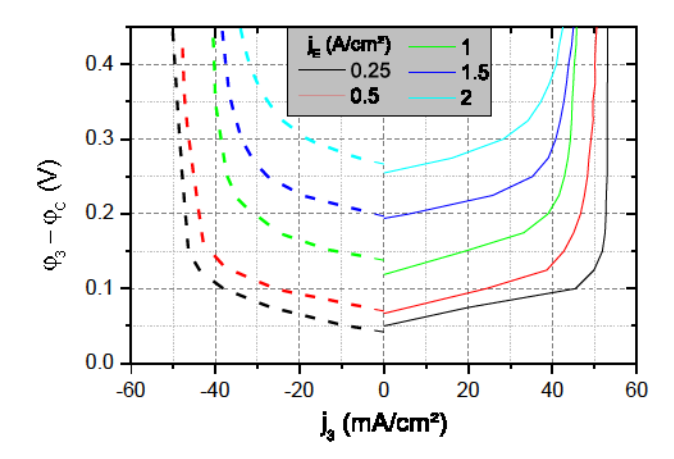


Figure 11.2.1: Measured potential difference between the additional electrode and the cathode  $(\varphi_3-\varphi_\mathbb{C})$  as a function of the current density  $j_3$ . This current density is attributable to the electrochemical mitigation of the hydrogen crossover. The potential  $\varphi_\mathbb{C}$  of the cathode serves as a reference for the potential  $\varphi_3$  of the additional electrode. The measurements were conducted at various fixed electrolysis current densities  $j_E$  between the anode and cathode. Because the measurements were performed under galvanostatic conditions, the fixed currents were affected by a negligible error. The measurement error of the voltage  $(\varphi_3-\varphi_\mathbb{C})$  attributable to unsteady permeation fluxes was below 10%. Positive currents and solid lines: setup using the electrochemical hydrogen pump according to Figure 11.1.1B. Negative currents and dashed lines: setup using the local fuel cell according to Figure 11.1.1C.

and the cathode ( $\varphi_3 - \varphi_C$ ). This effect is shown by the measurements in Figure 11.2.1, where the potential difference  $\varphi_3 - \varphi_C$  increases with  $j_E$  for a defined value of  $j_3$ . Furthermore, the potential of the additional electrode is influenced by the concentration of hydrogen and oxygen at the additional electrode. The catalytic reaction of both gases at the additional electrode leads to the mixing of their standard potentials at the catalyst. An increased oxygen concentration at the additional electrode for higher cell currents (as discussed before) thus may also lead to an increase of  $\varphi_3$ . Moreover, the electric field between the anode and cathode influences the potential of the additional electrode.

# 11.2.2 Influence of the additional electrode on the cell voltage

In order to measure the influence of the potential  $\varphi_3$  on the cell voltage, constant cell currents  $j_E$  were used. For this purpose, the voltage between the anode and cathode  $U_E$  (defined as cell voltage) was measured as a function of  $j_3$ . In addition, the voltage between the additional electrode and the cathode  $(\varphi_3 - \varphi_c)$  was measured and its in-

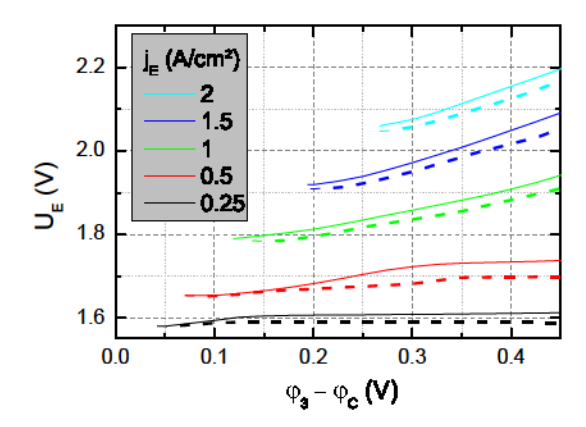


Figure 11.2.2: Measured voltage  $U_{\rm E}$  of the electrolysis cell at constant cell current densities  $j_{\rm E}$  as a function of the voltage between the additional electrode and the cathode ( $\varphi_3-\varphi_{\rm C}$ ). The influence of the potential of the additional electrode on the current density  $j_3$  is discussed in Figure 11.2.1. The cell voltage at constant cell currents increased with the potential of the additional electrode, caused by the altered potential distribution in the electrolyte. Solid lines: setup with hydrogen pump according to Figure 11.1.1B. Dashed lines: setup with local fuel cell according to Figure 11.1.1C.

fluence on the cell voltage was plotted in Figure 11.2.2.

A higher potential  $\varphi_3$  led to an increase of the cell voltage (Fig 11.2.2). The impact of this effect increased toward higher cell currents. This behavior is caused by the increased potential of the additional electrode with higher cell current, which results in a reduced potential difference between the anode and the additional electrode. Because the potential difference is the driving force for water electrolysis, the anodic half-reaction is consequently slowed down. Furthermore, the increase in the potential of the additional electrode influences the potential distribution inside the membrane, which may also influence the ohmic drop. The influence of an increased potential  $\varphi_3$ on the cell voltage was stronger by its connection to the cathode than that by its connection to the anode. In the latter case, the anodic overpotential slightly decreased due to the reaction of oxygen with the protons coming from the additional electrode. Therewith, the entire amount of water oxidized to oxygen and protons at the anodic catalyst is reduced by the reversed reaction stated in Figure 11.1.1. To employ the electrochemical mitigation of the hydrogen crossover, the potential  $\varphi_3$  must be increased. This increase of the potential  $\varphi_3$  means that higher cell voltages have to be applied in order to maintain the same cell current of water electrolysis.

# 11.3 Efficiency and anodic gas purity

In the following, the impact of the electrochemical mitigation of the hydrogen crossover on the cell efficiency and the anodic gas purity will be discussed. The usage of the additional electrode with the local fuel cell setup (Fig 11.1.1C) led to an increase of the cell voltage, as shown in Figure 11.2.2. Consequently, by using this setup, the voltage efficiency of the electrolysis cell is reduced by the electrochemical mitigation of the hydrogen crossover. In this configuration, the hydrogen at the additional electrode is reacted with anodic oxygen. Thereby, the current efficiency of this setup cannot be increased, since the produced hydrogen that permeates to the additional electrode is electrochemically converted with anodic oxygen to water. Accordingly, reduced voltage efficiency leads to a reduced cell efficiency. To summarize, the benefit of a slightly decreasing anodic potential due to the reverse reaction of the local fuel cell was overshadowed by an increase of the cell voltage. By connecting the additional electrode to the cathode (Fig 11.1.1B), the electrochemical mitigation of the hydrogen crossover also led to an increase of the cell voltage (Fig 11.2.2). However, an increase of the current efficiency can be expected, since the hydrogen cross-permeation from the cathode to the anode is reduced. Thus, the following deliberations focus on this configuration. Based on the measurements conducted, it will be shown, that with this configuration the relative increase of the current efficiency was higher than the reduction of the voltage efficiency. Hence, at partial loads (here defined as current densities below 0.5 A/cm<sup>2</sup>) an increase of the cell efficiency resulted, thanks to the electrochemical mitigation of the hydrogen crossover.

By Faraday's law (eq. 4.2.6), the mass flux density of the hydrogen lost due to crossover can be expressed as current density  $j_{loss}$  (Section 2.1.4). The hydrogen loss due to crossover was attributed to two causes: (i) Hydrogen is catalytically recombined with oxygen at the surface of the platinum catalyst at the cathode and the additional electrode (Section 2.1.4). The current density of this hydrogen loss is denoted as  $j_{cr}$ . (ii) Hydrogen permeates from the cathode to the anode. As examined in Section 9, hydrogen at the anode is not electrochemically oxidized at iridium oxide catalyst employed. Using these results it was assumed, that both gases do not catalytically react at the anodic catalyst [45], since the oxide layer probably avoids hydrogen adsorption. Thus, the hydrogen that permeates through the membrane mixes with the oxygen evolved at the anode. This hydrogen permeation flux from the cathode to the anode is in terms of Faraday's law expressed as an electrochemical current density, which is denoted as  $j_{cross}$ . Thus, the overall current loss  $j_{loss}$  due to the permeation of hydrogen through the membrane equals:

$$j_{\text{loss}} = j_{\text{cr}} + j_{\text{cross}}.\tag{11.3.1}$$

The anodic hydrogen content can be calculated as the ratio of hydrogen permeating through the PEM normalized to the anodic gas release rate (Section 9). Including the two- and four-electron processes for the electrochemical currents of hydrogen and oxygen production (Fig 11.1.1A), the anodic hydrogen content can be expressed by Faraday's law and equation 9.2.4 as:

$$H_2 \text{ in } O_2 = \frac{\frac{1}{2}j_{\text{cross}}}{\frac{1}{4}j_{\text{E}} + \frac{1}{2}j_{\text{cross}}}.$$
 (11.3.2)

Consequently, the anodic hydrogen content is a measure for the hydrogen permeation through the membrane (Section 9).

As further discussed in the attachment (Section 14.6), the additional electrode was positioned in the center of the membrane. When the additional electrode is not employed  $(j_3 = 0)$ , hydrogen permeates from the cathode to the anode. The partial pressure of hydrogen at the cathode was approximately 50 bar, while the absolute pressure at the anode was 1 bar. Accordingly, the concentration of hydrogen at the anode is negligible compared to that at the cathode (Section 9). When the current of the electrochemical mitigation of the hydrogen crossover is driven into the saturation current density j<sub>sat</sub> as shown in Figure 11.2.1, the concentration of hydrogen at the additional electrode is negligible. Hence, when the additional electrode is operated with  $j_3 = j_{sat}$ , the concentration difference of hydrogen between the cathode and the additional electrode is approximately equal to that between the cathode and the anode when  $j_3 = 0$ . However, the distance for the hydrogen permeation from the cathode to the additional electrode is half that from the cathode to the anode. According to Fick's law of diffusion, the permeation flux driven by the same concentration difference is reciprocally proportional to the distance (Section 9). For this reason, at  $j_3 = j_{\text{sat}}$  the permeation flux of hydrogen from the cathode to the additional electrode can be assumed to be twice as large as that from the cathode to the anode at  $j_3 = 0$ . This approximation is used in order to estimate  $j_{loss}$ :

$$j_{\rm loss} \approx \frac{1}{2} j_{\rm sat}. \tag{11.3.3}$$

The highest saturation current density in Figure 11.2.1 was  $j_{\rm sat} = 52\,{\rm mA/cm^2}$  at a cell current density of  $0.25\,{\rm A/cm^2}$ . Based on Fick's law of diffusion (eq. 2.3.3), the hydrogen permeation flux density from the cathode to the additional electrode can be estimated. By using Faraday's law (eq. 4.2.6), this permeation flux can be calculated to a current density of  $51\,{\rm mA/cm^2}$ . Thus, the measured and estimated values for saturation current density are approximately equal. The current efficiency is approximated

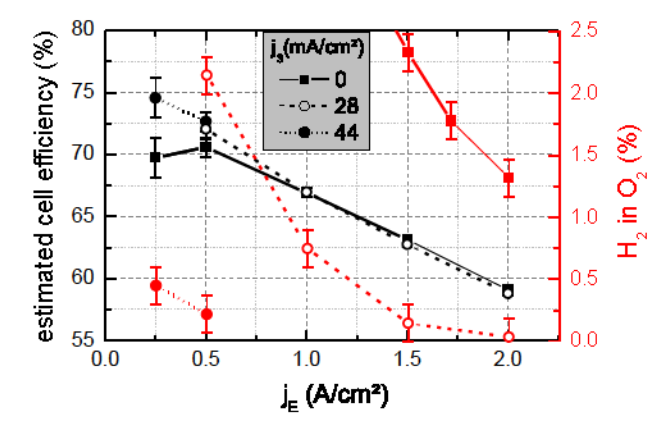


Figure 11.3.1: Left scale and black: Cell efficiency as estimated on the basis of equation 11.3.5. Right scale and red: Measured anodic hydrogen content (red) as a function of the cell current density  $(j_{\rm E})$  for various values of  $j_{\rm 3}$ . The additional electrode is connected to the cathode according to the setup with electrochemical hydrogen pump in Figure 11.1.1B. In the partial load range, an increase of the cell efficiency results thanks to the usage of the additional electrode.

using equation 10.2.1 and equation 11.3.3:

$$\eta_{\rm C} \approx 1 - \frac{1}{2} \frac{j_{\rm sat}}{j_{\rm E}} + \frac{1}{2} \frac{j_3}{j_{\rm E}}.$$
(11.3.4)

The last term accounts for the mitigation of current loss attributable to the electrochemical transport of hydrogen at the additional electrode back to the cathode. Accordingly, at  $j_3 = j_{\text{sat}}$  the current efficiency is 100 %.

In Section 2.1.4, the general definition of the efficiency was given by the ratio of the ideal power and the spend power for water electrolysis (eq. 2.1.26). To mitigate the hydrogen cross-permeation through the PEM, an additional voltage was applied between the additional electrode and the cathode. The energy consumed by the current resulting has to be also considered in order to calculate the cell efficiency. The power invested for the electrochemical hydrogen oxidation at the additional electrode equals  $(\varphi_3 - \varphi_C)$   $j_3$ . This contribution was added to the spend power for the electrochemical water decomposition:

$$\eta = \frac{P_{\text{ideal}}}{P_{\text{real}}} = \frac{1.23 \,\text{V} \,j_{\text{E}}}{U_{\text{E}} j_{\text{E}} + (\varphi_{3} - \varphi_{\text{C}}) \,j_{3}} \,\eta_{\text{c}} \tag{11.3.5}$$

In Figure 11.3.1, the measured anodic hydrogen content of the cell is plotted as a function of the cell current density. By using the additional electrode at open circuit potential ( $j_3 = 0$ ), the lower explosion limit of the anodic gas composition (4 %  $H_2$  in

 $O_2$ ) was estimated to be exceeded in the partial load range. Based on equation 11.3.5, the estimated cell efficiency is plotted in Figure 11.3.1. The error of the estimated cell efficiency was calculated by the propagation of uncertainty using the following errors of the measured parameters:  $U_E = \pm 5 \,\text{mV}$ ,  $j_{\text{sat}} = \pm 10 \,\%$ ,  $(\varphi_3 - \varphi_C) = \pm 10 \,\%$ . The currents adjusted for the measurements  $(j_3, j_E)$  were affected by a negligible error.

At 1 A/cm<sup>2</sup>, the estimated cell efficiency with applied electrochemical mitigation of the hydrogen crossover is equal to that with the additional electrode at open circuit voltage (Fig 11.3.1). As discussed before (Fig 11.2.2), the influence of the potential alteration of the additional electrode on the cell voltage increased with the cell current density. However, towards higher cell current densities, the influence of the hydrogen permeation flux on the current efficiency is reduced (eq 10.2.1). Accordingly, by using the electrochemical mitigation of the hydrogen crossover above 1 A/cm<sup>2</sup>, the decrease of the voltage efficiency overshadowed the slightly increased current efficiency. Hence, a reduced cell efficiency resulted in this current density range (Fig 11.3.1). At current densities below 0.5 A/cm<sup>2</sup>, the estimated cell efficiency increased by employing the electrochemical mitigation of the hydrogen crossover. In this case, the current efficiency is more affected by the hydrogen cross-permeation (eq 10.2.1). Furthermore, the influence of the increased potential of the additional electrode during the electrochemical mitigation of the hydrogen crossover on the cell voltage decreased towards smaller cell current densities (Fig 11.2.2). Thus, the reduction of the voltage efficiency due to the electrochemical mitigation of the hydrogen crossover is overshadowed by the increase of the current efficiency. Accordingly, in the partial load range the cell efficiency increased thanks to the usage of the electrochemical hydrogen pump setup according to Figure 11.1.1B.

# 11.4 Challenges for application

Thus far it was shown, that by using an additional electrode in between the cathode and the anode the hydrogen permeation through the membrane can be efficiently reduced. Thanks to the usage of an electrochemical hydrogen pump according to Figure 11.1.1B, an increase of the current efficiency resulted. Hydrogen at the additional electrode was sent back to the cathode where it was produced. The potential of the additional electrode was increased by an applied voltage, which increased the cell voltage and consequently reduced the voltage efficiency. However, in the partial load range (below  $j = 0.5 \,\mathrm{A/cm^2}$ ), the increase of the current efficiency overshadowed the decrease of the voltage efficiency. An increase of the cell efficiency resulted.

Besides the influence of the potential of the additional electrode on the cell voltage,

the implementation of the additional electrode into the electrolyte is accompanied by the following restrictions: (i) The electric contact of the catalyst layer by the additional electrode (here a titanium mesh) will increase the proton resistance between the anode and cathode. (ii) The in-plane conductivity of this electric contact limits the scalability of the technique, since the current for the electrochemical mitigation of the hydrogen crossover is applied at the margins of the electrolysis cell to the additional electrode.

The proton resistance of the membrane is typically measured by the high-frequency cell resistance using impedance spectroscopy as discussed in Section 2.2.2. However, in the case of an additional electrode embedded into the electrolyte, the pure proton resistance of the cell cannot be measured by this high-frequency cell resistance. The electric and ionic conductivities in the catalysts layers are connected by capacitive elements in the form of electrochemical double layers as described by the transmission line model in the literature [65]. Thus, by alternating currents, the proton current through a catalyst layer can be altered into an electric current and *vice versa*. Applied to the setup discussed, both, the electric and the ionic conductivities of the additional electrode can contribute to the high frequency resistance. In this sense, by measuring the high frequency cell resistance it is not possible to determine the influence of the additional electrode on the proton resistance of the electrolysis cell.

To estimate the proton cell resistance of the employed electrolysis cell with the additional electrode, we considered the voltage drop of this cell compared to that of a reference cell without the additional electrode. A cell with a Nafion<sup>®</sup> N117 membrane (similar thickness as two N1135 membranes) without an additional electrode served as reference. The Nafion N117 membrane was coated with equally produced anodes and cathodes as the cell with the additional electrode. This reference cell had a high-frequency resistance of approximately  $0.16\,\Omega$ . At a cell current of  $2\,\text{A/cm}^2$ , the cell voltage of this reference cell was  $1.925\,\text{V}$ , while that of the cell with the additional electrode was  $2.055\,\text{mV}$  for  $j_3=0\,\text{mA/cm}^2$  (Fig. 11.2.2). Based on Ohm's law, this voltage difference of  $0.13\,\text{V}$  equals an approximated increase of the cell resistance of  $0.065\,\Omega$  cm<sup>2</sup> which corresponds to a relative increase of 41 %.

In order to commercialize the electrochemical mitigation of the hydrogen crossover, this increase of the cell resistance must be reduced by the choice of materials and the reduction of contact resistances for protons between the membranes. Because hydrogen crossover and the correlated current efficiency loss is mitigated using the developed technique, thinner membranes with smaller proton cell resistance can be used for pressurized water electrolysis. Thereby, the voltage efficiency and current efficiency can be enhanced by employing the electrochemical mitigation of product

gas crossover. The material for the electric contact of the additional electrode must be corrosion resistant at the applied potentials in the acidic regime of the proton exchange membrane. Furthermore, this material must be a good electron conductor, mechanically stable and resistant to corrosion. Besides titanium, further promising materials that fulfill these requirements are tungsten, silver, and graphene.

# 11.5 Synopsis of the chapter

In this chapter, an additional electrode between the anode and cathode was integrated into the PEM of a water electrolyzer. The electrolyzer was operated at a cathodic pressure that was fifty times larger than the anodic pressure. The additional electrode was connected by a power supply to the cathode so that the hydrogen permeating through the membrane was electrochemically sent back to the cathode. This technique significantly increased the cell efficiency below  $0.5\,\mathrm{A/cm^2}$ . Furthermore, safety issues related to anodic hydrogen were avoided. Alternatively, when the additional electrode was connected by an electric load to the anode, the hydrogen at the additional electrode electrochemically reacted with oxygen at the anodic overpotential caused by the oxygen production was reduced. In summary, the concept of electrochemically mitigating gas crossover was shown to be an effective technique to increase the cell efficiency during high-pressure water electrolysis at partials loads. However, limited scalability and an increased cell resistance display a major drawback of this technique.

# 12 Discussion

In this chapter, the findings of the previous chapters and their relations to one another are discussed. First, the influence of microscopic structures of PEMs on their macroscopic proton conductivities and gas permeabilities are elucidated. Within this aim, prospects for the development of PEMs are given. Second, the efficiency of PEM water electrolysis is considered as a function of the physical membrane properties, temperature and operating pressures. Finally, the electrochemical mitigation of hydrogen crossover that was presented in the previous chapter is critically assessed.

# 12.1 Microscopic geometry and macroscopic properties of PEMs

In order to physically characterize proton conduction and gas permeation through the microscopic structure of Nafion<sup>®</sup>, the phase separation between the aqueous and solid polymeric phase reported in the literature (Section 2.4) was presupposed. An additional phase between the aqueous and solid phase was proposed which is a mixture of a polymeric and aqueous character. This phase was defined as the intermediate phase. Only water channels that connect the electrodes contribute to the overall proton conductivity of a PEM (Section 5). In contrast, gases can also permeate through the solid and intermediate phase (Chapter 6), which means that all different topologies of the water channels discussed in Chapter 5 can contribute to the gas permeability. Accordingly, the alternating permeation of gas molecules through the different phases of PEMs is not limited by percolation paths through the aqueous phase, which is however the case for the proton conduction.

The proton conductivity of fully hydrated Nafion<sup>®</sup> was measured to  $17\pm 2$  percent of that of an aqueous hydrochloric acid solution with an equal proton concentration as that in the aqueous phase (Section 5.2). Geometric restrictions related to the morphology of the aqueous phase were estimated by the developed network resistor model. As a result, the overall conductivity of fully hydrated Nafion<sup>®</sup> was estimated to 15 % of the conductivity of its aqueous phase (Section 7.1.3). The measured ratio of the proton conductivity of fully hydrated Nafion<sup>®</sup> to that of the aqueous solution and the simulated influence of the microscopic structure on the proton conductivity led within the measurement precision to equal values. On the basis of this agreement, the proton mobility in the water channels of fully hydrated Nafion<sup>®</sup> was estimated to equal that of aqueous solutions with an equal proton concentration (Section 5.2).

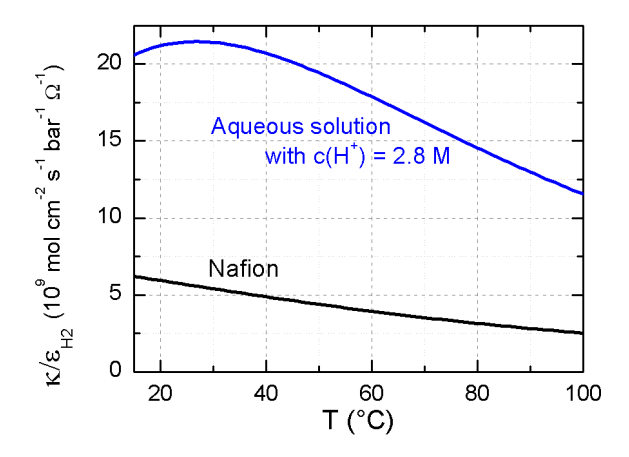


Figure 12.1.1: Ratios of the proton conductivity to the hydrogen permeability of Nafion<sup>®</sup> (black line) and an aqueous solution with a proton concentration of 2.8 M (blue line). This concentration equals the proton concentration in the aqueous phase of Nafion<sup>®</sup> membranes (Chapter 5). The proton conductivity of the aqueous solution and Nafion<sup>®</sup> was measured as discussed in Chapter 5. The measured hydrogen permeability of Nafion<sup>®</sup> was presented in Chapter 6. The hydrogen permeability of the aqueous solution was estimated by half the conductivity of water for the reasons that are discussed in Section 7.1.2.

A higher ratio of the proton conductivity to the hydrogen permeability of a PEM was discussed in Chapter 2.1.4 to increase the overall efficiency of a water electrolysis cell. Figure 12.1.1 shows this ratio for fully hydrated Nafion® and an aqueous solution of hydrochloric acid with a proton concentration of 2.8 M. This concentration equals that of protons in the aqueous phase of fully hydrated Nafion<sup>®</sup>. The data in this figure are based on the estimated gas permeability of the aqueous phase<sup>1</sup> and the experimental data on the proton conductivity and hydrogen permeability which were presented in Chapter 5 and 6. The smaller ratio of  $\kappa/\epsilon$  for fully hydrated Nafion® compared to that for the aqueous solution can attributed to two different causes: (i) A smaller mobility of the protons in the aqueous phase of Nafion® than that in aqueous solutions. (ii) Different permeation paths of gas molecules and ions. When in a PEM protons and gases permeate on the same paths and protons in the aqueous phase show equal mobility as those in an aqueous solution, the ratio of  $\kappa$  to  $\varepsilon$ would equal that of the aqueous reference solution (that has a similar ionic composition as the aqueous phase of the membrane). Reduced proton mobilities in the aqueous phase and the alternating permeation through all the phases reduce the value of  $\kappa/\varepsilon$  of the PEM. As discussed above, the mobilities in the aqueous phase of Nafion<sup>®</sup>

 $<sup>^1</sup>$ In Chapter 7, the influence of the acidity of the aqueous phase in Nafion<sup>®</sup> was estimated to reduce the hydrogen permeability by a factor of approximately 0.5 in comparison to that of water. The same factor is assumed to reduce the permeabilities of the aqueous hydrochloric acid solution.

154 12 Discussion

and aqueous solutions were estimated to be equal. Thus, the alternating permeation of hydrogen molecules through the aqueous, intermediate and solid phase causes a lower value of  $\kappa/\epsilon$  for Nafion<sup>®</sup> than that of the aqueous reference solution.

The values of  $\kappa/\varepsilon$  of aqueous solutions, Nafion<sup>®</sup> and other PEMs (Chapter 8) decrease toward higher temperatures. This decrease is stronger for PEMs than those of aqueous solutions, as the activation energy for the gas permeation through the solid phase of PEMs is higher than that of water (Chapter 6). Accordingly, the gas permeability of the solid phase increases more rapidly with temperature than that of the aqueous phase. With reference to effect of temperature on the ratio  $\kappa/\varepsilon$  of the aqueous and solid phase of PEMs, the decreasing trend toward higher temperatures is caused by the physical properties of the proton and gas permeation through the different phases. Hence, this trend can be expected to be valid for all types of PEMs. On the basis of the previous discussion, following physical drawbacks of PEMs can be faced: (i) The proton conductivity in the aqueous phase can only be as high as that in an aqueous solution with an equal proton concentration. (ii) The morphology of the aqueous phase directly influences the overall proton conductivity of a PEM. (iii) Diffusion of gases in the aqueous phase lead to high gas permeabilities of a PEM. (iv) A further increase of the gas permeability can result from the alternating permeation through the aqueous, intermediate and solid phase of the PEM. As the result of all these restrictions,  $\kappa/\varepsilon$  of an aqueous solution with the same ionic composition as that of the aqueous phase in the PEM displays the maximum value of this ratio that the PEM itself can reach.

In order to increase the ratio of proton conduction to hydrogen permeability of the aqueous phase in PEMs, higher proton concentrations in the aqueous phase than that in Nafion<sup>®</sup> membranes can be used. The proton concentration in the aqueous phase of Nafion<sup>®</sup> was estimated to 2.8 M. The highest conductivity of aqueous HCl solutions at 65 °C is at a concentration of approximately 5.5 M [179]. At this concentration the conductivity is approximately 1.25 times higher than that at 2.8 M [179]. Hence, higher proton conductivities of Nafion<sup>®</sup>-type PEMs may be achievable by higher proton concentrations in the aqueous phase. Moreover, an increase of the ion concentration in the aqueous phase could also reduce the gas permeability, as discussed in Section 7.1.2. However, by lowering the equivalent weight to achieve such higher proton concentrations excessive water uptake and the loss of the structural integrity of the PEM could result.

In Section 8, hydrocarbon membranes that show approximately two times higher values of  $\kappa/\varepsilon$  than that of Nafion<sup>®</sup> membranes were presented. Gubler *et al.* [139] also developed novel types of membranes with an organic chemistry and cross-linked io-

nomers, where the ratio of the proton conductivity to the hydrogen permeability was 1.5 times larger than that of Nafion<sup>®</sup>. In the latter paragraph, it was discussed that the proton conductivity in the aqueous phase of Nafion<sup>®</sup> could be increased by at maximum by 1.25 times with higher proton concentrations. Thus, the measured higher values of  $\kappa/\varepsilon$  of the hydrocarbon membranes are expected to be mainly attributable to a reduced hydrogen permeability. The different backbone chemistry might lead a lower hydrogen permeability of the polymeric phase.

To conclude, novel membrane types such as the hydrocarbon membranes examined in Section 8 can achieve higher values of  $\kappa/\epsilon$  than that of typically used Nafion<sup>®</sup> membrane. Thus, with these novel membrane types the efficiency of PEM water electrolysis cells can be increased, while the durability of hydrocarbon membranes might display an issue. With reference to the physics of gas and ion permeation in the aqueous phase of PEMs, the effect of gas cross-permeation cannot be avoided. Hence, independent of the choice of the PEM, gas-crossover can be expected to seriously affect the efficiency of pressurized PEM water electrolyzers, as discussed in the following section in detail.

# 12.2 Efficiency and operation parameters

The ratio of the proton conductivity to the hydrogen permeability of a PEM displays among kinetic contributions the most decisive impact on the cell efficiency (Chapter 10.2). The kinetic overvoltages during water electrolysis are dominated by the anodic half-reaction as the hydrogen evolution reaction on platinum is in terms of the current exchange density approximately nine orders of magnitudes smaller than that of the oxygen evolution reaction on iridium oxide<sup>2</sup>. To minimize kinetic overvoltages one typically aims at high operation temperatures of PEM water electrolyzers [225]. Moreover, the conductivity of the PEM increases towards higher temperatures, as shown in Chapter 5. However, the ratio of proton conductivity to hydrogen permeability of PEMs decrease toward higher temperatures (as shown in Figure 12.1.1). In addition, higher cell temperatures increase the thermodynamical work required for the *in-situ* pressurization of hydrogen (equation 2.5.4). Kinetic overvoltages can be added to the denominator of the voltage efficiency (eq. 10.2.3) and thereby included into the presented model. Using this approach, the presented model can also be used to optimize the operating temperature of water electrolyzers.

Mechanical compression *via* ionic liquid piston compressors was discussed to achieve lower temperatures during the compression process than the typically used tempera-

<sup>&</sup>lt;sup>2</sup>The current exchange density is a measure for the activity of a catalyst. This kinetic parameter for both reactions can be obtained from literature data, such as [220] and [224]

156 12 Discussion

ture of 80 °C for water electrolysis cells (Section 10.3). Consequently, the thermodynamic work required for the hydrogen compression during mechanical compression can be lower than that during the water electrolysis at 80 °C. However, the energy consumption of mechanical compression is affected by the compressor efficiency. In total, the lower operating temperature of a ionic liquid piston compressor in combination with its high mechanical efficiency lead to approximately the same compression efficiency as the direct isothermal compression during PEM water electrolysis at 80 °C (Section 10.3). However, higher pressures during water electrolysis increase the gas crossover and correlated efficiency losses. To balance the increasing crossover toward higher pressure thicker membranes are required. These thicker membranes reduce the voltage efficiency. As a result of these relations and on the basis of the developed model, water electrolysis operating at atmospheric pressure in combination with subsequent mechanical compression was calculated to show better efficiency than that of direct pressurization in the electrolysis cell.

Toward higher current densities the influence of the hydrogen and oxygen cross-permeation on the current efficiency decrease. Thus, thin membranes and dynamic pressure operation with low pressures at low loads and high pressures at high loads might be an approach to combine the advantages both, low-pressure and high-pressure PEM water electrolysis. Electrolytic gas evolution during PEM water electrolysis was shown to increase the pressures in the electrodes. These higher pressures inside the electrodes than that at the gas outlets were estimated to be a decisive factor for the efficiency of PEM water electrolysis. When catalyst layers with smaller partial pressure increase factors can be manufactured (as for example by higher porosities), the efficiency of PEM water electrolysis could be significantly enlarged (Section 10.3).

To mitigate hydrogen crossover during pressurized PEM water electrolysis, a new technique was introduced and examined, where hydrogen in the PEM is electrochemically oxidized at an additional electrode (see Chapter 11). Experimentally, this technique was shown to increase the efficiency of a PEM water electrolysis cell that operated at a cathodic pressure of 50 bar. Using this technique, the safety threshold of anodic hydrogen could be kept even at small loads. However, this technique requires a new cell design with a limited scalability and an increased cell resistance. It is questionable, if these drawbacks can be technically overcome in order to achieve higher efficiencies as low-pressure PEM water electrolysis in combination with mechanical compression. To summarize, the most efficient operation of PEM water electrolysis under dynamic loads may be achieved by dynamic pressure operation with thin membranes.

# 13 Summary

The aim of this thesis was to characterize the influence of the microscopic structure of polymer electrolyte membanes (PEMs) at length scales of approximately  $10^{-9}$  m on the macroscopic proton conductivity and gas permeability. Moreover, the impact of these transport processes on the macroscopic cell efficiency of PEM water electrolysis was quantified. As a result, a multiscale description of the physical transport processes of gases and protons through the PEM during water electrolysis was developed. First, physics that characterize the process of water electrolysis and its efficiency was reviewed from the literature. Proton conduction and gas permeation in PEMs and aqueous solutions was briefly elucidated. After discussing these fundamentals, experimental methods were introduced, focusing on novel modifications of the electrochemical impedance spectroscopy to measure proton conductivities and the electrochemical monitoring technique to measure gas permeablities of PEMs. Besides the experimental configurations of these setups, the physics to determine the proton conductivity and gas permeabilities from the measurements were discussed. Moreover, the developed experimental setup to precisely measure the anodic hydrogen content during PEM water electrolysis was presented.

The proton conductivities and hydrogen permeabilities of six different PEMs including Nafion were measured. Nafion is the best characterized PEM in the literature and was in focus of the experimental studies in this thesis, as reported data on the microscopic structure of other PEMs are scarce. Using electrochemical impedance spectroscopy with amplitude and frequency variation, the proton conductivity of Nafion was measured and derived to be independent of the length scales of the proton permeation. On the basis of these results, the proton conduction of Nafion was derived to be independent of scattering events between mobile protons and pore walls of water channels. An aqueous hydrochloric acid solution with an equal proton concentration as the water channels in Nafion was found to be 6.0  $\pm$  0.7 times more conductive to protons than Nafion membranes.

On the basis of reported data in the literature, a resistor network representative for the microscopic structure of Nafion<sup>®</sup> was developed. With this model, the influence of the morphology of the aqueous phase was estimated to increase the overall resistance of Nafion<sup>®</sup> by a factor of 6.7 compared to the mean proton conductivity inside the water channels. The measured difference between the proton conductivity of Nafion<sup>®</sup> and that of an aqueous solution was within the measurement error equal to the estimated influence of the water channel morphology by the resistor network model. With reference to this agreement, the proton mobility in the aqueous phase

158 13 Summary

of Nafion<sup>®</sup> was estimated to be similar to that in aqueous solutions of equal proton concentrations.

The hydrogen permeability of Nafion® membranes was found to be independent of applied pressures, which led to the conclusion that the impact of differential pressure as a driving force on the gas permeation is negligible. Accordingly, diffusion was identified as the dominating driving force for the gas permeation through Nafion<sup>®</sup>. Higher water contents of Nafion® membranes increased the hydrogen permeability, which is caused by the at least tenfold higher permeability of water than that of dry Nafion® membranes. The developed resistor network model was used to describe the gas permeation through the microscopic structure of Nafion® membranes. By comparing the measured and modeled permeabilities of hydrated Nafion®, the permeability of the solid phase of Nafion® was estimated to increase by water uptake. The origin of this increased permeability of the solid phase with water uptake was ascribed to weakened van der Waals forces between the polymer chains, as water penetrating into the polymer chains acts as plasticizer. The resulting softening of the solid phase by weakened van der Waals forces between the polymer chains was also reported by visco-elastic measurements in the literature. The ratio of the measured proton conductivity to the hydrogen permeability of Nafion® was estimated to be approximately four times smaller than that of an aqueous solution of similar proton concentration. The reason for this difference was attributed to the gas permeation through the intermediate and solid phase of Nafion<sup>®</sup>.

A physical model to calculate the gas crossover in operating PEM water electrolysis cells was developed and evaluated with measured anodic hydrogen contents. The *exsitu* measured proton conductivity, hydrogen permeability and oxygen permeability of Nafion<sup>®</sup> served as input parameters for the model. The influence of the proton permeation through the PEM during water electrolysis on the hydrogen and oxygen crossover was physically described. By comparison of the power law dependencies of the physically modeled anodic hydrogen content and *in-operando* measurements as a function of the current density, a significant impact of proton permeation on the hydrogen crossover could not be ascertained. Based on these observations, the amount of hydrogen dissolved in the hydration shell of the protons was estimated to be negligible. The mass transport in the catalyst layers of the PEM electrolysis cell was taken into account by the increase of the partial pressures of the evolved hydrogen and oxygen. The cathodic partial pressure increase during PEM water electrolysis was quantified by fits to measured anodic hydrogen contents.

On the basis of the physical description of the gas crossover in PEM water electrolysis cells, a model to calculate cell efficiencies as a function of operation parameters

and membrane properties was developed. The partial pressure increase in the electrodes caused by the gas evolution was estimated to significantly reduce the efficiency of PEM water electrolysis. The larger oxygen crossover at balanced pressure operation than that of differential pressure operation leads to smaller efficiencies. The membrane thickness of PEM water electrolysis cells was computationally optimized for various exemplarily operation conditions. Besides the membrane thickness, the ratio of proton conductivity to hydrogen permeability was identified as the decisive parameter of a PEM that influences the cell efficiency. From the six different PEMs examined in this thesis, those of a non-fluorinated chemistry showed the highest ratio of proton conductivity to hydrogen permeability, which was attributed to a lower permeability of their solid phase than those of the fluorinated materials like Nafion<sup>®</sup>. The efficiency of pressurized water electrolysis was compared to operation at atmospheric pressure in combination with subsequent mechanical compression. Atmospheric pressure operation in combination with state-of-the-art mechanical compressors was estimated to be more efficient than pressurized operation at 30 bar.

To reduce the efficiency losses that is caused by the hydrogen cross-permeation during pressurized water electrolysis, a novel technique was developed, where hydrogen is electrochemically oxidized at an additional electrode between the anode and the cathode. This additional electrode was integrated into the PEM of a water electrolyzer and connected by a power supply to the cathode, in order to send hydrogen at the additional electrode in the form of protons back to the cathode. This technique considerably increased the cell efficiency at a cathodic pressure of 50 bar and below  $0.5 \, \text{A/cm}^2$ . Moreover, using this technique at 50 bar operation pressure, anodic hydrogen contents below the lower explosion limit were achieved. Although a significant decrease of the hydrogen cross-permeation was achieved using this technique, the increased cell resistance by the additional electrode and its limited scalability were discussed to be a major drawback of this novel technique.

# 14 Attachment

In the following, details about the measurement techniques, experimental setups, fit data, and detailed information about the calculation procedure of the resistor network modeling will be given. Moreover, the relation between isentropic and isothermal compression will be discussed in detail.

# 14.1 Electrode preparation

In the following, the production of the catalyst layers used for the experiments will be described. Platinum supported on carbon (Johnson Matthey, Hispec9100) was used as the catalyst in the electrodes used for the electrochemical monitoring technique and the cathode for the electrolysis cells. Iridium oxide (Alfa Aesar) was used as the anodic catalyst for the water electrolysis cells. To produce the catalysts layers, solutions of 1.5 g Nafion® binder (Liquion LQ-1115, Ion Power Inc, consisting of 15 wt% Nafion® ionomer), 230 mg of the catalyst, 630  $\mu$ l water, 575  $\mu$ l 1-Propanol, 1725  $\mu$ l Isopropyl alcohol, and 100  $\mu$ l Ethylene glycol were first sonicated and then applied as films (270  $\mu$ m) on the PTFE foil substrates using a squeegee. After drying, the thickness of the catalyst layers was approximately 20  $\mu$ m. In order to fabricate catalyst coated membranes, the decal transfer method was used, where the catalyst layers were hotpressed on the Nafion® membranes. This hot-pressing procedure was conducted at 130 °C and 5 MPa/cm² for 180 s. The iridium oxide catalyst layers were produced with a loading of 2.2 mg/cm², while that of the Pt/C catalyst layer had a platinum loading of 0.5 mg/cm².

# 14.2 Additional information to the conductivity measurements

In this section, first the capacitances between the water channels of Nafion<sup>®</sup> membranes will be estimated. Second, the procedure to extract the proton conductivity of the aqueous HCl solution from the measured conductivities will be discussed. Third, the fitting procedure used to describe the temperature dependencies of the measured conductivities and the calculation of the statistic measurement errors will be elucidated. Fourth, the influence of the morphology on the proton conductivity of Nafion<sup>®</sup> will be physically characterized. Finally, the influence of the water content of fully hydrated Nafion<sup>®</sup> (that was taken from the literature) on the calculations presented will be discussed.

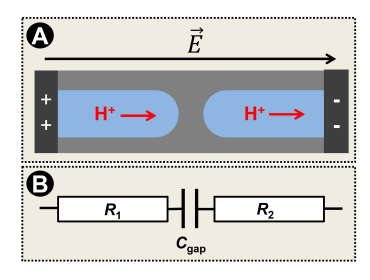


Figure 14.2.1: (A): Schematic illustration of two water channels that are separated by the solid polymeric phase. (B): Equivalent circuit for this alignment, while the polymeric phase is described by a plate capacitor geometry with the capacitance  $C_{\rm gap}$ . The resistances  $R_1$  and  $R_2$  correspond to the resistances of the proton conduction through the water channels.

# 14.2.1 Capacitances between the water channels

Figure 14.2.1 illustrates an assumed alignment of two by the polymeric phase separated water channels and the corresponding equivalent circuit. The impedance of these in series connected ohmic conductors in the form of the water channels and the capacitor in the form of the solid phase equals

$$Z = R_1 + \frac{1}{i\omega C_{\rm gap}} + R_2 \,, \tag{14.2.1}$$

where  $R_1$  and  $R_2$  denote the ohmic resistances of the water channels and  $C_{\rm gap}$  the capacitance of solid polymeric phase. The capacitance is approximated by a plate capacitor geometry

$$C = \varepsilon_0 \varepsilon_r \frac{A}{d_{\text{gap}}} \,, \tag{14.2.2}$$

where  $\varepsilon_0=8.85\times 10^{-12}\,\mathrm{A\,s\,V^{-1}\,m^{-1}}$  denotes the vacuum permittivity,  $\varepsilon_{\mathrm{r}}$  the permittivity of the polymeric phase, A the cross-sectional area of the water channels, and  $d_{\mathrm{gap}}$  the distance between the water channels. In models, which describe the microscopic structure of Nafion<sup>®</sup>, the functional groups are orientated to the water channels [21,144,160]. Based on these descriptions, the solid polymeric phase of hydrated Nafion<sup>®</sup> is mainly comprised by the polymeric backbone, which equals the structure of polytetrafluoroethylene (PTFE) [226]. Accordingly, the permittivity of the polymeric phase in Nafion<sup>®</sup> is assumed to be similar to that of PTFE, which equals  $\varepsilon_{\mathrm{r}}=2$  as reported by Baker-Jarvis et~al. [227].

The impedance of the aqueous phase in the alignment illustrated in Figure 14.2.1B equals

$$|Z_{\rm ap}| = R_1 + R_2 = \frac{d_1 + d_2}{A \kappa_{\rm ch}},$$
 (14.2.3)

162 14 Attachment

where  $R_1$  and  $R_2$  denote the resistances of the water channels,  $d_1$  and  $d_2$  their lengths, and  $\kappa_{\rm ch}$  their conductivity. The impedance of the polymeric capacitor between the water channels is:

$$|Z_{\rm sp}| = \frac{1}{|i\omega C|} = \frac{1}{\omega C} = \frac{d_{\rm gap}}{A\omega C}$$
 (14.2.4)

In this model, the ratio of the impedance of the solid polymeric phase to that of the aqueous phase equals:

$$\frac{|Z_{\rm sp}|}{|Z_{\rm ap}|} = \frac{\kappa_{\rm ch}}{\varepsilon_0 \, \varepsilon_{\rm r} \, \omega} \frac{d_{\rm gap}}{(d_1 + d_2)} \tag{14.2.5}$$

To calculate this ratio, the parameters were chosen to maximize the contributions of the capacitive conduction between the water channels:

- $d_1 + d_2 = 50 \,\mu\text{m}$ , which is a typical length scale for a polymer electrolyte membrane in fuel cells or water electrolyzers.
- $d_{\rm gap} = 2.5 \times 10^{-9}$  m, based on the domain spacing reported by Allen *et al.* [40].
- $\omega=100\,\mathrm{kHz}$ , which is the maximum frequency typically used for characterization of the proton conduction through PEMs by electrochemical impedance measurements.
- The proton conductivity of the water channels  $\kappa_{ch}$  was assumed to equal that of an aqueous solution with an equal molarity as the water channels in Nafion® ( $\kappa_{ch} \approx 0.6\,\mathrm{S~cm^{-1}}$  at 25 °C), based on the data stated in Table 14.2.1.

Using these values,  $Z_{sp}$  was estimated to be at least 2600 times larger than  $Z_{ap}$ . The impedances of more than one polymeric capacitors between the water channels are additive. Consequently, the impedances between the water channels are too small in order to contribute in a significant amount to the overall conductivity of Nafion<sup>®</sup> membranes.

# 14.2.2 Procedure to determine the proton conductivity of HCl

In order to separate the contributions of the  $Cl^-$  anions and the protons to the measured conductivity of the aqueous HCl solution, a KCl solution of similar molarity was used as a reference. Potassium cations (K<sup>+</sup>) and chloride ions (Cl<sup>-</sup>) show similar mobilities in aqueous solution, as characterized by their ion transport numbers (deviation below 1 % [10]), since they are of approximately equal weight and size. Hence, approximately half of the measured ionic conductivity of KCl is attributable to the movement of chloride, while the other half is attributable to the movement of the potassium cations. In a solution of HCl, the contributions of the chlorine ions to the conductivity are assumed to equal that in a solution of KCl with the same molarity.

Table 14.2.1: Parameters of the polymeric fits  $\kappa(T) = a + b \ T + c \ T^2 + d \ T^3$  that describe the mean of the measured conductivities of Nafion<sup>®</sup>, TMSA, HCl, and KCl as a function of temperature. The units S cm<sup>-1</sup> vs. °C were employed for the fit. Using these mean fits to the aqueous solutions, the parameters for the conductivity of H<sup>+</sup> in the aqueous solutions were determined by equation 14.2.6.

|                    | unit   | Nafion <sup>®</sup> | HCl    | KCl    | $H^+$  | TMSA   |
|--------------------|--|---------------------|--------|--------|--------|--------|
| а                  | $10^{-1}\mathrm{Scm^{-1}}$   | 0.493               | 3.855  | 2.371  | 2.669  | 2.585  |
| b                  | $10^{-2}\mathrm{Scm^{-1}^{\circ}C^{-1}}$                           | 0.138               | 1.181  | -0.038 | 1.200  | 0.828  |
| С                  | $10^{-6}  \mathrm{S}  \mathrm{cm}^{-1}  {}^{\circ}\mathrm{C}^{-2}$ | 3.873               | -9.428 | 113.5  | -66.17 | -8.465 |
| d                  | $10^{-8}\mathrm{Scm^{-1}^{\circ}C^{-3}}$                           | -3.395              | -9.596 | -81.70 | 31.25  | 1.190  |
| relative error / % |  | 8                   | 6      | 6      | 8      | 6      |

Accordingly, by subtracting the contributions of the chlorine ions to the conductivity of HCl, the proton conductivity  $\kappa_{H^+}$  of the aqueous HCl solution was estimated to:

$$\kappa_{\rm H^+} \approx \kappa_{\rm HCl} - \frac{1}{2} \kappa_{\rm KCl} \tag{14.2.6}$$

### 14.2.3 Fitting procedure and error calculation

Table 14.2.1 displays the values of the polynomial fits to the measured conductivities as a function of the temperature. The fitting procedure and the estimation of the statistical measurement error was conducted as follows:

- 1. The high frequency impedance of an electrolyte was measured more than five times as a function of the temperature.
- 2. Using the software 'Origin', the measured curves were averaged and the standard deviation was calculated.
- 3. A polynomial fit of third grade to the averaged curve was conducted. The parameters of these fits are stated in Table 14.2.1.

The high frequency impedances of four Nafion<sup>®</sup> NR212 (62 µm) and four Nafion<sup>®</sup> N117 (200 µm) membranes were examined, while the mean thicknesses stated in the brackets refer to the fully hydrated state (samples immersed in water at room temperature). The variations of the sample thicknesses were measured to approximately 5 %. Figure 14.2.2 shows the measured conductivities of these samples. The mean conductivities of the N117 and NR212 samples showed a standard deviation below 8 %. Within this deviation, which may be attributable to measurement errors, the conductivity of Nafion<sup>®</sup> is independent from the sample thickness. By using the propagation of errors and the values stated in Table 14.2.1, the error of  $\frac{\kappa_{as}}{\kappa_N}$  for the ionic conductivities of HCl and TMSA was estimated to 10 %. In the case of the ratio of the proton conductivity of HCL to the conductivity of Nafion<sup>®</sup> the error was estimated to 12 %.

164 14 Attachment

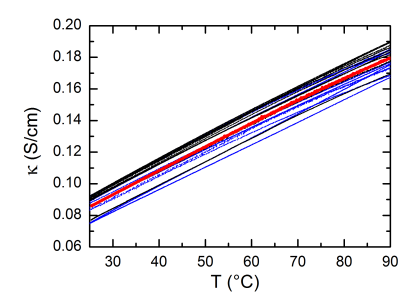


Figure 14.2.2: Conductivity of five Nafion<sup>®</sup> N117 (black) and five NR212 (blue) samples as a function of temperature. Red line: Mean of all the measurements.

### 14.2.4 Derivation of the geometric restrictions factor

In this section, the geometric restriction factor  $\zeta$  is derived and its physical origins are discussed. Within this aim, the influence of the volume fraction of the aqueous phase, the connectivity of the water channels, the tortuosity of the water channels, and the varying diameter of the water channels on the proton conductivity are physically described.

#### Mean cross-sectional area of the aqueous phase

The volume of a rectangular cuboid equals the product of the cross-sectional area A and the thickness d. May this volume be filled with a fully hydrated PEM. By dividing the rectangular cuboid into k slices with equal thicknesses  $d^i = d/k$ , the volume equals:

$$V = \sum_{i=1}^{k} d^{i} A^{i}$$
 (14.2.7)

With an infinitesimal discretization, the volume of the aqueous phase can be determined by

$$V_{\rm ap} = \sum_{i=1}^{k} d^i A_{\rm ap}^i \,, \tag{14.2.8}$$

where  $A_{ap}^{i}$  denotes the area of the aqueous phase of the *i*-th slice. Using the relation  $d^{i} = d/k$ , the latter equation can be rewritten to:

$$V_{\rm ap} = \frac{d}{k} \sum_{i=1}^{k} A_{\rm ap}^{i}$$
 (14.2.9)

With  $\frac{1}{k}\sum_{i=1}^{k}A_{ap}^{i}=\bar{A}_{ap}$ , the volume of the aqueous phase is a function of the mean cross-sectional area  $\bar{A}_{ap}$  of the aqueous phase:

$$V_{\rm ap} = d \bar{A}_{\rm ap} \tag{14.2.10}$$

By dividing the latter equation through V=d A, the volumetric water content  $\phi=\frac{V_{\rm ap}}{V}$  can be related to the mean cross-sectional area of the aqueous phase:

$$\phi = \frac{\bar{A}_{ap}}{A} \tag{14.2.11}$$

Thus, the mean cross-sectional area of the aqueous phase normalized to the overall cross-sectional area equals the volumetric water content.

#### Effect of connectivity

Water channels, which do not connect the electrodes cannot contribute to the proton conductivity. Such dead end water channels cannot contribute to the proton conductivity. Consequently, the effective volumetric water content of the aqueous phase  $V_{\rm ap}^{\rm eff}$  that is available for the proton conduction is smaller than the total volume of water  $V_{\rm ap}$ . The connectivity  $\psi$  is here defined as the ratio of both volumes and will be used to quantify the impact of the different topologies on the proton conductivity of Nafion<sup>®</sup>:

$$\psi = \frac{V_{\rm ap}^{\rm eff}}{V_{\rm ap}} \tag{14.2.12}$$

In other words, this ratio equals the water volume of the first and second topology normalized to the total volumetric water content. Thus, when  $\psi = 1$ , dead end water channels do not appear.

#### Effect of tortuosity

When a proton permeates through the microscopic structure of Nafion<sup>®</sup>, the geometric tortuosity  $\tau_{\rm geo}$  of the water channel causes a larger permeation length  $l_{\rm ap}$  than the distance l between the start and end point of this movement:

$$l_{\rm ap} = l \, \tau_{\rm geo} \tag{14.2.13}$$

The effective tortuosity  $\tau_{\rm eff}$  is here defined as the mean tortuosity of all percolation paths for the long range proton permeation between the electrodes. In this case, the mean permeation length  $l_{\rm eff}$  required for the proton conduction from one electrode to the other is connected to the effective tortuosity by:

$$l_{\text{eff}} = l \, \tau_{\text{eff}} \tag{14.2.14}$$

When all water channels have an equal geometric tortuosity and mean cross-sectional area, the connectivity can be represented by

$$\psi = \frac{l_{\text{geo}}}{l_{\text{eff}}} \tag{14.2.15}$$

166 14 Attachment

based on the definitions stated above. Thereby, the geometric and the effective tortuosity are related to one another using the connectivity  $\psi$ :

$$\tau_{\text{geo}} = \psi \, \tau_{\text{eff}} \tag{14.2.16}$$

The tortuosities are always equal or larger unity ( $\tau \geq 1$ ).

#### Effect of pore diameter variation

The mean cross-sectional area of the water channels equals the volume fraction of water in Nafion<sup>®</sup> (as derived above). In the case of more narrow segments of the water channels than the mean cross-section area, these local bottlenecks for the proton conduction decrease the proton conductivity through the water channels, as calculated in the following. In order to simplify the calculations, the resistance for the permeation of protons through a single water channel is considered. This specific trajectory through the considered water channel is denoted by the index j. The trajectory is separated into infinitesimal equal lengths  $l^i$ , that have an individual cross-sectional area  $A^i$  of the water channel. Each segment of this trajectory is expressed by a resistance. The total resistance of this trajectory is the series connection of the resistances of the segments

$$R^{j} = \sum_{i=1}^{k^{j}} R^{i} , \qquad (14.2.17)$$

where *k* denotes the amount of the segments. By including the geometry of the resistance segments the following equation results

$$R^{j} = \frac{1}{\kappa_{\rm ap}} \sum_{i=1}^{k^{j}} \frac{l^{i}}{A^{i}} \,, \tag{14.2.18}$$

where  $\kappa_{ap}$  denotes the mean conductivity of the aqueous phase. The mean diameter  $\bar{A}$  of the water channels is:

$$\bar{A} = \frac{1}{k^i} \sum_{i=1}^{k^i} A^i \tag{14.2.19}$$

Variations from this mean cross-sectional area increase the reciprocal sum of the areas  $\sum_{i=1}^{k^j} \frac{1}{A^i}$  in equation 14.2.18. In order to take these variations of the cross-sectional into account, the factor  $\delta$  will be used in the following:

$$\sum_{i=1}^{k^{j}} \frac{1}{A^{i}} = k^{j} \, \delta^{j} \, \frac{1}{\bar{A}} \tag{14.2.20}$$

The factor  $\delta$  is at least unity:  $\delta \geq 1$ .

The total permeation length  $l_{eff}^{j}$  equals sum of the infinitesimal lengths:

$$\sum_{i=1}^{k^{j}} l^{i} = l_{\text{eff}}^{j} = l \, \tau_{eff}^{j} \tag{14.2.21}$$

As a result, using the latter equations, the resistance of a trajectory is given by:

$$R^{j} = \frac{1}{\kappa_{\rm ap}} \frac{l \, \tau_{\rm eff}^{j} \, \delta^{j}}{\bar{A}^{j}} \tag{14.2.22}$$

#### Combination of all the restrictions

By considering the mean of the above discussed parameters, the mean resistance of all the water channels can be calculated on the basis of equation 14.2.22, which was used to describe the resistance of one trajectory:

$$\bar{R} = \frac{d}{\kappa_{\rm ap}} \frac{\tau_{\rm geo} \, \delta}{\psi \, \bar{A}_{\rm ap}} \,, \tag{14.2.23}$$

The conductivity  $\kappa_{ap}$  describes the mean conductivity of the aqueous phase. Using the relation between the conductivity and the resistance ( $\kappa = \frac{d}{AR}$ ), the conductivity of Nafion<sup>®</sup> is described by

$$\kappa_{\rm N} = \kappa_{\rm ap} \frac{\bar{A}_{\rm ap}}{A} \frac{\psi}{\tau_{\rm geo} \, \delta} = \kappa_{\rm ap} \, \zeta$$
(14.2.24)

where the influence of the geometric restrictions on the conductivity are here defined as the geometric restriction factor

$$\zeta = \frac{\bar{A}_{\rm ap}}{A} \frac{\psi}{\delta \tau_{\rm geo}} \tag{14.2.25}$$

which is per definition equal or smaller unity. Accordingly, all the factors that account for the geometric restrictions of the proton conduction ( $\frac{\bar{A}_{ap}}{A}$ ,  $\psi$ ,  $\delta$ , and  $\tau_{geo}$ ) increase the resistance for the proton conduction through Nafion<sup>®</sup> (eq. 14.2.22). By using resistor network modeling, the geometric restriction factor can be estimated as all the effects discussed above influence the modeled resistance.

Besides the geometric restrictions of the proton conduction, the decrease of the proton mobility due to the distribution and form of the anions in Nafion<sup>®</sup> in comparison to that of aqueous solutions was discussed in the Section 5. These differences of the mobilities is in the following described by the ratio of the proton mobility in aqueous

168 14 Attachment

phase of Nafion<sup>®</sup>  $\mu_{H^+}^{ap}$  to that of aqueous solutions  $\mu_{H^+}^{as}$ . Using these definitions, the mobilities and conductivities of the protons in the aqueous phase of Nafion<sup>®</sup> and in the aqueous solutions can be related to one another:

$$\kappa_{\rm ap} = \frac{\mu_{\rm H^+}^{\rm ap}}{\mu_{\rm H^+}^{\rm as}} \kappa_{\rm as} \tag{14.2.26}$$

Combining equation 14.2.24 and 14.2.26, the proton conductivity of Nafion<sup>®</sup> can be related to that of the aqueous solution with similar molarity:

$$\kappa_{\rm N} = \kappa_{\rm as} \frac{\mu_{\rm H^+}^{\rm ap}}{\mu_{\rm H^+}^{\rm as}} \zeta,$$
(14.2.27)

By transposing this equation, the factor that the Nafion<sup>®</sup> conducts protons less good than its aqueous phase can be expressed as:

$$\frac{\kappa_{\rm N}}{\kappa_{\rm as}} = \frac{\mu_{\rm H^+}^{\rm ap}}{\mu_{\rm H^+}^{\rm as}} \zeta$$
 (14.2.28)

#### 14.2.5 Influence of the water content on the estimated values

In the Section 5,  $\lambda \approx 20$  was assumed fully hydrated Nafion<sup>®</sup> based on data reviewed in the literature. Lufrano et~al.~[228] reported higher values of up to  $\lambda \approx 26$ . In the following, the calculations presented in Section 5 are exemplified for  $\lambda \approx 26$  in order to show, how the calculated values change with this parameter. A water content of  $\lambda = 26$  means a proton concentration of  $c_{\rm H^+} \approx 2.1\,{\rm mol}\,{\rm l}^{-1}$  that would reduce the conductivity of the aqueous phase. In the case of HCl, the conductivity is with a concentration of  $2.1\,{\rm mol}\,{\rm l}^{-1}$  approximately 82 % smaller than that with  $2.8\,{\rm mol}\,{\rm l}^{-1}$ . Accordingly, in the case of  $2.1\,{\rm mol}\,{\rm l}^{-1}$ , the ratio of the conductivities is  $\frac{\kappa_{\rm as}}{\kappa_{\rm N}} \approx 4.9\pm0.7$ . The inverse of this ratio equals approximately  $0.2\pm0.03$ .

# 14.3 Additional information to the permeability measurements

This chapter is based on a previously published study [Schalenbach2015]. In the following, the experimental settings used for the permeability measurements will be discussed in detail. Furthermore, the prefactors related to the activation energies in Table 6.1.1 are given in Table 14.3.1.

PTFE [185] H<sub>2</sub>O Nafion® (wet) PTFE\* Gas Prefactor Nafion® (dry) 1.82 [185] 3.17 #  $378 \pm 18$  $4.8 \pm 0.9$  $0.45 \pm 0.09$  $\varepsilon_0$  $4.9 \pm 0.3$  [124]  $H_2$  $D_0$ 0.65 #  $S_0$ 0.31 [185] 0.36 #  $0.72 \pm 0.1$  $506 \pm 227$  $0.10 \pm 0.02$  $\varepsilon_0$  $0.64^{\ [185]}$  $4.2 \pm 0.2^{\ [124]}$  $O_2$  $D_0$  $2.8 \times 10^{-4}$  [185]  $0.14 \, ^{\sharp}$  $S_0$ 

Table 14.3.1: Prefactors related to the activation energies stated in Table 6.1.1, using the same notation. Units:  $[\varepsilon_0] = 10^{-8} \text{ mol cm}^{-1} \text{ s}^{-1} \text{ bar}^{-1}$ ,  $[D_0] = 10^{-2} \text{ cm}^2 \text{ s}^{-1}$ ,  $[S_0] = 1 \text{ mol cm}^{-3} \text{ bar}^{-1}$ 

## 14.3.1 Electrochemical half-cell with sulfuric acid electrolyte

To measure the influence of temperature on the hydrogen and oxygen permeation through Nafion<sup>®</sup> (DuPont) and PTFE (Bola,  $55\mu$ m), setup C (Fig. 4.2.1C) was used. In this electrochemical cell, the sample and the electrodes were in contact with an aqueous solution of 1 M sulfuric acid. The gas, of which permeation through the sample was to be examined, was supplied through a titanium flow field. Carbon paper (Toray, TPG-H-120) between the membrane and the flow field acted as a gas diffusion layer to equally distribute the supplied gas along the sample. The gas was purged at a flow rate of 3 ml/min through the titanium flow field using a mass flow controller (Brooks, model 5850E). To avoid the dehydration of the Nafion® samples, the supplied gas was first humidified at 95 °C and then cooled to room-temperature before entering the flow field. Thus, the gas was saturated with water vapor and additionally carried liquid water. Accordingly, the Nafion® samples in this configuration were fully hydrated by the supply of liquid water from both sides of the samples. For the purpose of humidification, an in house-build membrane humidifier was used, where the gas was purged along a fully hydrated Nafion® NR212 (DuPont) membrane. Absolute pressures between 1 bar and 5 bar were applied to the gases (hydrogen/oxygen) at the titanium flow field, regulated by a pressure controller (Brooks, model 5866).

The working electrode (in the form of the catalyst coated carbon fleece) was laid directly onto the sample with the catalyst layer facing the sample. A platinum mesh contacted by a platinum wire was sandwiched between the working electrode and carbon paper. This carbon paper mechanically supported the weaker carbon fleece substrate of the working electrode (Fig. 4.2.1C). During the measurements, the electrolyte chamber was at atmospheric pressure. Applying pressure to the supplied gas in the flow field thus resulted in a differential pressure. In order to withstand this pressure, additional mechanical support of the working electrode was given by a perforated polycarbonate plate between the working electrode assembly and the electrolyte chamber, where a platinum mesh served as the counter electrode. Holes of

170 14 Attachment

4 mm in the perforated polycarbonate contacted the electrolyte between the working electrode and the counter electrode. The electrolyte chamber itself was also made of polycarbonate.

In order to mitigate the diffusion from the evolved gases at the counter electrode to the working electrode, the concentration of these gases in the electrolyte chamber were reduced by purging with nitrogen. To measure the influence of temperature on the permeability, the temperature of the cell was linearly swept at a rate of  $0.2\,\mathrm{K/min}$ . The heater was integrated into the steel end plates of the cell. At increasing or decreasing temperature of the sweep the permeabilities measured revealed equal temperature dependencies and values. Hence, using the discussed sweep rates, the changes in temperature did not lead to a delay of the permeability measured.

### 14.3.2 Electrochemical cell with Nafion® electrolyte

Setup D (Fig. 4.2.1D) was used to measure the hydrogen permeation through Nafion<sup>®</sup> as a function of differential pressure and relative humidity. In this setup, the working electrode and counter electrode consisted of catalyst-coated gas diffusion layers (Section 14.1). These electrodes were hot-pressed onto the Nafion<sup>®</sup> samples. These sample acted as the electrolyte for the electrochemical conversion of hydrogen cross-permeation. The gas diffusion layers of the electrodes were electrically contacted using in-house made platinum plated titanium flow fields. Hydrogen was purged along the flow field at the counter electrode, while nitrogen was purged along the flow field at the working electrode.

To measure the influence of pressure on the permeability (Fig.6.1.1), the gases were humidified at 95 °C and cooled to room temperature before they reached the cell. Using this configuration, the Nafion<sup>®</sup> sample was fully hydrated during the measurement, because it was in contact with liquid water and saturated water vapor pressure. A flow-rate of 3 ml/min for the hydrogen and nitrogen fluxes was applied during these measurements. Two pressure controllers (Model 5866, Brooks) were used to control the pressures of the supplied gases. No considerable difference of the measured hydrogen permeability of the fully hydrated Nafion<sup>®</sup> samples with setup C (Section 14.3.1 and Fig. 4.2.1) and this setup could be observed, as illustrated in Figure 6.1.2. Thus, at full hydration of the samples, the determined permeabilities with both electrochemical cells are equal with respect to the measurement precision.

The permeability measurements as a function of relative humidity were performed at atmospheric pressure of the supplied gases, which were purged with flow rates

of 50 ml/min through the flow fields of the cell. The temperature of the humidifiers was swept upwards with a rate of 0.1 K/min, while the temperature of the cell with the sample was constantly 80 °C. The relative humidity of the supplied humidified gases was determined by their dew point. After passing the cell, these gases were conducted through a small tube into an in house-made measurement system for the dew point. In this system, the gases were first heated in a stainless steel tube with the shape of a spiral. This spiral was immersed into a water bath with a temperature of 85 °C. Afterwards, the heated gases were conducted through a glas bottle, which was immersed into the same water bath as the steel spiral. In this glas bottle a temperature and humidity probe (HMP-77, Vaisala) was implemented, which measured the dew point of the gases. Within the measurement precision ( $\approx \pm 1$  °C), the dew point equaled the temperature of the membrane humidifiers. Using Antoine's equation (eq. 4.2.3), the temperatures of the membrane humidifiers was correlated with the partial pressure of the saturated water vapor. The ratio of this partial pressure of water vapor to that of saturated water vapor at the cell temperature was taken as the relative humidity.

In this setup, the electrochemical conversion of hydrogen cross-permeation through the membrane caused a proton flux in the opposing direction. This proton flux led to an electro-osmotic water drag [117,118]. Thereby, diluted hydrogen in the aqueous phase of the membrane was possibly also transported through the membrane sample. Thus, the permeation of water and protons possibly influenced the hydrogen cross-permeation through the membrane by convection. By measuring the fully hydrated Nafion<sup>®</sup> samples, this effect could not be observed, since setup C and setup D yielded equal permeabilities with respect to the measurement precision (Figure 6.1.2). However, the influence of the electro-osmotic water drag in setup C might influence the hydrogen diffusion at lower hydration levels and thus possibly enlarge the measurement error.

### 14.3.3 Cell for the measurement of the dry PEMs

To measure the permeability of the dry membrane samples, setup E was used (Figure 4.2.1E), where two cells were connected in series. In the first cell, hydrogen was purged with a flow rate of 3 ml/min along one side of the membrane. At the other side nitrogen was purged with a flow rate of 3 ml/min. The hydrogen permeating through the membrane was carried with the nitrogen flux to the second cell, where it was electrochemically converted. In this second cell, the nitrogen and hydrogen mixture was purged through the porous working electrode, which was fabricated as discussed above (Section 14.1). This working electrode was immersed into a 1 M H<sub>2</sub>SO<sub>4</sub> electrolyte, where the counter electrode was a platinum mesh. The hydrogen

172 14 Attachment

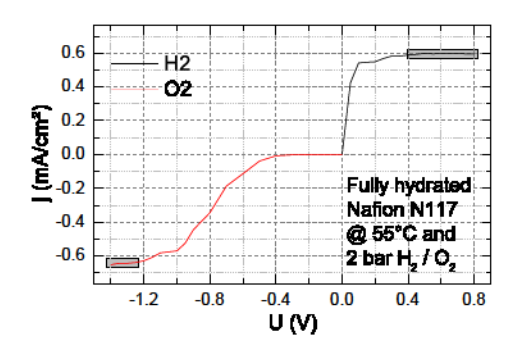


Figure 14.3.1: Voltage-current characteristic of setup C (Fig. 4.2.1C) with a Nafion N177 sample at 55 °C. Pressures of either 2 bar hydrogen or 2 bar oxygen were applied at the gas inlet of the cell. When the hydrogen permeation through the sample was measured, the working electrode was employed as the anode (+). In this case, the voltage and current were defined as positive. Voltage and current were defined as negative for the cathodic operation of the working electrode (-), which was used to reduce the oxygen coming through the sample. The voltages at which the saturation current densities were reached are shaded grayish.

at the working electrode was electrochemically converted and evolved at the counter electrode. In the cell, the counter electrode is arranged above the working electrode, so that the hydrogen bubbles evolved at the counter electrode rise upwards in the electrolyte and do not come in contact with the working electrode. Additionally, the electrolyte of the cell was purged with nitrogen to reduce the concentration of hydrogen in the electrolyte, to mitigate its diffusion from the counter electrode to working electrode. In the case of oxygen, the measurement were conducted using the equal procedure.

### 14.3.4 Saturation current density

By initially applying a constant voltage to both electrodes in the employed setups a time-dependent current resulted. This time-dependence was caused to capacitive double layers at the electrodes and dissolved gases in the electrolyte. After less than 10 min, these capacitive currents were negligible as the electrochemical capacitor that consists of the working electrode and counter electrode was charged. Therewith, a current plateau was reached. This current corresponded to the electrochemical conversion of the gas which instantaneously permeated through the membrane. Due to kinetic and ohmic losses, overvoltages must be spent in order to drive the electrochemical reactions at the electrodes.

To evaluate whether all of the hydrogen or oxygen that permeated through the sam-

ple was electrochemically converted, the voltage-current characteristics between the working electrode and counter electrode were considered. The current increased with the applied voltage until all of the hydrogen or oxygen at the working electrode was electrochemically converted. In this case, the diffusion limitation led to the saturation of the electrochemical current, as shown in Figure 14.3.1. In the acid regime, smaller overpotentials are required for the electrochemical oxidation of hydrogen than that for the reduction of oxygen [229]. Thus, the saturation current density for hydrogen was reached at a smaller voltage of 0.4 V between the working electrode and counter electrode than that for oxygen at -1.25 V.

To avoid corrosion of the carbon support at the working electrode during its anodic operation for the oxidation of hydrogen, the applied voltage was limited to 0.8 V. To measure oxygen permeation, the platinum mesh was used as the anode so that the applied voltage was only limited by the decomposition voltage of the employed electrolyte. In order to examine whether all of the oxygen permeating through the membrane was reduced at the working electrode without parasitic contributions caused by the electrochemical decomposition of water, the measurements of the oxygen cross-permeation for applied voltages of -1.3 V, -1.35 V, and -1.4 V were compared. In the case of equal measured currents over the entire temperature range for all these different voltages, all of the oxygen at the working electrode was reduced and the saturation current density was reached. When the saturation current density is not reached, the temperature dependence of the overvoltages of the electrochemical reaction would lead to different currents as a function of temperature and voltage. When water is electrolyzed during the measurements in measurable amount, higher currents at -1.4 V than at -1.3 V had result. Thus, the equality of the measurements also ensures a negligible influence of the electrochemical decomposition of the electrolyte on the current measured.

### 14.4 Resistor network modeling

The supporting information to Chapter 7.1 provided in the following includes the simulated oxygen permeabilities for fully hydrated Nafion<sup>®</sup>, the computer code to generate the calculation domain which reproduces the microscopic structure of Nafion<sup>®</sup> and which runs the diffusion simulations on this domain.

### 14.4.1 Simulated oxygen permeability of fully hydrated Nafion®

In order to simulate the oxygen permeability of fully hydrated Nafion<sup>®</sup>, the same procedure as discussed for the hydrogen permeability was used. As a result of the simulation of the hydrogen permeability, the set of parameters that described the per-

174 14 Attachment

meability as a function of the temperature and water content in the best way was obtained for the case A ( $\varepsilon_{ap}=0.5~\varepsilon_{w}$ ) and a softened solid phase. Based on these findings, the simulations of oxygen were conducted only for the case A. Figure 14.4.1 shows the simulated permeability for a increased intermediate phase, so that the simulated oxygen permeability was fitted to the measured oxygen permeability (fitting procedure same as for hydrogen). In order to get an agreement of the simulated permeability and the measured permeability at 80 °C, an interfacial permeation factor of  $\Lambda=9.6$  was used. In the case of  $\Lambda=1$ , the simulated permeability of fully hydrated Nafion<sup>®</sup> at 80 °C is approximately by a factor of 0.60 smaller than the measured permeability.

Figure 14.4.2 shows the simulated oxygen permeability with the parameters of the softened solid phase (Table 14.4.1). In the total temperature range, the simulated oxygen permeabilities match the measured oxygen permeabilities using this approach. Moreover, Figure 14.4.2 also shows the oxygen permeabilities of the softened solid phase for case A. At 80 °C and for case A, the permeability of the softened solid phase was approximately 2.4 times larger than that of dry Nafion<sup>®</sup>. The ratio of the softened permeability to the measured permeability equals approximately 0.55 in case A. In the case of dry Nafion<sup>®</sup>, the ratio of  $\varepsilon_{\rm dN}$  to  $\varepsilon_{\rm wN}$  equals approximately 0.13.

In the case of the hydrogen permeability of Nafion<sup>®</sup>, the deviation from the Boltzmann distribution were elucidated. In the case of the measured oxygen permeability of fully hydrated Nafion<sup>®</sup>, the trends of the deviation factors were not reproducible, since the measurement precision for oxygen compared to that of hydrogen is smaller (caused by the larger overpotentials for its electrochemical conversion [1st-part]). Hence, the precise measurement resolution of hydrogen below 2 % could not be achieved for the measured oxygen permeability. In addition, the deviations from linearity of the measurements of polytetrafluoroethylene (PTFE) and dry Nafion<sup>®</sup> [1st-part] were also not reproducible, since the hydrogen and oxygen permeabilities of these materials were at least fivefold smaller than that of fully hydrated Nafion<sup>®</sup>. Thus, the current measured was smaller, which made the measurement more sensitive to measurement errors and noise and led to a larger deviation than the 2 %.

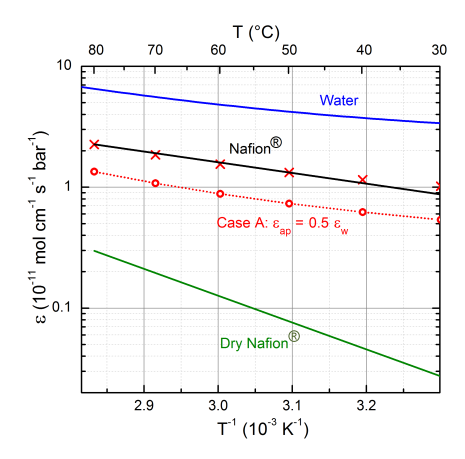


Figure 14.4.1: Oxygen permeabilities in a modified Arrhenius plot (logarithmic scale of  $\varepsilon$  vs. 1/T) for the case of an increased permeability of the intermediate phase. Black: Mean of the measured permeability of fully hydrated Nafion<sup>®</sup>. Dark green: Mean of the measured permeability of dry Nafion<sup>®</sup>. Red: Case A ( $\varepsilon_{\rm ap}=0.5\,\varepsilon_{\rm w}$ ). Open circles with dotted lines: Simulated permeabilities for  $\Lambda=1$ . Crosses: Simulated permeability for case A with  $\Lambda=9.6$ .

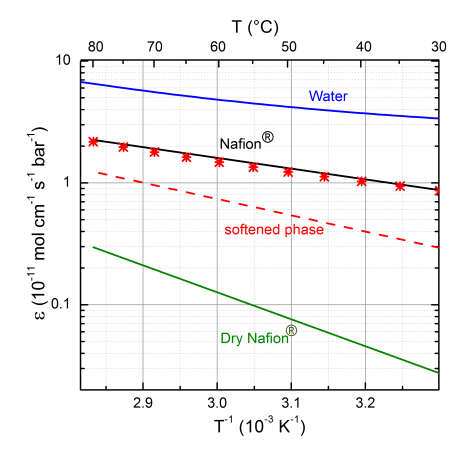


Figure 14.4.2: Oxygen permeabilities in a modified Arrhenius plot for the case of an increased permeability of the solid phase. Dotted red line: Permeability of the softened solid phase for case A (parameters stated in Table 14.4.1). Red stars: Simulated permeability for case A. Color code of the other lines equal that in Figure 14.4.1.

#### 14.4.2 Codes

In the following the computer code used to simulate the permeability are presented. The code to model the microscopic structure of Nafion<sup>®</sup> and to simulate the permeability looked as followed, as exemplified for case B ( $\varepsilon_{ap} = 0.8 \, \varepsilon_{w}$ ). Besides an

176 14 Attachment

Table 14.4.1: Prefactors and activation energies of the oxygen permeability that describe the softened solid phase of humidified Nafion<sup>®</sup> for case A. This enlarged permeability is the solution for the fit in Figure 14.4.2.

|        | $\varepsilon_0 (10^{-7}  \text{mol cm}^{-1}  \text{s}^{-1}  \text{bar}^{-1})$ | E <sub>e</sub> (10 <sup>-20</sup> J) |
|--------|---|--------------------------------------|
| case A | 7.57  | 4.25                                 |

installation of Python, the only required external packages are OpenPNM, SciPy and noise, as described in Section 7.1.

```
import scipy as sp
import OpenPNM as op
'''Define Functions for Assigning Permeation Resistances'''
def boltzman(physics, Ao, Ea, temperature='pore.temperature', **kwargs):
   T = physics[temperature]
   p = Ao*sp.exp(-Ea/(sp.constants.k*T))
   return p
def power(physics, A, B, C, D, E, F, temperature='pore.temperature', **
   kwargs):
   T = physics[temperature]
   p = F*(A + B*1000/T + C*sp.power(1000/T,2) + D*sp.power(1000/T,3) + E*
   sp.power(1000/T,4))
   return p
def perlin_noise(geometry, freq=1, octaves=4, mode='classic', **kwargs):
   from noise import pnoise3, snoise3
   import scipy.stats as spst
    net = geometry._net
    if mode == 'classic':
       model = pnoise3
    elif mode == 'simplex':
       model = snoise3
    freq = freq * octaves
   x = net.\_shape[0]
   y = net.\_shape[1]
   z = net.\_shape[2]
   temp = sp.ndarray((x, y, z))
   for k in range(z):
        for j in range(y):
            for i in range(x):
                temp[i, j, k] = model(i/freq, j/freq, k/freq, octaves) +
   0.5
```

```
# Assuming that the noise is normally distributed, find seeds of that
   dist
    temp = sp.reshape(temp, (temp.size,))
    x_mean = sp.mean(temp)
    x \text{ sigma} = \text{sp.sqrt}(1/(\text{temp.size}-1)*\text{sp.sum}((\text{temp} - x \text{ mean})**2))
    fn1 = spst.norm(loc=x_mean, scale=x_sigma)
    values = fn1.cdf(temp)
    values = values[geometry.map_pores(target=net, pores=geometry.Ps)]
    return values.flatten()
def continuum_conductance(network, phase, physics, conductivity, **kwargs)
    Psigma = phase['pore.'+conductivity.split('.')[-1]]
    P12 = network['throat.conns']
    Plen = network['pore.diameter'][P12]/2
    Parea = network['pore.area'][P12]
    gP12 = Psigma[P12]*Parea/Plen
    g_{\text{conduit}} = (1/gP12[:, 0] + 1/gP12[:, 1]) **(-1)
    values = g_conduit[phase.throats(physics.name)]
    return values
'''Set Up Calculation Domain'''
Lc = 2.1 # set the lattice constant of the network in Angstroem
hi_frac = 0.56 # set the proportion of the high phase
# set the dimensions of the network in voxels
x = 200
y = 200
z = 200
# construct the network
pn = op.Network.Cubic(shape=[y, x, z], spacing=Lc)
geom = op.Geometry.GenericGeometry(network=pn)
geom.set_locations(pores=pn.Ps, throats=pn.Ts)
# assign random number to the network using the simplex noise algorithm
geom.models.add(propname='pore.seed',
                model=perlin_noise,
                mode='simplex',
                 freq = 5,
                 octaves=4)
# use thresholding to assign the phases to the calculation domain
geom['pore.hydrophobic'] = geom['pore.seed'] > hi_frac
geom['pore.interface'] = False
Ps = pn.find_neighbor_pores(pores=pn.pores('hydrophobic'),
```

178 14 Attachment

```
mode='union',
                             excl_self=True)
geom['pore.interface'][Ps] = True
geom['pore.hydrophilic'] = False
Ps = pn.pores(['hydrophobic', 'interface'], mode='not')
geom['pore.hydrophilic'][Ps] = True
# set the dimensions of the individual voxels to cubic depending on Lc
geom['pore.area'] = Lc**2
geom['pore.diameter'] = Lc
geom['pore.length'] = Lc
geom['throat.area'] = Lc**2
geom['throat.diameter'] = Lc
ionomer = op. Phases. GenericPhase (network=pn, name='nafion')
# assign permation resistances to the solid phase
phys_ho = op.Physics.GenericPhysics(network=pn, phase=ionomer)
Ps_ho = geom.pores('hydrophobic')
phys_ho.set_locations(pores=Ps_ho)
phys_ho.models.add(propname='pore.perm',
                   model=boltzman,
                   Ea = 6.237e - 20
                   Ao = 3.781e - 6
# assign permation resistances to the aqueous phase
phys_hi = op.Physics.GenericPhysics(network=pn, phase=ionomer)
Ps_hi = geom.pores('hydrophilic')
phys_hi.set_locations(pores=Ps_hi)
phys_hi.models.add(propname='pore.perm',
                   model=power,
                   A = 2.615E - 8
                   B = -2.95649E - 8
                   C = 1.26657E - 8.
                   D = -2.42863E - 9
                   E = 1.75525E - 10.
                   F = 0.8)
# assign permation resistances to the intermediate phase
phys_int = op.Physics.GenericPhysics(network=pn, phase=ionomer)
Ps_int = geom.pores('interface')
phys_int.set_locations(pores=Ps_int)
phys_int.models.add(propname='pore.perm',
                   model=power,
                   A = 2.615E - 8,
                   B = -2.95649E - 8,
                   C = 1.26657E - 8,
                   D = -2.42863E - 9
```

```
E = 1.75525E - 10,
                   F = 0.8)
phys_all = op. Physics. GenericPhysics (network=pn, phase=ionomer)
phys_all.set_locations(throats=pn.Ts)
phys_all.models.add(propname='throat.diffusive_conductance',
                    model=continuum_conductance,
                    conductivity='pore.perm')
'''Begin Simulations'''
# initialize the algorithm object
DiffAlg = op. Algorithms. Fickian Diffusion (network=pn, phase=ionomer)
moleflux = []
ionomer['pore.temperature'] = 353
for phys in [phys_hi, phys_ho, phys_int]:
    phys.regenerate()
phys_all.regenerate()
# apply Dirichlet boundary conditions to the inlet (5 bar) and outlet (0.1
DiffAlg.set_boundary_conditions(pores=pn.pores('left'),
                              bcvalue=[5],
                               bctype='Dirichlet',
                              mode='overwrite')
DiffAlg.set_boundary_conditions(pores=pn.pores('right'),
                               bcvalue = [0.1],
                               bctype='Dirichlet',
                              mode='merge')
DiffAlg.run()
moleflux.append(DiffAlg.rate(pn.pores('right')))
# calculate the permeability through the calculation domain
eps = sp.array(moleflux)*x/((5-0.1)*(Lc*y*z))
```

# 14.5 Relation of adiabatic compression to isothermal compression

This part is based on a previously published study [45]. In the following, the thermodynamical adiabatic or isentropic work and efficiency of mechanical compression techniques will be related to those of isothermal compression processes. The calculations are exemplified for an adiabatic process, while all the equations are also valid for isentropic processes. The pressure and temperature of an isothermal process which leads to the same mole density as that of an adiabatic process are denoted as  $p_{\rm fin,iso}$  and  $T_{\rm iso}$ . The final state of the adiabatic process is described by  $p_{\rm f,ad}$  and  $T_{\rm f,ad}$ , while the initial state is

180 14 Attachment

described by  $p_{\text{ini,ad}}$  and  $T_{\text{ini,ad}}$ . Based on the ideal gas law (eq. 2.5.1), these pressures and temperatures can be correlated to one another for a gas with the same mole density at different temperatures:

$$\frac{p_{\text{fin,iso}}}{p_{\text{fin,ad}}} = \frac{T_{\text{iso}}}{T_{\text{fin,ad}}}$$
(14.5.1)

By inserting the latter equation into the equation that characterizes the temperature increase during an adiabatic process (eq. 2.5.8), the final pressure of the adiabatic compression can be expressed as a function of the initial temperature  $T_{i,ad}$  of the adiabatic process and a pressure  $p_{f,iso}$  and temperature  $T_{iso}$  of an isothermal process, which leads to the same molar density:

$$p_{\text{f,ad}} = \left(\frac{T_{\text{ini,ad}}}{T_{\text{iso}}} p_{\text{fin,iso}} \left(p_{\text{ini,ad}}\right)^{\frac{1-\gamma}{\gamma}}\right)^{\gamma}$$
(14.5.2)

Thus, the required pressure of an adiabatic process to achieve a defined mole density can be depicted as a function of the temperature and pressure of an isothermal process. By combing equation 14.5.2 and equation 2.5.10, the work of the adiabatic compression is expressed as a function of the final isothermal pressure:

$$W_{\rm ad}(p_{\rm f,iso}) = -\frac{5}{2} nRT_{\rm ini,ad} \left( \left( \frac{T_{\rm ini,ad}^{\gamma} p_{\rm fin,iso}^{\gamma} p_{\rm ini,ad}^{-\gamma}}{T_{\rm iso}^{\gamma}} \right)^{\frac{\gamma-1}{\gamma}} - 1 \right)$$
(14.5.3)

To reduce the temperature increase during an adiabatic compression, various stages for compression can be applied. In between these stages the compressed gas can be cooled. The total work required for those stages is additive

$$W_{\text{ad,t}} = \sum_{j} \frac{W_j^{\text{ad}}}{\eta_j^{ad}}, \qquad (14.5.4)$$

where  $W_j^{\rm ad}$  denotes the thermodynamic adiabatic work (eq 14.5.3) and  $\eta_j^{ad}$  the mechanical efficiency of the j-th adiabatic compression stage. The ratio of the work for isothermal compression (eq. 2.5.4) that of the adiabatic compression (eq. 14.5.4) relates the efficiency of an idealized adiabatic process to an idealized isothermal compression, which is defined as  $\eta_{\rm comp}^{\rm iso}$ :

$$\eta_{\text{comp}}^{\text{iso}} = \frac{W_{\text{iso}}(T_{\text{iso}})}{W_{\text{ad,t}}(T_{\text{ini,ad}})}$$
(14.5.5)

In the following, the isothermal compressor efficiency  $\eta_{\text{comp}}^{\text{iso}}$  will be determined for an idealized four stage adiabatic compression with cooling to  $30\,^{\circ}\mathrm{C}$  at 3, 10 and 30 bar absolute pressures in between the stages. This example represents a mechanical compressor, which does not allow heat exchange during the compression. During real mechanical compression, the temperature increase of the gas is due to the heat exchange with the environment smaller. The approximation of an idealized gas holds valid for the temperatures during the process (eq 2.5.8 and 14.5.2), while the deviations in the adiabatic index of  $\gamma = 1.4$  due to pressure and temperature enhancement are negligible [126]. Figure 14.5.1 illustrates the work and isothermal efficiency as a function of pressure. The assumed four stage mechanical compression has thermodynamically approximately 80 % (92 %) of the isothermal efficiency at 30 °C (80 °C) in the considered pressure range. Figure 10.3.2 showed, that with respect to a final hydrogen pressure of 30 bar at 80 °C, pressurized electrolysis is less efficient compared to electrolysis under atmospheric pressure with subsequent compression, when an isothermal compressor efficiency of 40 % at 30 °C can be achieved. This isothermal compressor efficiency corresponds to adiabatic compressor efficiencies of 50% for each of the assumed stage ( $\eta_{\text{comp}}^{\text{iso}} = 50\% \times 80\% = 40\%$ ). Because mechanical compression processes are isentropic ( $\gamma$  < 1.4), the adiabatic index was assumed to be higher than in real systems. Thus, the subsequent compression is from a thermodynamical point of view typically more efficiency

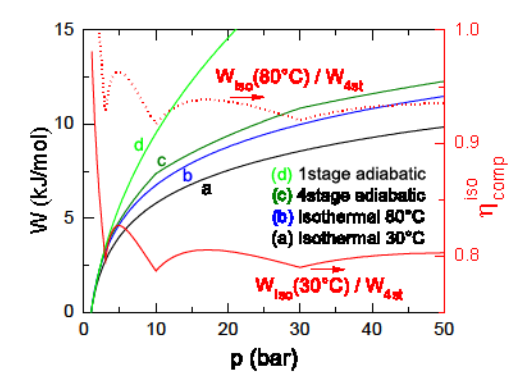


Figure 14.5.1: Left scale: Required thermodynamic work for an idealized isothermal compression (at 30 °C and 80 °C) and and adiabatic one and four stage compression (initial temperature at each stage: 30 °C). Right scale: Thermodynamic efficiency (eq 14.5.5) of idealized 4 stage adiabatic compression compared to idealized isothermal compression at 30 °C and 80 °C referring to equation 14.5.5.

than assumed here.

### 14.6 Setup to mitigate hydrogen crossover

All measurements were conducted under controlled current (galvanostatic) at a cell temperature of 85 °C. For the hydrogen pump configuration in Figure 11.1.1B, a Biologic HCP-1005 potentiostat was used to connect the additional electrode with the cathode. In order to connect the additional electrode to the anode for the local fuel cell configuration (Fig 11.1.1C), a current controlled electric load (Höckerl and Hackl GmbH, ZS Electronic Load) was used. The anodic hydrogen content was measured as described in Section 4.4. A PTFE gasket sealed the anode and a silicone gasket was used for the cathode sealing. Individual water circulation loops fed the anode and the cathode with water, respectively.

The membrane electrode assembly with the additional electrode was prepared as described in the following. One Nafion N1135 membrane was coated with two platinum-based catalyst layers on each side. Another Nafion N1135 membrane was coated with a platinum catalyst layer on one side and an iridium oxide catalyst layer on the other. The two N1135 membranes were layered on top of each other, so that the iridium oxide catalyst layer face upwards. Between the membranes an expanded titanium mesh of  $50\,\mu\mathrm{m}$  thickness (Dexmet) was immersed, which served as an electrical contact for the catalyst layers between the membranes. By hot-pressing at 145 °C, both membranes and the titanium mesh were melted together. The titanium mesh was larger than the membrane electrode assembly. The uncovered part of this mesh was electrically contacted by crocodile clips.

| 2.1.1 | voltage-current characteristic of a PEM water electrolyzer cell. Black points: Measured values of a PEM water electrolyzer cell with the setup described in Section 4.4. Gray line: Reversible voltage. Blue: Nernst voltage. The increase of the Nernst voltage toward higher current densities is ascribed to a partial pressure increase of hydrogen and oxygen in the electrodes (see Section 9.1 for detailed discussion). Green: Contributions of the Nernst voltage and the ohmic drop. Red line: Fit of equation equation 2.1.24 to the data. The kinetic overvoltages $\tilde{\eta}(j)$ were approximated by logarithmic shaped contributions of the Butler Volmer relation for the limit of |    |
|-------|---|----|
| 2.2.1 | large kinetic overvoltages [59]   | 12 |
| 2.2.1 | cribe the impedance measurements of electrochemical cells (based on [10, page 14]).   | 20 |
| 2.4.1 | Structural formula of Nafion $^{\circledR}$ adapted from [134]  | 26 |
| 4.1.1 | Schematic illustrations of the setups used to measure the impedance of membrane samples (A) and aqueous solutions (B)   | 36 |
| 4.2.1 | Schematic illustrations of the setups used for permeability measurements. WE: Working electrode. CE: Counter electrodes. (C): Electrochemical half-cell with aqueous sulfuric acid electrolyte. (D): Electrochemical cell, where the examined Nafion <sup>®</sup> membranes served as the electrolyte. (E): Setup used for dry Nafion <sup>®</sup> membranes.   | 40 |
| 4.4.1 | Measurements of the anodic hydrogen content as a function of the current density. The electrolysis cell was equipped with a Nafion <sup>®</sup> N117 membrane as discussed in the text in detail. Crosses: Measurements with the K1550 gas analyzer. Circles: Measurements with the XNX Transmitter gas analyzer.   | 43 |
| 4.4.2 | Time response of the measured anodic hydrogen content of a $25\mathrm{cm^2}$ PEM water electrolysis cell at $80^\circ$ C. Left to the green vertical line: Operation current density of $1.5\mathrm{Acm^{-2}}$ . Right to the green vertical line: Operation current density of $1\mathrm{Acm^{-2}}$ . Blue line: Balanced pressure operation. Red: Differential pressure operation   | 44 |
| 5.1.1 | Impedance spectra of a Nafion <sup>®</sup> N117 sample at room temperature recorded with amplitudes from 0.001 V to 1 V between the inner electrodes of setup A (Fig. 4.1.1). Top: Real part of the impedance. Bottom: Phase angle. The gray shaded area between 70 Hz and 70 kHz indicates the frequencies at which the impedance is dominated by the ohmic proton conduction. Toward higher frequencies capacitive contributions to the impedance increasingly contribute, while toward lower frequencies the influence of electrochemical electrode processes on the impedance increase  | 47 |
| 5.1.2 | Calculated permeation lengths $l$ of protons through the aqueous phase of Nafion <sup>®</sup> within one sign of the applied alternating voltage as a function of the frequency. Vertical dotted line: Mean diameter of the water channels of $2.5 \times 10^{-9}$ m as measured by Allen <i>et al.</i> [40]. Gray shaded area: Frequencies, where the ohmic resistance of the  |    |
|       | membrane dominates the impedance measured (Fig. 5.1.1)  | 49 |

| 5.2.1 | Nafion <sup>®</sup> as a function of temperature. The proton conductivity of the aqueous HCl solution denoted by H <sup>+</sup> was approximated as discussed in the attachment (Section 14.2). The aqueous solutions were of a molarity of $2.8  \text{mol}  1^{-1}$ , which corresponds to the molarity of the aqueous phase in fully hydrated Nafion <sup>®</sup> for $\lambda = 20$ . The fit parameters and a discussion of the measurement errors are also given in the attachment (Section 14.2). Squares: Literature data of the conductivity of HCl [179]. Dots: Literature data of the conductivity of KCl [180]. Bottom: Conductivities of the aqueous solutions (denoted as $\kappa_{as}$ ) in relation to that of Nafion <sup>®</sup> (denoted as $\kappa_N$ ). As discussed in the SI, the error of these ratios are approximately 12 % for the estimation of the proton conductivity of HCl and 10 % for HCl and TMSA | 52 |
|-------|--|----|
| 5.2.2 | Normalized conductivities of Nafion <sup>®</sup> as a function of the volume fraction of water $\phi$ exemplified for a temperature of 20 °C. Black: Normalization of the conductivity of Nafion <sup>®</sup> to the proton conductivity of an aqueous HCl solution. Red: Additional normalization to the water content. Vertical gray lines: Different relative humidities. Solid black and red lines: Based on the conductivities reported by Sone $et\ al.\ [41]$ . Points: Based on the conductivities measured in this study  | 54 |
| 6.1.1 | Measured hydrogen permeation flux density through a Nafion <sup>®</sup> N117 membrane as a function of the partial hydrogen pressure at the counter electrode. The absolute counter pressures of 1 bar (red dots) and 5 bar (black crosses) of humidified nitrogen at the working electrode led to equal current densities. Thus, differential pressure does not act as a driving force for gas permeation through Nafion <sup>®</sup> . The blue line represents the fit to the experimental data.  | 58 |
| 6.1.2 | Hydrogen permeability of Nafion <sup>®</sup> at 80 °C as a function of relative humidity (bottom) and normalized water content (top and vertical gray lines). See the text for the calculation of the normalized water content. Black points: Measured hydrogen permeability using setup D (Fig. 4.2.1D) of a Nafion <sup>®</sup> NR212 membrane. Blue cross and dotted blue line: Mean of the measured permeability at $rh = 100$ %. Blue circle: Mean of the measured permeability at fully humidified gas fluxes which also carried liquid water. Red cross and dotted red line: Mean of the measured permeability using setup C. Green star: Mean of the permeability of dry Nafion <sup>®</sup> measured with setup E (Fig. 4.2.1E)   | 60 |
| 6.1.3 | Measured hydrogen permeabilities ( $[\varepsilon] = \text{mol cm}^{-1}  \text{s}^{-1}  \text{bar}^{-1}$ ) of fully hydrated Nafion <sup>®</sup> membranes with various thicknesses as a function of temperature graphed in an Arrhenius plot. The permeabilities show an approximately linear relation in this depiction, which allows the estimation of their activation energies using the Boltzmann distribution (eq. 2.3.6)  | 61 |
| 6.1.4 | Modified Arrhenius plot (logarithmic scale of $\varepsilon$ instead of $\ln(\varepsilon)$ ) of the hydrogen permeabilities of water, Nafion <sup>®</sup> , and PTFE. Black points: Fully hydrated Nafion <sup>®</sup> (measured). Green Points: Dry Nafion <sup>®</sup> (measured). Red points: PTFE (measured). Blue line: Water [52,124] (calculated using eq. 2.3.17). Pointed gray line: guide to the eye with the slope of the permeability measurements of wet Nafion <sup>®</sup>   | 63 |
| 6.1.5 | Modified Arrhenius plot of the oxygen permeabilities of water, Nafion $^{(\!R\!)}$ , and PTFE. In this graph the same color code as that in Figure 6.1.4 was used  | 64 |

| 6.2.1 | Descriptive sketch of the pathways (red arrows) for the gas permeation through a segment of a PEM exemplified for hydrogen molecules. The solid polymeric phase (agglomerate of ionomers) is depicted as the gray area, water as the blue area and pores filled with gas as the white area. Left: Dry PEM. Right: Hydrated PEM. The hydration of the PEM leads to the formation of water channels, where the permeability is approximately tenfold larger than that of the solid phase. (A): Permeation of gas molecules through the solid phase. (B): Permeation of gas molecules through pores or water channels. (C): Mixed pathways as a combination of alternating permeation through the aqueous and solid phase of the PEM | 67         |
|-------|---|------------|
| 7.1.1 | Flow chart of the algorithm to construct a calculation domain that represents the microscopic structure of Nafion $(8)$ (block I, steps 1-6) and the subsequent algorithm to calculate the gas permeabilities of this calculation domain (block II, steps 7-10).  | 71         |
| 7.1.2 | Two dimensional cross-section of the modeled three dimensional cubic structure of Nafion <sup>®</sup> with an edge length of 200 segments. One segment of the mesh corresponds to a cube with 2.1 Å edge length. Gray area: Solid phase. Blue area: Aqueous phase. Green area: Intermediate phase.  | 72         |
| 7.1.3 | Schematic illustration of the microscopic phase distribution at a functional $SO_3^-$ group in hydrated Nafion. Blue area: Aqueous phase. Green area: Intermediate phase. Gray area: Solid phase. Red-rimmed gray area: $SO_3^-$ group. Black lines: Ionomer chains. Connection between the functional group and the solid phase by a side chain from an ionomer main chain. Dotted dark gray line: Separation between the phases as defined by Allen <i>et al.</i> [40]  | <b>7</b> 3 |
| 7.1.4 | Chord length distribution of the modeled structure of Nafion <sup>®</sup> in the $x$ , $y$ , and $z$ direction of the cubic network. Solid lines: High-phase (aqueous phase plus intermediate phase). Dotted lines: Solid phase.  | 74         |
| 7.1.5 | Modeled volume fraction of the intermediate phase (ip) as a function of the volume fraction of the aqueous phase (ap) as computed by varying their combined volume fraction.  | 75         |
| 7.1.6 | Ratio of the permeability of fully hydrated Nafion $^{\circledR}$ ( $\varepsilon_{wN}$ ) to that of aqueous solutions ( $\varepsilon_{as}$ ) based on the data presented in the previous chapter. Black: Ratio for the hydrogen permeabilities. Red: Ratio for the oxygen permeabilities. Solid lines: Permeability of the aqueous solution equals that of water. Dashed lines: Permeability of the aqueous phase is 50 % smaller than that of water (eq. 7.1.5), which could be a result of the acidity of the aqueous phase in Nafion $^{\circledR}$ (see text for further explanations)  | 78         |
| 7.1.7 | Modeled permeability of the resistor network as a function of the edge length of the cubic mesh. Black points connected with lines: Results of the iterative solver. Black crosses: Results of the direct solver. Red points and right scale: Computing time of the iterative solver.   | 80         |
| 7.1.8 | Geometric restriction factor $\zeta$ for the permeation through the aqueous phase of the Nafion® model domain (ratio of the simulated permeability when $\varepsilon_{sp}=\varepsilon_{ip}=0$ to the simulated permeability with the aqueous phase spanning the whole domain) as a function of the edge length of the model domain. This geometric restriction factor directly influences the proton conduction. The gas permeation is less influenced by the percolation paths required for the proton conduction, since the gases can also permeate through the solid and intermediate phase. Points with lines: Iterative solver. Crosses: Direct solver.  | 81         |

| 7.2.1 | Hydrogen permeabilities in a modified Arrhenius plot (logarithmic scale of $\varepsilon$ $vs$ . $1/T$ ) for the case of varying the permeability of the intermediate phase. Black: Mean of the measured permeability of fully hydrated Nafion <sup>®</sup> . Blue: Water (calculated). Dark green: Mean of the measured permeability of dry Nafion <sup>®</sup> . Red: Case A ( $\varepsilon_{ap}=0.5\ \varepsilon_{w}$ ). Ocher: Case B ( $\varepsilon_{ap}=0.8\ \varepsilon_{w}$ ). Open circles with dotted lines: Simulated permeabilities for $\Lambda=1$ . Crosses: Simulated permeability for case A with $\Lambda=10.3$ . Dots: Simulated permeability for case B with $\Lambda=2.2$  | 83  |
|-------|---|-----|
| 7.2.2 | Hydrogen permeabilities in a modified Arrhenius plot for the case of an increases permeability of the solid phase. Dashed red line: Permeability of the softened solid phase for case A (parameters stated in Table 7.2.1). Dashed ocher line: Permeability of the softened solid phase for case B. Red stars: Simulated permeability for case A. Ocher squares: Simulated permeability for case B. Color code of the other lines equal that in Figure 7.2.1.   | 85  |
| 7.2.3 | Deviation of the permeability from $\ln(\varepsilon) \propto 1/T$ expressed by the deviation factor $\alpha$ (eq. 7.2.2) as a function of the inverse temperature. Blue line: Water (calculated). Black points: Fully hydrated Nafion <sup>®</sup> (measured). Black line: Fully hydrated Nafion <sup>®</sup> (smoothed over a window of 500 measurement points). Cyan dots: Simulated permeability of Nafion <sup>®</sup> with an increased permeability of the intermediate phase. Red stars: Simulated permeability of Nafion <sup>®</sup> with the softened solid phase for case A. Ocher squares: Simulated permeability of Nafion <sup>®</sup> with the softened solid phase for case B | 86  |
| 7.3.1 | Schematic illustration of the hydrogen permeation through a water channel of Nafion <sup>®</sup> . In the case of the oxygen permeation the mechanisms may be similar. Red points: Hydrogen atoms. Blue points: Oxygen atoms. Dotted black lines: Hydrogen bonds. (A): Permeation in the intermediate phase between the aqueous phase and the pore walls. (B): Permeation through bulk of the aqueous phase. The less distinct hydrogen bond network in the intermediate phase possibly leads to a larger permeability than that through the bulk of the aqueous phase.   | 88  |
| 8.1.1 | Measured conductivities with setup A (Section 4.1) of the different PEMs as a function of temperature. See explanation in the beginning of this chapter for further information on the different examined PEMs.   | 96  |
| 8.2.1 | Measured hydrogen permeabilties of different PEMs as a function of the temperature.   | 97  |
| 8.3.1 | Ratio of the proton conductivities to the hydrogen permeabilities of the examined PEMs, calculated by the data graphed in Figure 8.1.1 and 8.2.1  | 98  |
| 9.0.1 | Schematic illustration showing the mechanisms that lead to the hydrogen and oxygen cross-permeation during PEM water electrolysis [45]. (A): Proton flux through the PEM. (B): Convective transport of dissolved oxygen and hydrogen in the aqueous phase caused by the proton flux through the PEM. The gases dissolved in the hydration shell of the protons may diffuse into the surrounding water as illustrated by tiny arrows. (C): Diffusion of oxygen and hydrogen through the PEM. (D): Permeation forced by differential pressure, which will be neglected based on the results in Chapter 6. (E): Catalytic reaction of hydrogen and oxygen on the cathodic platinum catalyst.     | 101 |

| 9.2.1 | Modeled relations of the hydrogen permeation that is caused by the proton permeation and diffusion as a function of the current density. Membrane thicknesses of $100  \mu m$ , $200  \mu m$ and $300  \mu m$ were used for the calculations as indicated by the color code in the figure. The calculations refer to a temperature of $80  ^{\circ} \text{C}$ and the permeation through the aqueous phase of Nafion for an effective tortuosity of $\tau_{\text{eff}} = 1.5$ . By multiplying the graphed values by $\hat{D}_{\text{H}_2}/\hat{D}_{\text{O}_2} = 2.2$ , the displayed ratios can be approximated for the oxygen permeation. Top: Estimated ratio of the drift velocity of protons in the $x$ -direction to the mean velocity of diffusion driven hydrogen molecules as calculated by equation 9.2.22. Bottom: Estimated ratio of the hydrogen permeation fluxes caused by the proton permeation to that caused by diffusion for a hydration shell factor of $h = 1$ as calculated by equation 9.2.19 | 111   |
|-------|---|-------|
| 9.2.2 | Simulated hydrogen (top) and oxygen (bottom) permeation fluxes through Nafion as a function of the current density for 80 °C and membrane thicknesses of 100 µm, 200 µm and 300 µm. A cathodic pressure of 30 bar, an anodic pressure of 1 bar and a hydration shell factor of unity were assumed for these calculations. Solid lines: Cross-permeation flux densities caused by diffusion and proton permeation. Dotted lines: Cross-permeation flux densities solely caused by diffusion  | 113   |
| 9.2.3 | Modeled concentration profiles of hydrogen (top) and oxygen (bottom) in the aqueous phase of a Nafion membrane with 150 µm thickness during water electrolysis at 80 °C for an effective tortuosity of 1.5 and hydration shell factor of unity. A cathodic pressure of 30 bar and an anodic pressure of 1 bar were assumed for these calculations   | s.118 |
| 9.2.4 | Modeled percental deviations of the separated and interacting description of the gas transport in the aqueous phase of Nafion during water electrolysis at 80 °C. A tortuosity of 1.5 and a hydration shell factor of unity were assumed for these calculations. Top: Deviations of the hydrogen cross-permeation fluxes. Bottom: Deviations of the oxygen permeation fluxes.   | 119   |
| 9.3.1 | Current densities of an electrochemical hydrogen pump as a function of time [45]. Further explanations of the experimental setup are given in the text. Either a platinum catalyst (blue line) or an iridium oxide catalyst (red and green line) was employed at the anode. The anode was purged either with humidified nitrogen or humidified hydrogen. The time with hydrogen supply at the anode is shaded grayish. At a voltage of 1.5 V, the measured current of approximately $10  \text{mA/cm}^2$ corresponded to the electrolysis of water.   | 120   |
| 9.3.2 | Anodic hydrogen content of an electrolysis cell operated at 80 °C and equipped with a Nafion N117 membrane. Cathodic pressures at the gas outlet of either 7 bar (black) of 10 bar (red) were applied. Points: Measurements at differential pressure operation with atmospheric anodic pressure. Crosses: Measurements at balanced pressure operation. Solid lines: Simulated anodic hydrogen content for $Y_{H_2} = 8  \mathrm{cm}^2  \mathrm{bar}  \mathrm{A}^{-1}$ . Dotted lines: Simulated anodic hydrogen content for $Y_{H_2} = 0  \mathrm{cm}^2  \mathrm{bar}  \mathrm{A}^{-1}$ . A hydration shell factor of $h = 0$ was assumed for all the calculations graphed in this figure   | 122   |
| 9.3.3 | Points, crosses, and color code: Same notation as in Figure 9.3.2. The different design of the lines correspond to hydration shell factors $h$ of 0, 0.5, or 1  | 124   |
| 9.3.4 | Modeled hydrogen cross-permeation fluxes for the fits to the cathodic pressure of 7 bar in Figure 9.3.3. The same notation as in Figure 9.3.3 is used   | 125   |
| 9.3.5 | Modeled anodic hydrogen content (eq 9.2.4) for membrane thicknesses from $50  \mu m$ to $250  \mu m$ and a cathodic partial pressure increase factor of $Y_{H_2} = 8  cm^2  bar  A^{-1}$ . Top: Cathodic pressure of 1 bar. Bottom: Cathodic pressure of 30 bar   | 126   |
|       | 10p. Cantonic pressure of 1 par. Dottom: Catholic pressure of 30 par  | 140   |

| 10.2.1 | Modeled efficiency loss for 30 bar balanced (red) and differential (black) pressure operation and a membrane thickness of 100 $\mu$ m. Top: $Y_{H_2}=2\text{cm}^2\text{bar}A^{-1}$ . Bottom: $Y_{H_2}=8\text{cm}^2\text{bar}A^{-1}$  | 131  |
|--------|--|------|
| 10.2.2 | Modeled efficiency loss that is caused by gas crossover, pressurized gas evolution and the ohmic drop of the PEM. Top: Atmospheric pressure operation Bottom: 30 bar differential pressure operation. The efficiency loss was modeled for two different partial pressure increase factors ( $Y_{\rm H_2}=2{\rm cm^2barA^{-1}}$ and $Y_{\rm H_2}=8{\rm cm^2barA^{-1}}$ ), as indicated in the plots, respectively. The efficiency loss was calculated for membrane thicknesses from $50\mu m$ to $250\mu m$ as indicated by the color code in the legend  | 132  |
| 10.3.1 | Sum of the modeled voltages that are caused by the pressurized gas evolution during water electrolysis and isothermal subsequent compression ( $U_N + U_{comp}$ ). Dotted black line: Modeled Nernst voltage of the direct hydrogen pressurization during water electrolysis at 30 bar cathodic pressure and atmospheric anodic pressure ( $U_{comp} = 0$ ). Solid black line: Modeled Nernst voltage at atmospheric pressure water electrolysis ( $U_{comp} = 0$ ). Colored lines: Modeled $U_N + U_{comp}$ of atmospheric pressure water electrolysis with subsequent isothermal compression at 30 °C. The compressor efficiencies are given by color code in the legend. Top: $Y_{H_2} = 2\text{cm}^2\text{bar}A^{-1}$ . Bottom: $Y_{H_2} = 8\text{cm}^2\text{bar}A^{-1}$   | 137  |
| 10.3.2 | Comparison of the modeled efficiency loss of pressurized water electrolysis (dotted black line, membrane thickness of $100\mu\text{m})$ to atmospheric pressure electrolysis (solid black line, membrane thickness of $50\mu\text{m})$ in combination with subsequent mechanical compression (colored lines) of different compression efficiencies. A final pressure of 30 bar at 30 °C is considered for both cases   | 138  |
| 11.1.1 | Schematic illustration of the electrochemical mitigation of the hydrogen cross-permeat during water electrolysis [46]. Left: Setups for the electrochemical mitigation of hydrogen cross-permeation through the membrane during differential pressure PEM water electrolysis. The red and blue shadings qualitatively represent the concentrations of hydrogen and oxygen in the PEM. Hydrogen is permeating from the cathode to the anode (from left to right), while oxygen is permeating in the opposite direction. Right: Electrochemical reactions at the electrodes of the different setups. (A): Acid water electrolysis. The reactions at the anode and the cathode also occur in the other setups. (B): Connection of the additional electrode to the cathode by a power supply. The hydrogen that permeates from the cathode to the additional electrode is electrochemically sent back to the cathode. (C) Connection of the additional electrode to the anode by a resistance. The hydrogen at the additional electrode electrochemically reacts with anodic oxygen, reducing the anodic overpotential | tion |
| 11.2.1 | Measured potential difference between the additional electrode and the cathode $(\varphi_3 - \varphi_C)$ as a function of the current density $j_3$ . This current density is attributable to the electrochemical mitigation of the hydrogen crossover. The potential $\varphi_C$ of the cathode serves as a reference for the potential $\varphi_3$ of the additional electrode. The measurements were conducted at various fixed electrolysis current densities $j_E$ between the anode and cathode. Because the measurements were performed under galvanostatic conditions, the fixed currents were affected by a negligible error. The measurement error of the voltage $(\varphi_3 - \varphi_C)$ attributable to unsteady permeation fluxes was below 10 %. Positive currents and solid lines: setup using the electrochemical hydrogen pump according to Figure 11.1.1B. Negative currents and dashed lines: setup using the local fuel cell according to Figure 11.1.1C   | 144  |
|        | using the local fuel cell according to figure 11.1.1C  | 144  |

| 11.2.2 | function of the voltage between the additional electrode and the cathode ( $\varphi_3 - \varphi_C$ ). The influence of the potential of the additional electrode on the current density $j_3$ is discussed in Figure 11.2.1. The cell voltage at constant cell currents increased with the potential of the additional electrode, caused by the altered potential distribution in the electrolyte. Solid lines: setup with hydrogen pump according to Figure 11.1.1B. Dashed lines: setup with local fuel cell according to Figure 11.1.1C   | 145                               |
|--------|--|-----------------------------------|
| 11.3.1 | Left scale and black: Cell efficiency as estimated on the basis of equation 11.3.5. Right scale and red: Measured anodic hydrogen content (red) as a function of the cell current density ( $j_E$ ) for various values of $j_3$ . The additional electrode is connected to the cathode according to the setup with electrochemical hydrogen pump in Figure 11.1.1B. In the partial load range, an increase of the cell efficiency results thanks to the usage of the additional electrode.   | 148                               |
| 12.1.1 | Ratios of the proton conductivity to the hydrogen permeability of Nafion <sup>®</sup> (black line) and an aqueous solution with a proton concentration of 2.8 M (blue line). This concentration equals the proton concentration in the aqueous phase of Nafion <sup>®</sup> membranes (Chapter 5). The proton conductivity of the aqueous solution and Nafion <sup>®</sup> was measured as discussed in Chapter 5. The measured hydrogen permeability of Nafion <sup>®</sup> was presented in Chapter 6. The hydrogen permeability of the aqueous solution was estimated by half the conductivity of water for the reasons that are discussed in Section 7.1.2 | 153                               |
| 14.2.1 | (A): Schematic illustration of two water channels that are separated by the solid polymeric phase. (B): Equivalent circuit for this alignment, while the polymeric phase is described by a plate capacitor geometry with the capacitance $C_{\rm gap}$ . The resistances $R_1$ and $R_2$ correspond to the resistances of the proton conduction through the water channels   | 161                               |
| 14.2.2 | Conductivity of five Nafion $^{\textcircled{R}}$ N117 (black) and five NR212 (blue) samples as a function of temperature. Red line: Mean of all the measurements   | 164                               |
| 14.3.1 | Voltage-current characteristic of setup C (Fig. 4.2.1C) with a Nafion <sup>®</sup> N177 sample at 55 °C. Pressures of either 2 bar hydrogen or 2 bar oxygen were applied at the gas inlet of the cell. When the hydrogen permeation through the sample was measured, the working electrode was employed as the anode (+). In this case, the voltage and current were defined as positive. Voltage and current were defined as negative for the cathodic operation of the working electrode (-), which was used to reduce the oxygen coming through the sample. The voltages at which the saturation current  |                                   |
| 14.4.1 | densities were reached are shaded grayish  | <ul><li>172</li><li>175</li></ul> |
| 14.4.2 | Oxygen permeabilities in a modified Arrhenius plot for the case of an increased permeability of the solid phase. Dotted red line: Permeability of the softened solid phase for case A (parameters stated in Table 14.4.1). Red stars: Simulated permeabi-  | 1/3                               |
|        | lity for case A. Color code of the other lines equal that in Figure 14.4.1   | 175                               |

| 14.5.1 | Left scale: Required thermodynamic work for an idealized isothermal compression                                      |     |
|--------|--|-----|
|        | (at 30 $^{\circ}\text{C}$ and 80 $^{\circ}\text{C}$ ) and and adiabatic one and four stage compression (initial tem- |     |
|        | perature at each stage: $30^{\circ}$ C). Right scale: Thermodynamic efficiency (eq 14.5.5) of                        |     |
|        | idealized 4 stage adiabatic compression compared to idealized isothermal compres-                                    |     |
|        | sion at 30 °C and 80 °C referring to equation 14.5.5.  | 181 |

| 2.3.1  | 2.3.14) of hydrogen and oxygen in water  | 24       |
|--------|--|----------|
| 6.1.2  | Activation energies ( $E_{\rm A}$ ) in $1\times 10^{-20}$ J for the diffusion, solubility and permeability of hydrogen and oxygen in water, fully hydrated (wet) Nafion®, dry Nafion® and PTFE. Approximations obtained from linear fits in the Arrhenius plot ( $\ln(\varepsilon)\ vs\ 1/T$ ) to the measurements of this study are marked with '*', where the errors were determined by the standard deviations between the measurements. Approximations obtained by linear fits in the Arrhenius plot to the data from the literature ( [52, 124], eq. 2.3.17 and 2.3.15) are marked with '\f'. Data from the literature of different authors that varied heavily [52] and that does not allow precise conclusions to be drawn is marked with '\f'. Information not available in the literature is marked with '-'. Cited data from the literature is marked with the reference. The prefactors related to these activation energies are given in the attachment (Section 14.3) | 64       |
| 7.1.1  | Volume fractions of the modeled phases in this study and those measured by Allen <i>et al.</i> [40]. As discussed in the text, the volumetric water content was modeled to approximately 40 %, which is smaller than that reported by Allen <i>et al.</i> , since the influence of the cryogenic environment in his setup expanded the volume of the accusage phase.   | 70       |
| 7.2.1  | the volume of the aqueous phase  | 73<br>84 |
| 9.2.1  | Remarks on the notation used in this section exemplified for an arbitrary physical property $P$  | 109      |
| 9.2.2  | Diffusion coefficients and solubilities of hydrogen and oxygen in water at 80 °C extracted from literature data [52,124]   | 114      |
| 9.3.1  | Numeric values of the parameters that were used to calculate the anodic hydrogen content. (a): Obtained by the fits in Figure 9.3.2. (b): Estimated based on equation  |          |
|        | 9.1.5. (c): Data from Chapter 6  | 123      |
| 14.2.1 | Parameters of the polymeric fits $\kappa(T) = a + b T + c T^2 + d T^3$ that describe the mean of the measured conductivities of Nafion <sup>®</sup> , TMSA, HCl, and KCl as a function of temperature. The units S cm <sup>-1</sup> $vs$ . °C were employed for the fit. Using these mean fits to the aqueous solutions, the parameters for the conductivity of H <sup>+</sup> in the aqueous solutions were determined by equation 14.2.6   | 163      |
| 14.3.1 | Prefactors related to the activation energies stated in Table 6.1.1, using the same notation. Units: $[\varepsilon_0] = 10^{-8} \text{ mol cm}^{-1} \text{ s}^{-1} \text{ bar}^{-1}, [D_0] = 10^{-2} \text{ cm}^2 \text{ s}^{-1}, [S_0] = 1 \text{ mol}$   | 100      |
|        | $cm^{-3} bar^{-1} \dots \dots$   | 169      |

| 14.4.1 | Prefactors and activation energies of the oxygen permeability that describe the sof- |     |
|--------|--|-----|
|        | tened solid phase of humidified Nafion® for case A. This enlarged permeability is    |     |
|        | the solution for the fit in Figure 14.4.2  | 176 |

### **Nomenclature**

#### Roman Letters

- a Activity, dimensionless
- A Area,  $cm^2$
- C Cunningham correction factor, dimensionless
- c Concentration, mol 1<sup>-1</sup>
- C Capacity, F
- D Diffusion coefficient,  $cm^2 s^{-1}$
- $D_0$  Prefactor diffusion coefficient, cm<sup>2</sup> s<sup>-1</sup>
- *d* Membrane thickness, μm
- $d^*$  Mean diameter of water channels, Å
- E Energy, J
- $E_A$  Activation energy (general), J
- $E_D$  Activation energy of the diffusion, J
- $E_{\varepsilon}$  Activation energy of the permeability, J
- $E_t$  Activation energy of the viscosity, J
- $\vec{E}$  Electric field, V m<sup>-</sup>-1
- f Reaction rate, mol s<sup>-1</sup>
- $\vec{F}$  Force, kg m s<sup>-2</sup>
- F Faraday constant, 96485.3 C mol<sup>-1</sup>
- $\tilde{F}$  Free energy,
- $\tilde{G}$  Gibbs free energy, kJ mol<sup>-1</sup>
- *h* Hydration shell factor, which representes the hydrogen concentration in the hydration shell of the protons normalized to that in water, dimensionless
- $\tilde{H}$  Enthalpy, kJ mol<sup>-1</sup>
- $\Delta H_S$  Heat of solution, J
- K V-value, which correlates the solubility of gases in electrolytic solutions to that of water,  $l \mod^{-1}$
- $k_B$  Boltzmann constant,  $1.3806 \times 10^{-23}$  J K<sup>-1</sup>
- I Current, A
- j Current density, A cm<sup>-2</sup>
- l Lenght, m
- *n* Amount of substance, mol
- *n*<sub>d</sub> Drag coefficient, dimensionless
- p Pressure, bar
- $p_{\rm gas}$  Partial pressure of a gas, bar
- P Power, W
- Q Charge, C
- q Charge normalized to elementary charge, dimensionless
- r Radius, m
- rh Relative humidity, percent
- R Gas constant,  $8.314 \,\mathrm{J}\,\mathrm{mol}^{-1}\,\mathrm{K}^{-1}$
- R Resistance,  $\Omega$
- $R_{area}$  Area Resistance,  $\Omega$  cm<sup>-2</sup>
- $\hat{R}$  Permeation resistance, s bar mol<sup>-1</sup>
- Solubility coefficient, mol bar $^{-1}$  cm $^{-3}$
- $S_0$  Prefactor solubility coefficient, mol bar<sup>-1</sup> cm<sup>-3</sup>

- $S_1$  Parameter for mole solubility, dimensionless
- S<sub>2</sub> Parameter for mole solubility, K
- S<sub>3</sub> Parameter for mole solubility, dimensionless
- $\tilde{S}$  Entropy, kJ mol<sup>-1</sup> K<sup>-1</sup>
- t Time, s
- $\tilde{t}$  Scattering time, s
- T Temperature, K
- U Voltage, V
- $U_0$  Amplitude, V
- $U_{\Omega}$  Ohmic drop at the membrane, V
- *U<sub>N</sub>* Nernst Voltage, V
- $\tilde{U}$  Internal energy, J mol<sup>-1</sup>
- v Velocity, m s<sup>-1</sup>
- V Volume, m<sup>3</sup>
- W Work,  $I \text{ mol}^{-1}$
- Y Fraction of particles, dimensionless
- z Amount of electrons, number
- Z Impedance,  $\Omega$
- Z' Real part of the impedance,  $\Omega$
- Z'' Imaginary part of the impedance,  $\Omega$
- $Z_W$  Warburg impedance element,  $\Omega$
- Ž Compressibility factor, dimensionless

#### **Greek Symbols**

- $\alpha$  Deviation factor, mol s<sup>-1</sup> cm<sup>-1</sup> bar<sup>-1</sup>
- $\alpha_n$  Normalization factor, mol s<sup>-1</sup> cm<sup>-1</sup> bar<sup>-1</sup>
- $\beta$  Geometry factor of diffusing molecules, m
- $\gamma$  Adiabatic index, dimensionless
- $\Gamma$  Production rate density, mol s<sup>-1</sup> cm<sup>-2</sup>
- $\varepsilon$  Permeability, mol s<sup>-1</sup> cm<sup>-1</sup> bar<sup>-1</sup>
- $\varepsilon_0$  Prefactor permeability, mol s<sup>-1</sup> cm<sup>-1</sup> bar<sup>-1</sup>
- $\varepsilon_{\rm r}$  Permittivity, dimensionless
- $\tilde{\epsilon}_0$  Vacuum permittivity, A<sup>2</sup> s<sup>4</sup> kg<sup>-1</sup> m<sup>-3</sup>
- *ζ* Geometric restrictions factor, dimensionless
- $\eta$  Efficiency, dimensionless
- $\eta_{\rm U}$  Voltage efficiency, dimensionless
- $\eta_{\rm C}$  Current efficiency, dimensionless
- $\tilde{\eta}$  Kinetic overpotential, V
- $\theta$  contact angle, degrees
- $\iota$  Viscosity, kg s<sup>-1</sup> ms<sup>-1</sup>
- $t_0$  Prefactor viscosity, kg s<sup>-1</sup> m s<sup>-1</sup>
- $\kappa$  Conductivity, S cm<sup>-1</sup>
- $\lambda$  Water uptake per functional group, dimensionless
- Λ Interfacial increase factor, dimensionless
- μ Chemical potential, J
- $\mu$  Mobility, s kg<sup>-1</sup>
- $\tilde{\mu}$  Electrical mobility, m<sup>2</sup> V<sup>-1</sup> s<sup>-1</sup>
- *ν* Stoichiometric number, dimensionless
- $\xi$  Extent of reaction, dimensionless
- $\rho$  Mass density, kg l<sup>-1</sup>
- $\hat{\rho}$  Mole density, mol m<sup>-3</sup>

- $\sigma$  Surface tension, N m<sup>-1</sup>
- au Tortuosity, dimensionless
- $Y_{H_2}$  Cathodic partial pressure increase factor, bar cm<sup>2</sup> A<sup>-1</sup>
- $Y_{O_2}$  Anodic pressure increase factor, bar cm<sup>2</sup> A<sup>-1</sup>
- $\varphi$  Potential, V
- *φ* Volumetric water content, dimensionless
- $\Phi$  Permeation flux density, mol s<sup>-1</sup> cm<sup>-2</sup>
- $\chi$  Mole fraction of the solubility, mol  $l^{-1}$
- $\omega$  Angular frequency, Hz

#### Superscripts

- a Anode
- c Cathode
- diff Diffusion
- drag Delectro-osmotic water drag
- i Property of the *i*-th specie
- w Water
- x In the *x*-direction

#### Subscripts

- 0 Standard ambient Temperature and pressure
- 3 Referring to the addional (third) electrode
- 4st Four stage adiabatic compression process
- ad adiabatic
- an Anode
- ap Aqueous phase
- cat Cathode
- cell Cell
- comp Compressor
- cr Catalytic recombination
- cross Cross-permeation
- ct Charge transfer
- dif Diffusion
- dl Double Layer
- dN Dry Nafion®
- dp Differential pressure
- drag Electro-osmotic drag
- D Drift
- eff Effective
- fin Final
- fit Fitted function
- gap Gap
- geo Geometric
- H<sub>2</sub> Hydrogen
- H<sup>+</sup> Proton
- HCl Hydrochloric acid
- ini Initial
- ideal Ideal
- iso Isothermal
- j Sum index
- KCl Aqueous potassium chloride solution

loss Loss

N Nafion®

O<sub>2</sub> Oxygen

pro Production

real Real

ref Reference

rev Reversible

sat Saturation

sp Solid phase

t Total

U Voltage

wN Fully hydrated (wet) Nafion®

#### Abbreviations

AC Alternating current

CE Counter electrode

DC Direct current

HCl Hydrochloric acid

IrO<sub>2</sub> Iridium oxide

KCl Aqueous potassium chloride solution

Pt/C Carbon supported platinum

PEM Polymer electrolyte membrane

PTFE Polytetrafluoroethylene

RE Reference electrode

WE Working electrode

- [1] M. Faraday. Experimental researches in electricity. Third series. Philosophical Transactions of the Royal Society of London, 123 (1833), 23
- [2] W. Kreuter, H. Hofmann. Electrolysis: The Important Energy Transformer. International Journal of Hydrogen Energy, 23 (1998), 661
- [3] D. L. Stojic, M. P. Marceta, S. P. Sovilj, S. S. Miljanic. Hydrogen generation from water electrolysis-possibilities of energy saving. Journal of Power Sources, 118 (2003), 315
- [4] B. C. Steele, A. Heinzel. Materials for fuel-cell technologies. Nature, 414 (2001), 345
- [5] W. Wei, G. Jinlong. Methanation of carbon dioxide: An overview. Frontiers of Chemical Science and Engineering, 5 (2010), 2
- [6] C. White, R. Steeper, A. Lutz. The hydrogen-fueled internal combustion engine: a technical review. International Journal of Hydrogen Energy, 31 (2006), 1292
- [7] B. Bensmann, R. Hanke-Rauschenbach, I. Peña Arias, K. Sundmacher. Energetic evaluation of high pressure PEM electrolyzer systems for intermediate storage of renewable energies. Electrochimica Acta, 110 (2013), 570
- [8] K. Zeng, D. Zhang. Recent progress in alkaline water electrolysis for hydrogen production and applications. Progress in Energy and Combustion Science, 36 (2010), 307
- [9] A. Ursua, L. M. Gandia, P. Sanchis. Hydrogen Production From Water Electrolysis: Current Status and Future Trends. IEEE, 100 (2012), 410
- [10] C. H. Hamann, W. Vielstich. Elektrochemie. Wiley-VCH, Weinheim, 4 edition, 2005
- [11] C. A. Grimes, K. V. Oomman. Hydrogen generation by water splitting. In: Light, Water, Hydrogen, volume 2. Springer US, 2008, pages 35–113
- [12] J. H. Russell, L. J. Nuttall, A. P. Fickett. Hydrogen generation by solid polymer electrolyte water electrolysis. American Chemical Society Division of Fuel Chemistry Preprints, 18 (1973), 24
- [13] Y. Leng, G. Chen, A. J. Mendoza, T. B. Tighe, M. A. Hickner, C.-Y. Wang. Solid-state water electrolysis with an alkaline membrane. Journal of the American Chemical Society, 134 (2012), 9054
- [14] M. R. Hibbs, M. A. Hickner, T. M. Alam, S. K. Mcintyre, C. H. Fujimoto, C. J. Cornelius, V. Pennsyl. Transport Properties of Hydroxide and Proton Conducting Membranes. Chem. Matter, 20 (2008), 2566

[15] T. A. Zawodzinski, C. Derouin, S. Radzinski, R. J. Sherman, V. T. Smith, T. E. Springer, S. Gottesfeld. Water Uptake by and Transport Through Nafion 117 Membranes. Journal of The Electrochemical Society, 140 (1993), 1041

- [16] P. W. Majsztrik, M. B. Satterfield, A. B. Bocarsly, J. B. Benziger. Water sorption, desorption and transport in Nafion membranes. Journal of Membrane Science, 301 (2007), 93
- [17] E. Roche, M. Pineri, R. Duplessix. Phase Separation in Perfluorosulfonate Ionomer Membranes. Journal of Polymer Science, 20 (1982), 107
- [18] G. Merle, M. Wessling, K. Nijmeijer. Anion exchange membranes for alkaline fuel cells: A review. Journal of Membrane Science, 377 (2011), 1
- [19] S. Peighambardoust, S. Rowshanzamir, M. Amjadi. Review of the proton exchange membranes for fuel cell applications. International Journal of Hydrogen Energy, 35 (2010), 9349
- [20] E. Spohr, P. Commer, A. A. Kornyshev. Enhancing Proton Mobility in Polymer Electrolyte Membranes: Lessons from Molecular Dynamics Simulations. The Journal of Physical Chemistry B, 106 (2002), 10560
- [21] R. Jorn, G. A. Voth. Mesoscale Simulation of Proton Transport in Proton Exchange Membranes. The Journal of Physical Chemistry C, 116 (2012), 10476
- [22] R. Leroy. Industrial water electrolysis: Present and future. International Journal of Hydrogen Energy, 8 (1983), 401
- [23] T. Schmidt, H. Gasteiger, G. Stäb, P. Urban, C. Kolb, R. Behm. Characterization of High-Surface-Area Electrocatalysts Using a Rotating Disk Electrode Configuration. Journal of The Electrochemical Society, 145 (1998), 2354
- [24] Johnson Matthey Fuel Cells. HiSPEC Fuel Cell Catalysts. http://www.jmfuelcells.com/products/fuel\_cell\_catalysts (2015), 1
- [25] C. C. Pavel, F. Cecconi, C. Emiliani, S. Santiccioli, A. Scaffidi, S. Catanorchi, M. Comotti. Highly Efficient Platinum Group Metal Free Based Membrane-Electrode Assembly for Anion Exchange Membrane Water Electrolysis. Angewandte Chemie, 126 (2014), 1402
- [26] M. Felgenhauer, T. Hamacher. State-of-the-art of commercial electrolyzers and on-site hydrogen generation for logistic vehicles in South Carolina. International Journal of Hydrogen Energy, 40 (2015), 2084
- [27] T. Sakai, H. Takenaka, E. Torikai. Gas Diffusion in the Dried and Hydrated Nafions. Journal of The Electrochemical Society, 133 (1986), 88
- [28] S. S. Kocha, J. D. Yang, J. S. Yi. Characterization of Gas Crossover and Its Implications in PEM Fuel Cells. AIChE, 52 (2006), 1916

[29] B. Bensmann, R. Hanke-Rauschenbach, I. Peña Arias, K. Sundmacher. Energetic evaluation of high pressure PEM electrolyzer systems for intermediate storage of renewable energies. Electrochimica Acta

- [30] S. A. Grigoriev, A. A. Kalinnikov, P. Millet, V. I. Porembsky, V. N. Fateev. Mathematical modeling of high-pressure PEM water electrolysis. Journal of Applied Electrochemistry, 40 (2009), 921
- [31] S. Grigoriev, V. Porembskiy, S. Korobtsev, V. Fateev, F. Auprêtre, P. Millet. High-pressure PEM water electrolysis and corresponding safety issues. International Journal of Hydrogen Energy, 36 (2011), 2721
- [32] H. Janssen, J. Bringmann, B. Emonts, V. Schroeder. Safety-related studies on hydrogen production in high-pressure electrolysers. International Journal of Hydrogen Energy, 29 (2004), 759
- [33] F. Marangio, M. Santarelli, M. Cali. Theoretical model and experimental analysis of a high pressure PEM water electrolyser for hydrogen production. International Journal of Hydrogen Energy, 34 (2009), 1143
- [34] K. A. Mauritz, R. B. Moore. State of Understanding of Nafion. Chemical reviews, 104 (2004), 4535
- [35] K. Schmidt-Rohr, Q. Chen. Parallel cylindrical water nanochannels in Nafion fuel-cell membranes. Nature materials, 7 (2008), 75
- [36] E. J. Roche, M. Pineri, R. Duplessix, A. M. Levelut. Small-angle scattering studies of nation membranes. Journal of Polymer Science: Polymer Physics Edition, 19 (1981), 1
- [37] J.-C. Perrin, S. Lyonnard, F. Volino. Quasielastic Neutron Scattering Study of Water Dynamics in Hydrated Nafion Membranes. The Journal of Physical Chemistry C, 111 (2007), 3393
- [38] E. Aleksandrova, R. Hiesgen, K. A. Friedrich, E. Roduner. Electrochemical atomic force microscopy study of proton conductivity in a Nafion membrane. Physical chemistry chemical physics, 9 (2007), 2735
- [39] R. Hiesgen, S. Helmly, T. Morawietz, X.-Z. Yuan, H. Wang, K. A. Friedrich. Atomic force microscopy studies of conductive nanostructures in solid polymer electrolytes. Electrochimica Acta, 110 (2013), 292
- [40] F. I. Allen, L. R. Comolli, A. Kusoglu, M. A. Modestino, A. M. Minor, A. Z. Weber. Morphology of Hydrated As-Cast Nafion Revealed through Cryo Electron Tomography. ACS Macro Letters, 4 (2015), 1
- [41] Y. Sone, P. Ekdinge, D. Simonsson. Proton Conductivily of Nafion 117 as Measured by a Four-Electrode AC Impedance Method. Journal of the Electrochemical Society, 143 (1996), 1254

[42] A. Anantaraman, C. Gardner. Studies on ion-exchange membranes. Part 1. Effect of humidity on the conductivity of Nafion. Journal of Electroanalytical Chemistry, 414 (1996), 115

- [43] A. Venkatnathan, R. Devanathan, M. Dupuis. Atomistic simulations of hydrated nafion and temperature effects on hydronium ion mobility. The journal of physical chemistry. B, 111 (2007), 7234
- [44] V. A. Sethuraman, S. Khan, J. S. Jur, A. T. Haug, J. W. Weidner. Measuring oxygen, carbon monoxide and hydrogen sulfide diffusion coefficient and solubility in Nafion membranes. Electrochim Acta, 54 (2009), 6850
- [45] M. Schalenbach, M. Carmo, D. L. Fritz, J. Mergel, D. Stolten. Pressurized PEM water electrolysis: Efficiency and gas crossover. International Journal of Hydrogen Energy, 38 (2013), 14921
- [46] M. Schalenbach, D. Stolten. High-pressure water electrolysis: Electrochemical mitigation of product gas crossover. Electrochimica Acta, 156 (2015), 321
- [47] G. Wedler. Lehrbuch der physikalischen Chemie. VCH, Weinheim, 3 edition, 1987
- [48] T. Fliessbach. Statistische Physik. Spektrum Akademischer Verlag, Heidelberg, 5 edition, 2010
- [49] R. F. Mann, J. C. Amphlett, M. A. Hooper, H. M. Jensen, B. A. Peppley, P. R. Roberge. Development and application of a generalised steady-state electrochemical model for a PEM fuel cell. J Power Sources, 86 (2000), 173
- [50] R. L. LeRoy. Hydrogen Production by the Electrolysis of Water. Journal of The Electrochemical Society, 130 (1983), 2158
- [51] H. Zhang, G. Lin, J. Chen. Evaluation and calculation on the efficiency of a water electrolysis system for hydrogen production. International Journal of Hydrogen Energy, 35 (2010), 10851
- [52] H. Ito, T. Maeda, A. Nakano, H. Takenaka. Properties of Nafion membranes under PEM water electrolysis conditions. International Journal of Hydrogen Energy, 36 (2011), 10527
- [53] J. Zhang, Y. Tang, C. Song, J. Zhang, H. Wang. PEM fuel cell open circuit voltage (OCV) in the temperature range of 23C to 120C. Journal of Power Sources, 163 (2006), 532
- [54] I. Barin, G. Platzki. Thermochemical data of pure substances, volume 3.ed. Weinheim, 3 edition, 1995
- [55] B. Hammer. Theoretical Surface Science and Catalysis Calculations and Concepts. Advances in Catalysis, 45 (2000), 71
- [56] H. Vogel. Gerthsen Physik. Springer, Berlin, Heidelberg, 23 edition, 2006

[57] W. Hong, M. Risch, K. A. Stoerzinger, A. J. L. Grimaud, J. Suntivich, Y. Shao-Horn. Toward the rational design of non-precious transition metal oxides for oxygen electrocatalysis. Energy and Environmental Science, 8 (2015), 1404

- [58] M. Carmo, D. L. Fritz, J. Mergel, D. Stolten. A comprehensive review on PEM water electrolysis. International Journal of Hydrogen Energy, 8 (2013), 4901
- [59] R. Mann, J. Amphlett, B. Peppley, C. Thurgood. Application of Butler-Volmer equations in the modelling of activation polarization for PEM fuel cells. Journal of Power Sources, 161 (2006), 775
- [60] P. Choi. A simple model for solid polymer electrolyte (SPE) water electrolysis. Solid State Ionics, 175 (2004), 535
- [61] W. Xu, K. Scott. The effects of ionomer content on PEM water electrolyser membrane electrode assembly performance. International Journal of Hydrogen Energy, 35 (2010), 12029
- [62] N. Rajalakshmi, K. Dhathathreyan. Catalyst layer in PEMFC electrodes Fabrication, characterisation and analysis. Chemical Engineering Journal, 129 (2007), 31
- [63] S. Litster, G. McLean. PEM fuel cell electrodes. Journal of Power Sources, 130 (2004), 61
- [64] J. Xu, R. Miao, T. Zhao, J. Wu, X. Wang. A novel catalyst layer with hydrophilic-hydrophobic meshwork and pore structure for solid polymer electrolyte water electrolysis. Electrochemistry Communications, 13 (2011), 437
- [65] R. Makharia, M. F. Mathias, D. R. Baker. Measurement of Catalyst Layer Electrolyte Resistance in PEFCs Using Electrochemical Impedance Spectroscopy. Journal of The Electrochemical Society, 152 (2005), A970
- [66] S. Siracusano, V. Baglio, A. Stassi, L. Merlo, E. Moukheiber, A. Arico'. Performance analysis of short-side-chain Aquivion perfluorosulfonic acid polymer for proton exchange membrane water electrolysis. Journal of Membrane Science, 466 (2014), 1
- [67] D. R. P. Morris, S. P. Liu, D. V. Gonzalez, J. T. Gostick. Effect of Water Sorption on the Electronic Conductivity of Porous Polymer Electrolyte Membrane Fuel Cell Catalyst Layers. ACS Applied Materials and Interfaces, 6 (2014), 18609
- [68] A. A. Kulikovsky. The regimes of catalyst layer operation in a fuel cell. Electrochimica Acta, 55 (2010), 6391
- [69] R. O'Hayre, D. M. Barnett, F. B. Prinz. The Triple Phase Boundary. Journal of The Electrochemical Society, 152 (2005), A439
- [70] C. Boyer, S. Gamburzev, O. Velev, S. Srinivasan, A. J. Appleby. Measurements of proton conductivity in the active layer of PEM fuel cell gas diffusion electrodes. Electrochim Acta, 43 (1998), 3703

[71] M. M. Jaksic. Volcano plots along the periodic table, their causes and consequences on electrocatalysis for hydrogen electrode reactions. Journal of New Materials for Electrochemical Systems, 182 (2000), 167

- [72] J. Greeley, T. F. Jaramillo, J. Bonde, I. B. Chorkendorff, J. K. Nørskov. Computational high-throughput screening of electrocatalytic materials for hydrogen evolution. Nature materials, 5 (2006), 909
- [73] E. Fabbri, A. Habereder, K. Waltar, R. Kötz, T. J. Schmidt. Developments and perspectives of oxide-based catalysts for the oxygen evolution reaction. Catalysts Science and Technology, 4 (2014), 3800
- [74] B. Conway, J. O. M. Bockris. The d-Band Character of Metals and the Rate and Mechanism of the Electrolytic Hydrogen Evolution. Nature, 178 (1956), 488
- [75] R. Subbaraman, D. Tripkovic, K.-C. Chang, D. Strmcnik, A. P. Paulikas, P. Hirunsit, M. Chan, J. Greeley, V. Stamenkovic, N. M. Markovic. Trends in activity for the water electrolyser reactions on 3d M(Ni,Co,Fe,Mn) hydr(oxy)oxide catalysts. Nature Materials, 11 (2012), 550
- [76] M. Nesselberger, S. Ashton, J. C. Meier, I. Katsounaros, K. J. J. Mayrhofer, M. Arenz. The Particle Size Effect on the Oxygen Reduction Reaction Activity of Pt Catalysts: Influence of Electrolyte and Relation to Single Crystal Models. Journal of the American Chemical Society, 133 (2011), 17428
- [77] E. Antolini. Carbon supports for low-temperature fuel cell catalysts. Applied Catalysis B: Environmental, 88 (2009), 1
- [78] H. Gasteiger, J. Panels, S. Yan. Dependence of PEM fuel cell performance on catalyst loading. Journal of Power Sources, 127 (2004), 162
- [79] L. A. Silva, V. A. Alves, M. A. P. Silva, S. Trasattit, J. F. C. Boodtst. Oxygen evolution in acid solution on IrO2 + TiO2 ceramic films. A study by impedance, voltammetry and SEM. Electrochemical Acta, 42 (1997), 271
- [80] J. Xu, G. Liu, J. Li, X. Wang. The electrocatalytic properties of an IrO2/SnO2 catalyst using SnO2 as a support and an assisting reagent for the oxygen evolution reaction. Electrochimica Acta, 59 (2012), 105
- [81] T. Smolinka. Encyclopedia of electrochemical power sources. Elsevier B.V., 2009
- [82] P. Vanýsek. Electrochemical Series. In: W. M. Haynes (Editor), Handbook of Chemixtry and Physics. Taylor and Francis Group, 95 edition, 2014, pages 5\_80 – 5\_89
- [83] M. Pourbaix. Electrochemical corrosion of metallic biomaterials. Biomaterials, 5 (1984), 122
- [84] M. Peuckert, F. Coenen, H. Bonzel. XPS Study of the Electrochemical Surface Oxidation of Platinum in 1 N H2SO4 Acid Electrolyte. Electrochimica Acta, 29 (1984), 1305

[85] N. Danilovic, R. Subbaraman, K.-C. Chang, S. H. Chang, Y. J. Kang, J. Snyder, A. P. Paulikas, D. Strmcnik, Y.-T. Kim, D. Myers, V. R. Stamenkovic, N. M. Markovic. Activity-Stability Trends for the Oxygen Evolution Reaction on Monometallic Oxides in Acidic Environments. The Journal of Physical Chemistry Letters, 5 (2014), 2474

- [86] S. Trasatti. Electrocatalysis in the Anodic Evolution of Oxygen and Chlorine. Electrochimica Acta, 29 (1984), 1503
- [87] S. Grigoriev, P. Millet, S. Volobuev, V. Fateev. Optimization of porous current collectors for PEM water electrolysers. International Journal of Hydrogen Energy, 34 (2009), 4968
- [88] P. Millet, A. Ranjbari, F. de Guglielmo, S. Grigoriev, F. Auprêtre. Cell failure mechanisms in PEM water electrolyzers. International Journal of Hydrogen Energy, 37 (2012), 17478
- [89] R. Clarke, S. Giddey, S. Badwal. Stand-alone PEM water electrolysis system for fail safe operation with a renewable energy source. International Journal of Hydrogen Energy, 35 (2010), 928
- [90] H. Kita, S. Ye, A. Aramata, N. Furuya. Adsorption of hydrogen on platinum single crystal electrodes in acid and alkali solutions. Journal of Electroanalytical Chemistry and Interfacial Electrochemistry, 295 (1990), 317
- [91] V. O. Mittal, H. R. Kunz, J. M. Fenton. Effect of Catalyst Properties on Membrane Degradation Rate and the Underlying Degradation Mechanism in PEMFCs. Journal of The Electrochemical Society, 153 (2006), A1755
- [92] M. Inaba, T. Kinumoto, M. Kiriake, R. Umebayashi, A. Tasaka, Z. Ogumi. Gas crossover and membrane degradation in polymer electrolyte fuel cells. Electrochim Acta, 51 (2006), 5746
- [93] B. Bensmann, R. Hanke-Rauschenbach, K. Sundmacher. In-situ measurement of hydrogen crossover in polymer electrolyte membrane water electrolysis. International Journal of Hydrogen Energy, 39 (2014), 49
- [94] S. Grigoriev, P. Millet, S. Korobtsev, V. Porembskiy, M. Pepic, C. Etievant, C. Puyenchet, V. Fateev. Hydrogen safety aspects related to high-pressure polymer electrolyte membrane water electrolysis. International Journal of Hydrogen Energy, 34 (2009), 5986
- [95] M. Eikerling, A. A. Kornyshev, A. M. Kuznetsov, J. Ulstrup, S. Walbran. Mechanisms of Proton Conductance in Polymer Electrolyte Membranes. The Journal of Physical Chemistry B, 105 (2001), 3646
- [96] K.-D. Kreuer, S. J. Paddison, E. Spohr, M. Schuster. Transport in proton conductors for fuel-cell applications: simulations, elementary reactions, and phenomenology. Chemical reviews, 104 (2004), 4637
- [97] P. Choi, N. H. Jalani, R. Datta. Thermodynamics and Proton Transport in Nafion. Journal of The Electrochemical Society, 152 (2005), E123

[98] A. Luzar, D. Chandler. Hydrogen-Bond Kinetics in Liquid Water. Nature, 379 (1996), 55

- [99] J. D. Smith, C. D. Cappa, K. R. Wilson, B. M. Messer, R. C. Cohen, R. J. Saykally. Energetics of Hydrogen Bond Network Rearrangements in Liquid Water. Science (New York, N.Y.), 306 (2004), 851
- [100] M. L. Cowan, B. D. Bruner, N. Huse, J. R. Dwyer, B. Chugh, E. T. J. Nibbering, T. Elsaesser, R. J. D. Miller. Ultrafast Memory Loss and Energy Redistribution in the Hydrogen Bond Network of Liquid H2O. Nature, 434 (2005), 199
- [101] K. Kreuer. On the complexity of proton conduction phenomena. Solid State Ionics, 136-137 (2000), 149
- [102] O. Markovitch, H. Chen, S. Izvekov, F. Paesani, G. a. Voth, N. Agmon. Special pair dance and partner selection: elementary steps in proton transport in liquid water. The Journal of Physical Chemistry B, 112 (2008), 9456
- [103] L. X. Dang, J. E. Rice, J. Caldwell, P. A. Kollmad. Ion Solvation in Polarizable Water: Molecular Dynamics Simulations. American Chemical Society, 113 (1991), 2481
- [104] J. A. White, E. Schwegler, G. Galli, F. Gygi. The solvation of Na+ in water: First-principles simulations. The Journal of Chemical Physics, 113 (2000), 4668
- [105] R. Jimenez, G. Fleming, P. V. Kumar, M. Maroncelli. Femtosecond solvation dynamics of water. Nature, 369 (1994), 471
- [106] A. L. Sobolewski, W. Domcke. Ab Initio Investigation of the Structure and Spectroscopy of Hydronium - Water Clusters. Journal of Physical Chemistry A, 106 (2002), 4158
- [107] M. H. Begemann, R. J. Saykally. A study of the structure and dynamics of the hydronium ion by high-resolution infrared laser spectroscopy. I. The  $\nu 3$  band of H3 16O+. The Journal of Chemical Physics, 82 (1985), 3570
- [108] O. Markovitch, N. Agmon. Structure and energetics of the hydronium hydration shells. The Journal of Physical Chemistry A, 111 (2007), 2253
- [109] D. Marx, M. Tuckerman, J. Huttler, M. Parrinello. The nature of the hydrated excess proton in water. Nature, 397 (1999), 601
- [110] L. I. Yeh, M. Okumura, J. D. Myers, J. M. Price, Y. T. Lee. Vibrational spectroscopy of the hydrated hydronium cluster ions H3O+(H2O)n (n=1, 2, 3). The Journal of Chemical Physics, 91 (1989), 7319
- [111] L. Yeh, Y. Lee, J. Hougen. Vibration-Rotation Spectroscopy of the Hydrated Hydronium Ions H5O+2 and H9O+4, 1994
- [112] D. Marx. Proton Transfer 200 Years after von Grotthuss: Insights from Ab Initio Simulations. Chemphyschem, 7 (2006), 1848
- [113] N. Agmon. The Grotthuss mechanism. Chemical Physics Letters, 244 (1995), 456

[114] H. Lapid, N. Agmon, M. K. Petersen, G. A. Voth. A bond-order analysis of the mechanism for hydrated proton mobility in liquid water. The Journal of Chemical Physics, 122 (2005), 14506

- [115] M. Tuckerman, K. Laasonen, M. Sprik, M. Parrinello. Ab initio molecular dynamics simulation of the solvation and transport of hydronium and hydroxyl ions in water. The Journal of Chemical Physics, 103 (1995), 150
- [116] X. Yuan, H. Wang, J. Colinsun, J. Zhang. AC impedance technique in PEM fuel cell diagnosis A review. International Journal of Hydrogen Energy, 32 (2007), 4365
- [117] X. Ren, S. Gottesfeld. Electro-osmotic Drag of Water in Poly(perfluorosulfonic acid) Membranes. Journal of The Electrochemical Society, 148 (2001), A87
- [118] T. A. Zawodzinski, J. Davey, J. Valerio, S. Gottesfeld. The water content dependence electro-osmotic drag in proton-conducting polymer electrolytes. Electrochemical Acta, 40 (1995), 297
- [119] K. Onda, T. Murakami, T. Hikosaka, M. Kobayashi, R. Notu, K. Ito. Performance Analysis of Polymer-Electrolyte Water Electrolysis Cell at a Small-Unit Test Cell and Performance Prediction of Large Stacked Cell. Journal of The Electrochemical Society, 149 (2002), A1069
- [120] M. Schalenbach, T. Hoefner, P. Paciok, M. Carmo, W. Lueke, D. Stolten. Gas Permeation Through Nafion. Part 1: Measurements. Physical Chemistry C, 119 (2015), 25145
- [121] C. Rogers. Permeation of Gases and Vapours in Polymers. Elsevier Applied Science Publishers, 1985
- [122] A. Einstein. Über die von der molekularkinetischen Theorie der Wärme geforderte Bewegung von in ruhenden Flüssigkeiten suspendierten Teilchen. Annalen der Physik, 332 (1905), 549
- [123] T. Dorfmueller, W. T. Hering, K. Stierstadt, G. Fischer. Lehrbuch der Experimentalphysik Band 1. Walter De Gruyter, Berlin New York, 11 edition, 1998
- [124] D. Wise, G. Houghton. The diffusion coefficients of ten slightly soluble gases in water at 10-60ÂřC. Chemical Engeneering Science, 21 (1966), 999
- [125] D. M. Himmelblau. Diffusion of Dissolved Gases in Liquids. Chem. Rev, 64 (1964), 527
- [126] National Institute of Standards and Technology. http://webbook.nist.gov/chemistry/fluid/
- [127] M. Hess, R. G. Jones, J. Kahovec, T. Kitayama, P. Kratochvíl, P. Kubisa, W. Mormann, R. F. T. Stepto, D. Tabak, J. Vohlídal, E. S. Wilks. Terminology of polymers containing ionizable or ionic groups and of polymers containing ions (IUPAC Recommendations 2006). Pure and Applied Chemistry, 78 (2006), 2067
- [128] B. Smitha, S. Sridhar, A. Khan. Solid polymer electrolyte membranes for fuel cell applications a review. Journal of Membrane Science, 259 (2005), 10

[129] H. L. Yeager, a. Steck. Ion-exchange selectivity and metal ion separations with a perfluorinated cation-exchange polymer. Analytical Chemistry, 51 (1979), 862

- [130] A. Steck, H. Yeager. Water Sorption and Cation-Exchange Selectivity of a Perfluorosulfonate Ion-Exchange Polymer. Analytical Chemistry, 52 (1980), 1215
- [131] H. Yeager, A. Steck. Cation and Water Diffusion in Nation Ion Exchange Membranes: Influence of Polymer Structure. Journal of The Electrochemical Society, 128 (1982), 1880
- [132] J. Divisek, M. Eikerling, V. M. H. Schmitz, U. Stimming, Y. M. Volfkovichb. A Study of Capillary Porous Structure and Sorption Properties of Nafion Proton-Exchange Membranes Swollen in Water. Journal of The Electrochemical Society, 145 (1998), 2677
- [133] S. Stucki, G. G. Scherer, S. Schlagowski, E. Fischer. PEM water electrolysers: evidence for membrane failure in 100 kW demonstration plants. Journal of Applied Electrochemistry, 28 (1998), 1041
- [134] K.-D. Kreuer. Ion Conducting Membranes for Fuel Cells and other Electrochemical Devices. Chemistry of Materials, 26 (2014), 361
- [135] T. J. Peckham, S. Holdcroft. Structure-morphology-property relationships of non-perfluorinated proton-conducting membranes. Advanced materials (Deerfield Beach, Fla.), 22 (2010), 4667
- [136] M. Rikukawa, K. Sanui. Proton-conducting polymer electrolyte membranes based on hydrocarbon polymers. Progress in Polymer Science, 25 (2000), 1463
- [137] D. Zhao, J. Li, M.-K. Song, B. Yi, H. Zhang, M. Liu. A Durable Alternative for Proton-Exchange Membranes: Sulfonated Poly(Benzoxazole Thioether Sulfone)s. Advanced Energy Materials, 1 (2011), 203
- [138] G. Wei, L. Xu, C. Huang, Y. Wang. SPE water electrolysis with SPEEK/PES blend membrane. International Journal of Hydrogen Energy, 35 (2010), 7778
- [139] L. Gubler. Polymer Design Strategies for Radiation Grafted Membranes. Advanced Energy Materials, 4 (2014), 1300827
- [140] L. Zhang, C. Ma, S. Mukerjee. Oxygen permeation studies on alternative proton exchange membranes designed for elevated temperature operation. Electrochimica Acta, 48 (2003), 1845
- [141] V. A. Sethuraman, J. W. Weidner, A. T. Haug, L. V. Protsailo. Durability of Perfluorosulfonic Acid and Hydrocarbon Membranes: Effect of Humidity and Temperature. J Electrochem Soc, 155 (2008), B119
- [142] R. W. Kopitzke, C. A. Linkous, H. R. Anderson, G. L. Nelson. Conductivity and Water Uptake of Aromatic-Based Proton Exchange Membrane Electrolytes. Journal of The Electrochemical Society, 147 (2000), 1677

[143] R. W. Kopitzke, C. A. Linkous, H. R. Anderson, G. L. Nelson. Conductivity and Water Uptake of Aromatic-Based Proton Exchange Membrane Electrolytes. Journal of The Electrochemical Society, 147 (2000), 1677

- [144] M. H. Eikerling, P. Berg. Poroelectroelastic Theory of Water Sorption and Swelling in Polymer Electrolyte Membranes. Soft Matter, 7 (2011), 5976
- [145] V. A. Sethuraman, J. W. Weidner, A. T. Haug, S. Motupally, L. V. Protsailo. Hydrogen Peroxide Formation Rates in a PEMFC Anode and Cathode. J Electrochem Soc, 155 (2008), B50
- [146] Verein Deutscher Ingenieure. VDI-Richtlinien: Abnahme- und Leistungsversuche an Verdichtern. VDI-Richtlinien, VDI 2045 (1993), 40
- [147] T. Sakai. Gas Permeation Properties of Solid Polymer Electrolyte (SPE) Membranes. Journal of The Electrochemical Society, 132 (1985), 1328
- [148] R. Hiesgen, S. Helmly, I. Galm, T. Morawietz, M. Handl, K. A. Friedrich. Microscopic analysis of current and mechanical properties of Nafion studied by atomic force microscopy. Membranes, 2 (2012), 783
- [149] S. K. Young, S. F. Trevino, N. C. Beck Tan. Small-angle neutron scattering investigation of structural changes in nation membranes induced by swelling with various solvents. Journal of Polymer Science Part B: Polymer Physics, 40 (2002), 387
- [150] S. K. Young, S. F. Trevino, N. C. Beck Tan. Small-Angle Neutron Scattering Investigation of Structural Changes in Nafion Membranes Induced by Swelling with Various Solvents. Journal of Polymer Science Part B: Polymer Physics, 40 (2002), 387
- [151] K.-D. Kreuer. The Role of Internal Pressure for the Hydration and Transport Properties of Ionomers and Polyelectrolytes. Solid State Ionics, 252 (2013), 93
- [152] J. T. Gostick, A. Z. Weber. Resistor-Network Modeling of Ionic Conduction in Polymer Electrolytes. Electrochimica Acta, 6
- [153] C. E. Evans, R. D. Noble, S. Nazeri-Thompson, B. Nazeri, C. A. Koval. Role of Conditioning on Water Uptake and Hydraulic Permeability of Nafion Membranes. Journal of Membrane Science, 279 (2006), 521
- [154] T. A. Zawodzinski, C. Derouin, S. Radzinski, R. J. Sherman, V. T. Smith, T. E. Springer, S. Gottesfeld. Water Uptake by and Transport Through Nation 117 Membranes. Journal of The Electrochemical Society, 140
- [155] N. E. Cipollini. Chemical Aspects of Membrane Degradation. ECS Transactions, 11 (2007), 1071
- [156] K. D. Kreuer, G. Portale. A Critical Revision of the Nano-Morphology of Proton Conducting Ionomers and Polyelectrolytes for Fuel Cell Applications. Materials Views, 23 (2013), 5390

[157] A. Z. Weber, J. Newman. Transport in Polymer-Electrolyte Membranes. Journal of The Electrochemical Society, 151 (2004), A311

- [158] A. Weber, E. Ivers-Tiffée. Materials and concepts for solid oxide fuel cells (SOFCs) in stationary and mobile applications. Journal of Power Sources, 127 (2004), 273
- [159] Q. Zhao, P. Majsztrik, J. Benziger. Diffusion and interfacial transport of water in Nafion. The journal of physical chemistry. B, 115 (2011), 2717
- [160] S. J. Paddison, R. Paul, T. A. Zawodzinski. A Statistical Mechanical Model of Proton and Water Transport in a Proton Exchange Membrane. Journal of The Electrochemical Society, 147 (2000), 617
- [161] J. Karo, A. Aabloo, J. O. Thomas, D. Brandell. Molecular Dynamics Modeling of Proton Transport in Nafion and Hyflon Nanostructures. The journal of physical chemistry. B, 114 (2010), 6056
- [162] S. Feng, G. A. Voth. Proton solvation and transport in hydrated nation. The Journal of Physical Chemistry B, 115 (2011), 5903
- [163] B. F. Habenicht, S. J. Paddison, M. E. Tuckerman. The effects of the hydrophobic environment on proton mobility in perfluorosulfonic acid systems: an ab initio molecular dynamics study. Journal of Materials Chemistry, 20 (2010), 6342
- [164] Y.-K. Choe, E. Tsuchida, T. Ikeshoji, S. Yamakawa, S.-A. Hyodo. Nature of proton dynamics in a polymer electrolyte membrane, nation: a first-principles molecular dynamics study. Physical chemistry chemical physics, 11 (2009), 3892
- [165] R. Devanathan, A. Venkatnathan, R. Rousseau, M. Dupuis, T. Frigato, W. Gu, V. Helms. Atomistic simulation of water percolation and proton hopping in Nafion fuel cell membrane. The Journal of Physical Chemistry B, 114 (2010), 13681
- [166] T. J. Peckham, J. Schmeisser, M. Rodgers, S. Holdcroft. Main-chain, statistically sulfonated proton exchange membranes: the relationships of acid concentration and proton mobility to water content and their effect upon proton conductivity. Journal of Materials Chemistry, 17 (2007), 3255
- [167] M. K. Petersen, G. a. Voth. Characterization of the solvation and transport of the hydrated proton in the perfluorosulfonic acid membrane Nafion. The Journal of Physical Chemistry B, 110 (2006), 18594
- [168] H. Lapid, N. Agmon, M. K. Petersen, G. A. Voth. A bond-order analysis of the mechanism for hydrated proton mobility in liquid water. The Journal of Chemical Physics, 122 (2005), 14506
- [169] M. Eikerling, A. A. Kornyshev, U. Stimming. Electrophysical Properties of Polymer Electrolyte Membranes: A Random Network Model. Journal of Physical Chemistry B, 101 (1997), 10807

[170] D. M. Bernardi, M. W. Verbrugge. A Mathematical Model of the Solid-Polymer-Electrolyte Fuel Cell. Journal of the Electrochemical Society, 139 (1992), 2477

- [171] M. Devanathan, Z. Stachurski. The adsorption and diffusion of electrolytic hydrogen in palladium. Proceedings of the Royal Society of London A, 270 (1962), 90
- [172] X. Cheng, J. Zhang, Y. Tang, C. Song, J. Shen, D. Song, J. Zhang. Hydrogen crossover in high-temperature PEM fuel cells. Journal of Power Sources, 167 (2007), 25
- [173] B. E. Poling, J. M. Prausnitz, J. P. O'Connell. The Properties of Gases and Liquids. McGraw-Hill, fifth edition, 2001
- [174] P. H. Huang. Humidity Standard of Compressed Hydrogen for Fuel Cell Technology. ECS Transactions, 12 (2008), 479
- [175] OpenPNM simulation package
- [176] M. Schalenbach, W. Lueke, W. Lehnert, D. Stolten. The influence of the water channel geometry and the proton mobility on the conductivity of Nafion. Electrochimica Acta, accepted
- [177] E. Riedel. Anorganische Chemie. deGruyter, fifth edition, 2002
- [178] P. Atkins. Physical Chemistry. Oxforf University press, 9 edition, 2010
- [179] W. J. Hamer, H. J. DeWane. Electrolyte Conductance and the Conductances of the Halogen Acids in Water. National Standard Reference Data System, 33 (1970), 1
- [180] I. Zaytsev, G. Aseyev. Properties of Aqueous Solutions of Electrolytes. CRC Press, Boca Raton, 1992
- [181] H.-G. Haubold, T. Vad, H. Jungbluth, P. Hiller. Nano Structure of NAFION: A SAXS Study. Electrochimica Acta, 46 (2001), 1559
- [182] R. Krishna, J. A. Wesselingh. The Maxwell-Stefan approach to mass transfer. Chemical Engineering Science, 52 (1997), 861
- [183] E. N. Lightfoot, E. L. Cussler, R. L. Rettig. Applicability of the Stefan-Maxwell Equations to Multicomponent Diffusion in Liquids. A.I.Ch.E., 8 (1962), 708
- [184] G. D. Mehta, T. F. Morse, E. A. Mason, M. H. Daneshpajooh. Generalized Nernst-Planck and Stefan-Maxwell equations for membrane transport. The Journal of Chemical Physics, 64 (1976), 3917
- [185] R. Pasternak, M. Christensen, J. Heller. Diffusion and Permeation of Oxygen, Nitrogen, Carbon Dioxide, and Nitrogen Dioxide through Polytetrafluoroethylene. Macromolecules, 3 (1969), 366
- [186] A. Bondi. van der Waals Volumes and Radii. The Journal of Physical Chemistry, 68 (1964), 441

[187] H. Gray. Chemical Bonds: An Introduction to Atomic and Molecular Structure. University Science Books, Sausalito, 1 edition, 1994

- [188] T. E. Springer, T. A. Zawodzinski, S. Gottesfeld. Polymer Electrolyte Fuel Cell Model. J Electrochem Soc, 138 (1993), 2334
- [189] M. Schalenbach, M. Hoeh, J. Gostick, W. Lueke, D. Stolten. Gas Permeation through Nafion. Part 2: Resistor network model. Physical Chemistry C, 119 (2015), 25156
- [190] M. Olano, J. C. Hart, W. Heidrich, B. Mark, K. Perlin. Real-time shading languages. SIGGRAPH, Course 36
- [191] A. Lagae, S. Lefebvre, R. Cook, T. DeRose, G. Drettakis, D. Ebert, J. Lewis, K. Perlin, M. Zwicker. A Survey of Procedural Noise Functions. Computer Graphics Forum, 29 (2010), 2579
- [192] Phython noise package
- [193] S. Torquato. Random Heterogeneous Materials: Microstructure and Macroscopic Properties. Springer Science & Business Media, 2013
- [194] K. Modig, B. Pfrommer, B. Halle. Temperature-Dependent Hydrogen-Bond Geometry in Liquid Water. Physical Review Letters, 90 (2003), 075502
- [195] E. Narita, F. Lawson, K. N. Han. Solubility of Oxygen in Aqueous Electrolyte Solutions. Hydrometallurgy, 10 (1983), 21
- [196] P. Ruetschi, R. F. Amlie. Solubility of Hydrogen in Potassium Hydroxide and Sulfuric Acid. Salting-out and Hydration. The Journal of Physical Chemistry, 70 (1966), 718
- [197] K. E. Gubbins, R. D. J. Walker. The Solubility and Diffusivity of Oxygen in Electrolytic Solutions. Journal of The Electrochemical Society, 112 (1965), 469
- [198] R. E. Davis, G. L. Horvath, C. W. Tobias. The Solubility and Diffusion Coefficient of Oxygen in Potassium Hydroxide Solutions. Electrochimica Acta, 12 (1967), 287
- [199] B. F. H. Rhodes, C. B. Barbour. The Viscosities of Mixtures of Sulfuric Acid and Water. Industrial and Engineering Chemistry, 15 (1923), 850
- [200] Concentrative Properties of Aqueous Solutions: Density, Refractive Index, Freezing Point Depression, and Viscosity. In: Handbook of Chemistry and Physics. Taylor and Francis Group, LLC, 96 edition, 2015, pages 123–148
- [201] Scipy python library
- [202] G. Gebel. Structural Evolution of Water Swollen Perfluorosulfonated Ionomers from Dry Membrane to Solution. Polymer, 41 (2000), 5829
- [203] Y. Li, Q. T. Nguyen, C. L. Buquet, D. Langevin, M. Legras, S. Marais. Water Sorption in Nafion Membranes Analyzed with an Improved Dual-Mode Sorption Model-Structure/Property Relationships. Journal of Membrane Science, 439 (2013), 1

[204] T. Yasuda, T. Okuno, H. Yasuda. Contact Angle of Water on Polymer Surfaces. Langemuir, 10 (1994), 2435

- [205] M. E. Tadros, P. Hu, A. W. Adamson. Adsorption and Contact Angle Studies I. Water on Smooth Carbon, Linear Polyethylene, and Stearic Acid-Coated Copper. Journal of Colloid and Interface Science, 49 (1974), 184
- [206] A. S. Michaels, H. J. Bixler. Flow of Gases Through Polyethylene. Journal of Polymer Science, 50 (1961), 413
- [207] A. S. Michaels, H. J. Bixler. Solubility of Gases in Polyethylene. Journal of Polymer Science, 50 (1961), 393
- [208] DuPont Fuel Cells. DuPont Nafion PFSA Membranes. http://www2.dupont.com/FuelCells/en\_US/products/nafion.html, 2015
- [209] K. E. Ayers, C. Capuano, E. B. Anderson. Recent Advances in Cell Cost and Efficiency for PEM-Based Water Electrolysis. ECS Transactions, 41 (2012), 15
- [210] M. Schalenbach. Corrigendum to "Pressurized PEM water electrolysis: Efficiency and gas crossover" [ Int J Hydrogen Energy 38 (2013) 14921-14933]. International Journal of Hydrogen Energy, 41 (2015), 729
- [211] M. Schalenbach, G. Tjarks, M. Carmo, W. Lueke, M. Mueller, D. Stolten. Acidic or alkaline? Towards a new perspective on the efficiency of water electrolysis. Journal of the Electrochemical Society, 163 (2016), F3197
- [212] Y. Tanaka, K. Kikuchi, Y. Saihara, Z. Ogumi. Bubble visualization and electrolyte dependency of dissolving hydrogen in electrolyzed water using Solid-Polymer-Electrolyte. Electrochimica Acta, 50 (2005), 5229
- [213] K. Kikuchi, S. Nagata, Y. Tanaka, Y. Saihara, Z. Ogumi. Characteristics of hydrogen nanobubbles in solutions obtained with water electrolysis. Journal of Electroanalytical Chemistry, 600 (2007), 303
- [214] M. Schalenbach, W. Lueke, D. Stolten. Hydrogen diffusivity and electrolyte permeability of the Zirfon diaphragm for alkaline water electrolysis. Journal of Membrane Science, 163 (2016), F1480
- [215] C. Ziegler, S. Thiele, R. Zengerle. Direct three-dimensional reconstruction of a nanoporous catalyst layer for a polymer electrolyte fuel cell. Journal of Power Sources, 196 (2011), 2094
- [216] W. K. Epting, J. Gelb, S. Litster. Resolving the Three-Dimensional Microstructure of Polymer Electrolyte Fuel Cell Electrodes using Nanometer-Scale X-ray Computed Tomography. Materials Views, 22 (2012), 555
- [217] R. L. LeRoy, C. T. Bowen, D. J. LeRoy. The Thermodynamics of Aqueous Water Electrolysis. Journal of the Electrochemical Society, 127 (1980), 1954

[218] Y. Tanaka, S. Uchinashi, Y. Saihara, K. Kikuchi, T. Okaya, Z. Ogumi. Dissolution of hydrogen and the ratio of the dissolved hydrogen content to the produced hydrogen in electrolyzed water using SPE water electrolyzer. Electrochimica Acta, 48 (2003), 4013

- [219] K. Kikuchi, Y. Tanaka, Y. Saihara, M. Maeda, M. Kawamura, Z. Ogumi. Concentration of hydrogen nanobubbles in electrolyzed water. Journal of colloid and interface science, 298 (2006), 914
- [220] K. C. Neyerlin, W. Gu, J. Jorne, H. A. Gasteiger. Study of the Exchange Current Density for the Hydrogen Oxidation and Evolution Reactions. Journal of The Electrochemical Society, 154 (2007), B631
- [221] J. C. F. Boodts, S. Trasatti. Hydrogen evolution on iridium oxide cathodes. Journal of Applied Electrochemistry, 19 (1989), 255
- [222] J. D. E. McIntyre, W. F. Peck, S. Nakahara. Oxidation State Changes and Structure of Electrochromic Iridium Oxide Films. Journal of The Electrochemical Society, 127 (1980), 1264
- [223] The Linde Group. Hydrogen technologies: The Ionic Compressor 90 MPa IC90 (Datasheet), 2015
- [224] M. H. Miles, E. A. Klaus, B. P. Gunn. The Oxygen Evolution Reaction on Platinum, Iridium, Ruthenium and their Alloys at 80C in Acid Solutions. Electrochemica Acta 1978, 23 (1977), 521
- [225] V. Antonucci, a. Di Blasi, V. Baglio, R. Ornelas, F. Matteucci, J. Ledesma-Garcia, L. Arriaga, a.S. Aricò. High temperature operation of a composite membrane-based solid polymer electrolyte water electrolyser. Electrochimica Acta, 53 (2008), 7350
- [226] S. J. Sondheimer, N. J. Bunce, C. A. Fyfe. Structure and Chemistry of Nafion-H: a Fluorinated Sulfonic Acid Polymer. Journal of Macromolecular Science, Part C: Polymer Reviews, 26 (1986), 353
- [227] J. Baker-Jarvis, E. J. Vanzura, W. A. Kissick. Improved Technique for Determining Complex Permittivity with the Transmission / Reflection Method. IEE Transactions on Microwave Theory and Techniques, 38 (1990), 1096
- [228] F. Lufrano, G. Squadrito, A. Patti, E. Passalacqua. Sulfonated Polysulfone as Promising Membranes for Polymer Electrolyte Fuel Cells. Journal of Applied Polymer Science, 77 (2000), 1250
- [229] J. K. Nørskov, J. Rossmeisl, A. Logadottir, L. Lindqvist, J. Kitchin, T. Bligaard, H. Jonsson. Origin of the Overpotential for Oxygen Reduction at a Fuel-Cell Cathode. Journal of Physical Chemistry B, 108 (2004), 17886

### Acknowledgment

Firstly, I would like to express my sincere gratitude to my advisor Prof. Dr. Detlef Stolten for the continuous support of my Ph.D study and related research. His guidance and scientific support helped me in all the time of research and writing of this thesis.

Secondly, I would like to thank Prof. Dr. Eckhard Spohr for being the second referee for the thesis. I would like to thank the rest of my thesis committee.

My sincere thanks also goes to Dr. Marcelo Carmo, Dr. Jürgen Mergel and Dr. Wiebke Lüke, who provided me the opportunity to join their team as intern. Without they precious support it would not be possible to conduct this research. In particular, I am grateful to Marcelo and Jürgen for enlightening me the first glance of research and their patience especially in the first months.

I thank my fellow PhD students, namely Geert Tjarks, Manuel Langemann, Tobias Höfner, Paul Paciok and Michael Höh for most importantly all the fun we had together. I can remember endless scientific and private discussions with Paul and Michael, which guided me through an interesting time at the institute.

Several people that helped me to develop experimental setups have to be thanked. A few of those I would like to mention here are Daniel Holtz, Thomas Pütz und Michelle Poestges, Stefanie Fischer, Fabian Tigges, Norbert Commerscheidt and Richard Wegner, who were able to solve all technical issues. Also thanks to the rest of the team in the IEK-3 of the Forschungszentrum Jülich for their support.

Last but not the least, I would like to thank my family. My parents, Ulrike and Horst, who have provided me through moral, emotional and financial support in my life. Very special thanks to my brother, Marcus, the person who most influenced me in my life and from whom I have learned most. I will always love and miss you, rest in peace. Viola, my girlfriend, helped me in difficult times with her endless support, for which I would like to convey special thanks. I would also like to express my gratitude to all my friends and the rest of my family.

Band / Volume 413

Mechanismen der chrombasierten Degradation von metallgestützten Festoxid-Brennstoffzellen

A. Beez (2018), VIII, 144 pp ISBN: 978-3-95806-306-8

Band / Volume 414

Entwicklung eines Werkzeugs zur Modellierung der Nettoerosion im Hauptraum der Brennkammer eines Tokamaks und Studium der Plasma-Wand-Wechselwirkung an DEMO1

M. Beckers (2018), XIX, 150 pp ISBN: 978-3-95806-307-5

Band / Volume 415

Fehlstellendotierung von Eisenoxid- und Bismutsulfid-Nanopartikeln

J. P. Mock (2018), v, 187 pp ISBN: 978-3-95806-309-9

Band / Volume 416

Nanocrystalline Silicon Oxide in Silicon Heterojunction Solar Cells

A. Richter (2018), 166 pp ISBN: 978-3-95806-310-5

Band / Volume 417

Gas-to-Particle Partitioning of Major Oxidation Products from Monoterpenes and Real Plant Emissions

G. Gkatzelis (2018), xii, 128 pp ISBN: 978-3-95806-314-3

Band / Volume 418

The Dynamics of Electrons in Linear Plasma Devices and its Impact on Plasma Surface Interaction

M. Hubeny (2018), 141 pp ISBN: 978-3-95806-316-7

Band / Volume 419

Tomographic reconstruction of gravity wave parameters from satellite-borne airglow observations

R. Song (2018), 136 pp ISBN: 978-3-95806-317-4

Band / Volume 420

Reduktion von Edelmetallen in der Wasserstoffelektrode bei der Polymerelektrolyt-Wasserelektrolyse

P. Paciok (2018), VII, 187 pp ISBN: 978-3-95806-320-4 Band / Volume 421

# Mechanismen des Hochtemperaturrisswachstums in einem ferritischen Stahl an Luft und in Wasserdampf

T. Fischer (2018), VIII, 216 pp ISBN: 978-3-95806-326-6

Band / Volume 422

# Selbstheilende plasmagespritzte Mn<sub>1,0</sub>Co<sub>1,9</sub>Fe<sub>0,1</sub>O<sub>4</sub>-Schutzschichten in Festoxidbrennstoffzellen

N. Grünwald (2018), viii, 137 pp ISBN: 978-3-95806-327-3

Band / Volume 423

# Sonochemical Synthesis of Silicon Hydride Polymers and Silicon Nanoparticles from Liquid Silanes

A. P. Cádiz Bedini (2018), viii, 132, XVIII pp

ISBN: 978-3-95806-329-7

Band / Volume 424

# Synthesis and Stability Assessment of Uranium Microparticles: Providing Reference Materials for Nuclear Verification Purposes

R. Middendorp (2018), X, 145 pp

ISBN: 978-3-95806-330-3

Band / Volume 425

#### Herstellung und Charakterisierung von Lithiumlanthanzirkonat-Funktionsschichten für Lithium-Festkörperbatterien

T. Reppert (2018), vii, 187 pp ISBN: 978-3-95806-331-0

Band / Volume 426

# Proton Conduction and Gas Permeation through Polymer Electrolyte Membranes during Water Electrolysis

M. Schalenbach (2018), VI, 212 pp

ISBN: 978-3-95806-333-4

Weitere Schriften des Verlags im Forschungszentrum Jülich unter http://www.zb1.fz-juelich.de/verlagextern1/index.asp

Energie & Umwelt / Energy & Environment Band / Volume 426 ISBN 978-3-95806-333-4

